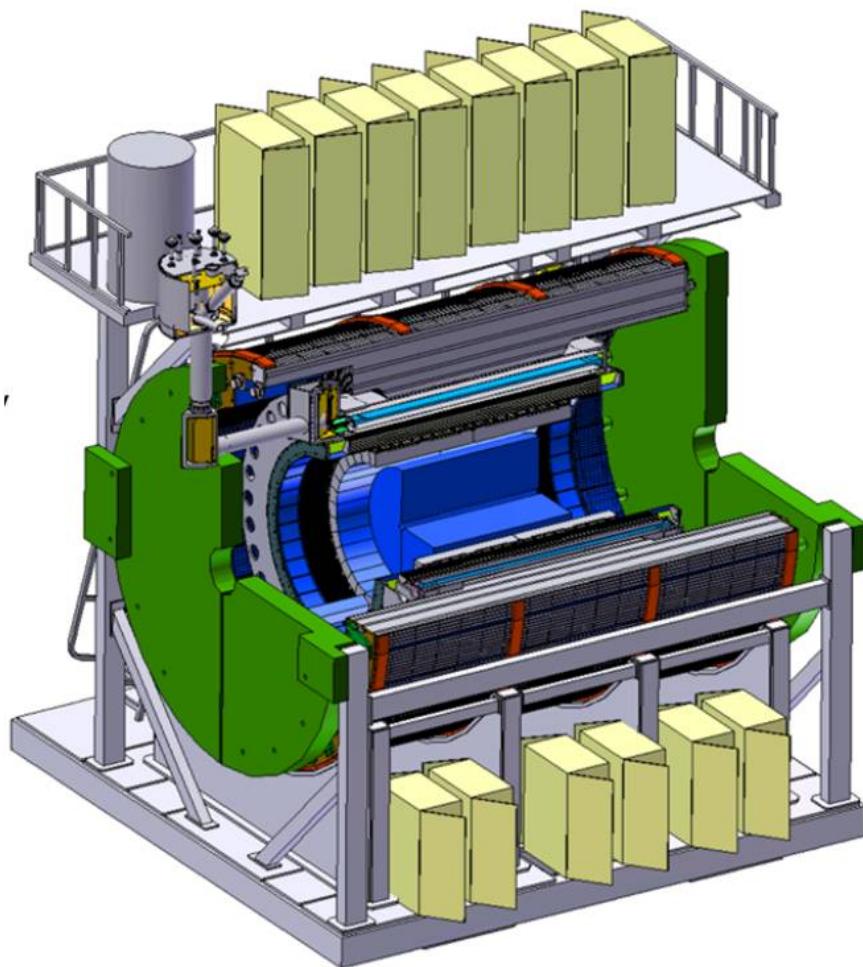




# sPHENIX preConceptual Design Report

October 27, 2015







# Executive Summary

sPHENIX[1] is a proposal for a new experiment at RHIC capable of measuring jets, jet correlations and upsilons to determine the temperature dependence of transport coefficients of the quark-gluon plasma. The detector needed to make these measurements require electromagnetic and hadronic calorimetry for measurements of jets, a high resolution and low mass tracking system for reconstruction of the Upsilon states, and a high speed data acquisition system.

This document describes a design for a detector capable of carrying out this program of measurements built around the BaBar solenoid. As much as possible, the mechanical, electrical, and electronic infrastructure developed for the PHENIX experiment from 1992-2016 is reused for sPHENIX. The major new systems are the superconducting magnet, a high precision tracking system, and electromagnetic and hadronic calorimeters.

Several alternatives for tracking technologies have been explored, and the physics capability of a reference design consisting of silicon pixel and strip sensors has been evaluated, and the feasibility of surrounding them with a small TPC has been studied.

The electromagnetic calorimeter is a compact tungsten-scintillating fiber design located inside the solenoid. There are two sections of hadronic calorimeter, one inside the solenoid and the other outside made of steel-scintillator in a somewhat novel arrangement in which scintillator tiles with light collected by wavelength shifting fiber are sandwiched between tapered absorber plates that project nearly radially from the interaction point. The calorimeters use a common set of silicon photomultiplier photodetectors and amplifier and digitizer electronics.

The detector design has been evaluated by means of GEANT4 simulation and measurements with early prototypes of some of the detectors. Additional simulation and testing of components is being pursued to finalize the design.



# Contents

<b>1 Scientific Objective and Performance</b>	<b>1</b>
1.1 Coupling Strength of the QGP	3
1.2 Probing Different Length Scales in the QGP	4
1.3 The Temperature Dependence of the QGP	6
1.4 Evolution of Parton Virtuality in the QGP	9
1.5 Current Jet Probe Measurements	10
1.6 Using Jets at RHIC to Constrain Theoretical Calculations	13
1.7 Fragmentation Functions	16
1.8 Heavy Quark Jets	18
1.9 Quarkonia in the QGP	21
1.10 Jet Rates and Physics Reach	25
<b>2 Detector Overview</b>	<b>33</b>
2.1 Acceptance	36
2.2 Segmentation	37
2.3 Energy Resolution	38
2.4 Tracking	38
2.5 Triggering	39
<b>3 Superconducting Magnet</b>	<b>41</b>
3.1 Magnet Mechanical Design	41
3.2 Cryogenics	48
3.3 Magnet Power Supply	52
3.4 Tests for the Superconducting Solenoid Magnet	57
<b>4 Tracker</b>	<b>67</b>
4.1 Physics requirements	67

4.2	General Remarks about Tracking . . . . .	68
4.3	Overview of Tracking Options . . . . .	72
4.4	Reuse of the PHENIX Pixel Detector . . . . .	72
4.5	MAPS Pixel . . . . .	74
4.6	Silicon Strip Outer Tracker Option . . . . .	77
4.7	TPC option . . . . .	94
4.8	Alternative technologies . . . . .	127
<b>5</b>	<b>Electromagnetic Calorimeter . . . . .</b>	<b>129</b>
5.1	Physics Requirements . . . . .	129
5.2	Detector Design . . . . .	130
5.3	Simulations . . . . .	141
5.4	Prototyping and R&D . . . . .	149
5.5	Alternative Technologies . . . . .	150
<b>6</b>	<b>Hadronic Calorimeter . . . . .</b>	<b>159</b>
6.1	HCAL Requirements and Overview . . . . .	159
6.2	Detector Design . . . . .	160
6.3	Simulations . . . . .	168
6.4	Prototyping and R&D . . . . .	178
<b>7</b>	<b>Calorimeter Electronics . . . . .</b>	<b>193</b>
7.1	Optical Sensors . . . . .	194
7.2	Readout Electronics . . . . .	204
7.3	Power Systems and Ground . . . . .	211
7.4	Radiation Tolerance . . . . .	211
7.5	Alternative Technologies . . . . .	212
<b>8</b>	<b>Data Acquisition and Trigger . . . . .</b>	<b>215</b>
8.1	Data Acquisition . . . . .	215
8.2	Triggering. . . . .	219
<b>9</b>	<b>Infrastructure. . . . .</b>	<b>223</b>
9.1	Auxiliary Buildings at the Experimental Site . . . . .	223
9.2	Central Pedestal . . . . .	223
9.3	Electronics Racks . . . . .	225

9.4 Beam Pipe . . . . .	225
9.5 Shield Walls and Openings . . . . .	225
9.6 Electrical Power . . . . .	226
9.7 Safety System and Control Room Monitoring & Alarm System . . . . .	226
9.8 Cooling Water . . . . .	226
9.9 Climate Control . . . . .	226
9.10 Cryogenics . . . . .	227
<b>10 Installation and Integration.</b> . . . .	<b>229</b>
10.1 Specifications and Requirements . . . . .	230
10.2 Component Integration . . . . .	236
10.3 Installation . . . . .	240
10.4 Testing and Commissioning . . . . .	244
10.5 Alternative Integration/Installation Concepts Considered . . . . .	245
<b>11 Project Management</b> . . . . .	<b>247</b>
11.1 Project Organization . . . . .	247
11.2 Work Breakdown Structure . . . . .	250
11.3 Cost Range and Basis of Estimate . . . . .	251
11.4 Schedule and Labor . . . . .	252
11.5 Risk . . . . .	253
11.6 Quality Assurance . . . . .	256
11.7 Environment, Safety and Health . . . . .	258
<b>List of Tables</b> . . . . .	<b>261</b>
<b>List of Figures</b> . . . . .	<b>263</b>
<b>References</b> . . . . .	<b>279</b>



# Chapter 1

## Scientific Objective and Performance

Results from RHIC and the LHC indicate that a new state of matter is formed in ultra-relativistic collisions of heavy nuclei. Initial temperatures  $T > 300$  MeV [2] at RHIC and  $T > 420$  MeV [3] at the LHC have been extracted from the spectrum of directly-emitted photons from the system. The formation of this state, called the quark-gluon plasma (QGP), was predicted by Lattice QCD and various models and to have existed at similar temperatures prior to the formation of hadrons just microseconds after the Big Bang.

The temperature scales at RHIC and LHC result in an intrinsically non-perturbative system. The difference in the initial temperature created in RHIC and LHC collisions is expected to be associated with changes in the nature of the QGP being probed. Such changes in the properties of the system must be determined in order to properly characterize the new QGP state of matter. Furthermore, to understand the many-body collective effects in the QGP and their temperature dependence near the transition temperature requires considerable further investigation.

The scientific objective of the sPHENIX experiment [1] is to gain an understanding of the evolution of the system and its coupling strength at RHIC from the initial high temperatures, where short distance scales prevail, through expansion and cooling to the transition temperature and longer distance scales. This will be accomplished by using hard-scattered partons that traverse the medium and the Upsilon states to investigate the medium at the different length scales. The fragmentation products of partons in the form of jets and the three Upsilon states, which span a large range in binding energy and size, are complementary and excellent probes for this purpose. The variables in this investigation are the temperature of the QGP, the length scale probed in the medium, and the virtuality of the hard process.

The QGP is expected to transform from a weakly-coupled system at high temperature to a more strongly-coupled system near  $T_c$ . In general, for many systems a change in coupling strength is related to quasi-particle excitations or strong coherent fields. To study these phenomena usually requires that the medium be investigated at a variety of length scales. The collisions at RHIC and the LHC involve a time evolution during

which the temperature decreases as the QGP expands. Determination of the temperature dependence of the properties of the QGP is expected to come from calculations that describe simultaneously all observables measured at both energies. Typically, all the non-scaling behavior is found near the transition. It is therefore crucial to perform measurements near the phase transition and compare with results from experiments done farther above  $T_c$ .

These measurements at RHIC will provide information complementary to those at the LHC. The measurement of jets over the broadest possible energy scale is key to investigating the potential quasi-particle nature of the QGP. Jets at the LHC reach the highest energies, the largest initial virtualities, and large total energy loss to probe the shortest distance scales. The lower underlying event activity at RHIC will allow extension of jet measurements to lower energies and lower initial virtualities than at LHC, thus probing the important longer distance scales in the medium. Figure 1.1 (left), which will be discussed in more detail in Section 1.4, displays as a function of temperature the expected evolution of virtuality in vacuum, from medium contributions, and combined for a QGP. Figure 1.1 (right) shows a scenario for what may be resolved in the QGP by probing at the length scales indicated by the magnifying glasses on the left. In addition to the investigation of jets, precision measurements of the three Upsilon states will allow further insight and understanding of the behavior on different distance scales.

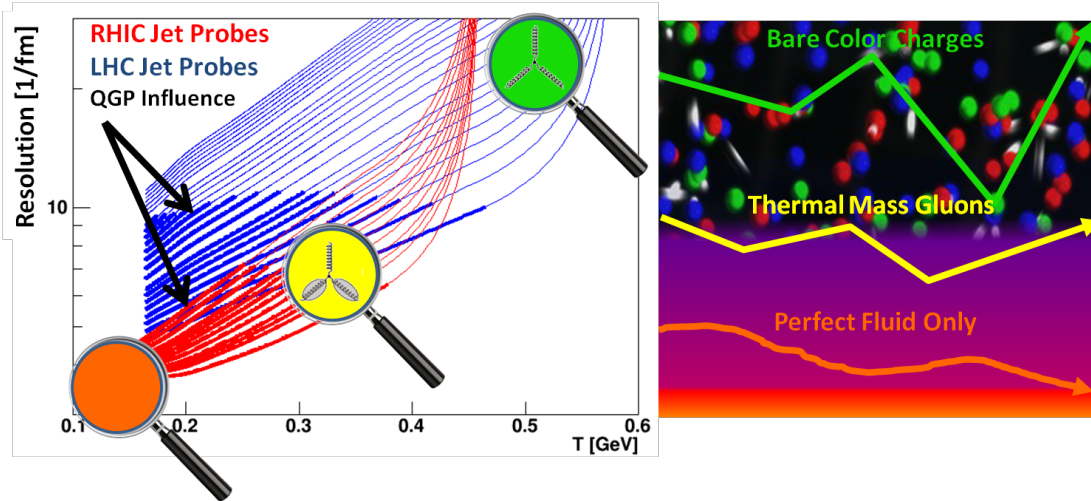


**Figure 1.1:** Virtuality evolution as a function of temperature as represented (left) by the resolution of jet probes at the LHC (blue curves) and at RHIC (red curves). The potential range of influence of the QGP that is being investigated is represented by the bolder curves for each case. The magnified views are meant to represent pQCD scattering from bare quarks and gluons in the medium (green), scattering from thermal gluons (yellow), and a final state integration over all possible objects probed in the medium (orange). (right) Graphical depiction of the objects being probed at the various resolutions on the left.

In this Chapter we start by presenting our current understanding of the role of the coupling strength in the QGP, how it can be probed at different length scales, the temperature



dependence of a few observables of the QGP and the evolution of parton virtuality in the QGP. We then present the case for utilizing hard-scattering (parton) probes to constrain theories and compare a few examples of theoretical calculations with recent LHC data and their differing predictions for RHIC. We relate these aspects to specific observables that can be measured with sPHENIX. These include fragmentation functions from photon-jet correlations, hadron-jet and di-jet measurements, open heavy flavor jets and beauty quarkonia. We conclude with the rates and other performance measures of sPHENIX that will enable precision measurements to be made across a comprehensive jet and quarkonium program at RHIC.

## 1.1 Towards Understanding the Coupling Strength of the QGP

It was originally thought that even at temperatures as low as  $2\text{--}5 T_c$ , the QGP could be described by a weakly-coupled perturbative approach, despite being quite far from energy scales typically associated with asymptotic freedom. One very surprising result discovered at RHIC was the fluid-like flow of the QGP [4], in stark contrast to some expectations that the QGP would behave as a weakly-coupled gas of quarks and gluons. RHIC and LHC heavy ion experiments have since provided a wealth of data for understanding the physics of the QGP.

The QGP created in heavy ion collisions expands and cools, eventually passing through the phase transition to a state of hadrons, which are then measured by experiment. Extensive measurements of the radial and flow coefficients of various hadrons, when compared to hydrodynamics calculations, imply a very small ratio of shear viscosity to entropy density,  $\eta/s$  [5]. In the limit of very weak coupling (i.e., a non-interacting gas), the shear viscosity is quite large as particles can easily diffuse across a velocity gradient in the medium. Stronger inter-particle interactions inhibit diffusion to the limit where the strongest interactions result in a very short mean free path and thus almost no momentum transfer across a velocity gradient, resulting in almost no shear viscosity.

The shortest possible mean free path is of order the de Broglie wavelength, which sets a lower limit on  $\eta/s$  [6]. A more rigorous derivation of the limit  $\eta/s \geq 1/4\pi$  has been calculated within string theory for a broad class of strongly coupled gauge theories by Kovtun, Son, and Starinets (KSS) [7]. Viscous hydrodynamic calculations assuming  $\eta/s$  to be temperature independent through the heavy ion collision time evolution are consistent with the experimental data where  $\eta/s$  is within 50% of this lower bound for strongly coupled matter [5, 8, 9, 10, 11, 12]. Even heavy quarks (i.e., charm and beauty) are swept up in the fluid flow and theoretical extractions of the implied  $\eta/s$  are equally small [13].

Other key measures of the coupling strength to the medium can be found in the passage of a hard-scattered parton through the QGP. As the parton traverses the medium it accumulates transverse momentum as characterized by  $\hat{q} = d(\Delta p_T^2)/dt$  and transfers energy to the medium via collisions as characterized by  $\hat{e} = dE/dt$ . Once in vacuum, the hard-scattered

parton creates a conical shower of particles referred to as a jet. In the QGP, the lower energy portion of the shower may eventually be equilibrated into the medium, thus giving a window on the rapid thermalization process in heavy ion collisions. This highlights part of the reason for needing to measure the fully reconstructed jet energy and the correlated particle emission with respect to the jet at all energy scales. In particular, coupling parameters such as  $\hat{q}$  and  $\hat{e}$  are scale dependent and must take on weak-coupling values at high enough energies and strong-coupling values at thermal energies.

Continued developments in techniques for jet reconstruction in the environment of a heavy ion collision have allowed the LHC experiments to reliably recover jets down to 40 GeV [14, 15], which is well within the range of reconstructed jet energies at RHIC in the future. This overlap opens the possibility of studying the QGP at the same scale but under different conditions of temperature and coupling strength.

Apart from the temperature and coupling strength differences in the medium created at RHIC and the LHC, the difference in the steepness of the hard scattering  $p_T$  spectrum plays an important role. The less steeply falling spectrum at the LHC has the benefit of giving the larger reach in  $p_T$  with reconstructed jets expected up to 1 TeV. At RHIC, the advantage of the more steeply falling spectrum is the greater sensitivity to the medium coupling and QGP modifications of the parton shower. This greater sensitivity may enable true tomography in particular with engineering selections for quarks and/or gluons with longer path length through the medium. In addition, for correlations, once a clean direct photon or jet tag is made, the underlying event is 2.5 times smaller at RHIC compared to the LHC thus giving cleaner access to the low energy remnants of the parton shower and possible medium response. Therefore one focus of this proposal is the measurement of jet probes of the medium as a way of understanding the coupling of the medium, the origin of this coupling, and the mechanism of rapid equilibration.

## 1.2 Probing Different Length Scales in the QGP

In electron scattering, the length scale is set by the virtuality of the exchanged photon,  $Q^2$ . By varying this virtuality one can obtain information over an enormous range of scales: from pictures of viruses at length scales of  $10^{-5}$  meters, to the partonic make-up of the proton in deep inelastic electron scattering at length scales of less than  $10^{-18}$  meters.

For the case of hard-scattered partons in the quark-gluon plasma, the length scale probed is initially set by the virtuality of the hard-scattering process. Thus, at the highest LHC jet energies, the parton initially probes a very short length scale. Then as the evolution proceeds, the length scale is set by the virtuality of the gluon exchanged with the color charges in the medium, as shown in the circular diagram on the right of Figure 1.2. However, if the exchanges are coherent, the total coherent energy loss through the medium may set the length scale.

If the length scale being probed is very small then one expects scattering directly from

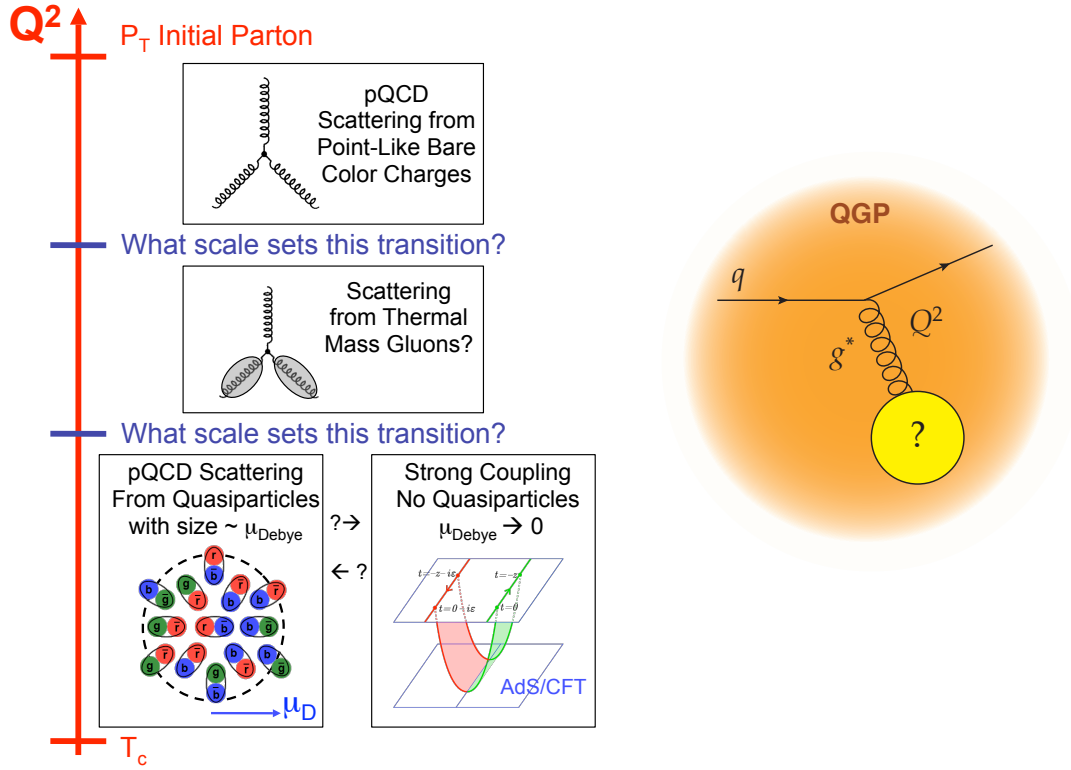


**Figure 1.2:** Interaction scale for the interaction of partons with the QGP and possibilities for the recoil objects. (left) Diagram of the net interaction of a parton with the medium and the range of possibilities for the recoil objects as a function of  $Q^2$ . (right) Diagram for a quark exchanging a virtual gluon with an unknown object in the QGP. This highlights the uncertainty for what sets the scale of the interaction and what objects or quasiparticles are recoiling.

point-like bare color charges, most likely without any influence from quasiparticles or deconfinement. This can be seen in Figure 1.2 (left). As one probes longer length scales, the scattering may be from thermal mass gluons and eventually from possible quasiparticles with size of order the Debye screening length (lower in Figure 1.2). In Ref. [16], Rajagopal states that “at some length scale, a quasiparticle picture of the QGP must be valid, even though on its natural length scale it is a strongly-coupled fluid. It will be a challenge to see and understand how the liquid QGP emerges from short-distance quark and gluon quasiparticles.” This is the challenge to be met by sPHENIX.

The extension of jet measurements over a wide range of energies and with different medium temperatures again gives one the largest span along this axis. What the parton is scattering from in the medium is tied directly to the balance between radiative energy loss and inelastic collisional energy loss in the medium (encoded in  $\hat{q}$  and  $\hat{e}$ ). In the limit that the scattering centers in the medium are infinitely massive, one only has radiative energy loss—as was assumed for nearly 10 years to be the dominant parton energy loss

effect. In the model of Liao and Shuryak [17], the strong coupling near the quark-gluon plasma transition is due to the excitation of color magnetic monopoles, and this should have a significant influence on the collisional energy loss and equilibration of soft partons into the medium.

In a model by Coleman-Smith [18, 19] consisting of parton showers propagating in a medium of deconfined quarks and gluons, one can directly vary the mass of the effective scattering centers and extract the resulting values for  $\hat{e}$  and  $\hat{q}$ . Figure 1.3 shows  $T\hat{e}/\hat{q}$  as a function of the mass of the effective scattering centers in the medium in this model. In the limit of infinitely massive scattering centers, the interactions are elastic and no energy is transferred to the medium.

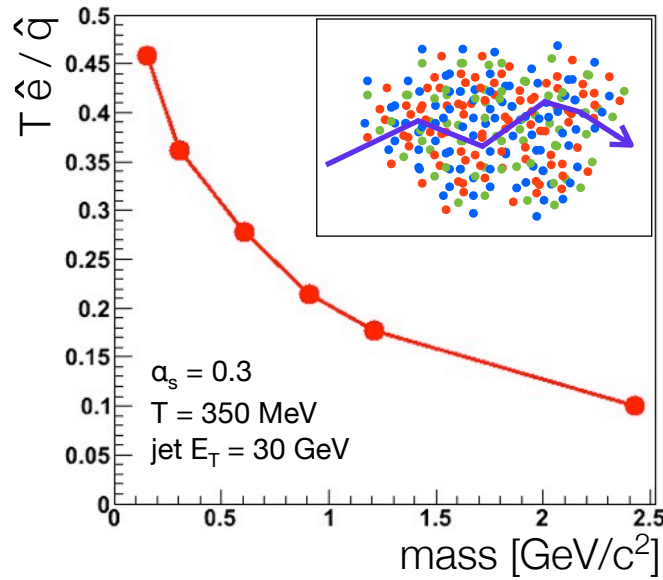


**Figure 1.3:**  $T\hat{e}/\hat{q}$  as a function of the mass of the effective scattering centers in the medium. As the mass increases, the parton is less able to transfer energy to the medium and the ratio drops.

## 1.3 The Temperature Dependence of the QGP

### 1.3.1 Shear viscosity to entropy density ratio $\eta/s$

It is well known that near a phase boundary familiar substances governed by quantum electrodynamics demonstrate interesting behavior such as the rapid change in the shear viscosity to entropy density ratio,  $\eta/s$ , near the critical temperature,  $T_c$ . This is shown in Figure 1.4 (left) for water, nitrogen, and helium [20]. Despite the eventual transition to superfluidity at temperatures below  $T_c$ ,  $\eta/s$  for these materials remains an order of magnitude above the conjectured quantum bound of Kovtun, Son, and Starinets (KSS) derived

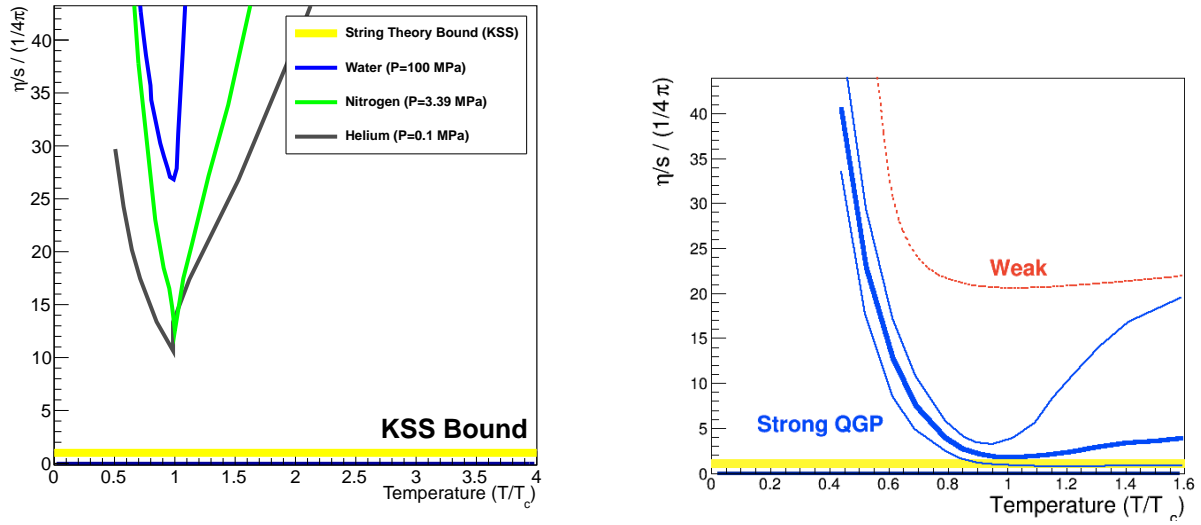


**Figure 1.4:** (left) The ratio of shear viscosity to entropy density,  $\eta/s$ , normalized by the conjectured KSS bound as a function of the reduced temperature,  $T/T_c$ , for water, nitrogen, and helium. The cusp for Helium corresponds to the case at the critical pressure. (right) Calculation for a weakly-coupled system (pQCD) and for various models of a strongly-coupled QGP.

from string theory [7]. Such observations provide a deeper understanding of the nature of these materials: for example the coupling between the fundamental constituents, the degree to which a description in terms of quasiparticles is important, and the description in terms of normal and superfluid components.

The dynamics of the QGP are dominated by Quantum Chromodynamics and the experimental characterization of the dependence of  $\eta/s$  on temperature will lead to a deeper understanding of strongly coupled QCD near this fundamental phase transition. Theoretically, perturbative calculations in the weakly-coupled limit indicate that  $\eta/s$  decreases slowly as one approaches  $T_c$  from above, but with a minimum still a factor of 20 above the KSS bound [21].

Hydrodynamic modeling of the bulk medium does provide constraints on  $\eta/s$ , and recent work has been done to understand the combined constraints on  $\eta/s$  as a function of temperature utilizing both RHIC and LHC flow data sets [22, 23, 24, 25] and result in values near the KSS bound around  $T_c$  as seen in Figure 1.4 (right).

### 1.3.2 Jet probe parameters $\hat{q}$ and $\hat{e}$

The above discussion was focused on  $\eta/s$  as the measure of the coupling strength of the QGP. However, both  $\eta/s$  and jet probe parameters such as  $\hat{q}$  and  $\hat{e}$  are sensitive to the

underlying coupling of the matter, but in distinct ways. Establishing for example the behavior of  $\hat{q}$  around the critical temperature is therefore essential to a deep understanding of the QGP. Hydrodynamic modeling may eventually constrain  $\eta/s(T)$  very precisely, though it will not provide an answer to the question of the microscopic origin of the strong coupling (something naturally available with jet probes).

Since the expected scaling of  $\hat{q}$  with temperature is such a strong function of temperature, jet quenching measurements should be dominated by the earliest times and highest temperatures. In order to have sensitivity to temperatures around  $1\text{--}2\ T_c$ , measurements at RHIC are needed in contrast to the LHC where larger initial temperatures are produced, as depicted graphically in Figure 1.1. In addition, the ability of RHIC to provide high luminosity heavy-ion collisions at a variety of center of mass energies can be exploited to probe the detailed temperature dependence of quenching right in the vicinity of  $T_c$ .

Theoretical developments constrained simultaneously by data from RHIC and the LHC have been important in discriminating against some models with very large  $\hat{q}$ , see Ref. [26] and theory references therein. Models such as PQM and ASW with very large values of  $\hat{q}$  have been ruled out by the combined constraint. Shown in the left panel of Figure 1.5 is a recent compilation of four theoretical calculations with a directly comparable extraction of  $\hat{q}$ . It is notable that a number of calculations favor an increased coupling strength near the transition temperature. Developments on the theory and experimental fronts have significantly narrowed the range of  $\hat{q}$ [27]. This theoretical progress lends credence to the case that the tools will be available on the same time scale as sPHENIX data to have precision determinations of  $\hat{q}$  and then ask deeper additional questions about the quark-gluon plasma and its underlying properties.

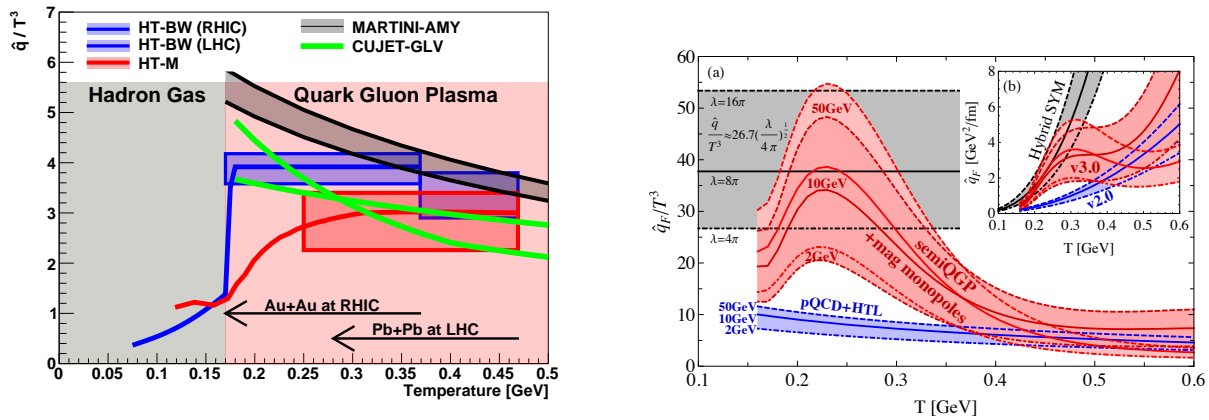


**Figure 1.5:** Calculations of  $\hat{q}/T^3$  vs temperature, constrained by RHIC and LHC  $R_{AA}$  data — including near  $T_c$  enhancement scenarios of  $\hat{q}/T^3$ . (left) Calculations from four jet quenching frameworks constrained by RHIC and LHC  $R_{AA}$  data with results for  $\hat{q}/T^3$  as a function of temperature. Details of the calculation are given in Ref. [27]. (right) Results from calculations within CUJET 3.0 with magnetic monopole excitations that result in enhanced coupling near  $T_c$ . Plotted are the constraints on  $\hat{q}/T^3$  as a function of temperature as shown in Ref. [28]

Ref. [29] states that “Comparing weak coupling scenarios with data, NTC [near  $T_c$  enhancement] is favored. An answer to this question will require a systematic picture across several different high  $p_T$  observables.” In Ref. [17], Liao and Shuryak use RHIC measurements of single hadron suppression and azimuthal anisotropy to infer that “the jet quenching is a few times stronger near  $T_c$  relative to the quark-gluon plasma at  $T > T_c$ .”

Most recently this strong coupling picture with color magnetic monopole excitations has been implemented within CUJET 3.0 for a broader comparison with experimental observables and previous theory calculations [28]. Shown in Figure 1.5 (right panel) are results from their constrained RHIC and LHC data fit for the temperature dependence of the scaled quenching power  $\hat{q}/T^3$ .

Within the jet quenching model WHDG [30], the authors constrain  $\hat{q}$  by the PHENIX  $\pi^0$  nuclear modification factor. They find the prediction scaled by the expected increase in the color charge density created in higher energy LHC collisions when compared to the ALICE results [31] over-predicts the suppression. This over-prediction based on the assumption of an unchanging probe-medium coupling strength led to the title of Ref. [30]: “The surprisingly transparent sQGP at the LHC.” They state that “one possibility is the sQGP produced at the LHC is in fact more transparent than predicted.” Similar conclusions have been reached by other authors [32, 33, 34]. Recently work has been done to incorporate the running of the QCD coupling constant [35].

It is important to note that most calculations predict a stronger coupling near the transition, even if just from the running of the coupling constant  $\alpha_s$ . The goal is to determine experimentally the degree of this effect. Lower energy data at RHIC also provides important constraints – see for example Refs. [36, 37]. The full set of experimental observables spanning the largest range of collision energy, system size, and path length through the medium is needed to determine the coupling strength as a function of temperature.

## 1.4 Evolution of Parton Virtuality in the QGP

The initial hard-scattered parton starts out very far off-shell and in  $e^+e^-$ ,  $p+p$  or  $p+\bar{p}$  collisions the virtuality evolves in vacuum through gluon splitting down to the scale of hadronization. In heavy ion collisions, the vacuum virtuality evolution is interrupted at some scale by scattering with the medium partons which increase the virtuality with respect to the vacuum evolution. Figure 1.1 (left) shows the expected evolution of virtuality in vacuum, from medium contributions, and both combined (in a QGP).

If this picture is borne out, it “means that [a] very energetic parton hardly notices the medium for the first 3–4 fm of its path length [38].” Spanning the largest possible range of virtuality (initial hard process  $Q^2$ ) is very important, but complementary measurements at both RHIC and LHC of produced jets at the same virtuality (around 50 GeV) will test the interplay between the vacuum shower and medium scattering contributions.

In some theoretical frameworks — for example Refs [39, 40, 41] — the parton splitting is simply dictated by the virtuality and in vacuum this evolves relatively quickly from large to small scales. The  $Q$  evolution means that the jet starts out being considerably off mass shell when produced, and this off-shellness is reduced by successive splits to less virtual partons. In these calculations, the scattering with the medium modifies this process of parton splitting. The scale of the medium as it relates to a particular parton is  $\hat{q}$  times the parton lifetime (this is the mean transverse momentum that the medium may impart to the parent and daughter partons during the splitting process). When the parton's off-shellness is much larger than this scale, the effect of the medium on this splitting process is minimal. As the parton drops down to a lower scale, the medium begins to affect the parton splitting more strongly.

Shown in Figure 1.6 (left) is the single hadron  $R_{AA}$  measured in central Au+Au collisions at 200 GeV and in heavy ion collisions at other beam energies. One can see in Figure 1.6 (right) that inclusion of the virtuality evolution for the YAJEM calculation leads to a 50% rise in  $R_{AA}$  from 20–40 GeV/c, and a 100% rise in the HT-M calculation. A strong rise in  $R_{AA}$  measured at higher  $p_T$  at the LHC has been observed, and measurement of the effect within the same framework at RHIC is a key test of this virtuality evolution description. It is notable that the JEWEL calculation, which accurately describes the rising  $R_{AA}$  at the LHC [42], results in a nearly flat  $R_{AA}$  over the entire  $p_T$  range at RHIC. As detailed in Ref. [43, 44], many formalisms assuming weakly coupled parton probes are able to achieve an equally good description of the single-inclusive hadron ( $R_{AA}$ ) data at RHIC and the LHC. The single high  $p_T$  hadron suppression constrains the  $\hat{q}$  value within a model, but is not able to discriminate between different energy loss mechanisms and formalisms for the calculation. sPHENIX will perform precision measurements of charged hadrons over an extended  $p_T$  range, as shown in the projected uncertainties, that will strongly discriminate between the various energy loss mechanisms and model assumptions about the virtuality evolution in the medium.

## 1.5 Current Jet Probe Measurements

Jet quenching (i.e., the significant loss of energy for partons traversing the QGP) was discovered via measurements at RHIC of the suppression of single hadron yields compared to expectations from  $p+p$  collisions [45, 46]. Since the time of that discovery there has been an enormous growth in jet quenching observables that have also pushed forward a next generation of analytic and Monte Carlo theoretical calculations to confront the data.

Two-hadron correlations measure the correlated fragmentation between hadrons from within the shower of one parton and also between the hadrons from opposing scattered partons. These measurements, often quantified in terms of a nuclear modification  $I_{AA}$  [47, 48, 49], have been a challenge for models to describe simultaneously [50].

The total energy loss of the leading parton provides information on one part of the parton-



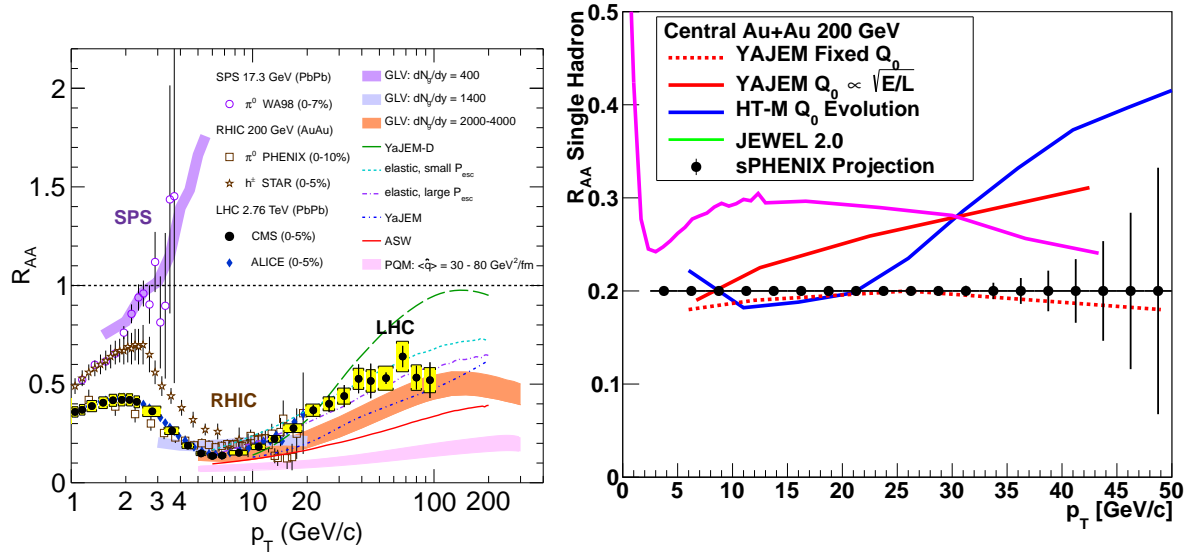


**Figure 1.6:** (left) The nuclear modification factor  $R_{AA}$  as a function of transverse momentum in A+A collisions at the SPS, RHIC, and LHC. Comparisons with various jet quenching calculations as detailed in Ref. [26] and references therein are shown. The simultaneous constraint of RHIC and LHC data is a powerful discriminator. (right) Predictions of  $R_{AA}$  for single hadrons to  $p_T \sim 50$  GeV/c in central Au+Au at 200 GeV. Also shown are the projected sPHENIX uncertainties.

medium interaction. Key information on the nature of the particles in the medium being scattered from is contained in how the soft (lower momentum) part of the parton shower approaches equilibrium in the QGP. This information is accessible through full jet reconstruction, jet-hadron correlations, di-jets and  $\gamma$ -jet correlation observables.

The measurements of fully reconstructed jets and the particles correlated with the jet (both inside and outside the jet) are crucial to testing the various models and their energy loss mechanisms. Not only does the strong coupling influence the induced radiation from the hard parton (gluon bremsstrahlung) and its inelastic collisions with the medium, but it also influences the way soft partons are transported by the medium outside of the jet cone as they fall into equilibrium with the medium. Thus, the jet observables combined with correlations are a means to access directly the coupling of the hard parton to the medium and the parton-parton coupling for the medium partons themselves.

### 1.5.1 LHC results

The first results from the LHC based on reconstructed jets in heavy ion collisions were the centrality-dependent dijet asymmetries measured by ATLAS [51] and CMS [52] as shown

on the left panels of Figures 1.7 and 1.8. The measured dijet asymmetry  $A_J$  is defined by ATLAS as  $A_J = (E_1 - E_2)/(E_1 + E_2)$  and  $A_J = (p_1 - p_2)/(p_1 + p_2)$  by CMS. These results indicate a substantial broadening of the dijet asymmetry  $A_J$  distribution for increasingly central Pb+Pb collisions and a lack of modification to the dijet azimuthal correlations (not shown). The broadening of the  $A_J$  distribution points to substantial energy loss for jets and the unmodified azimuthal distribution shows that the opposing jet  $\Delta\phi$  distribution is not broadened as it traverses the matter.

Direct photon-jet measurements are also a powerful tool to study jet quenching. Unlike dijet measurements the photon passes through the matter without losing energy, providing a cleaner measure of the expected jet  $p_T$  [53]. CMS has results for photons with  $p_T > 60$  GeV/c correlated with jets with  $p_T > 30$  GeV/c [54]. Though with modest statistical precision, the measurements indicate energy transported outside the  $R = 0.3$  jet cone through medium interactions. Similar results from the ATLAS experiment again indicate a shift of the energy outside the opposing jet cone.

Reconstructed jets have significantly extended the kinematic range for jet quenching studies at the LHC, and quenching effects are observed up to the highest reconstructed jet energies ( $> 300$  GeV) [55]. They also provide constraints on the jet modification that are not possible with particle-based measurements. For example, measurements from ATLAS constrain the modification of the jet fragmentation in Pb+Pb collisions from vacuum fragmentation to be small [56]. CMS results on jet-hadron correlations have shown that the lost energy is recovered in low  $p_T$  particles far from the jet cone [52]. The lost energy is transported to very large angles and the remaining jet fragments as it would in the vacuum.

## 1.5.2 RHIC results

There are preliminary results on fully reconstructed jets from both STAR [57, 58, 59, 60] and PHENIX experiments [61, 62]. However, a comprehensive jet detector, such as sPHENIX, with large, uniform acceptance and a high-rate capability can be combined with the newly completed increase in RHIC luminosity to perform these key measurements definitively to access this important physics. In addition to extending the RHIC observables to include fully reconstructed jets and  $\gamma$ -jet correlations, theoretical development is required for converging to a coherent 'standard model' of the medium coupling strength and the nature of the probe-medium interaction. In the next section, we present predictions for a sample of future RHIC measurements based on theory that has been calibrated through successful reproduction of recent LHC measurements.

## 1.6 Using Jets at RHIC to Constrain Theoretical Calculations

The theoretical community is actively working to understand the details of probe-medium interactions. Much work has been carried out by the Topical Collaboration on Jet and Electromagnetic Tomography of Extreme Phases of Matter in Heavy-ion Collisions [63]. The challenge is to understand not only the energy loss of the leading parton, but how the parton shower evolves in medium and how much of the lost energy is re-distributed in the QGP. Monte Carlo approaches have been developed (as examples [64, 65, 66, 19, 67, 68]) to overcome specific theoretical hurdles regarding analytic parton energy loss calculations and to couple these calculations with realistic models of the QGP space-time evolution. Theoretical calculations attempting to describe the current data from RHIC and LHC have yet to reconcile some of the basic features. Some models include large energy transfer to the medium as heat (for example [69]) while others utilize mostly radiative energy loss (for example [70, 71]). Measurements at RHIC energies with jets over a different kinematic range allow specific tests of the different mechanisms.

Jets provide a rich spectrum of physics observables, ranging from single-jet observables such as  $R_{AA}$ , to correlations of jets with single particles and correlations of trigger jets with other jets in the event. Triggers ranging from single hadrons to ideally reconstructed jets are used to form correlations with hadrons or another jet in the event. Different triggers demonstrate different degrees of surface bias in the production point of the “dijet”, i.e. the hard-scattering vertex location, and this bias itself has been used as leverage in the investigation of the properties of the medium. Examples of different trigger biases that can be exploited have been presented in calculations by Renk [72].

In this section, we present a brief review of a subset of calculations that employ different mechanisms for jet-medium interactions. These are compared to jet observables that still need to be measured at RHIC, with an emphasis on their particular sensitivity to the underlying physics, and represent the potential constraining power of a comprehensive jet physics program by sPHENIX at RHIC.

### 1.6.1 Di-jet Asymmetry $A_J$

Results of calculations from Coleman-Smith and collaborators [18, 19] for the dijet asymmetry  $A_J$  at the LHC are presented along with the data in Figure 1.7 (left) [18]. The parton showers are extracted from PYTHIA (with hadronization turned off) and then embedded into a deconfined QGP, modeled at constant temperature using the VNI parton cascade [73] with fixed  $\alpha_s = 0.3$ . One feature of the calculation is that it provides the ability to track the time evolution of each individual parton, not only the scattered partons from the shower, but also partons from the medium, which through interactions can contribute particles to the reconstructed jets. Jets in the calculation are reconstructed with the anti- $k_T$  algorithm with radius parameter  $R = 0.5$  and then smeared by a simulated jet resolution of  $100\%/\sqrt{E}$ , and with requirements of  $E_{T1} > 120$  GeV and  $E_{T2} > 50$  GeV on the leading

and sub-leading jet, respectively. The calculated  $A_J$  distributions reproduce the CMS experimental data [52].

In Figure 1.7 (right panel) the calculation is repeated with a medium temperature appropriate for RHIC collisions and with RHIC observable jet energies,  $E_{T1} > 20$  GeV and  $R = 0.2$ . The calculation is carried out for different coupling strengths  $\alpha_s$  between partons in the medium themselves and the parton probe and medium partons. The variation in the value of  $\alpha_s$  should be viewed as changing the effective coupling in the many-body environment of the QGP. It is interesting to note that in the parton cascade BAMPS the authors find that an effective coupling of  $\alpha_s \approx 0.6$  is required to describe the bulk medium flow [74]. These results indicate sizable modification to the dijet asymmetry and thus excellent sensitivity to the effective coupling to the medium at RHIC energies.

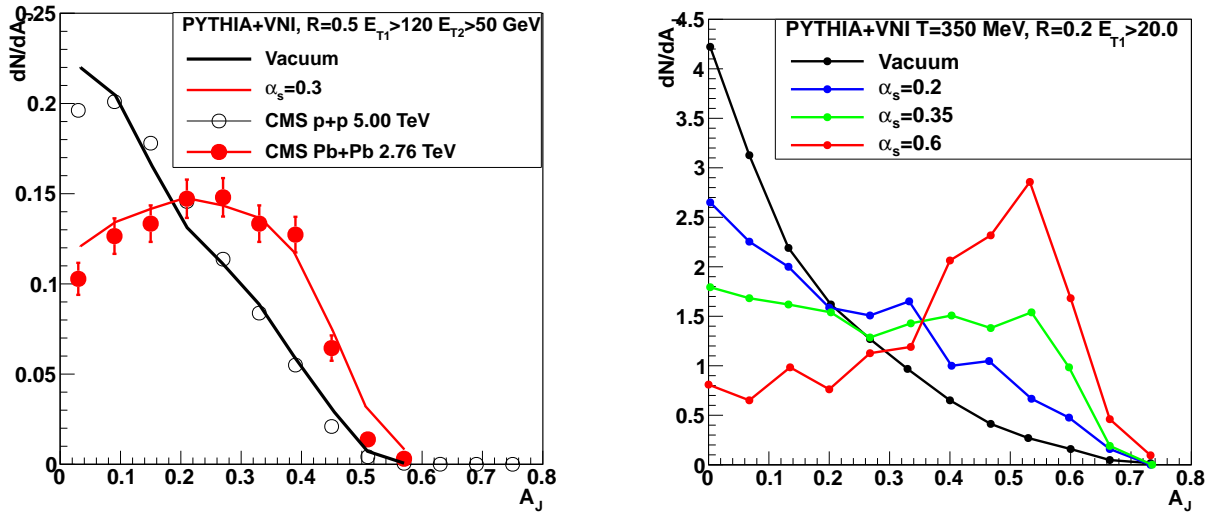


**Figure 1.7:** (left) Calculation in VNI parton cascade of dijet  $A_J$  with  $T = 0.35$  GeV and  $\alpha_s = 0.3$  compared to the CMS data [18]. (right) Calculation for RHIC jet energies,  $E_{T1} > 20$  GeV, for a circular geometry of radius 5 fm of  $A_J$  for different values of  $\alpha_s$  increasing to  $\alpha_s = 0.6$  (red line) [75].

The results of calculations for  $A_J$  from two other groups are presented in Figure 1.8. In the calculation of Qin and collaborators [76, 77] a differential equation governing the evolution of the radiated gluon distribution is solved to predict the propagation of the jet through the medium. Energy contained inside the jet cone is lost by dissipation through elastic collisions and by scattering of shower partons to larger angles. The model calculations of Young, Schenke and collaborators [66] utilize a jet shower Monte Carlo, referred to as MARTINI [78], and embed the shower on top of a hydrodynamic space-time background, using the model referred to as MUSIC [79]. Each of the above approaches reproduce the  $A_J$  data measured at LHC quite well [80, 76] as shown in Figure 1.8 (left). Figure 1.8 (right) shows the jet energy dependence of  $A_J$  predicted for RHIC energy di-jets with

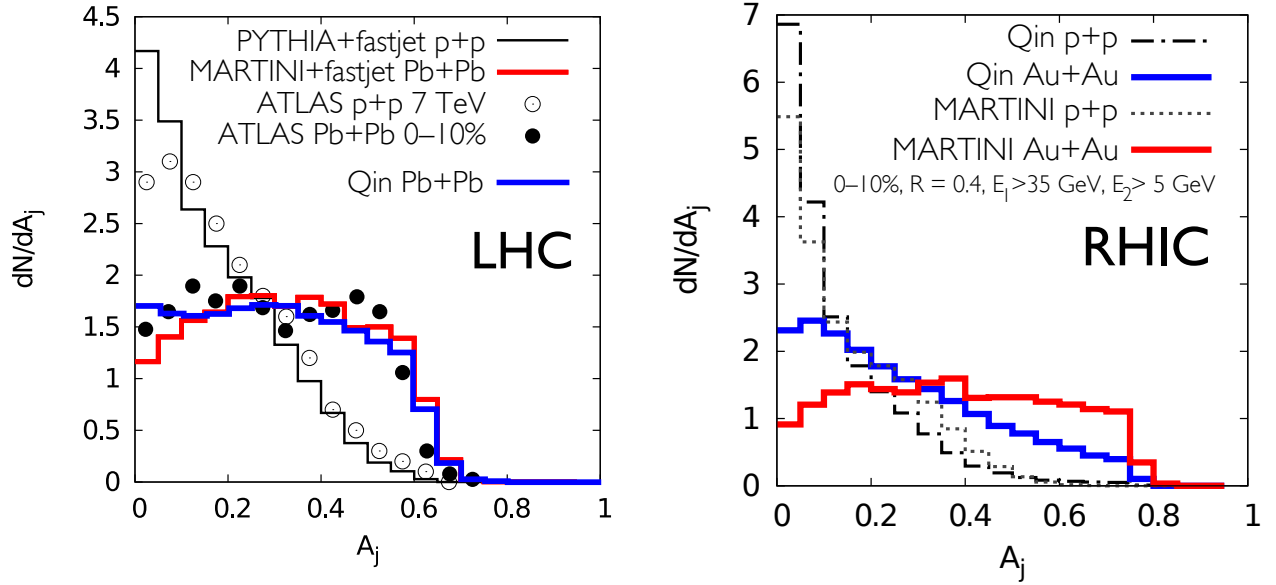


**Figure 1.8:**  $A_j$  distributions in MARTINI+MUSIC [81] and the model of Qin et al. [77]. (left) Comparison of  $A_j$  calculations in MARTINI+MUSIC and by Qin et al for Pb+Pb collisions at 2.76 TeV (red line, Qin et al; blue line, MARTINI+MUSIC). Both calculations show a similar broad  $A_j$  distribution. (right) Same as left panel, but for Au+Au collisions at 200 GeV (with leading jet  $E_T > 35$  GeV). These results indicate a substantially different modification predicted by these models for di-jets propagating through the QGP at RHIC.

$E_{T1} > 35$  GeV with  $E_{T2} > 5$  GeV by the two model calculations. A significant difference in shape is observed between the two models at RHIC energy with a peak developing at small  $A_j$  in the Qin et al. model while the MARTINI+MUSIC calculation retains a shape similar to those seen at the LHC energy.

### 1.6.2 Jet Shapes

Calculations from Vitev and collaborators [82, 83, 84] predict a jet radius  $R$  and energy dependence for inclusive jet  $R_{AA}$ , in contrast to the results from Qin et al. Vitev et al. utilize a Next-to-Leading-Order (NLO) calculation and consider not only final-state inelastic parton interactions in the QGP, but also parton energy loss effects from the cold nuclear matter. This can be seen in Figure 1.9, which exhibits significant radius and energy dependences. Because the high energy jets originate from hard scattering of high Bjorken  $x$  partons, a modest energy loss of these partons results in a reduction in the inclusive jet yields. At RHIC cold nuclear matter measurements will be made with  $p$ +Au running in sPHENIX at the same collision energy to determine the strength of cold nuclear matter and any other effects as a baseline to the heavy ion measurements.

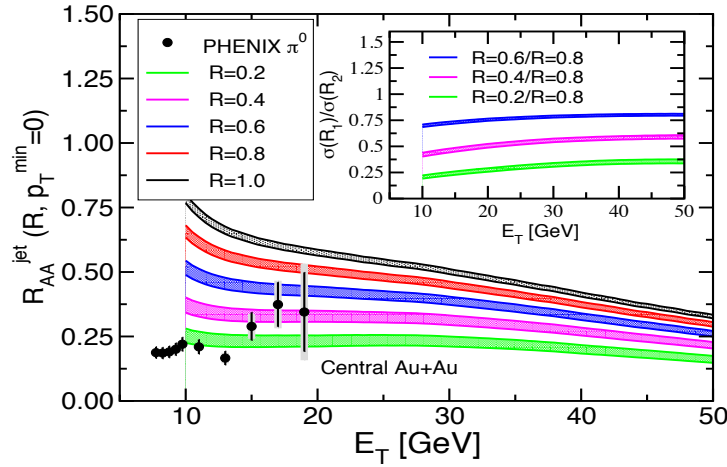


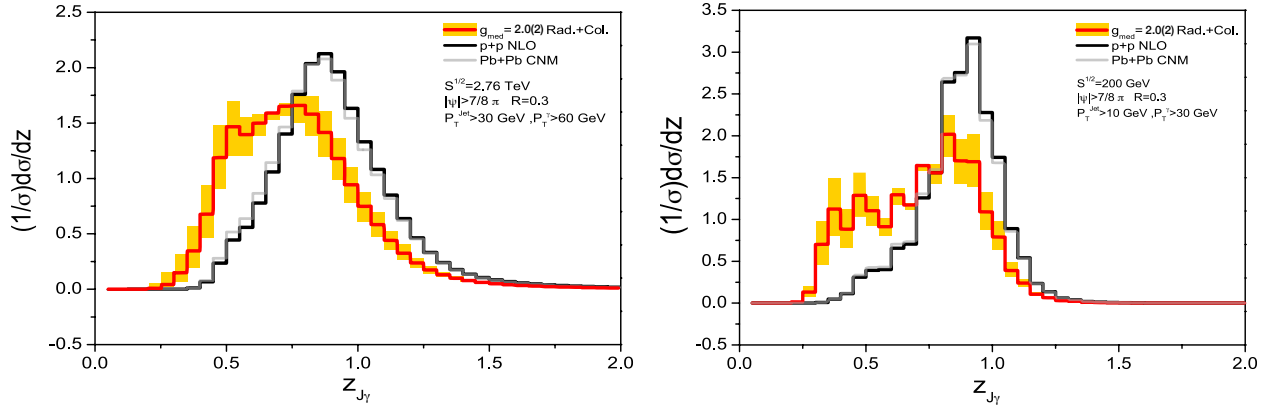
**Figure 1.9:** Calculations from Vitev et al. for the inclusive jet  $R_{AA}$  as a function of the jet energy and radius. Also shown for reference are PHENIX  $\pi^0$   $R_{AA}$  results. Inset presents ratios for jets of various radii relative to those measured with  $R = 0.8$ .

## 1.7 Fragmentation Functions

### 1.7.1 Direct photon-jet correlations

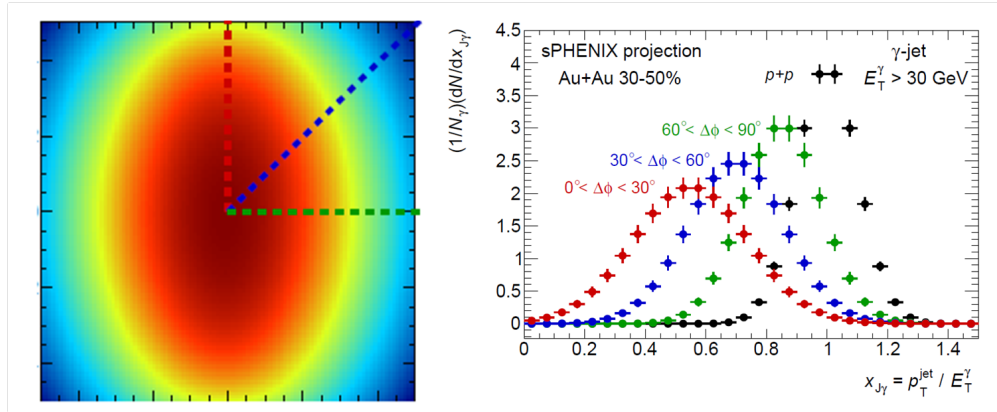
Ideally, one would like to understand how a quark or gluon of known energy interacts while traversing the QGP and the redistribution of energy and particles both longitudinal and transverse to the initial parton direction. The initial quark energy can be identified from binary scattering kinematics by measuring its direct photon [53] scattering “partner” on the opposite side. One can study fully reconstructed jets opposite the photon for various jet radii to investigate the redistribution in transverse energy. ATLAS has presented results on photon-jet  $R_{AA}$ . A suppression of the away-side jet is observed for two different jet-radius parameters.

Figure 1.10 presents the result of calculations of the event distribution of the ratio of the reconstructed jet energy (with  $R = 0.3$ ) relative to the direct photon energy [85]. The authors note: “The steeper falling cross sections at RHIC energies lead not only to a narrow  $z_{J_\gamma}$  distribution in  $p+p$  collisions but also to a larger broadening and shift in  $\langle z_{J_\gamma} \rangle$  in A+A collisions.” This results in a greater sensitivity to the redistribution of energy, which is again sensitive to the balance of processes including radiative and collisional energy loss. With an underlying event energy at RHIC that is a factor of 2.5 lower than that at the LHC, sPHENIX will be able to reconstruct jets over a very broad range of radii and energies opposite the direct photons. Shown in Figure 1.11 are the projected sPHENIX photon - jet correlation uncertainties measured differentially with respect to the path length through the QGP.



**Figure 1.10:** Calculations by Vitev et al. of the vacuum and medium-modified  $z_{J_\gamma}$  distributions for direct photon-triggered reconstructed jet events at LHC (left) and RHIC (right) energies [85].

With charged particle tracking one can also measure the longitudinal redistribution of hadrons opposite the direct photon. sPHENIX will have excellent statistical reach for such direct photon measurements.



**Figure 1.11:** Schematic of different potential path lengths through the QGP (left) and projected sPHENIX uncertainties in the photon-jet channel for these different length scales traversed in the QGP.

At the same time, it is advantageous to measure modified fragmentation functions within inclusive reconstructed jets and via correlations as well. The original predictions of jet quenching in terms of induced forward radiation had the strongest modification in the longitudinal distribution of hadrons from the shower (i.e., a substantial softening of the fragmentation function). One may infer from the nuclear suppression of  $\pi^0$  in central Au+Au collisions  $R_{AA} \approx 0.2$  that the high  $z$  (large momentum fraction carried by the hadron) showers are suppressed.

### 1.7.2 Hadron-jet correlations

In sPHENIX, fragmentation functions via precision charged-track measurements are available from high- $z$ , where the effects are predicted to be largest, to low- $z$  where medium response and equilibration effects are relevant. The independent measurement of jet energy (via calorimetry) and the hadron  $p_T$  via tracking is important. This independent determination also dramatically reduces the fake-track contribution by the coincidence required with a high energy jet.

One can also access somewhat less directly this transverse and longitudinal redistribution of energy and particles via trigger high  $p_T$  hadrons and narrow reconstructed jets. Such measurements have been undertaken by STAR [86]. The large kinematic reach of sPHENIX will provide very high statistics observables that span a reach where the opposing parton is mostly a gluon near 20 GeV with increasing quark fraction for higher energy triggers. This is another complement between the kinematics at RHIC and the LHC as shown in Figure 1.12 that compares the quark-quark, quark-gluon, gluon-gluon relative contributions as a function of  $p_T$ .

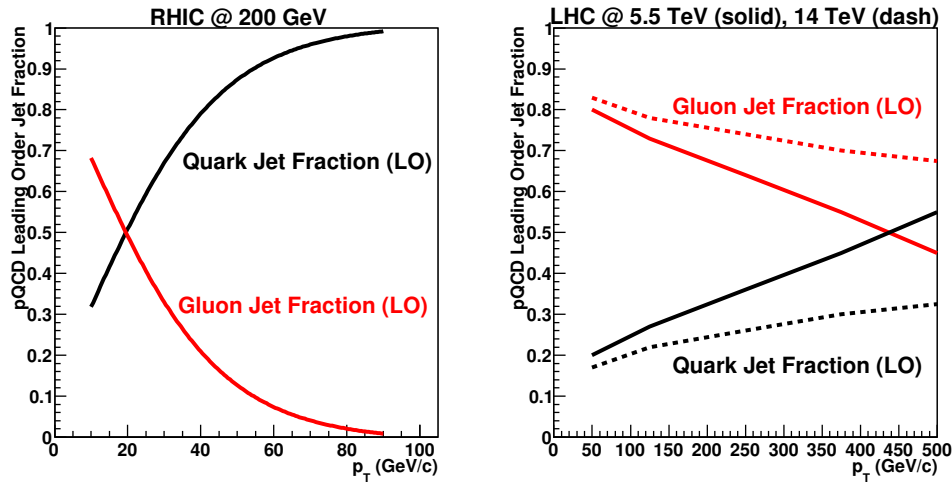


**Figure 1.12:** Comparison of the fraction of quark and gluon jets from leading order pQCD calculations as a function of transverse momentum for RHIC (left) and LHC (right) energies.

## 1.8 Heavy Quark Jets

The motivation for studying heavy flavor jets in heavy ion collisions is to understand the processes involved in parton-medium interactions and to further explore the issue of *strong versus weak* coupling [87]. As elaborated in Section 1.2, a major goal is understanding the constituents of the medium and how fast partons transfer energy to the medium.



Heavy quarks are particularly sensitive to the contribution of collisional energy loss, due to suppressed radiative energy loss from the “dead cone” effect [88]. Measurements of beauty-tagged jets and reconstructed  $D$  mesons over the broadest kinematic reach will enable the disentangling of  $\hat{q}$  and  $\hat{e}$ .

There are important measurements currently being made of single electrons from semileptonic  $D$  and  $B$  decays and direct  $D$  meson reconstruction with the current PHENIX VTX and STAR Heavy Flavor Tracker (HFT). The sPHENIX program can significantly expand the experimental acceptance and physics reach of this program with its ability to reconstruct full jets with a heavy flavor tag. The rates for heavy flavor production from perturbative QCD calculations [89] are shown in Figure 1.13.

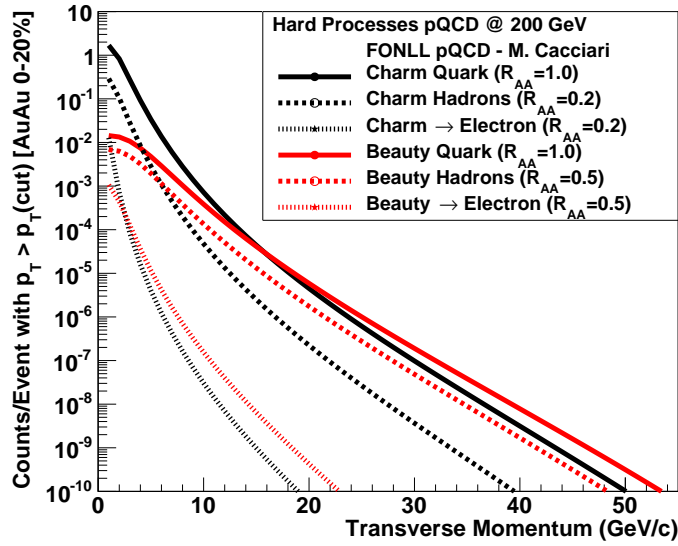


**Figure 1.13:** FONLL calculations [89] for heavy flavor (charm and beauty) jets, fragmentation hadrons ( $D, B$  mesons primarily), and decay electrons as a function of transverse momentum. The rates indicate expected counts for  $p_T$  above a minimum transverse momentum threshold,  $p_T(\text{cut})$ , as a function of  $p_T(\text{cut})$  for Au+Au 0–20% central collisions.

Calculations including both radiative and collisional energy loss for light quark and gluon jets, charm jets, and beauty jets have been carried out within the CUJET 2.0 framework [90]. The resulting  $R_{AA}$  values in central Au+Au at RHIC and Pb+Pb at the LHC for  $\pi, D, B$  mesons are shown as a function of  $p_T$  in Figure 1.14. The mass orderings are a convolution of different initial spectra steepness, different energy loss mechanisms, and the final fragmentation. Measurements of  $D$  mesons to high  $p_T$  and reconstructed beauty-tagged jets at RHIC will provide particularly sensitive constraints in a range where, due to their large masses, the charm and beauty quark velocities are not near the speed of light.

The tagging of charm and beauty jets has an extensive history in particle physics experiments. There are multiple ways to tag heavy flavor jets. First is the method of tagging via

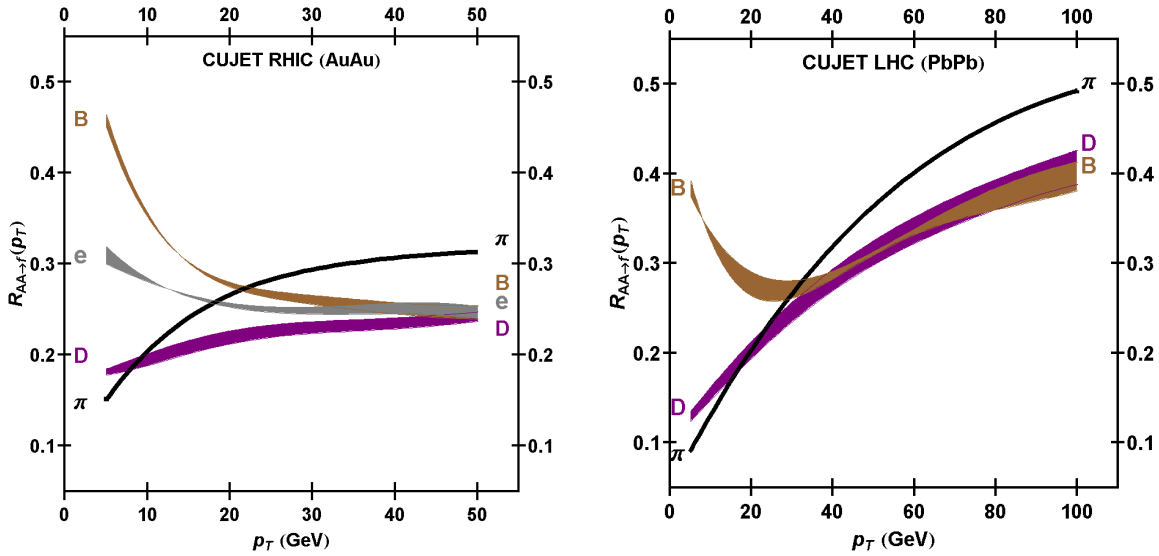


**Figure 1.14:** Calculations within the CUJET 2.0 [90] framework of the  $R_{AA}$  in central Au+Au collisions at RHIC (left) and Pb+Pb collisions at the LHC (right), with light, charm and beauty hadrons and electrons shown as separate curves.

the selection of a high  $p_T$  electron with a displaced vertex inside the jet. In minimum bias Au+Au collisions at  $\sqrt{s_{NN}} = 200$  GeV, the fraction of inclusive electrons from  $D$  and  $B$  meson decays is already greater than 50% for  $p_T > 2$  GeV/c. The sPHENIX tracking can confirm the displaced vertex of the electron from the collision point, further enhancing the signal. Since the semileptonic branching fraction of  $D$  and  $B$  mesons is approximately 10%, this method provides a reasonable tagging efficiency. Also, the relative angle of the lepton with respect to the jet axis provides a useful discriminator for beauty jets as well, due to the decay kinematics. Second, the direct reconstruction of  $D$  mesons is possible within sPHENIX (see Figure 4.37 of Ref. [1]).

The third method utilizes jets with many tracks that do not point back to the primary vertex. This technique is detailed by the  $D0$  collaboration to identify beauty jets at the Tevatron [91, 92], and employed with variations by ATLAS and CMS at the LHC. This method exploits the fact that most hadrons with a beauty quark decay into multiple charged particles all with a displaced vertex. The performance metrics for tagged beauty jets are given in Section 4.7 of Ref. [1]).

Measurements at the LHC provide tagging of heavy flavor probes as well – initial results on beauty tagged jets from CMS are shown in Figure 1.15. As detailed in Ref. [93], beauty tagged jets at the LHC come from a variety of initial processes. In fact, most often a tagged beauty jet does not have a back-to-back partner beauty jet. At RHIC energies the pair creation process represents  $\sim 35\%$  of the beauty jet cross-section, which is a larger fractional contribution than at the LHC, though flavor excitation still produces  $\sim 50\%$  of all  $b$ -jets at RHIC. Measurements at RHIC offer a different mixture of initial processes, and

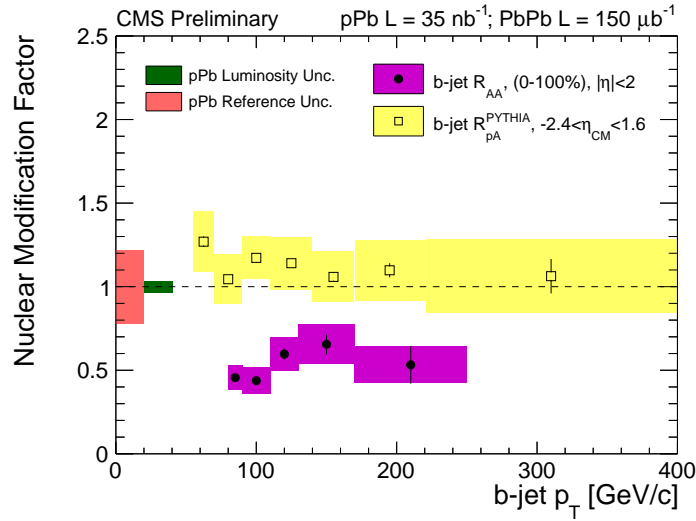


**Figure 1.15:** CMS results on the  $R_{AA}$  for beauty tagged jets in Pb+Pb collisions at the LHC.

thus kinematics, when looking at correlated back-to-back jets including heavy flavor tags, and will complement similar measurements at the LHC to constrain theories.

## 1.9 Quarkonia in the QGP

Motivated by a desire to observe the suppression of  $J/\psi$  production by color screening in the QGP an extensive program of  $J/\psi$  measurements in A+A collisions has been carried out at the SPS ( $\sqrt{s_{NN}} = 17.3$  GeV) and RHIC ( $\sqrt{s_{NN}} = 200$  GeV) and the LHC ( $\sqrt{s_{NN}} = 2.76$  TeV). Strong suppression is observed at all three energies, but it has become clear that the contribution of color screening to the observed modification cannot be uniquely determined without a good understanding of two strong competing effects.

The first of these, the modification of the  $J/\psi$  production cross section in a nuclear target, has been addressed at RHIC using  $d$ +Au collisions and at the SPS using  $p$ +Pb collisions, and is being addressed at the LHC using  $p$ +Pb collisions. A more recently recognized complicating effect arises from the possibility that previously unbound heavy quark pairs could coalesce into bound states due to interactions with the medium. This introduces the possibility that if a sufficient density of heavy quark pairs is produced initially, then coalescence of heavy quarks may increase the production cross section beyond the initial population of bound pairs [94].

Using  $p$ +Pb and  $d$ +Au data as a baseline, and under the assumption that cold nuclear matter (CNM) effects can be factorized from hot matter effects, the suppression in central collisions due to the presence of hot matter in the final state has been estimated to be about 25% for Pb+Pb at the SPS [95], and about 50% for Au+Au at RHIC [96], both measured at midrapidity. The first  $J/\psi$  data in Pb+Pb collisions at  $\sqrt{s_{NN}} = 2.76$  TeV have been

measured from ALICE [97]. Interestingly, the suppression in central collisions is far greater at RHIC than at the LHC. This is qualitatively consistent with a predicted [94] strong coalescence component due to the very high  $c\bar{c}$  production rate in a central collision at LHC. There is great promise that, with CNM effects estimated from  $p$ +Pb data, comparison of these data at widely spaced collision energies will lead to an understanding of the role of coalescence.

### 1.9.1 $\Upsilon$ State Measurements

Upsilon measurements have a distinct advantage over charmonium measurements as a probe of deconfinement in the quark-gluon plasma. The  $\Upsilon(1S)$ ,  $\Upsilon(2S)$  and  $\Upsilon(3S)$  states can all be observed with comparable yields via their dilepton decays. Therefore, it is possible to compare the effect of the medium simultaneously on three bottomonium states—all of which have quite different radii and binding energies.

At the LHC, CMS has measured Upsilon modification data at midrapidity in Pb+Pb collisions at 2.76 GeV that indicate strong differential suppression of the 2S and 3S states relative to the 1S state [98]. ALICE has measured the  $\Upsilon(1S)$  modification at forward rapidity in Pb+Pb collisions at 2.76 GeV [99], and in  $p$ +Pb collisions at 5.02 TeV [100]. With longer Pb+Pb runs, and corresponding  $p$ +Pb modification data to establish a CNM baseline, the LHC measurements will provide an excellent data set within which the suppression of the three upilon states relative to  $p$ +Pb can be measured simultaneously at LHC energies.

At RHIC, upilon measurements have been hampered by a combination of low cross sections and acceptance, and insufficient momentum resolution to resolve the three states. So far, there are measurements of the modification of the three states combined in Au+Au by PHENIX [101] and STAR [102]. However a mass-resolved measurement of the modifications of the three upilon states at  $\sqrt{s_{NN}} = 200$  GeV would be extremely valuable for several reasons.

First, the core QGP temperature is approximately  $2T_c$  at RHIC at 1 fm/ $c$  and is at least 30% higher at the LHC (not including the fact that the system may thermalize faster) [103]. This temperature difference results in a different color screening environment. Figure 1.16 shows the temperature as a function of time for the central cell in Au+Au and Al+Al collisions at 200 GeV and Pb+Pb collisions at 2.76 TeV from hydrodynamic simulations that include earlier pre-equilibrium dynamics and post hadronic cascade [104]. Superimposed are the lattice expected dissociation temperatures with uncertainties for the three upilon states. The significant lever arm in temperature between RHIC and LHC, and the use of either centrality or system size, allow one to bracket the expected screening behavior.

Second, the bottomonium production rate at RHIC is lower than that at the LHC by  $\sim 100$  [96]. As a result, the average number of  $b\bar{b}$  pairs in a central Au+Au collision at RHIC is  $\sim 0.05$  versus  $\sim 5$  in central Pb+Pb at the LHC. Qualitatively, one would

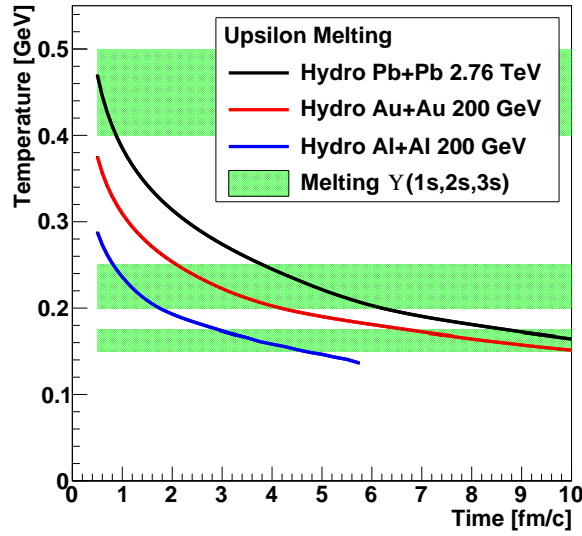


**Figure 1.16:** Temperature as a function of time for the central cell in Au+Au and Al+Al collisions at 200 GeV and Pb+Pb collisions at 2.76 TeV from hydrodynamic simulations that include earlier pre-equilibrium dynamics and post hadronic cascade [104]. Superimposed are the lattice expected dissociation temperatures with uncertainties for the three upsilon states.

expect this to effectively remove at RHIC any contributions from coalescence of bottom quarks from different hard processes, making the upsilon suppression at RHIC dependent primarily on color screening and CNM effects. This seems to be supported by recent theoretical calculations [105] where, in the favored scenario, coalescence for the upsilon is predicted to be significant at the LHC and small at RHIC.

Finally, it is of interest at RHIC energy to directly compare the modifications of the  $J/\psi$  and the  $Y(2S)$  states as a way of constraining the effects of coalescence by studying two states - in the same temperature environment - that have very similar binding energies and radii, but quite different underlying heavy quark populations.

An example theoretical calculation for both RHIC and the LHC is shown in Figure 1.17 indicating the need for substantially improved precision and separation of states in the temperature range probed at RHIC.

STAR has constructed a Muon Telescope Detector (MTD) to measure muons at midrapidity [106]. The MTD has coverage over  $|\eta| < 0.5$ , with about 45% effective azimuthal coverage. The MTD will have a muon to pion enhancement factor of 50–100, and the mass resolution will provide a clean separation of the  $Y(1S)$  from the  $Y(2S+3S)$ , and likely the ability to separate the  $Y(2S)$  and  $Y(3S)$  by fitting. While STAR has already taken data in the 2014 run with the MTD installed, the upgrade to sPHENIX will provide better mass resolution and approximately 10 times higher yields per run for upsilon measurements as

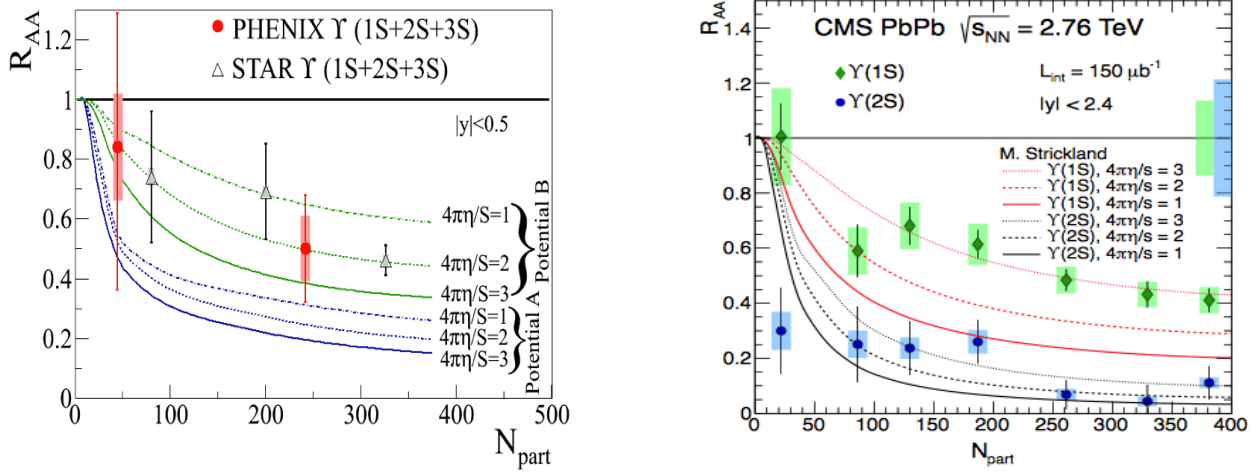


**Figure 1.17:** Calculations for Upsilon state suppression at RHIC and LHC energies as a function of collision centrality. The current state of measurements are also shown from PHENIX, STAR and CMS.

shown in Figure 1.18. In concert with the expected higher statistics results from the LHC experiments, sPHENIX data will provide the required precision to discriminate models of breakup in the dense matter and the length scale probed in the medium.

### 1.9.2 Quarkonia in $p(d) + A$ collisions

Measurements of quarkonia production in proton-nucleus collisions have long been considered necessary to establish a cold nuclear matter baseline for trying to understand hot matter effects in nuclear collisions. It has become clear, however, that the physics of  $p+A$  collisions is interesting in its own right [96]. Modification of quarkonia production in a nuclear target has been described by models that include gluon saturation effects (see for example [107]), breakup of the forming quarkonia by collisions with nucleons in the target [108, 109], and partonic energy loss in cold nuclear matter [110]. These mechanisms, which are all strongly rapidity and collision energy dependent, have been used, in combination, to successfully describe  $J/\psi$  and  $\Upsilon(1S)$  data in  $p(d)+A$  collisions.

The observation of what appears to be hydrodynamic effects in  $p+Pb$  collisions at the LHC [111, 112, 113] and  $d+Au$  collisions at RHIC [114] has raised questions about the longstanding assumption that  $p(d)+A$  collisions are dominated by cold nuclear matter effects. For quarkonia, it raises the obvious question: does the small hot spot produced in the  $p(d)+A$  collision affect the quarkonia yield? Recent measurements of the modification of quarkonia excited states in  $p(d)+A$  collisions have produced unexpected and puzzling results.

The situation has become more interesting with the release of data from CMS on produc-

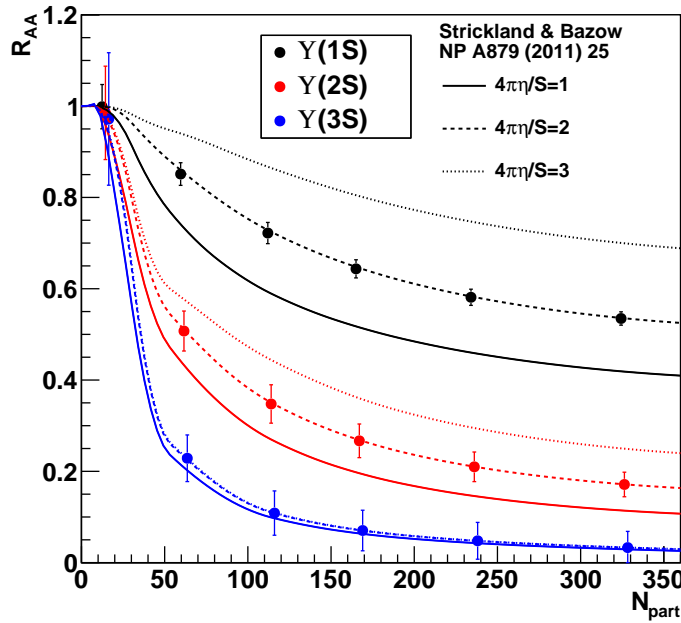


**Figure 1.18:** Estimate of the statistical precision of a measurement of the Y states in Au+Au collisions using sPHENIX, assuming that the measured  $R_{AA}$  is equal to the results of a recent theory calculation by Strickland & Barzow referenced in the legend. The yields assume 100 billion recorded Au+Au events.

tion of Upsilon excited states in  $p$ +Pb collisions. They find that the  $Y(2S)$  to  $Y(1S)$  ratio is suppressed by about 20% in minimum bias  $p$ +Pb collisions, while for the  $Y(3S)$  the differential suppression in minimum bias collisions is about 30%. The effect will be considerably larger in the most central collisions, but data showing the centrality dependence are not released yet.

A comprehensive  $p$ +A collision program with sPHENIX will provide Upsilon measurements in  $p$ +Au collisions at RHIC energy with all three states resolved from each other.

## 1.10 Jet Rates and Physics Reach

In order to realize the proposed comprehensive program of jet probes, direct photon-tagged jets, and Upsilon measurements requires very high luminosities and the ability to sample events without selection biases.<sup>1</sup> In addition to the Upsilon capabilities summarized in Figure 1.18, the extensive set of reconstructed jet measurements made available by

<sup>1</sup>The effect of the completed stochastic cooling upgrade to the RHIC accelerator [115] has been incorporated into the RHIC beam projections [116]. Utilizing these numbers and accounting for accelerator and experiment uptime and the fraction of collisions within  $|z| < 10$  cm, the nominal full acceptance range for

sPHENIX will provide detailed information about the quark-gluon plasma properties, dynamics, time evolution, and structure at  $1\text{--}2\ T_c$ . The theoretical bridgework needed to connect these measurements to the interesting and unknown medium characteristics of deconfined color charges is under active construction by many theorists. Combining this work with new results from the flexible and high luminosity RHIC collider facility can produce new discoveries in heavy ion collisions with an appropriate set of baseline measurements provided sPHENIX apparatus is constructed. The sPHENIX jet detector at RHIC is best able to take advantage of these opportunities.

### 1.10.1 Inclusive jet rates

The inclusive jet yield within  $|\eta| < 1.0$  in 0–20% central Au+Au collisions at 200 GeV has been calculated for  $p+p$  collisions by Vogelsang in a Next-to-Leading-Order (NLO) perturbative QCD formalism [117] and scaled by the expected number of binary collisions. This is presented in Figure 1.19. Also shown are results from the calculation for  $\pi^0$  and direct and fragmentation photon yields. The bands correspond to the renormalization scale uncertainty in the calculation (i.e.,  $\mu, \mu/2, 2\mu$ ). Figure 1.19 provides the counts per event with  $p_T$  larger than the value on the x-axis for the most central 20% Au+Au collisions at  $\sqrt{s_{NN}} = 200$  GeV. With 20 billion events per RHIC year for this centrality selection, this translates into jet samples from 20–80 GeV and direct photon statistics out beyond 40 GeV. It is notable that within the acceptance of the sPHENIX detector, over 80% of the inclusive jets will also be accepted dijet events. The necessary comparable statistics are available with 10 weeks of  $p+p$  and 10 weeks of  $p+\text{Au}$  running.

### 1.10.2 Constraining the path length through the medium

An observable that has been especially challenging for energy loss models to be able to reproduce is the azimuthal anisotropy of  $\pi^0$  production with respect to the reaction plane. A weak dependence on the path length in the medium is expected from radiative energy loss. This translates into a small elliptic flow  $v_2$  value for high  $p_T$  particles, and thus would represent only a modest difference in parton energy loss when traversing a short versus long path length in the QGP.

A strong path length dependence is naturally described by strongly-coupled energy-loss models [118, 119]. Note that one can obtain a larger  $v_2$  by using a stronger coupling, larger  $\hat{q}$ , but at the expense of over-predicting the average level of suppression. New strong

---

the detector, the sPHENIX detector can record 100 billion Au+Au minimum bias collisions in a one-year 22 week run. With the latest luminosity projections, for the purely calorimetric jet and  $\gamma$ -jet observables with modest trigger requirements, one can sample 0.6 trillion Au+Au minimum bias collisions. Note that the PHENIX experiment has a nearly dead-timeless high-speed data acquisition and trigger system that has already sampled tens of billions of Au+Au minimum bias collisions, and maintaining this high rate performance with the additional sPHENIX components is an essential design feature.



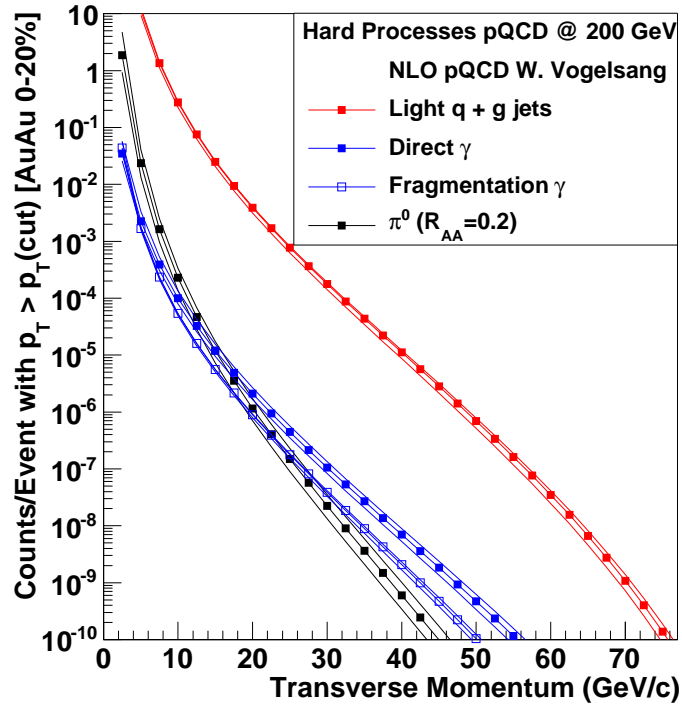


**Figure 1.19:** Jet, photon and  $\pi^0$  rates for  $|\eta| < 1.0$  from NLO pQCD [117] calculations scaled to Au+Au central collisions for  $\sqrt{s_{NN}} = 200$  GeV. The scale uncertainties on the pQCD calculations are shown as additional lines. Ten billion Au+Au central collisions correspond to one count at  $10^{-10}$  at the bottom of the y-axis range. A nominal 22 week RHIC run corresponds to 20 billion central Au+Au events.

coupling models [120, 121] will need to confront the full set of observables measured at RHIC.

The measurement of jet quenching observables, as a detailed function of orientation with respect to the reaction plane, is directly sensitive to the coupling strength and the path length dependence of any modification to the parton shower. In addition, medium response may be optimally measured in mid-central collisions where there is a lower underlying event and where the medium excitations are not damped out over a longer time evolution as in more central collisions or which may be the case also at LHC. Shown in Figure 1.20 are projected uncertainties from sPHENIX for the direct photon and reconstructed jet observables in three orientation selections. One expects no orientation dependence for the direct photons and the question is whether the unexpectedly large dependence for charged hadrons persists in reconstructed jets up to the highest  $p_T$ . Note that the same measurements can be made for beauty tagged jets, charged hadrons up to 50 GeV/c, and a full suite of correlation measurements including jet-jet, hadron-jet,  $\gamma$ -jet.

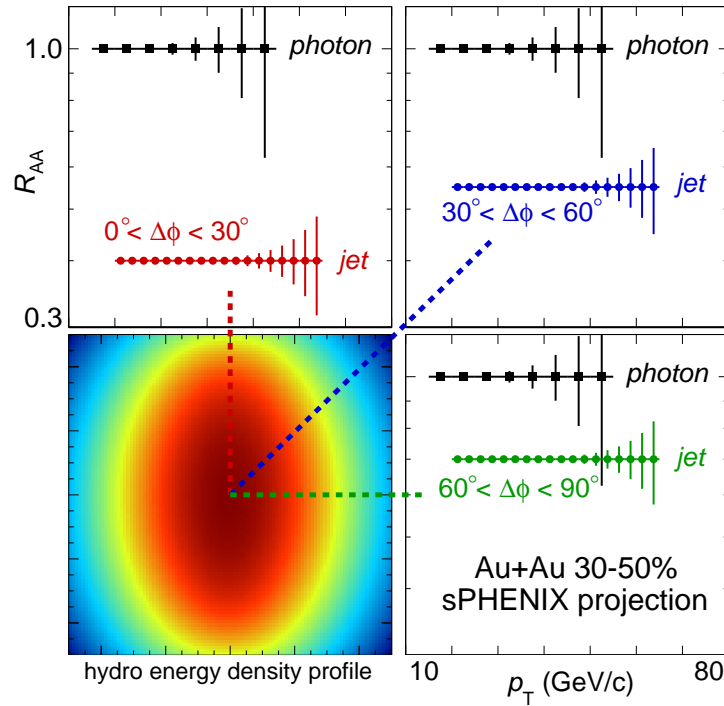


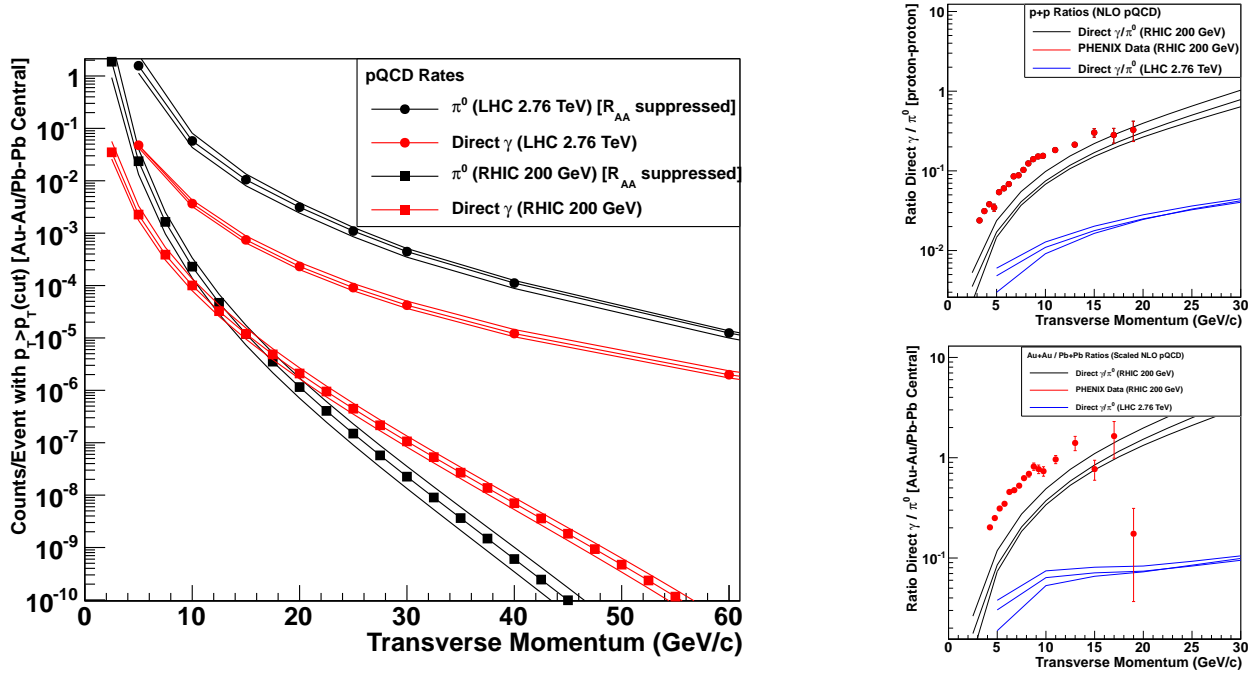
**Figure 1.20:** Demonstration of the statistical reach for azimuthally-sensitive hard probes measurements in sPHENIX. Each panel shows the projected statistical uncertainty for the  $R_{AA}$  of inclusive jets and photons, with each a panel a different  $\Delta\phi$  range with respect to the reaction plane in 30–50% Au+Au events. sPHENIX would additionally have tremendous statistical reach in the analogous charged hadron  $R_{AA}$ .

All measurements in heavy ion collisions are the result of emitted particles integrated over the entire time evolution of the reaction, covering a range of temperatures. Similar to the hydrodynamic model constraints, the theory modeling for jet probes requires a consistent temperature and scale dependent model of the quark-gluon plasma and is only well constrained by precision data through different temperature evolutions, as measured at RHIC and the LHC.

### 1.10.3 Rates for Direct Photons

Measurement of direct photons requires them to be separated from the other sources of inclusive photons, largely those from  $\pi^0$  and  $\eta$  meson decay. The left panel of Figure 1.21 shows the direct photon and  $\pi^0$  spectra as a function of transverse momentum for both  $\sqrt{s} = 200$  GeV and 2.76 TeV  $p+p$  collisions. The right panels show the  $\gamma/\pi^0$  ratio as a function of  $p_T$  for these energies with comparison PHENIX measurements at RHIC. At the LHC, the ratio remains below 10% for  $p_T < 50$  GeV while at RHIC the ratio rises sharply and exceeds one at  $p_T \approx 30$  GeV/c. In heavy ion collisions the ratio is further enhanced

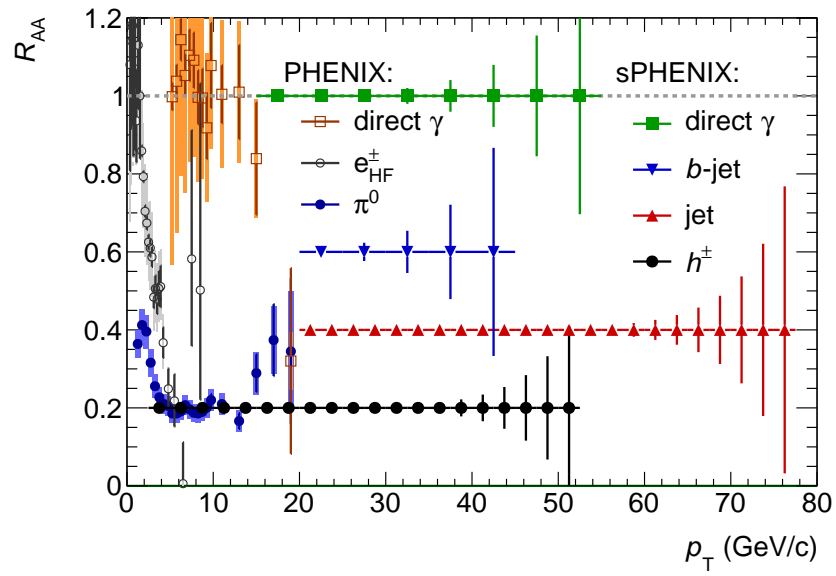
because the  $\pi^0$ s are significantly suppressed. Taking the suppression into account, the  $\gamma/\pi^0$  ratio at RHIC exceeds one for  $p_T > 15$  GeV/c. The large signal to background means that it will be possible to measure direct photons with the sPHENIX calorimeter alone, even before applying isolation cuts. Beyond measurements of inclusive direct photons, this enables measurements of  $\gamma$ -jet correlations and  $\gamma$ -hadron correlations.



**Figure 1.21:** NLO pQCD calculations of direct photons and  $\pi^0$  for RHIC and LHC. The plot on the left shows the counts per event in Au+Au or Pb+Pb collisions (including the measured  $R_{AA}$  suppression factor for  $\pi^0$ ). The upper (lower) panel on the right shows the direct  $\gamma$  to  $\pi^0$  ratio in  $p+p$  (Au+Au or Pb+Pb) collisions, in comparison with measurements from the PHENIX experiment at RHIC [122, 123].

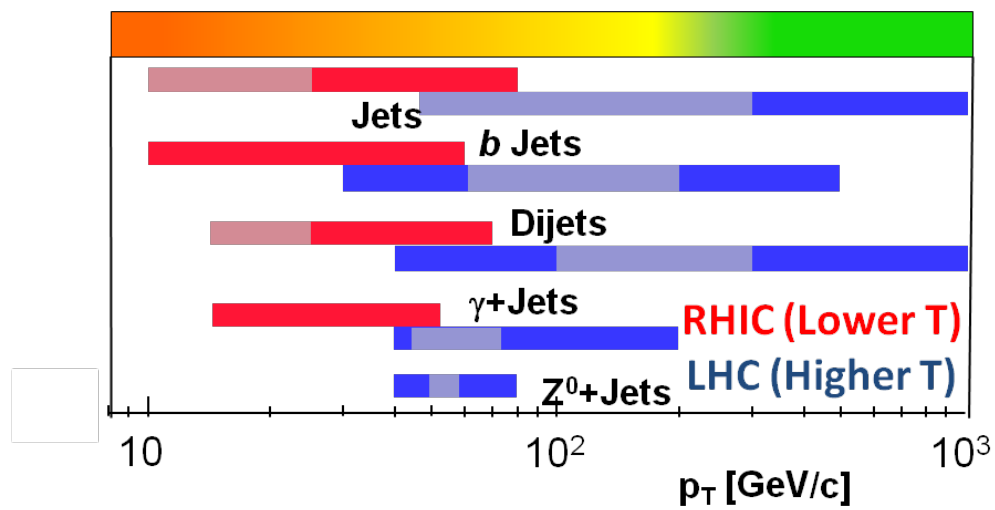
#### 1.10.4 Hard probe statistics and range in $p_T$

Figure 1.22 summarizes the current and future state of hard probes measurements in A+A collisions in terms of their statistical reach, showing the most up to date  $R_{AA}$  measurements of hard probes in central Au+Au events by the PHENIX Collaboration plotted against statistical projections for sPHENIX channels measured after the first two years of data-taking. While these existing measurements have greatly expanded our knowledge of the QGP created at RHIC, the overall kinematic reach is constrained to  $< 20$  GeV even for the highest statistics measurements. Figure 1.23 shows the expected range in  $p_T$  for sPHENIX as compared to measurements at the LHC. Due to the superior acceptance, detector capability and collider performance, sPHENIX will greatly expand the previous kinematic range studied at RHIC energies (in the case of inclusive jets, the data could



**Figure 1.22:** Statistical projections for the  $R_{AA}$  of various hard probes vs  $p_T$  in 0–20% Au+Au events with the sPHENIX detector after two years of data-taking, compared with a selection of current hard probes data from PHENIX.

extend to 80 GeV/c, four times the range of the current PHENIX  $\pi^0$  measurements) and will allow access to new measurements entirely (such as fully reconstructed  $b$ -tagged jets).



**Figure 1.23:** Anticipated range in  $p_T$  of various hard probe measurements using sPHENIX at RHIC (red) and measurements made at the LHC (blue). The color strip across the top corresponds to the regions presented initially in Figure 1.1 (left) for scattering in the medium from bare quarks and gluons (green), from thermal gluons (yellow), and integration over all possible objects that are probed (orange).



# Chapter 2

## Detector Overview

The sPHENIX Detector is a cylindrical detector covering  $|\eta| \leq 1.1$  and the full azimuth. It is built around the former BaBar superconducting solenoid with a reference design that incorporates an inner tracker out to 80 cm in radius followed by a electromagnetic calorimeter, the first of two longitudinal segments of a hadronic calorimeter, the magnet cryostat and the second longitudinal segment of the hadronic calorimeter which also serves as the magnet flux return.

sPHENIX has been designed to satisfy a set of performance requirements that are needed to carry out the physics program described in Chapter 1. The sPHENIX physics program rests on several key measurements, and the requirements that drive any particular aspect of the detector performance come from a broad range of considerations related to those measurements. A comprehensive assessment of the physics requirements has led to the development of the reference design shown in Figure 2.1.

The primary components of the sPHENIX reference design are as follows.

**Magnetic Solenoid** Built for the BaBar experiment at SLAC, the magnet became available after the termination of the BaBar program. The cryostat has an inner radius of 140 cm and is 33 cm thick, and can produce a central field of 1.5 T.

**Tracker** Four options are being studied for the sPHENIX Tracker with two options focusing on inner radius tracking and two options for the outer radius tracking

Inner radius tracking options for precision inner track positioning and vertex reconstruction:

[Existing Pixels] Two layers of hybrid silicon sensors reconfigured from the existing PHENIX vertex detector

[New Pixels] Two or three layers of monolithic silicon sensors

Outer radius tracking options to complete the track measurement:

[Silicon Strips] Five layers of hybrid silicon strip sensors

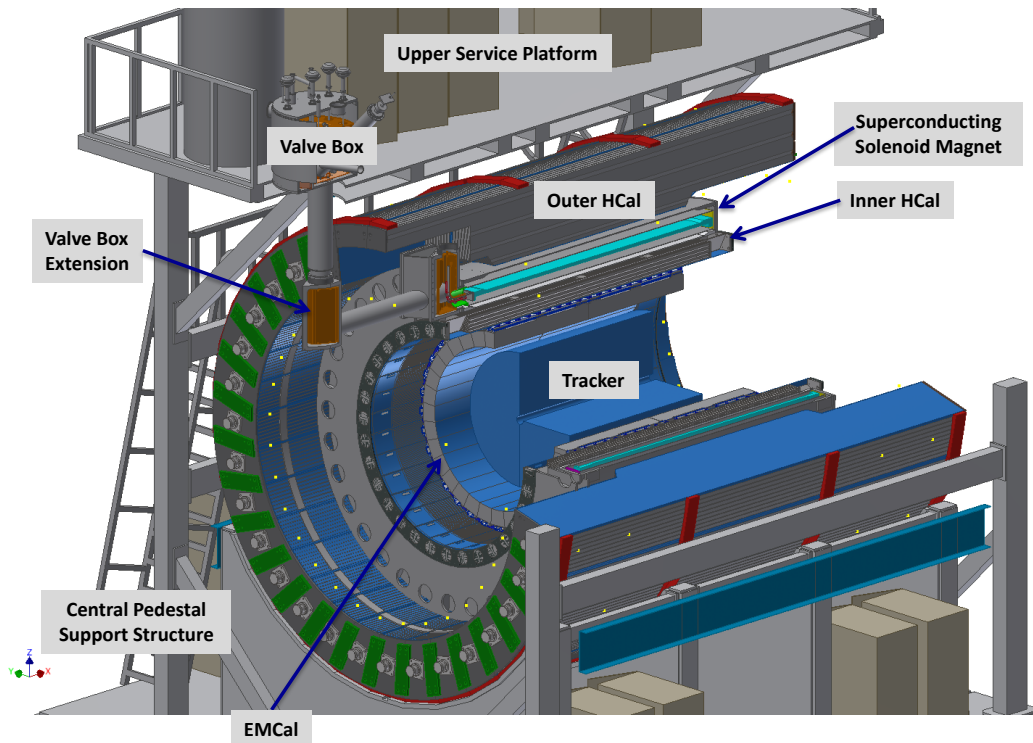


**Figure 2.1:** View of the sPHENIX detector with its component subdetectors.

[Compact TPC] A compact time projection chamber

**Electromagnetic Calorimeter** Tungsten-scintillating fiber sampling calorimeter inside the magnet bore read out with silicon photo-multipliers. The calorimeter has a small Molière radius and short radiation length, allowing for a compact design.

**Inner Hadronic Calorimeter** Sampling calorimeter of non-magnetic metal and scintillator located inside the magnet bore.

**Outer Hadronic Calorimeter** Sampling calorimeter of magnet steel scintillator located outside the cryostat which doubles as the flux return for the solenoid.

In the following list we provide a high-level mapping between physics aims and various detector requirements. The justification for these requirements is then discussed in more detail in subsequent sections.



**Upsilon** The key to the physics is high statistics  $p+p$ ,  $p+A$ , and  $A+A$  data sets, with mass resolution and signal-to-background sufficient to separate the three states of the  $Y$  family.

- large geometric acceptance ( $\Delta\phi = 2\pi$  and  $|\eta| < 1.1$ )
  - high rate data acquisition (15 kHz)
  - trigger for electrons from  $Y \rightarrow e^+e^-$  ( $> 90\%$  efficiency) in  $p+p$  and  $p+A$
  - track reconstruction efficiency  $> 90\%$  and purity  $> 90\%$  for  $p_T > 3$  GeV/c
  - momentum resolution of 1.2% for  $p_T$  in the range 4-10 GeV/c.
  - electron identification with efficiency  $> 70\%$  and charged pion rejection of 90:1 or better in central Au+Au at  $p_T = 4$  GeV/c.
- 

**Jets** The key to the physics is to cover jet energies of 20–70 GeV, for all centralities, for a range of jet sizes, with high statistics and performance insensitive to the details of jet fragmentation.

- energy resolution  $< 120\% / \sqrt{E_{\text{jet}}}$  in  $p+p$  for  $R = 0.2$ –0.4 jets
  - energy resolution  $< 150\% / \sqrt{E_{\text{jet}}}$  in central Au+Au for  $R = 0.2$  jets
  - energy scale uncertainty  $< 3\%$  for inclusive jets
  - energy resolution, including effect of underlying event, such that scale of unfolding on raw yields is less than a factor of three
  - measure jets down to  $R = 0.2$  (segmentation no coarser than  $\Delta\eta \times \Delta\phi \sim 0.1 \times 0.1$ )
  - underlying event influence event-by-event (large coverage HCal/EMCal) (ATLAS method)
  - energy measurement insensitive to softness of fragmentation (quarks or gluons) — HCal + EMCal
  - jet trigger capability in  $p+p$  and  $p+A$  without jet bias (HCal and EMCal)
  - rejection ( $> 95\%$ ) of high  $p_T$  charged track backgrounds (HCal)
- 

**Dijets** The key to the physics is large acceptance in conjunction with the general requirements for jets as above

- $> 80\%$  containment of opposing jet axis
  - $> 70\%$  full containment for  $R = 0.2$  dijets
  - $R_{AA}$  and  $A_J$  measured with  $< 10\%$  systematic uncertainty (also key in  $p+A$ , onset of effects)
- 

**Fragmentation functions** The key to the physics is unbiased measurement of jet energy

- excellent tracking resolution out to  $> 40 \text{ GeV}/c$  ( $dp/p < 0.2\% \times p$ )
- independent measurement of  $p$  and  $E$  ( $z = p/E$ )

---

**Heavy quark jets** The key to the physics is tagging identified jets containing a displaced secondary vertex

- precision DCA ( $< 100$  microns) for electron  $p_T > 4 \text{ GeV}/c$
  - electron identification for high  $p_T > 4 \text{ GeV}/c$
- 

**Direct photon** The key to the physics is identifying photons

- EMCal segmentation  $\Delta\eta \times \Delta\phi \sim 0.024 \times 0.024$
  - EMCal resolution for photon ID ( $< 15\%/\sqrt{E}$ )
  - EMCal cluster trigger capability in  $p+p$  and  $p+A$  with rejections  $> 100$  for  $E_\gamma > 10 \text{ GeV}$
- 

**High statistics** Ability to sample high statistics for  $p+p$ ,  $p+A$ ,  $A+A$  at all centralities — requires high rate, high throughput DAQ (15 kHz).

In the following sections, we detail the origin of key requirements.

## 2.1 Acceptance

The large acceptance and high rate of sPHENIX are key enablers of the physics program detailed in Chapter 1. The total acceptance of the detector is determined by the requirement of high statistics jet measurements and the need to fully contain both single jets and dijets. To fully contain hadronic showers in the detector requires both large solid angle coverage and a calorimeter deep enough to fully absorb the energy of hadrons up to 70 GeV.

The PYTHIA event generator has been used to generate a sample of  $p+p$  at 200 GeV events which can be used to demonstrate the pseudorapidity distribution of jets. The left panel in Figure 2.2 shows the pseudorapidity distribution of jets with  $E_T$  above 20, 30, and 40 GeV. The right panel in Figure 2.2 shows the fraction of events where a trigger jet with  $E_T$  greater than a given value within a pseudorapidity range has an away side jet with  $E_T > 5 \text{ GeV}$  accepted within the same coverage. In order to efficiently capture the away side jet, the detector should cover  $|\eta| < 1$ , and in order to fully contain hadronic showers within this fiducial volume, the calorimetry should cover slightly more than that. Given the segmentation to be discussed below, the calorimeters are required to cover  $|\eta| < 1.1$ .

It should be noted that reduced acceptance for the away-side jet relative to the trigger suffers not only a reduction in statistics for the dijet asymmetry and  $\gamma$ -jet measurements but also results in a higher contribution of low energy fake jets (upward fluctuations in the

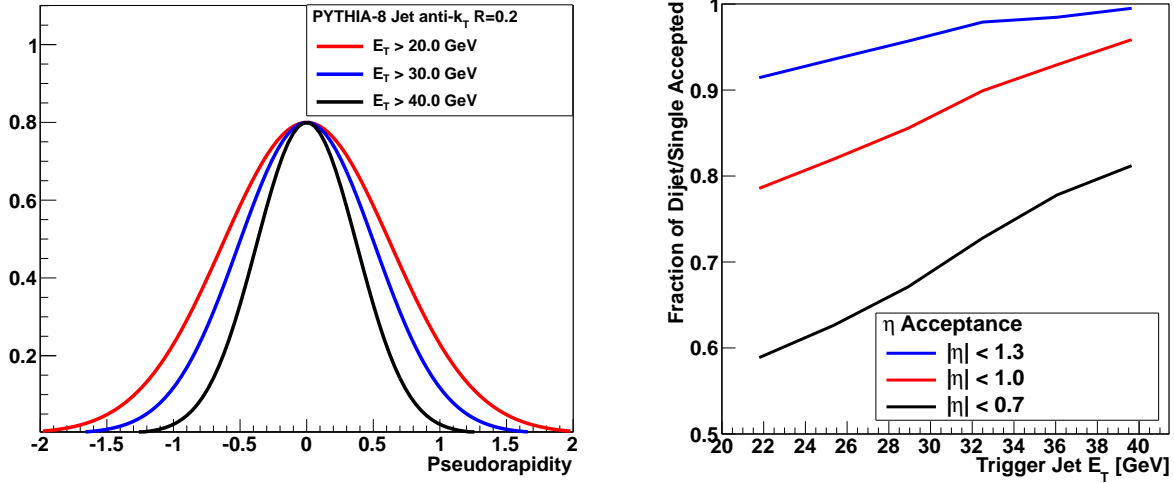


**Figure 2.2:** (Left) Pseudorapidity distribution of PYTHIA jets reconstructed with the FASTJET anti- $k_T$  and  $R=0.2$  for different transverse energy selections. (Right) The fraction of PYTHIA events where the leading jet is accepted into a given pseudorapidity range where the opposite side jet is also within the acceptance. Note that the current PHENIX acceptance of  $|\eta| < 0.35$  corresponds to a fraction below 30%.

background) in those events where the away side jet is out of the acceptance. For the latter effect, the key is that both jet axes are contained within the acceptance, and then events can be rejected where the jets are at the edge of the detector and might have partial energy capture.

## 2.2 Segmentation

Jets are reconstructed from the four-vectors of the particles or measured energies in the event via different algorithms, and with a typical size  $R = \sqrt{\Delta\phi^2 + \Delta\eta^2}$ . In order to reconstruct jets down to radius parameters of  $R = 0.2$  a segmentation in the hadronic calorimeter of  $\Delta\eta \times \Delta\phi = 0.1 \times 0.1$  is required. The electromagnetic calorimeter segmentation should be finer as driven by the measurement of direct photons for  $\gamma$ -jet correlation observables. The compact electromagnetic calorimeter design being considered for sPHENIX has a Molière radius of  $\sim 15$  mm, and with a calorimeter at a radius of about 100 cm, this leads to an optimal segmentation of  $\Delta\eta \times \Delta\phi = 0.024 \times 0.024$  in the electromagnetic section.

## 2.3 Energy Resolution

The requirements on the jet energy resolution are driven by considerations of the ability to reconstruct the inclusive jet spectra and dijet asymmetries and the fluctuations on the fake jet background. The total jet energy resolution is typically driven by the hadronic calorimeter resolution and many other effects including the bending of charged particles in the magnetic field out of the jet radius. Expectations of jet resolutions approximately 1.2 times worse than the hadronic calorimeter resolution alone are typical.

In a central Au+Au event, the average energy within a jet cone of radius  $R = 0.2$  ( $R = 0.4$ ) is approximately 10 GeV (40 GeV) resulting in an typical RMS fluctuation of 3.5 GeV (7 GeV). This sets the scale for the required reconstructed jet energy resolution, as a much better resolution would be dominated by the underlying event fluctuations regardless. A measurement of the jet energy for  $E = 20$  GeV with  $\sigma_E = 120\% \times \sqrt{E} = 5.4$  GeV gives a comparable contribution to the underlying event fluctuation. A full study of the jet energy resolution with a GEANT4 simulation of the detector configuration has been performed and is discussed in the sPHENIX proposal required and is presented in the Physics Performance chapter of the sPHENIX Proposal [1].

Different considerations set the scale of the energy resolution requirement for the EMCal. The jet physics requirement is easily met by many EMCal designs. For the direct  $\gamma$ -jet physics, the photon energies being considered are  $E_\gamma > 10$  GeV where even a modest  $\sigma_E/E = 12\%/\sqrt{E}$  represents only a blurring of 400 MeV. In Au+Au central events, the typical energy in a  $3 \times 3$  tower array is also approximately 400 MeV. These values represent a negligible performance degradation for these rather clean photon showers even in central Au+Au events.

Most of these physics measurements require complete coverage over a large range of rapidity and azimuthal angle ( $\Delta\eta \leq 1.1$  and  $\Delta\phi = 2\pi$ ) with good uniformity and minimal dead area. The calorimeter should be projective (at least approximately) in  $\eta$ . For a compact detector design there is a trade-off in terms of thickness of the calorimeter and Molière radius versus the sampling fraction and, therefore, the energy resolution of the device. Further optimization if these effects will be required as we work towards a final design.

## 2.4 Tracking

The requirements on tracking capabilities are tied to three particular elements of the sPHENIX physics program. The measurement of the upsilon family of quarkonia states, heavy flavor tagged jets, and fragmentation functions at high and at low  $z$ , together set the performance specification for the sPHENIX Tracker.

To fully utilize the available luminosity, the tracking systems should have large, uniform

acceptance and be capable of fast readout. Measuring fragmentation functions at low  $z$  means looking for possibly wide angle correlations between a trigger jet and a charged hadron. This places only moderate requirements on the momentum resolution ( $\Delta p/p \simeq 1\% \cdot p$ ), but reinforces the requirement of large acceptance.

Fragmentation functions at high  $z$  place more stringent requirements on momentum resolution and can be a design constraint at large momentum well above 10 GeV/c. In order to unfold the full fragmentation function,  $f(z)$ , the smearing due to momentum uncertainty should be very small compared to the corresponding smearing due to the calorimetric jet measurement for a cleanly identified jet. For a 40 GeV jet this condition is satisfied by a tracking momentum resolution of  $\Delta p/p \simeq 0.2\% \cdot p$  or better.

The measurement of the  $Y$  family places the most stringent requirement on momentum resolution below 10 GeV/c. The large mass of the  $\Upsilon$  means that one can focus primarily on electrons with momenta of  $\sim 4 - 10$  GeV/c. The  $Y(3S)$  has about 3% higher mass than the  $Y(2S)$  state; to distinguish them clearly one needs invariant mass resolution of  $\sim 100$  MeV, or  $\sim 1\%$ . This translates into a momentum resolution for the daughter  $e^\pm$  of  $\sim 1.2\%$  in the range  $4 - 10$  GeV/c.

The  $Y$  measurement also generates requirements on the purity and efficiency of electron identification. The identification needs to be efficient because of the low cross section for  $Y$  production at RHIC, and it needs to have high purity against the charged pion background to maintain a good signal to background ratio. Generally speaking, this requires minimizing track ambiguities by optimizing the number of tracking layers, their spacing, and the segmentation of the strip layers. Translating this need into a detector requirement can be done only by performing detailed simulations with a specific tracking configuration, followed by evaluation of the tracking performance.

Tagging heavy-flavor jets introduces the additional tracking requirement of being able to measure the displaced vertex of a D or B meson decay. The  $c\tau$  for D and B decays is  $123 \mu\text{m}$  and  $457 \mu\text{m}$ , respectively, and the displaced vertex needs to be identified with a resolution sufficient to distinguish these decays against backgrounds.

## 2.5 Triggering

The jet energy should be available at the Level-1 trigger as a standard part of the PHENIX dead-timeless Data Acquisition and Trigger system. This triggering ability is important as one requires high statistics measurements in proton-proton, proton-nucleus, light nucleus-light nucleus, and heavy nucleus-heavy nucleus collisions with a wide range of luminosities. It is important to have combined EMCal and HCal information available so as to avoid a specific bias on the triggered jet sample.



## Chapter 3

# Superconducting Magnet

The magnet and tracking system should be capable of order of 1% momentum resolution at 10 GeV/ $c$  over  $|\eta| < 1.1$  and the full azimuth. The BaBar solenoid, with a central field of  $\sim 1.5$  T and an inner radius of  $\sim 140$  cm, is an excellent match to the sPHENIX physics requirements. The magnet became available in late 2012, and the ownership of the coil and related equipment have been transferred to BNL.

### 3.1 Magnet Mechanical Design

The superconducting solenoid magnet was manufactured by Ansaldo and delivered to the BABAR experiment at SLAC in 1997. The magnet was successfully commissioned in 1998, and it was operated and remained in good condition through the end of the BaBar experiment in April 2008. The solenoid was then shipped to BNL in February 2015. Upon installation in sPHENIX at BNL, the magnet will remain unchanged except for an extension to the connection to the exiting power leads and cryogenic line structure (referred to as the valve box) to eliminate interference with the sPHENIX outer calorimeter.

Partly to simplify track finding and fitting, the magnitude of the magnetic field within the tracking volume should be constant within a few percent. The field will be measured to better than 1% in the whole cryostat area to correct for nonuniformities, especially close to the plug doors.

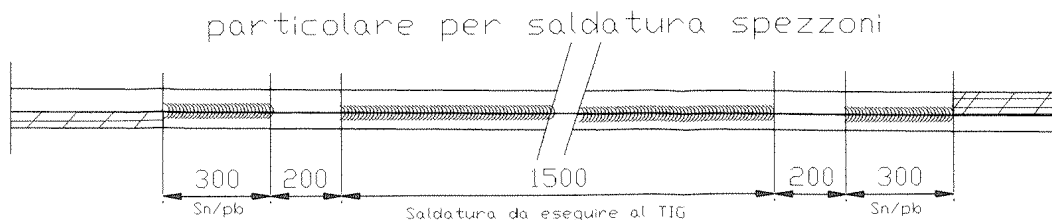
#### 3.1.1 Conductor

The conductor is composed of a niobium titanium “Rutherford-type” superconducting cable which was co-extruded with an outer aluminum matrix. The cable is made of sixteen strands of 0.8 mm diameter wire with a copper to superconductor ratio of 1:1, filament size less than 40  $\mu\text{m}$ , and twist pitch of 25  $\mu\text{m}$ . The final superconducting cable is rectangular in

shape and 1.4 mm by 6.4 mm in size. The aluminum matrix into which the superconductor is co-extruded is of two sizes; 8.49 mm thick by 20 mm wide in the body of the magnet, and 4.93 mm thick by 20 mm wide in the coil end regions. The thinner aluminum matrix in the ends permits higher current density in the coil ends to extend the axial region of uniform solenoid field. The critical current of the conductor is 12,680 A at 2.5 T and 4.2 K, which provides a safety margin of 2.75 over the operating current of 4,596 A. The conductor is wrapped with fiberglass cloth which is later impregnated with epoxy, the combination of which provides both electrical insulation for the conductor and mechanical support for the completed coil.

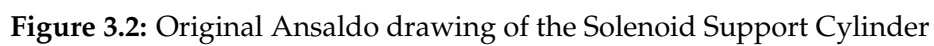
### 3.1.2 Coil

The solenoid coil consists of two conductor layers. Both conductor layers were internally wound inside an aluminum support mandrel — first the outer layer and then the inner layer. Winding was started at the end where the conductor leads would ultimately exit the coil, using the narrow conductor. After a specified number of windings the narrow conductor was spliced to the thick conductor using two 30 cm long soldered lap connections, spaced 20 cm on either side of a 1.5 m long region where the edges of the overlapping thin and thick aluminum matrices were welded together (Figure 3.1). The completed splice region was hand wrapped with fiberglass cloth when complete and winding using the thick conductor was completed to a specified number of turns, after which a similar splice back to thin conductor was installed and the winding of the outer layer completed to the desired dimensions. A third splice, this one to connect to the inner coil layer, was installed, and inner layer winding was completed in a fashion similar to the outer layer using thin, then thick, a finally thin, conductor. The number of thin and thick conductor windings, for the inner (outer) layer, counting from the exiting lead end of the coil, are 184, 164, and 183 (188, 159, and 189). When the winding was completed, the coil was impregnated using epoxy to create a rigid structure. G-10 parts were used in transition locations and to adjust the overall length of the coil to meet the aluminum support mandrel end flanges.



**Figure 3.1:** Internal splices (extracted from the original Ansaldo drawing): 1500 mm weld of aluminum edges + 200 mm gap + 300 mm solder of aluminum faces on both sides of the weld. The welding was done with the TIG (Tungsten Inert Gas) technique.





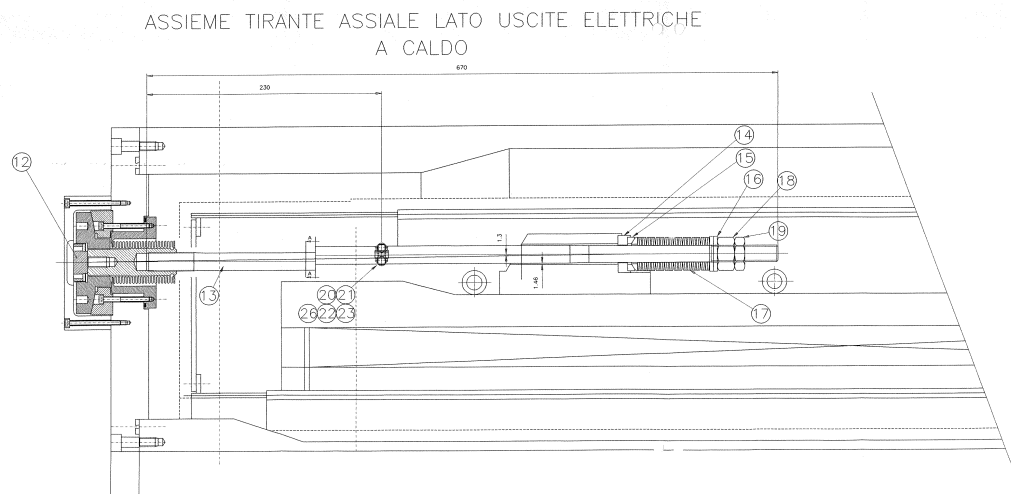


**Figure 3.3:** Original Ansaldo drawing: Axial Tie Rod Assembly

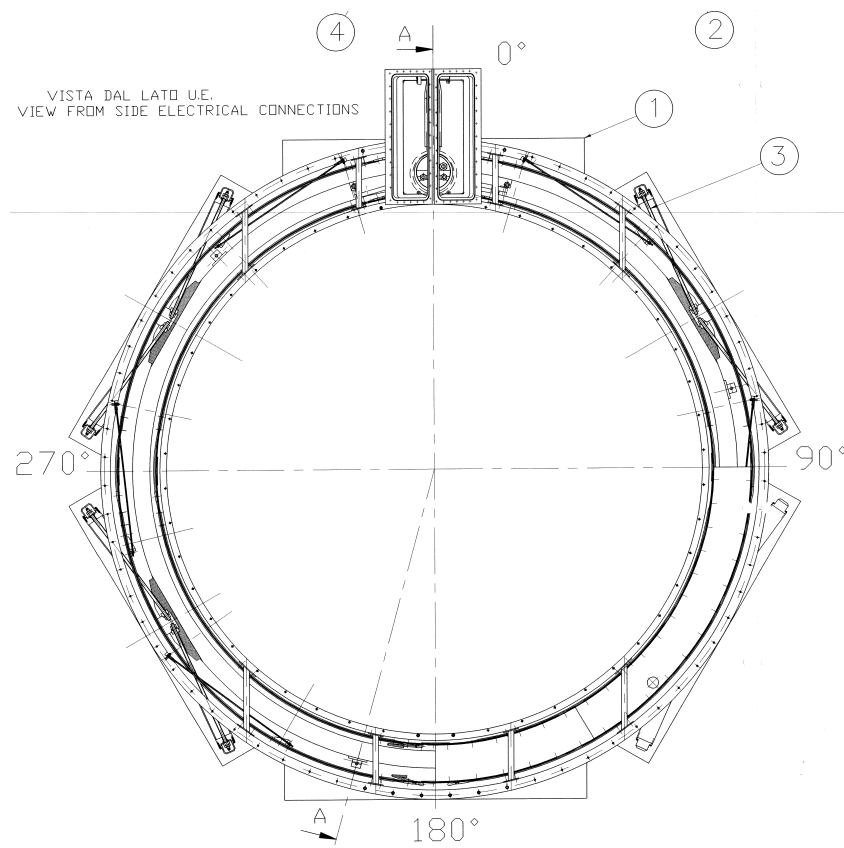


**Figure 3.4:** Original Ansaldo drawing: Cryostat Assembly



**Figure 3.5:** (Left) Exiting leads — aluminum removed and niobium titanium soldered to heavy copper stabilizer leads (overlapping aluminum; (Right) Outer heat shield.

### 3.1.3 Cold Mass and Cryostat

The aluminum support mandrel provides both mechanical support and cooling to the solenoid coil (Figure 3.2). Conductive cooling is provided via helium which circulates in lines welded to the outside surface of the support mandrel. An outer heat shield which is actively cooled to 40 K using helium gas from the cold mass cooling line boil-off that is returned to the helium reservoir, along with conductively cooled heat shield end plates and inner heat shield (connected to the outer shield) assist with maintaining a uniform 4 K coil temperature. Support from outward radial and axial Lorentz forces is provided by the strength of the aluminum cylinder. Gravity loads, as well as magnetic field alignment, are provided by a system of tangential and axial Inconel tie rods which develop tension on cool down to 4 K. Tie rods connect the coil support cylinder directly to the aluminum outer cryostat (Figure 3.3) but are heat stationed to the outer heat shield. The coil is positioned with a 30 mm axial offset toward the lead end with respect to the outer cryostat. The

outer heat shield is independently supported by the outer cryostat by separate tie rods (Figures 3.4 and Figures 3.5).

### 3.1.4 Valve Box

The cryostat connects to a vertical tower (valve box, Figure 3.6), which contains all the electrical (vapor cooled) power leads, instrumentation wire leads, helium supply and return lines for coil and heat shield, and vacuum connections. During installation in sPHENIX this valve box will be extended away from the magnet to provide clearance for the outer calorimeter, by adding a 1 m transfer line extension which carries all of the aforementioned lines from magnet to valve box.

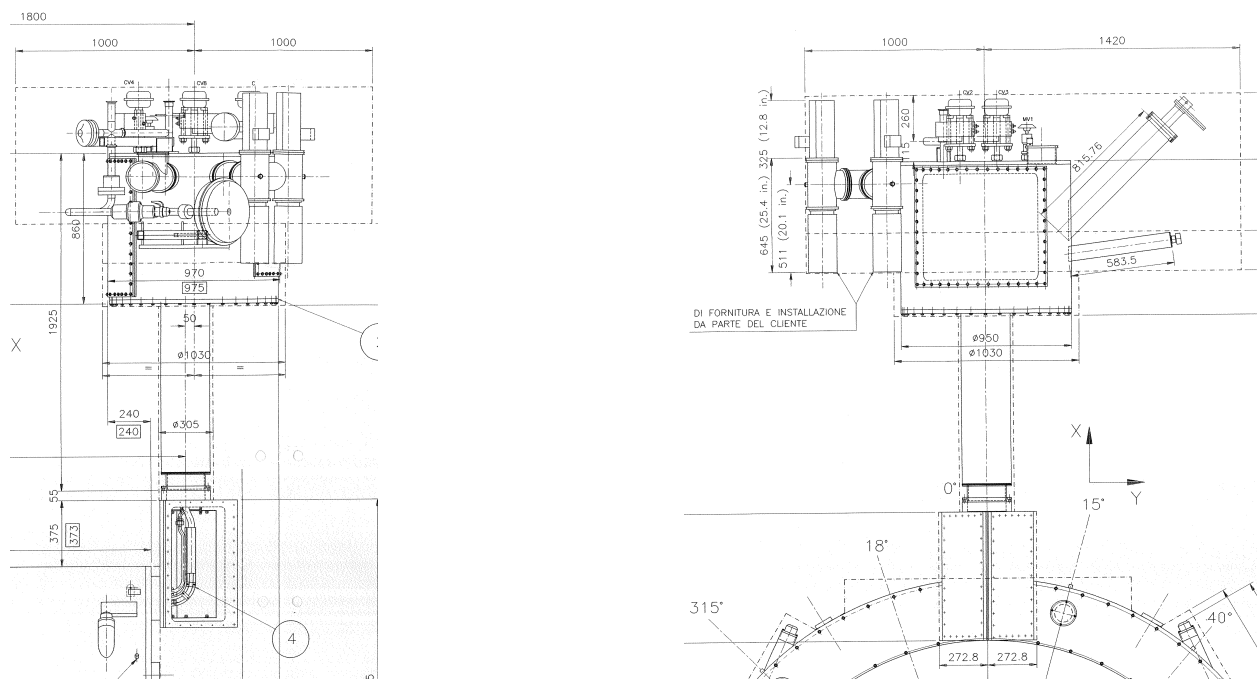


**Figure 3.6:** Original Ansaldo drawing of the valve box.

Figures 3.6 and 3.7 show the placement of the cryostat, the extension and the valve box. Figure 3.8 shows different portions of the extension that is connected to the valve box.

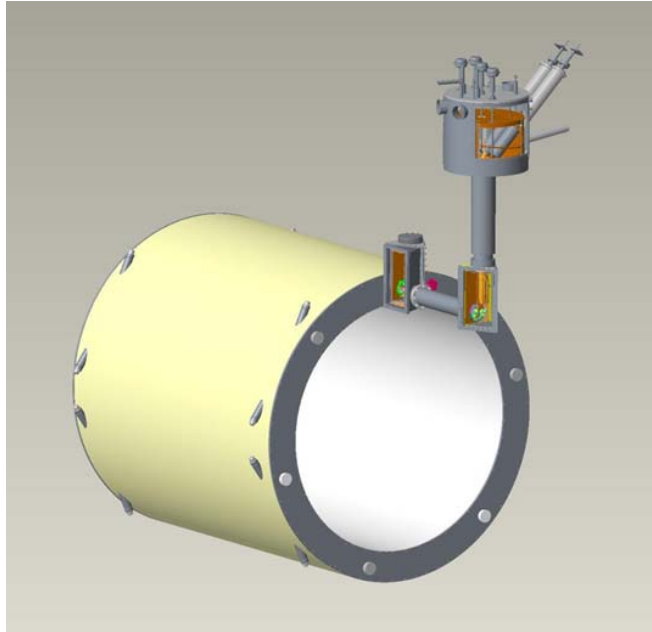


**Figure 3.7:** The cryostat, the extension and the valve box.

## 3.2 Cryogenics

### 3.2.1 Magnet Cryostat System

The coil of the magnet is attached to a cylindrical aluminum mandrel which is cooled by boiling liquid helium in eleven parallel aluminum tubes welded to the mandrel. A separate valve-box cryostat located above the solenoid cryostat, outside the return flux iron serves to interface the power and cryogenics to the solenoid. The valve-box contain the cryogenic valves, the siphon phase separator vessel, current leads, and relief devices. A vacuum jacketed interconnect containing the cryogenic lines and superconducting current cables, and instrument wiring, connects the solenoid cryostat to the valvebox.

### 3.2.2 Magnet 4.5 K Cooling

The originally design of the cooling loop is a thermo-siphon loop in which liquid is drawn from the phase separator vessel and fed to the bottom of solenoids cooling loop and returns back to the phase separator. It has not been operated in the thermo-siphon for most if its normal operating life at its previous facility. The magnet was cooled by, instead of feeding the liquid to the phase separator, the liquid helium was fed directly from the cryogenic supply to the solenoids cooling loop, with the return flow still coming back to the valve-box phase separator. This operating point was still sub-critical, and thus nucleate

boiling still occurred and the flow is two phase returning to the phase separator. Nominal load is 70 W to the 4.5 K loop.

### 3.2.3 Superconducting Current Leads

The two superconducting current (SC) leads, after exiting the coil are cooled by conduction to the 2-phase flow return tube. The superconducting lead cables are attached to copper bars, which are cooled by this return line going back to the valve box. The SC leads terminate at the lead pots, which each contain the normal conducting copper vapor cooled current lead, that transitions to the room temperature connection for the external power supply. The lead pot is cooled by liquid drawn from the main siphon phase separator. The entire lead pot is electrically hot, and isolation is done with an isolator at the tubing connections that feed liquid and return cold vapor, and on the tubing connection where the lead cooling exit the warm end of the current lead, with the actual pot vessel isolated with a G-10 spacer at the flange on the warm end of the lead pot vessel. The nominal lead cooling flow is 0.2 g/s controlled by a 0.5 g/s thermal mass flow controller.

### 3.2.4 Thermal Shield

Thermal shields surround the solenoid coil/mandrel assembly in both annular spaces (inner and out diameter) between the coil and the cryostat vacuum vessel. Some of the 4.5 K cold vapor from the separator vessel is taken through the shield loop and returns back to the cryosystem to a warmup heater (liquefaction load on the plant) or returns cold at approximately 40 K to the cryo plants coldbox. Nominal shield flow is 0.35 g/s with a return temperature of around 60 K for a load of 110 W.

### 3.2.5 Valve Box

The valve box serves as the cryogenic, power supply, vacuum, and instrumentation interface between the solenoid and the rest of the facility. It contains the following equipment on the valve box and interfaces: cryogenic control valves, the relief devices, the electrical feedthroughs for all the solenoid instrumentation, turbo vacuum pump, vacuum gages, pressure sensors, TE, SC level, LHe bath heaters.

### 3.2.6 Relief Devices

The helium volume is protected by an ASME relief valve and ASME burstdisk, and a cryogenic dump globe valve from a relief line originating the phase separator. The reliefs were sized to handle a full magnet quench and loss of insulating vacuum to air.

### 3.2.7 Cryogenic Plant System

The magnet will be cooled by a stand-alone plant, with its coldbox located atop the detector superstructure. A 500 L liquid helium storage dewar will be located next to it. Cryogenic lines between the coldbox and the dewar, and between the dewar and the solenoid valve box make up the balance of the equipment. Thus the piping connections from the building side to the detector superstructure platform are the room temperature helium lines, the LN2 supply line, the relief header. The cryogenic system will travel with the detector when it is in the assembly hall for testing.

An alternative configuration ties the magnet into the RHIC cryogenic system (which is not described here) and would produce a cost difference of possibly on the order of \$1 million. Nevertheless, this option will constrain us to only operating the magnet for not more than 1 day at a time during the shutdown and only continuously when RHIC is cooled down which starts only at the beginning of each RHIC run and is not desirable if we want to commission the Superconducting Magnet in Bldg. 1008 well before the start of a RHIC run.

### 3.2.8 Liquid Helium Storage Dewar

A 500 L ASME U-Stamped storage dewar with a net liquid inventory of 300 Liters is required to allow liquid draw of 5 g/s and 1 g/s of vapor generation (6 g/s = 180 LPH) to allow rampdown of the magnet within one hour.

### 3.2.9 Helium Compressor

The compressor system for the helium plant will be located in the service building or separate shack. From there the piping for the room temperature helium gas will run to the experimental hall building. Dimensions: 2.3 m x 2.0 m x 2.0 m High, [8ft x 7 ft x 7ft High]. Depending on location the compressor will have its own cooling air duct to remove heat released to air to the outside of the building to prevent overloading of building air conditioning.

### 3.2.10 Coldbox

The plant coldbox will be located on top of the detector superstructure next to the liquid helium storage dewar and near the magnets valve box. A 325 W to 400 W plant is budgeted.



Item	Load	Equivalent capacity 4.5 K
Magnet load and valvebox	70 W	70 W
Shield	0.5 g/s	50 W
Vapor cooled leads	0.5 g/s	50 W
Transfer lines	10 W [+100 W]*	10 W [+100 W]*
500 L Storage Dewar + Bayonets	2 W + 2 W	4 W
TOTAL		184 W [ $\approx$ 280 W]*

\*If a plant is not located on the structure of the superconducting magnet but in the service building, additional cryogenic transfer is required.

### 3.2.11 Liquid Nitrogen Supply Line

Liquid nitrogen is supplied via a 250 ft long cryogenic transfer line from the liquid nitrogen storage dewar located in the front of the experimental hall building. Besides supplying the 4.5 K coldbox, two additional taps are provided, one for supplying the start-up purifier and another tap will be run into the assembly hall, for when the detector is moved there.

### 3.2.12 Helium Interface Piping RHIC Cryogenic System

A warm line will be installed, such that inventory will be allowed to move between RHIC cryogenic system and the sPHENIX system.

### 3.2.13 Local Gas Storage: 6,000 Gal @13 bar

A local gas storage tank is proposed to allow summer shutdown testing in the event the helium interface line to RHIC system is not able to transfer inventory.

### 3.2.14 Small 2 g/s Purifier

A small LN2 bath cooled cryogenic purifier is required to for start-up cleanout or cleanout after maintenance.

### 3.2.15 Utilities

#### A. Electric

Service building: Helium Compressor: 150 kW, 480VAC

Coldbox and magnet valvebox: 6 kW, 120VAC

- B. Cooling Water, Tower  
50 GPM at 20 psid
- C. Conditioned water for cryogenic expanders work extraction heatexchangers  
4 LPM, 50/50
- D. Instrument Air  
Dry air dewpoint  $-40^{\circ}\text{C}$ , 8 SCFM, 80 psig
- E. Liquid Nitrogen  
Liquid nitrogen will be provided from the existing storage dewar located outside of the experimental hall building via a new cryogenic transfer line.

### 3.2.16 Controls

Controls of the valvebox items will be done by a Modicon 340 series PLC and I/O chassis, located in a 19" rack along with the temperature sensors controllers, SC level probe controllers and vacuum pump controllers. The cryogenic plant will come with its own PLC system and controls the plants coldbox and compressor system. The PLCs will be interfaced to the RHIC Cryogenic Systems DCS/HMI control system via Ethernet on its own subnet. Figure 3.9 present a flow-chart of the cryogenic control system.

## 3.3 Magnet Power Supply

### 3.3.1 Elements of the Power Supply System

Figure 3.10 shows the main elements of the sPHENIX Magnet powering system.

**L Solenoid = 2.5 Hy** The solenoid is represented as two inductors in series, as it constructed in two layers. The connection between the two layers is brought outside the solenoid, to be used by the quench protection system. It is close, but not exactly, a true center tap. The two layers have slightly different number of turns (531 vs 536), and the inner winding has greater capacitive coupling to the support cylinder.

**Rd = 68 m $\Omega$**  Rd is energy dump resistor, used to quickly reduce the current in the solenoid if a quench is detected. This minimizes the energy absorbed within the solenoid. It is split in two, with a soft reference to ground at the center point. With this split, the voltage on either side of the solenoid to ground is only half the full dump voltage.

**Rg = 67 m $\Omega$**  Rg limits the ground current, should the coil fault to ground. The voltage across Rg is monitored by a ground fault detector.

**Magnet ZFCT** The magnet zero flux current transducer (ZFCT) accurately measures the current into the solenoid. It differs from the power supply current by the current flowing through the dump resistor. For this reason, this is the ZFCT used to regulate the current in the power supply.

**DC Contactor** In the event of a quench, the DC contactors are opened, and the power supply is disconnected from the solenoid. The full solenoid current is then directed through the energy dump resistor.

**Rc = 1.25 mΩ (SLAC Configuration)** Rc is the cable resistance. It determines the time to ramp down the current through the freewheeling diode (FWD) when the power supply turns off.

**PS ZFCT** The power supply ZFCT is for testing purposes, as it does not represent the solenoid current as accurately as the magnet ZFCT.

**FWD** The freewheeling diode (FWD) provides a current path when the power supply is turned off or trips.

**PS** The power supply (PS) nominally operates 4.6 kA and less than 20 V. The unit is manufactured to operate up to 8 kA and 40 V. Taps on the input transformer are used to reduce the maximum operating voltage.

### 3.3.2 Operating Conditions

#### 1. Ramping Up to Full Current

Under the conditions where the current is ramped from zero to 4.6 kA at a rate of 2.5 A/sec:

- (a) The time to reach full current is  $(4,600 \text{ A}) / (2.5 \text{ A/sec}) = 1,840 \text{ seconds}$   
= 30.7 minutes.
- (b) The voltage across the magnet is  $V_m = L di/dt = 2.5 \text{ Hy} \times 2.5 \text{ A/sec} = 6.25 \text{ V}$ .
- (c) The current through Rd is  $V_m / R_d = 6.25 \text{ V} / 68 \text{ m}\Omega = 92 \text{ Amps}$
- (d) The peak power supply voltage is  $R_c (I_m + I_d) + V_m$   
=  $1.25 \text{ m}\Omega (4.600 + 92) + 6.25 = 12.1 \text{ V}$ .

#### 2. Slow Discharge through FWD and Rc

- (a) Time constant  $\tau = L / R_c = 2.5 \text{ Hy} / 1.25 \text{ m}\Omega = 2,000 \text{ seconds} = 33.3 \text{ minutes}$
- (b) Time to decay from 4.6 kA to 100 A (as an example),  
 $T_d = -\tau \ln(I / I_o) = -33.3 \ln(100 / 4,600) = 127.5 \text{ minutes} = 2.1 \text{ hours}$

#### 3. Fast Discharge through Dump Resistor

- (a) Time constant  $\tau = L / R_d = 2.5 \text{ Hy} / 68 \text{ m}\Omega = 36.76 \text{ seconds}$
- (b) Time to decay from 4.6 kA to 100 A (as an example),  
 $T_d = -\tau \ln(I / I_0) = -36.76 \ln(100 / 4,600) = 140.4 \text{ seconds} = 2.34 \text{ minutes}$

### 3.3.3 Monitoring the Solenoid

The change in state of a conductor from superconducting to resistive is called a quench. The function of the quench detector is to measure small values of resistance by the voltage they create. Figure 3.11 shows the wires connected to parts of the solenoid to sense internal voltages.

#### Quench Detection During Ramping

The quench detector should be sensitive to a voltage rise of about 100 mV. This is simple when the current in the solenoid is constant. But, when the current is ramping up or down, the induced voltage,  $V = L di/dt$ , is much greater than 100 mV. With a ramp rate of 2.5 A/sec,  $V = 6.25 \text{ V}$ .

There is a voltage tap at the connection between the inner and outer solenoid windings. During ramping, if the inductance of these windings were identical, the voltage across the top coil (VT05 with respect to VT07) would be exactly negative of the voltage across the bottom coil with respect to the same point (VT10 with respect to VT09).

The sum of these two voltages would add to zero. An imbalance caused by a 100 mV quench voltage can then be detected in the sum.

#### Practical Considerations

The inner and outer coil inductances are not identical.

1. The winding turns are not equal. The number is slightly different, 531 vs 536. This can be corrected by scaling the voltage tap value slightly before summing the two halves of the solenoid voltages.
2. The inner coil has greater capacitive coupling to the supporting cylinder than the outer coil. Even if the coils had identical initial inductances, this coupling imbalance will cause an imbalance in induced voltage. This effect is a function of ramp rate. To reduce this effect, the summing correction for the static inductance difference is adjusted for a given ramp rate.

## Energy Extraction

When a quench is detected, DC contactors are opened, removing the power supply from the load and directing the load current through the energy dump resistor.

The energy dump resistor causes the current in the solenoid to decay with a time constant of 36.8 seconds. This minimizes the heating of the quenched portion of the magnet. The peak voltage across the magnet is approximately 640 V, which due to the center ground reference at the energy dump resistor, is a maximum of 320 V with respect to ground on either side of the solenoid. By comparison, the time constant for a slow decay through the freewheeling diode for a normal shut down is 33.3 minutes.

The quench protection of the BaBar magnet was externally reviewed in October 1996. At the end of that review, additional information was requested and a second review was held in January 1997. The final report was delivered in March 1997. The report concluded that the quench analysis was complete. Based on this analysis it was shown that, even without a fast discharge, a quench would not develop temperatures that would cause a catastrophic magnet failure. As a key component of the fast discharge, the energy dump resistor was also studied, and found to provide adequate protection for the magnet.

## Development of a New Quench Detector

Fifteen years have passed since the original quench detection system in the BaBar experiment has been designed and implemented. In the future implementation which will be done by the cooperation of Superconducting Magnet Division and the Collider-Accelerator Department, new hardware and software will make more accurate and reliable quench detection possible for this Magnet.

### 3.3.4 Magnetic Field Simulations

As the return yoke in sPHENIX is very different than the original BaBar configuration, detailed field simulations are needed to understand the changes in shape and strength of the field. In a first step 2D simulations were done using the standard commercial OPERA software package.

These 2D simulations, Fig. 3.12, assume a rotational symmetry of the setup and are a starting point for GEANT4 detector and physics simulations.

As the field depends on the dimensions and shape of the return yoke, which is not completely symmetric, and specifically on the distance of the two plug-doors with the beam openings, more detailed 3D simulation are necessary. To simplify the simulations the return yoke was first replaced by a solid cylinder of magnet steel with the appropriate density, Fig. 3.13. The calculated magnetic field through this structure, at 4596 A, along the

longitudinal axis (beam direction) is shown in Fig. 3.14.

These simulations can also be used to calculate the forces on the solenoid. Apart from the mechanical forces due to the cool down, the dimensions and shape of the yoke and plug doors as well as the position of the coil within the return yoke creates sizable forces on the coil.

The plate structure of the return yoke is a challenging setup for the finite-element analysis, but these details are needed for understanding possible changes in the shower shape due to the scintillator gaps, Fig. 3.15.

### 3.3.5 Magnetic Force Simulations

The BaBar superconducting coil will be placed inside a non-symmetric flux return yoke as a part of the sPHENIX magnet assembly. This can give rise to axial offset forces on the coil. Simulations with OPERA have been run to understand what these forces and torques will be on the coil during its operation at 4596 A, where the central field is about 1.4 T.

Figure 3.16 shows the non-symmetric model for the sPHENIX flux return yoke in the OPERA simulation, it is modelled using 1006 steel. The notch in the south end door is to allow for the valve box, as previously shown in Figure 3.7.

In the symmetric model the forces along the beam axis are symmetric, the simulation for the total forces are balanced at about  $\pm 5.65 \times 10^6$  N. The calculated forces on the two end doors are about  $\pm 8 \times 10^5$  N.

From the simulations of this model, the magnetic forces and torques at the yoke center due to the coils being misaligned are shown in Table 3.1.

**Table 3.1:** Magnetic forces ( $F_x, F_y, F_z$ ) and torques ( $T_x, T_y, T_z$ ) in the non-symmetric model.

	$F_x$ [N]	$F_y$ [N]	$F_z$ [N]	$T_x$ [N-cm]	$T_y$ [N-cm]	$T_z$ [N-cm]
No misalignments	-1043	-14072	15640	335007	160904	0
Coils shift, $dx=2$ mm	9412	-14077	15647	335345	157079	-2815
Coils shift, $dz=3$ mm	-1033	-13903	21207	354464	159326	0

### 3.3.6 Field Mapping

To achieve the required momentum resolution the solenoid field has to be mapped in detail, specially towards the edges of the tracker acceptance where deviations from the ideal solenoidal field are expected.

There will be three separate monitoring and mapping tasks. The low and full field tests scheduled for late 2015 and 2016 will be just a monitoring task where we plan to use hall probes that had been used for the PHENIX magnet mapping. For the low field test, with a maximal current of 100 A, a series of probes will be placed inside the solenoid and read out by a Keithley 7002 Switch System. These monitoring probes provide a few comparison points to field calculations.

For the full field test at a current of 4596 A, more of the original probes together with high resolution NMR probes will be installed in the magnet. The NMR probes will provide a high resolution measurement of the field and will later be installed as permanent monitoring probes in the final setup.

A detailed field map for track reconstruction has to be measured once the final return yoke, together with the plug doors, is completed. The shape of the field depends very much on the shape and material of the yoke.

We will employ the CERN magnet mapping group which has years of experience in magnetic field mapping. This group mapped e.g. the STAR magnet [124] and more recent the CMS [125] and ATLAS [126] magnets, see Figures 3.17 and 3.18.

Over the years the hardware has been improved and currently uses compact hall probes which measure three orthogonal directions.

The CERN group will ship, install and setup the device in the solenoid, in total the mapping will take about 2–3 weeks plus analysis time. This field map will then be compared to 3D OPERA calculations and translated into a three dimensional field map that will be used for tracking and further detector simulations.

### 3.4 Tests for the Superconducting Solenoid Magnet

There were a series of tests done at room temperature in April 2015 for the initial inspection and acceptance of the superconducting solenoid after it was shipped to BNL. The high potential (hipot) tests (up to 520 V) recorded a leakage current of  $0.15 \mu\text{A}$ . The impulse test done at 400 V was successful in that the waveform measured didn't indicate any turn-to-turn short in the magnet coils. We also ramped the current across the solenoid slowly from 0 to 2 A and 5 V to measure the inductance of the solenoid to be about 2.3 H (very close to 2.2 H that was measured in 1997). In addition, we have also performed a leak check which found no noticeable leaks and a 6.6 bar pressure test which was also successful (even up to 85 psi).

At the end of 2015, a low-field and low-current test will be performed for the superconducting solenoid. We will cool the magnet with helium down to about 4.5 K and bring the current to 100 A. This is as much a test for the entire cryogenic system as it is to test and verify the expected magnetic field (about 300 Gauss in the center). P. Joshi will try to test his quench protection system that he has used in the Superconducting Magnet Division

for other purposes.

In 2016, we further plan to perform a high-field and high-current test for the magnet. Then, we will raise the current gradually to 4596 A which was the nominal operating current that the BaBar experiment has used for this magnet during their years of operation. The entire solenoid cryostat will be surrounded by steel plates, in a box configuration, which serves as the media for the return field. The above-mentioned quench protection system will have its realistic test and usage in this high-field test.



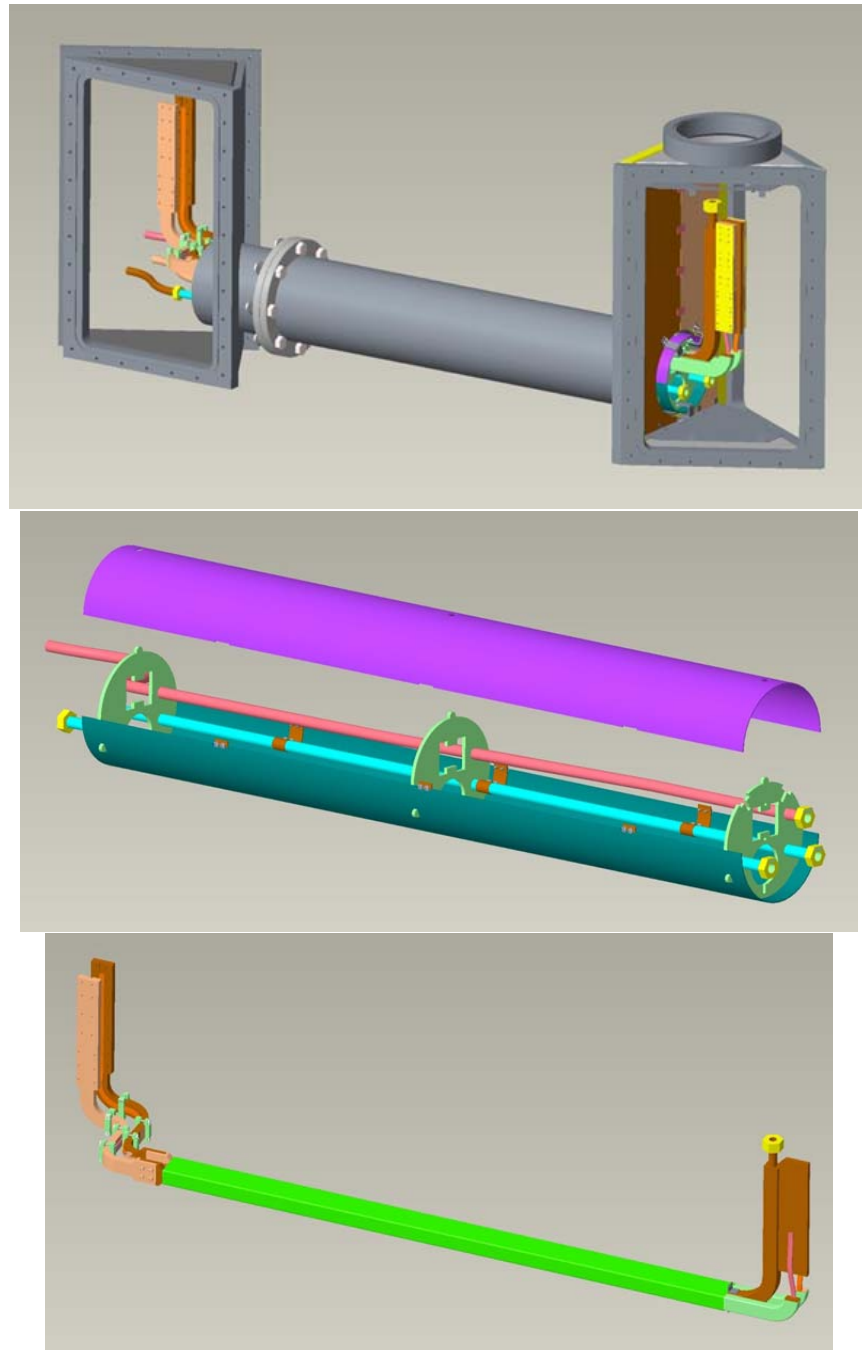


**Figure 3.8:** Top: from the junction box (at the cryostat) to the valve box; Middle: coil helium supply line and heat shield; Bottom: extension lead assembly with flexible (laminated copper) connections to accommodate thermal contraction on the left and coil return helium to cool exiting leads on the right.

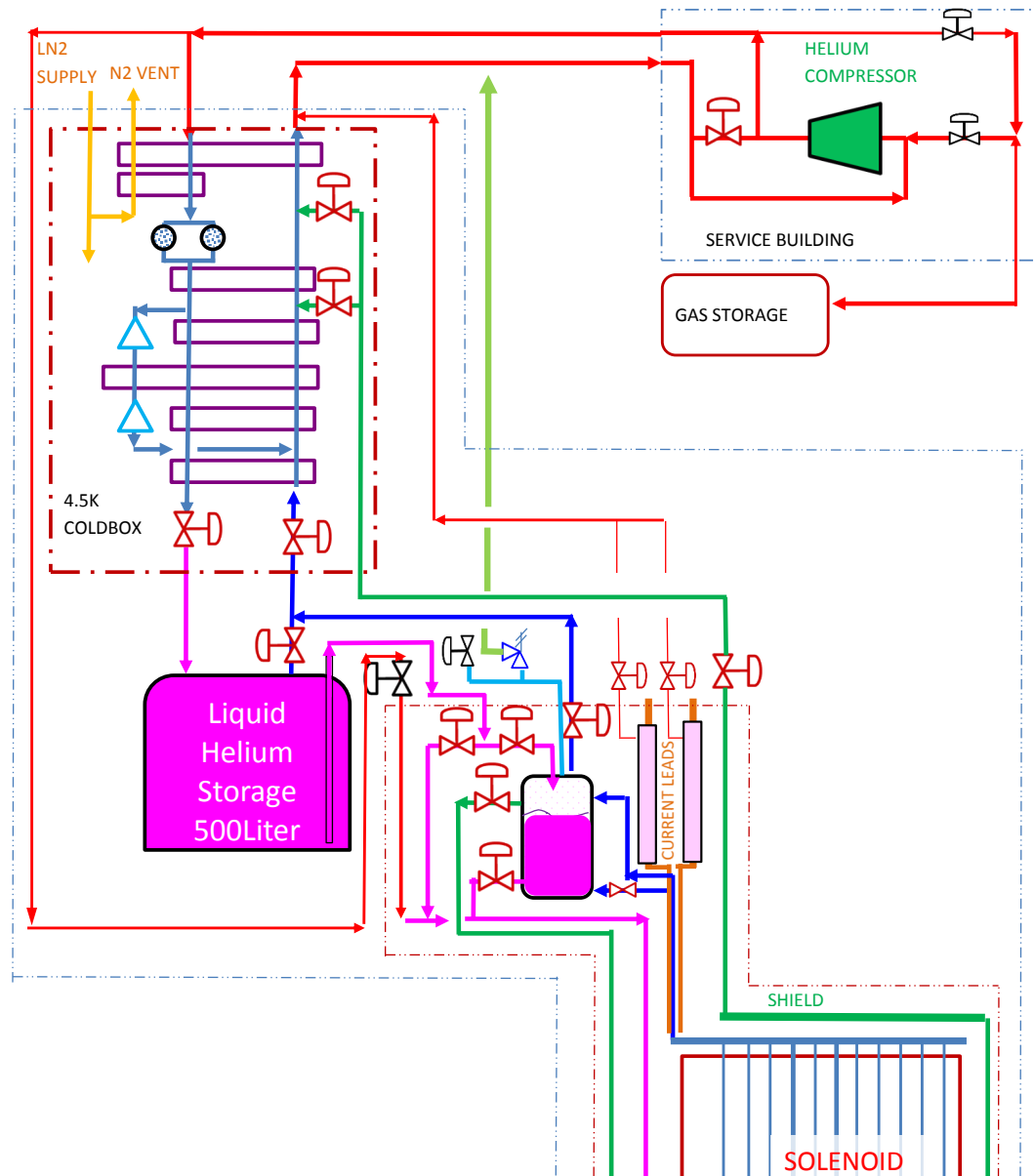


Figure 3.9: sPHENIX Magnet Cryogenic Control System

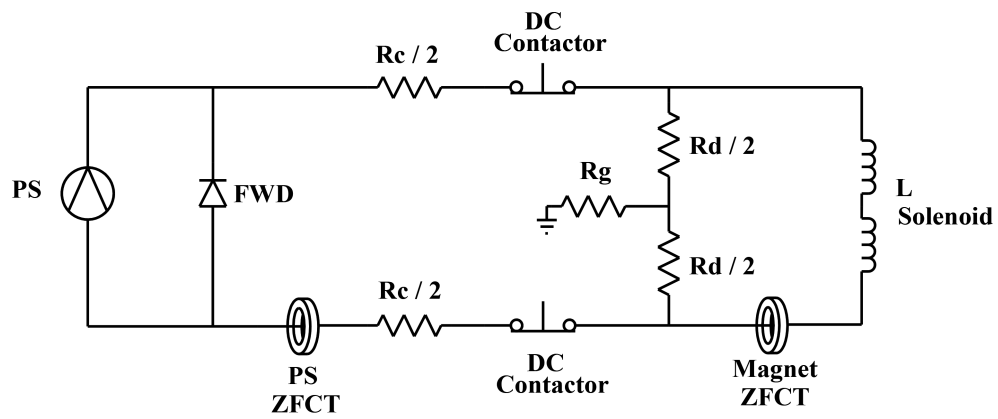


Figure 3.10: sPHENIX Magnet powering system

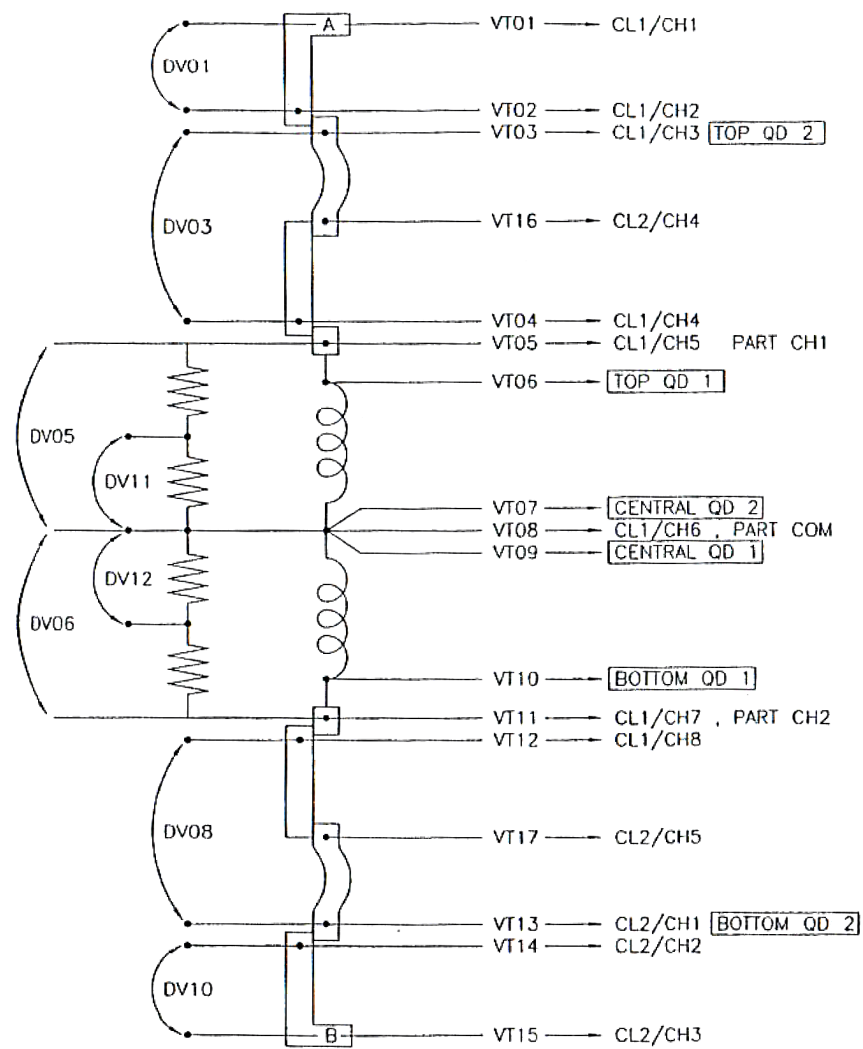


Figure 3.11: sPHENIX Magnet voltage taps

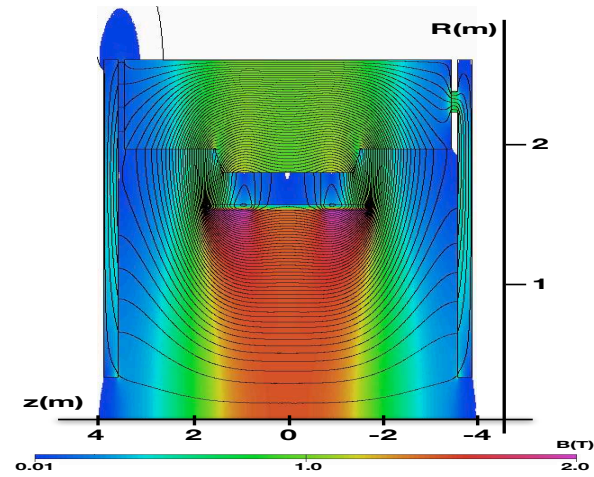


Figure 3.12: 2D OPERA simulations of the sPHENIX setup

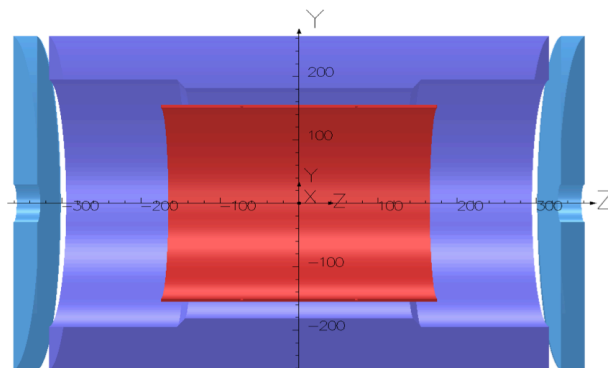
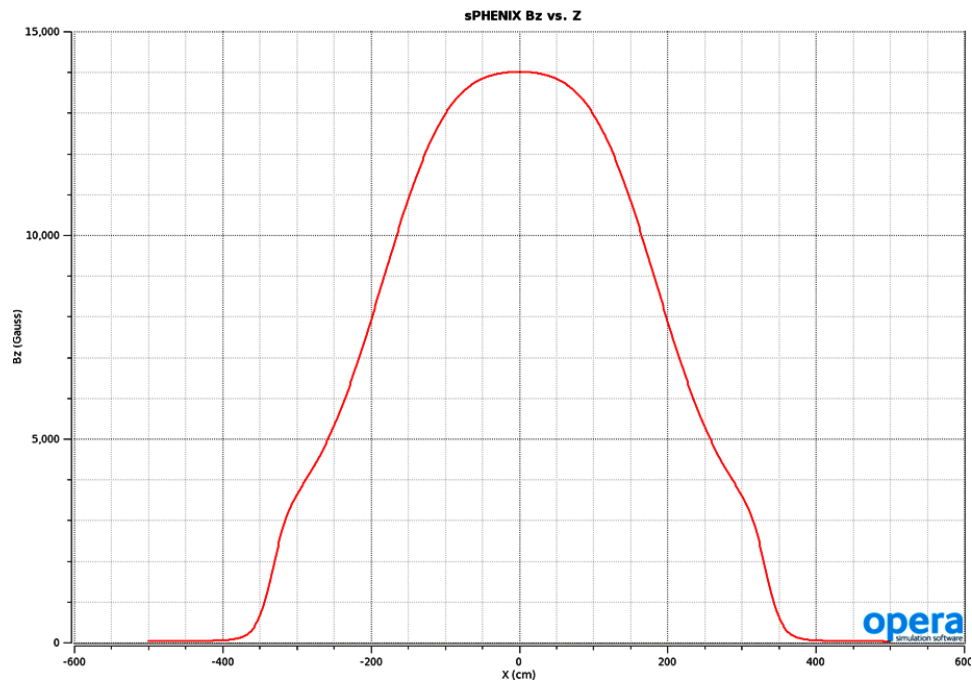
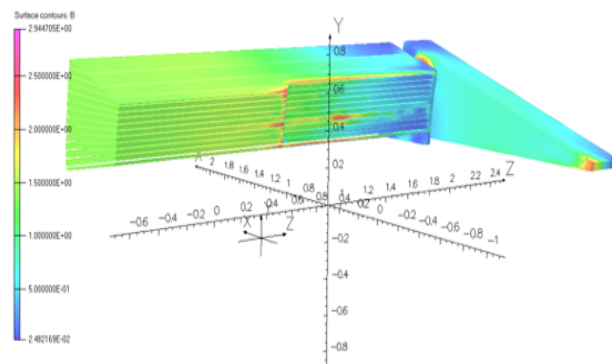


Figure 3.13: 3D OPERA Model



**Figure 3.14:** Calculated magnetic field along the longitudinal axis (beam direction) for the symmetric return yoke model



**Figure 3.15:** 3D OPERA model detail of the field in the HCal plates

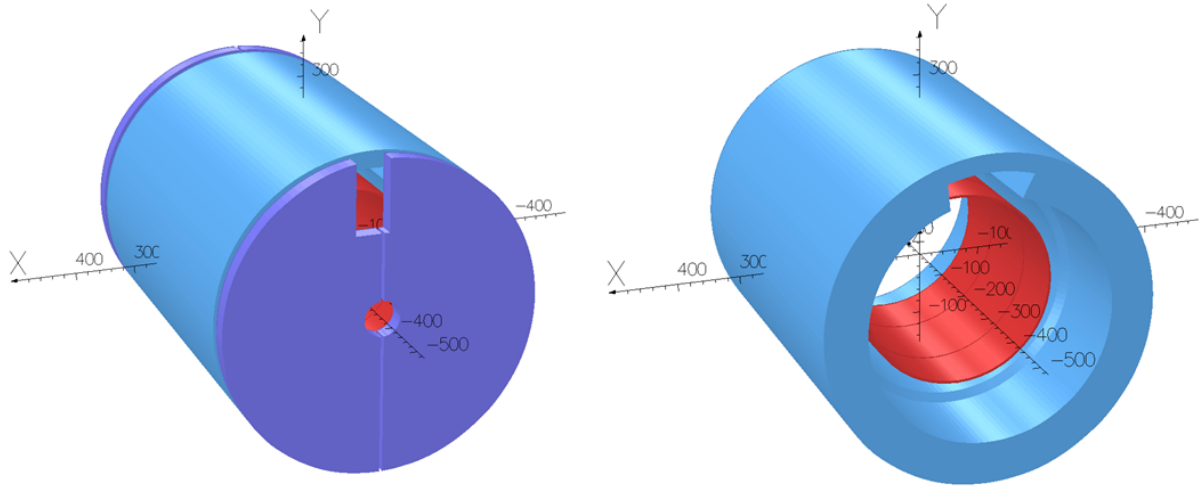


**Figure 3.16:** Yoke and end-cap cuts from the OPERA Model, as viewed from the "south" or the "lead" end.

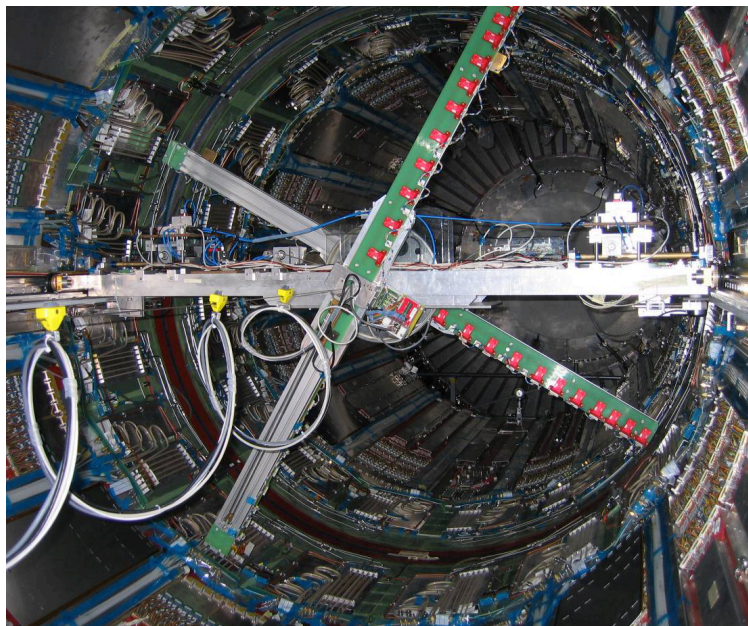


**Figure 3.17:** The CERN field mapper installed in the ATLAS solenoid



**Figure 3.18:** Detail of the CERN field mapper, the red tabs are the 3D Hall sensors



# Chapter 4

## Tracker

### 4.1 Physics requirements

Four elements of the sPHENIX physics program drive the performance parameters of sPHENIX tracking. Three of these, the measurement of the Upsilon family of quarkonia states, fragmentation functions at high and at low  $z$ , and heavy flavor tagged jets together set the momentum resolution spec for the Tracker. The fourth element, the tagging of heavy-flavor jets, requires that the inner tracking system has the ability to measure the displaced vertex of a D or B meson decay. In addition, to fully utilize the available RHIC luminosity the tracking systems should have large, uniform acceptance and be capable of fast readout.

The measurement of the Y family places the most stringent requirement on momentum resolution at lower momentum. The large mass of the Upsilon means that one can primarily focus on electrons with momenta of  $\sim 4 - 10$  GeV/c. The Y(3S) has about 3% higher mass than the Y(2S) state and to distinguish them clearly one needs invariant mass resolution of  $\sim 100$  MeV, or  $\sim 1\%$ . This translates into a momentum resolution for the daughter  $e^\pm$  of  $\sim 1.2\%$  in the range  $4 - 10$  GeV/c. The Y measurement also generates requirements on the purity and efficiency of electron identification. The identification needs to be efficient because of the low cross section for Y production at RHIC, and it needs to have high purity against the charged hadron background to maintain a good signal to background ratio. This requires minimizing track ambiguities. For a multi-layer device such as a silicon tracker one must optimize the number of tracking layers, their spacing, and the segmentation of the strip layers. For a continuous tracking device such as a TPC one must optimize the two-track separation through the appropriate choice of granularity of the readout plane, and control of space charge and pile-up effects. Translating this need into a detector requirement can be done only by performing detailed simulations with a specific tracking configuration, followed by evaluation of the tracking performance.

Fragmentation functions at high  $z$  also place stringent requirements on momentum res-

olution and at larger momentum than the  $Y$  reconstructions. In order to unfold the full fragmentation function,  $f(z)$ , the smearing due to momentum uncertainty should be very small compared to the corresponding smearing due to the calorimetric jet measurement for a cleanly identified jet. For a 40 GeV jet this condition is satisfied by a tracking momentum resolution of  $\Delta p/p \simeq 0.2\% \cdot p$  or better.

Measuring fragmentation functions at low  $z$  requires looking for possibly wide angle correlations between a trigger jet and a charged hadron. This places only moderate requirements on the momentum resolution ( $\Delta p/p \simeq 1\% \cdot p$ ), but reinforces the requirement of large acceptance.

Tagging heavy-flavor jets introduces the additional tracking requirements. At minimum this demands the ability to measure the displaced track originating from a D or B meson decay. The  $c\tau$  for D and B decays is 123  $\mu\text{m}$  and 457  $\mu\text{m}$ , respectively, and the displaced track would need to be identified with a resolution sufficient to distinguish these decays against backgrounds. Furthermore, heavy-flavor jet identification algorithms such as DCA-counting methods require multiple large DCA tracks to be found simultaneously within a jet and will require a large single track efficiency to keep the overall identification suitably efficient. Other heavy flavor jet identification methods such as those based on fully reconstructing individual secondary vertices can place additional demands on the individual track position resolution and impact the inner pixel segmentation.

## 4.2 General Remarks about Tracking

### 4.2.1 Magnetic Field

The field produced by the Babar magnet is shown in Figure 4.1. The sPHENIX application of this coil is rather close to the original BaBar design with an EMCAL inside the coil and tracking extending to  $\sim 80$  cm. A standard solenoid with length equal to diameter has significant radial magnetic field components at each end and thereby does not produce an idealized field shape. A return yoke with a small opening (*e.g.* STAR) will compensate for this shortcoming while severely limiting possibilities for upgrades in the forward direction. The BaBar magnet attacks this classic problem by using an increased winding density at each end, thereby sacrificing uniformity of the field at large radius, for an extended “sweet spot” of field in the middle. Thus the region in which sPHENIX plans to install tracking features a close-to-ideal magnetic field shape. It should further be noted that the calculations of Figure 4.1 are done with a “future upgrade” return yoke that allows for a full capability tracker in the forward direction.

Detailed results from GEANT simulations are presented later in this chapter. In addition, because of the near-ideal field, the momentum resolution effects due to multiple scattering and position resolution, can be calculated analytically and in closed form. These results can be further extended to include Bremsstrahlung losses (significant only for the electrons)

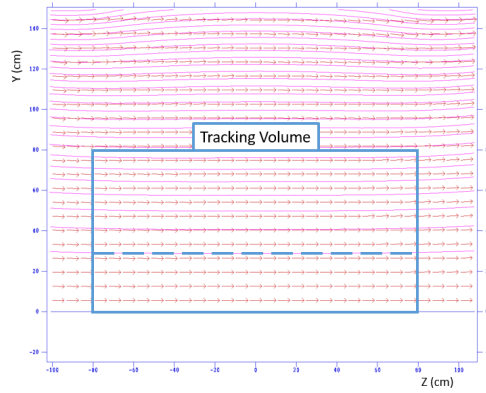


**Figure 4.1:** The BaBar magnet field superimposed with the dimensions of the tracker volume. This calculation includes the effect of the field return as envisioned for future upgrades (forward arm spectrometer). The dashed line indicates the inner radius of the TPC tracking volume.

using a semi-analytical technique. The analytic results are discussed because they provide insight into which features of the tracker limit the tracking performance. In this section, we will outline the analytic and semi-analytic results, and later in the TPC discussion of results we will show that they are in excellent agreement with full GEANT simulations.

#### 4.2.2 Glückstern Formula

In 1963, R.L. Glückstern [127] analytically solved the problem of charge particles traversing a uniform magnetic field while experiencing the effects of multiple Coulomb scattering. Figure 4.2 shows the contribution to the transverse momentum resolution from the detector's position resolution. For a uniform magnetic field, the sagitta is proportional to the inverse of the particle's transverse momentum, thereby making the fractional error in the transverse momentum rise linearly with the transverse momentum of the particle itself. Assuming  $N$  equally spaced measurements each carrying error  $\sigma_x$ , we get the final result:

$$\frac{\sigma_{p_T}}{p_T} = \sqrt{\frac{720}{N + 4}} \frac{\sigma_x}{0.3L^2B} p_T \quad (4.1)$$

where  $B$  is the magnetic field strength,  $N$  is the number of track points measured and  $L$  is the length over which the particle is tracked.

Multiple Coulomb scattering is addressed in Figure 4.3 wherein we see that since the material-dependent angular deflection varies as the inverse transverse momentum this contribution is effectively a constant yielding the final result:

$$\frac{\sigma_{p_T}^{MS}}{p_T} = \frac{0.052}{\beta BL} \sqrt{\frac{L}{\chi_0}} \left[ 1 + 0.038 \ln \left( \frac{L}{\chi_0} \right) \right] \quad (4.2)$$

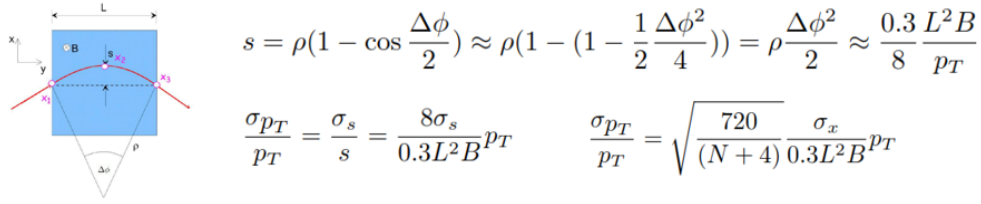


**Figure 4.2:** This figure demonstrates the contribution of position resolution to momentum resolution.

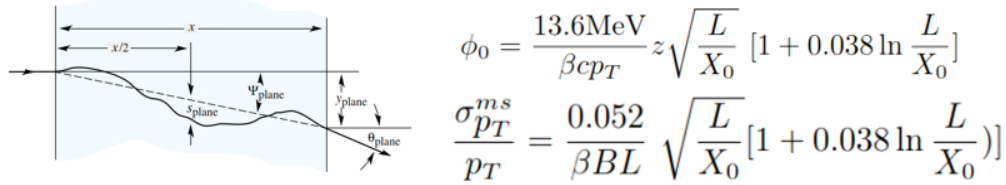


**Figure 4.3:** This figure demonstrates the contribution of multiple Coulomb scattering to momentum resolution.

The Glückstern result is simply the sum of these two terms in quadrature and yields the familiar expression:

$$\frac{\sigma_{p_T}}{p_T} = \sqrt{a^2 + (b p_T)^2} \quad (4.3)$$

wherein the constant  $a$  is driven primarily by the material thickness ( $\chi_0$ ), and the constant  $b$  is driven primarily by the intrinsic detector resolution ( $\sigma_x$ ).

### 4.2.3 Beyond Glückstern

The Glückstern formula correctly describes the transverse momentum resolution of a spectrometer with a uniform distribution of material and uniformly-spaced measurements along the radius with equal position resolution. Two extensions of this result are important to the sPHENIX spectrometer design. First, since the  $\eta$  bite is large, and most detector designs result in different transverse and longitudinal position resolutions, we must account for the differing behavior of the zed component. Second, since our primary design goal involves the measurement of Upsilon states via the dielectron decay channel, we must explicitly account for Bremsstrahlung losses as the electrons traverse our detector volumes.

The extension to three dimensions is conceptually simple, and adds both a multiple scattering and position-error term for the  $p_Z$  resolution. Bringing all the terms together in

quadrature we determine the fractional error in the full momentum to be:

$$\frac{\sigma_p}{p} = \sqrt{\left(\frac{\sigma_{MS}}{\sqrt{\sin \theta}}\right)^2 + (\sigma_{det} p \sin \theta)^2 + (\sigma_{\theta}^{det} \cos \theta)^2 + \left(\frac{\sigma_{\theta}^{MS}}{\sqrt{\sin \theta}} \frac{\cot \theta}{p}\right)^2} \quad (4.4)$$

where the first and third terms are the familiar Glückstern result and the second and third terms are the contribution of the z-component.

Finally, we must consider the effects of Bremsstrahlung. The passage of an electron through material will result in the occasional loss of energy via the emission of single photons. As a consequence, the electron's subsequent trajectory will be determined by the reduced momentum. For this reason, some electrons will be entirely unaffected (having never emitted a photon) while others will measure a momentum below that at the production point, thereby creating low-side tails in both the momentum and mass spectra. The asymmetric nature of the effect precludes the description of Bremsstrahlung as a simple resolution term. We have handled this by a trivial Monte Carlo calculation.

Figure 4.4 summarizes the necessary input to the calculation. Here  $k$  is the fractional energy loss due to the Bremsstrahlung photon, whose probability (cross section) follows the parametric function shown in the figure. This analytic approximation yields an infinite total cross section, and must be integrated across the limits  $k_{min}$  to  $k_{max}$  to determine the photon yield,  $N_{\gamma}$ , as a function of the material thickness in radiation lengths  $\frac{L}{\chi_0}$ . In our semi-analytical calculation, Bremsstrahlung is folded into the analytical resolution function using  $N_{\gamma}$  as the mean to a Poisson probability distribution for the number of photons emitted and  $\frac{d\sigma}{dk}$  for their energy spectrum.

It is worth noting that all the detailed considerations here concern only the change in the momentum magnitude. It is shown elsewhere that shifts in the apparent initial direction, generate mass errors orders of magnitude smaller than those already considered and hence ignored with no loss in validity of the generated results.

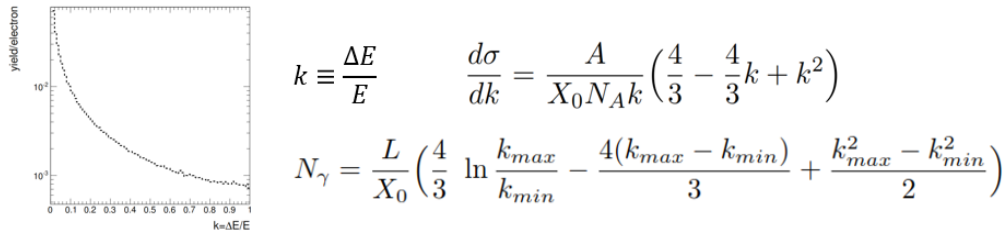


**Figure 4.4:** This figure indicates how Bremsstrahlung is calculated via single photon emission as a contributor to momentum resolution.

## 4.3 Overview of Tracking Options

The tracking can logically be divided into an inner tracker, primarily responsible for measurements of displaced vertices for the identification of heavy flavor decays, and an outer tracker, primarily responsible for the momentum resolution needed to separate the Upsilon states and to specify the high- $z$  fragmentation.

There are two options under consideration for the inner tracker. One uses the reconfigured PHENIX pixel detectors, the other is a new detector using MAPS sensors. Two options have been considered for the outer tracker as well: a silicon strip tracker with five layers, and a small TPC. In the following sections we discuss each of the four options in detail.

## 4.4 Reuse of the PHENIX Pixel Detector

### 4.4.1 Detector Description

In this option, we re-use the pixel detector ladders of the PHENIX VTX detector. The PHENIX VTX is made of 4 layers of silicon detectors, and its inner two layers are made of 30 ladders of pixel detectors. The first layer, made of 10 ladders, is at a radius of approximately 2.5 cm from the beam pipe and the second layer, made of 20 ladders, is at 5 cm. They cover about 80% of  $2\pi$ .

One pixel ladder is made of 4 sensor modules on a stave made of CFRP, which provides mechanical support and cooling. A sensor module is made of a pixel sensor (5.672cm (L)  $\times$  1.50 cm (w)  $\times$  200  $\mu$ m (t)) and 4 ALICE pixel read-out chips bump bonded on the sensor. Each of the ALICE chips reads out 8192 pixels, arranged as  $32 \times 256$ . The size of a pixel is  $\Delta\phi \times \Delta z = 50\mu\text{m} \times 425\mu\text{m}$ . A pixel ladder is read-out from both ends by read-out boards, called SPIRO, through high density buses. The total radiation length of a pixel ladder is approximately 1.28%.

The pixel detectors were built by RIKEN. In addition to the 30 ladders in the PHENIX VTX, RIKEN has 6 new spare ladders.

After the 2016 run, the PHENIX detector and the VTX detector will be decommissioned, and the pixel ladders will be saved along with their read-out electronics. We will reconfigure the 30 pixel ladders and the 6 spare pixel ladders to make two inner pixel layers for the sPHENIX tracker. The radial position of the two layers and the number of ladders in each layer will be adjusted so that the detector will cover  $2\pi$  in azimuth. A possible configuration of the pixel layers is shown in Table 4.2.

#### 4.4.2 Detector performance from Simulations

The DCA track resolution is an important parameter for the heavy flavor tagged jet program. Figure 4.5 shows the DCA resolution obtained in central HIJING events with the combination of the reused PHENIX pixels and the outer silicon tracker. The simulated performance is found to be adequate for the heavy flavor tagged jet program.

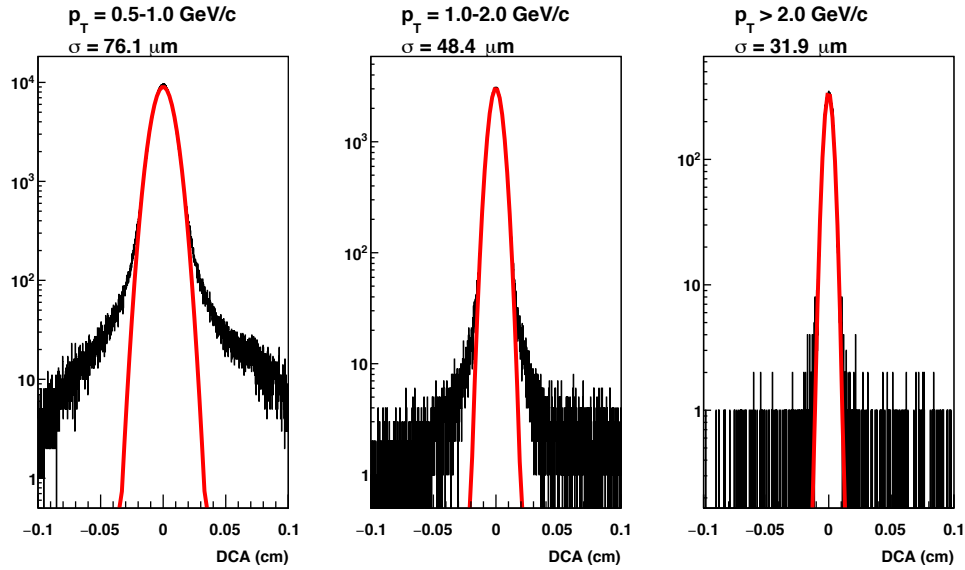


**Figure 4.5:** The DCA resolution of the silicon tracker in three track momentum ranges, from tracks reconstructed in central HIJING events.

The PHENIX pixel detectors have significant dead areas. A snapshot taken during the 2015 RHIC run showed that 92.5% of the first pixel layer and 72.5% of the second pixel layer were live. The effect of this on the tagged heavy flavor program is that the effective acceptance for a single track is reduced by about 1/3, if a displaced track measurement is needed. As discussed in the next section, this results in a significant loss of efficiency for B tagged jet measurements.

We also need to consider whether this has any effect on the Upsilon program, where any loss of acceptance or resolution would be a serious problem. Therefore we have made Upsilon simulations in which 7.5% of the pixels in the innermost pixel layer and 27.5% of those in the second pixel layer were randomly disabled. For the analysis of these events the tracker was set to accept tracks with hits in only six of the seven layers. No significant loss of acceptance was observed. The mass resolution became a few percent worse - but was still within our  $< 100 \text{ MeV}$  specification. It is likely that much of the slight loss of mass resolution when requiring hits in only six of the seven layers could be recovered by a careful tuning of the tracking.

One expected effect of the loss of live area in a pixel layer is that the rate of fake tracks will increase, due to the need to require hits in only six of the seven tracking layers (in the case

of the silicon strip tracker) for a track. This effect, and how to deal with it in the tracking, has not been explored in detail yet.

### 4.4.3 Summary of PHENIX Pixel Layers

A precise vertex position measurement is needed to measure heavy quark production, and measurement of  $D$  mesons in high  $p_T$  and  $b$ -tagged jets is one of the main physics goals of sPHENIX. Two layers of the existing pixel detectors achieves the design goal of a DCA resolution of less than  $100\ \mu$ . The DCA resolution observed in PHENIX at high  $p_T$  was about  $50\ \mu\text{m}$ , limited by the beam position resolution.

The main advantage of this option that we have 30 pixel ladders and 6 spares along with read-out electronics. The detector has been used in PHENIX and it is demonstrated that it can achieve DCA resolution that is sufficient to separate heavy flavor electrons from charm and bottom decays from light hadron sources and to separate charm decay electrons and bottom decay electrons. A read out speed of approximately 15 kHz has been demonstrated in system tests in PHENIX. This option provides a cost effective implementation of two inner most tracking layers of sPHENIX for heavy quark measurements, and the next steps are to evaluate the live area likely to be usable in the sPHENIX era and to make a detailed plan to reconfigure the readout electronics.

## 4.5 MAPS Pixel

### 4.5.1 Detector Description

We have considered the feasibility of constructing new inner tracking sensors to improve the precision of the tracking system for an expanded physics reach with the tracker and to mitigate known issues with the reconfiguration of the PHENIX pixel sensors. The technology considered for the new set of silicon sensors would be monolithic active pixel sensor (MAPS) based vertex detector technology under development by the ALICE experiment.

A low mass high, efficiency vertex tracking detector is required for the heavy flavor physics program in sPHENIX. An exploration of silicon pixel sensor technology with low power consumption, and thus a smaller mass in the cooling system, is the only way to go beyond the current pixel systems. The latest MAPS based pixel vertex detector being developed for the ALICE Inner Tracking System Upgrade proposes to reduce the material budget from  $\sim 1\%$  down to  $\sim 0.3\%X_0$  with a reduced pixel size of  $\sim O(30\mu\text{m} \times 30\mu\text{m})$ . The same technology, albeit with a different readout configuration, has been adopted in the latest STAR inner vertex detector upgrade at RHIC. For sPHENIX a minimum of two layers is required to provide the coverage with high tracking efficiency and precision. The



inner layer could be just outside the beam pipe, at a radius of  $R \sim 2.4\text{cm}$ . With very low power front-end electronics (40 nW per channel), the whole detector can be cooled by air, with minimal cooling materials. The ALICE ITS ALPIDE architecture provides a  $4\ \mu\text{sec}$  integration time and less than  $50\ \text{mW}/\text{cm}^2$  power consumption, and appears best suited to our needs.

**Table 4.1:** Summary of geometries for an inner MAPS tracker with 3 layers.

Layer	radius (cm)	sensor			total thickness $X_0\%$	length (cm)	area ( $\text{m}^2$ )
		pitch ( $\mu\text{m}$ )	length ( $\mu\text{m}$ )	depth ( $\mu\text{m}$ )			
1	2.4	28	28	50	0.3	27	0.041
2	$\sim 4$	28	28	50	0.3	27	$\sim 0.068$
3	$\sim 6-15$	28	28	50	0.3	$\sim 27-39$	$\sim 0.102-0.368$

The characteristics of an inner MAPS tracker could closely resemble those of the ALICE inner ITS. The inner ladders of the ALICE ITS extend 27 cm in length. These are suitable for the sPHENIX coverage for radii within 6 cm. Should layers outside of 6 cm be required, longer staves will need to be produced to preserve the pseudo-rapidity coverage for all vertices within  $\pm 10\text{cm}$ . A summary of the geometry for the inner tracker is provided in Table 4.1.

## 4.5.2 Detector Performance

The DCA resolution of the MAPS based pixel detector described above is improved by a factor of 1.8 - 2.0 over that of the reused PHENIX pixels, due to the smaller pixel size and the use of three pixel layers. The DCA resolution determined for all reconstructed tracks in 2000 central HIJING events is shown in Figure 4.6. These simulations used the inner tracker parameters shown in Figure 4.1, and the five layer silicon strip tracker with the parameters shown in table 4.2.

## 4.5.3 Summary of MAPS Inner Layers

A new set of tracking layers utilizing a developed yet modern technology, such as the MAPS sensors discussed above, can alleviate some concerns with the reconfiguration of the existing PHENIX sensors.

[Tracking inefficiencies] The existing pixel layers in PHENIX have significant dead areas, as discussed previously. MAPS sensors being developed for the ALICE upgrade have shown tracking efficiency  $> 99\%$ , and new detectors could presumably be made without dead areas. MAPS detectors intrinsically eliminate one of the

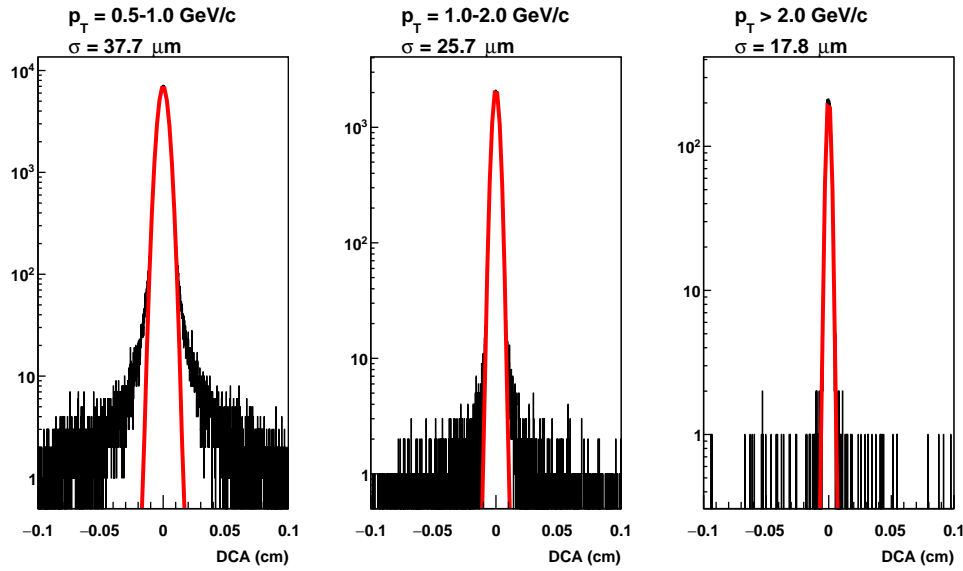


**Figure 4.6:** The DCA resolution of the silicon tracker in three track momentum ranges, when the inner tracker is composed of three layers of a MAPS based detector with  $30\text{ }\mu\text{m} \times 30\text{ }\mu\text{m}$  pixel size. These are from all tracks reconstructed in 2000 central HIJING events.

failure mode of the pixel detectors (loss of contact via flaws in bump wire bonds) since these contacts are fully integrated into the silicon.

[Material thickness] The existing pixel ladders have a 1.28% radiation thickness per layer. Modern MAPS based ladder designs can improve dramatically on those values with a thickness per layer of only 0.3%  $X_0$ . The radiative tails on the Upsilon mass peaks due to Bremsstrahlung losses of electrons in the tracker would be significantly reduced as a result of the smaller mass of the inner tracker.

[Tracking precision] The existing pixel ladders have large pixel dimensions by modern standards. The pitch of the pixels ( $50\text{ }\mu\text{m} \times 425\text{ }\mu\text{m}$ ) is optimized in one direction to facilitate DCA based measurements in the transverse plane. The ALICE MAPS design can achieve much narrower pitch ( $30\text{ }\mu\text{m} \times 30\text{ }\mu\text{m}$ ) opening the possibility of reconstructing individual secondary vertexes with two-track comparisons and an additional approach to b-jet identification.

[DAQ rate limit] A system test of the existing pixels ran at 14 kHz with about 60% live time, although it may be possible to improve on this performance. A new set of tracking layers would free sPHENIX to establish a larger event collection rate and ensure the 15 kHz design goal is fully achieved.

[TPC integration] The integration of a compact TPC would offer additional benefits that will be detailed in a later subsection. The Tracker is a unified system and must be designed as such. The final design of the inner silicon will thus be influenced, particularly in the placement of the large radius layers, by design choices of the

outer tracking. A newly constructed set of materially-thin tracking layers has the flexibility to meet the design needs should the TPC option need a third layer of pixels to complete the matching between the TPC and pixel layers.

## 4.6 Silicon Strip Outer Tracker Option

### 4.6.1 Detector Description

The silicon strip tracker covers the acceptance  $|\eta| < 1$  and has full azimuthal coverage,  $\Delta\phi = 2\pi$ . It consists of 3 stations (from inner to outer, called S0, S1 and S2) as illustrated in Figure 4.7. In each of the S0 and S1 stations, sensor modules are mounted on the front and back of a single support and cooling structure to form two closely spaced tracking layers. To achieve hermeticity, alternate support and cooling structures are staggered in radius and offset in azimuthal angle so that the alternating sensor modules overlap in azimuth. The S2 station contains a single tracking layer, again with alternate support and cooling structures staggered in radius and offset in azimuth to achieve hermeticity of the active area. The radius and dimensions of each station and its layers are summarized in table 4.2. The barrel structures of the 3 stations are presented in Figure. 4.8.

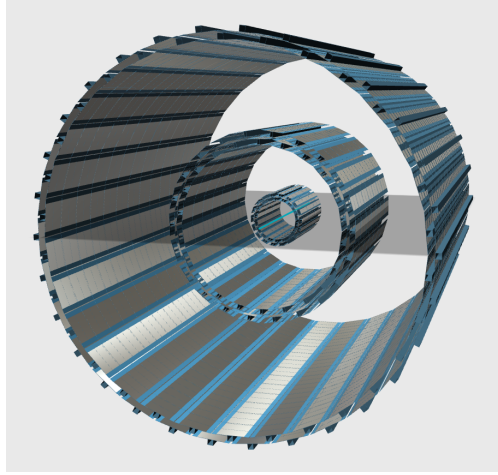


**Figure 4.7:** CAD drawing of the silicon strip tracker.

As discussed in a later section, we have developed a prototype sensor for S2, manufactured by HPK. This prototype sensor is  $320\ \mu\text{m}$  thick, the standard thickness produced by HPK. HPK also has the technology to manufacture  $240\ \mu\text{m}$  thick sensors. We are now prototyping the sensor for the S1 layer, and HPK is manufacturing the prototype with both  $320\ \mu\text{m}$  and  $240\ \mu\text{m}$  thickness. Our aim is for both S0a/b and S1a/b to be  $240\ \mu\text{m}$  thick to minimize multiple scattering within the sensor material. The details of the technology will be discussed in a later section.

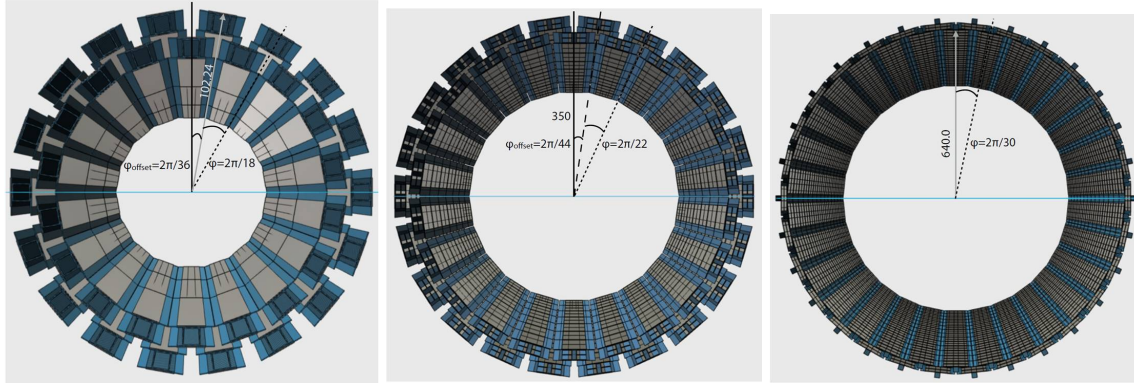


**Figure 4.8:** (From left to right) The 3D CAD drawings for S0, S1 and S2 barrels.

**Table 4.2:** Summary of geometries for the silicon strip tracker and the inner tracker made of reused pixels from PHENIX.

Station	Layer	radius (cm)	pitch ( $\mu\text{m}$ )	sensor length (cm)	depth ( $\mu\text{m}$ )	total thickness $X_0\%$	area ( $\text{m}^2$ )
Pixel	1	2.4	50	0.425	200	1.3	0.034
Pixel	2	4.4	50	0.425	200	1.3	0.059
S0a	3	7.5	58	9.6	240	1.0	0.18
S0b	4	8.5	58	9.6	240	1.0	0.18
S1a	5	31.0	58	9.6	240	0.6	1.4
S1b	6	34.0	58	9.6	240	0.6	1.4
S2	7	64.0	60	9.6	320	1.0	6.5

The FPHX chip, which was developed for the PHENIX FVTX detector, is conceived to be the readout chip for the sPHENIX silicon tracker. The readout scheme is therefore very similar to that of the FVTX. The primary reasons for this choice are (1) we can adapt the read-out chain used for the FVTX with minimal changes and (2) the power consumption of the chip is only 64 mw per chip (for 128 channels). Reuse of the SVX4 used in the PHENIX VTX stripixel detector and MPC-EX detector was also considered, but the power consumption of the SVX4 is more than 5 times higher than that of the FPHX chip, making it unavoidable to use liquid cooling for the SVX4 readout. Using the FPHX chip makes it possible to operate the silicon modules with air cooling. Thus the use of the FPHX chip simplifies the cooling system, and substantially reduces its mass.

The numbers of silicon modules, ladders, and sensors are summarized for each station in table 4.3.

Shown in Figure 4.9 is the conceptual design layout of the strip and readout lines for the S2 sensor. The dimensions of the active area are 96 mm (in  $z$ )  $\times$  92.16 mm (in azimuth), and

**Table 4.3:** Number of channel summary for the silicon strip tracker.

station	sub-layer	silicon modules per ladder	# of ladders	# of sensors
s0	2	3	36	216
s1	2	7	44	616
s2	1	14	48	672

it is divided into  $10 \times 12$  blocks. The 128 strips in each block are  $60 \mu\text{m}$  in pitch and 9.6 mm long, and run parallel to the beam line. The silicon sensor readout lines are aligned perpendicularly to the strip direction as illustrated in Figure 4.9. The upper and lower 6 blocks are connected upwards and downwards, respectively. This reduces the number of readout channels to save cost. Although signals in 6 blocks are combined and cannot be distinguished in the readout electronics, the origin of a hit in a given block is to be identified in offline analysis by requiring that tracks have a good  $\chi^2$  when fitted to all of the tracking layers. The occupancy is sufficiently low to allow this to work. The number of blocks that have to be combined is smaller for S1 because the smaller azimuthal size of the sensors requires fewer blocks. For S0, all strips are read out.

#### 4.6.2 Silicon Tracker Performance from Simulations

The goal of the Geant 4 simulations is to characterize the performance of the silicon tracker as it pertains to major aspects of the physics program. The performance has been simulated using the configuration summarized in table 4.2 for the following:

- Tracking efficiency in central AuAu HIJING events
- Track purity in central AuAu HIJING events
- Track DCA resolution in central AuAu HIJING events
- Single particle momentum resolution
- Upsilon mass resolution

The simulations are conducted with a GEANT 4 model of the silicon tracker that includes our best estimates of the material thickness of the tracker and the correct cell sizes for the inner pixels and outer strips. The model is simplified by distributing the material uniformly in a cylindrical geometry for each tracking layer. A GEANT 4 model of the tracker is being constructed that contains all of the geometric details of the ladders - support structure and cooling, sensors, readout cards and readout cables. However implementation of the

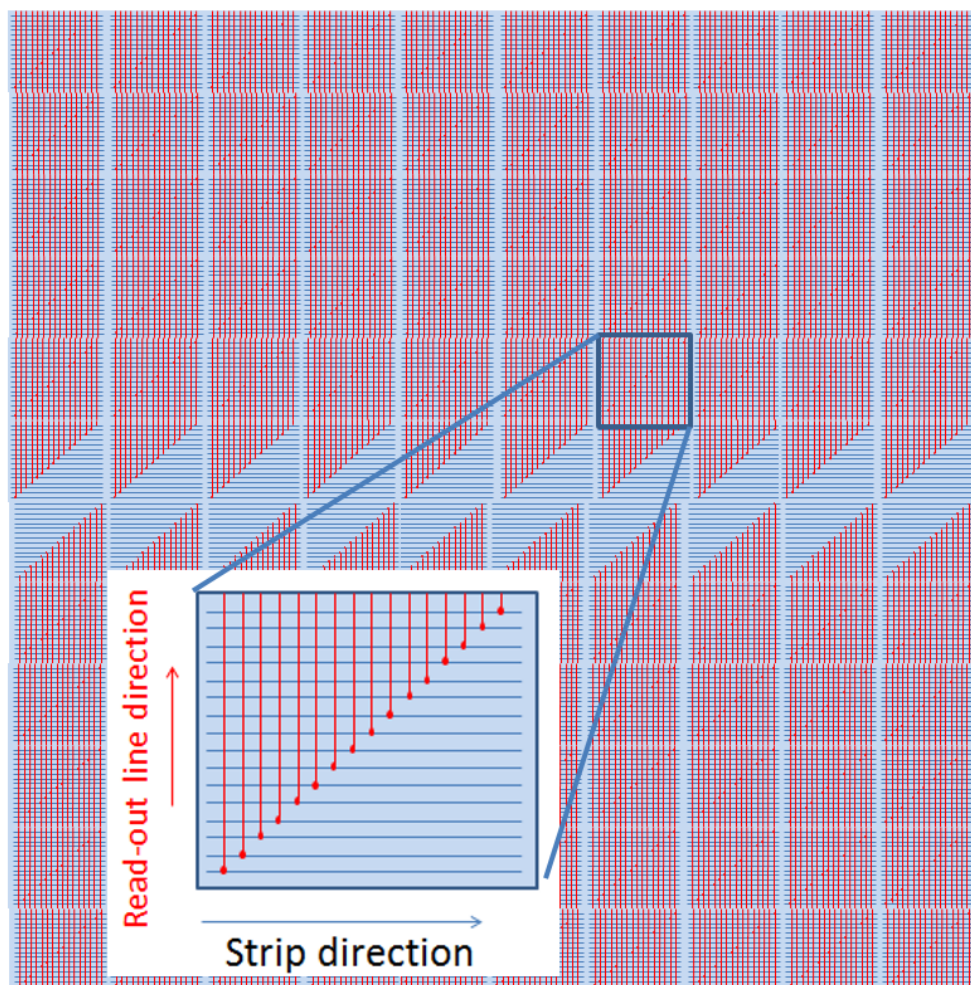


**Figure 4.9:** Schematic layout strip and readout lines of the sensor.

full tracker geometry in GEANT 4 awaits completion of the detailed mechanical design of the readout for all three layers of the silicon strip tracker. The overlap of the sensors in azimuthal angle that is needed for hermeticity is included in the material budget for the simplified model used here.

The simulated tracks are reconstructed using a tracking package that forms clusters from the hit cells (pixels or strips), finds tracks using a Hough transformation, and uses a Kalman filter to determine the track properties. The track reconstruction results presented here are all obtained from reconstructed track parameters only, without any use of truth information. The only use of truth information is for assessing reconstructed track efficiency and track purity.

The tracking efficiency and reconstructed track purity are studied using 5000 central collisions (impact parameter 0-4 fm) of AuAu events simulated in HIJING. The results obtained for track efficiency and track purity are shown in Figure 4.10. The tracking

efficiency is determined by finding the fraction of all truth tracks from GEANT that are reconstructed with a momentum that lies within  $3\sigma$  of the truth momentum. The momentum resolution used for determining the tracking efficiency is obtained from reconstructions of single pion tracks, which will be discussed below. The tracking efficiency, shown on the left in Figure 4.10, is found to be about 98% for tracks with momentum above 2 GeV/c, dropping to 92% at 1 GeV/c. Importantly, the tracking efficiency remains above about 75% for tracks of momentum more than a few hundred MeV.

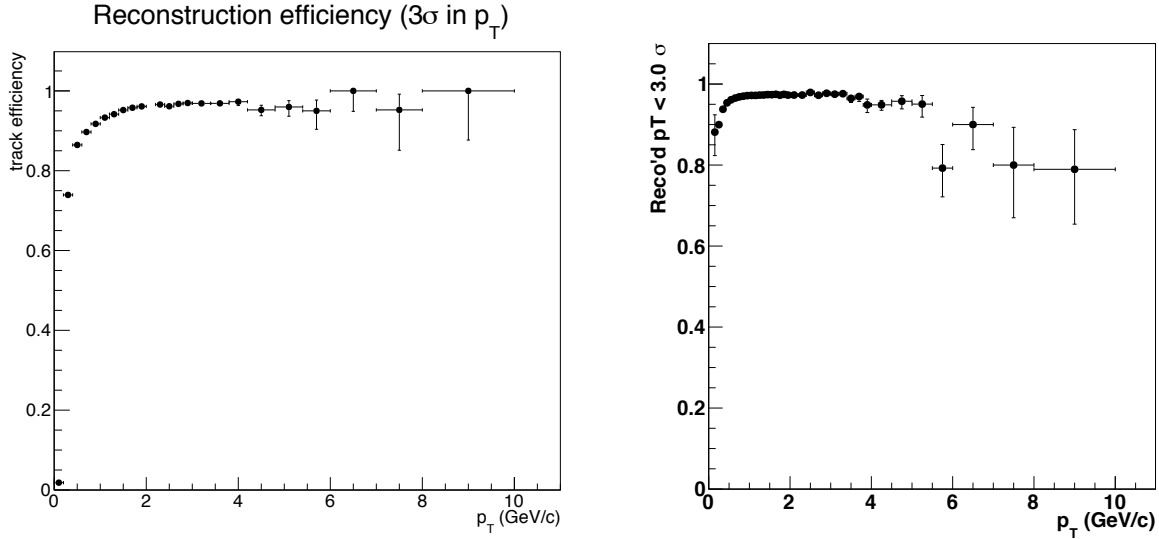


**Figure 4.10:** Left: The fraction of all truth tracks in a central AuAu HIJING event that are reconstructed with a momentum within  $3\sigma$  of the truth momentum. Right: The fraction of all reconstructed tracks in a central AuAu HIJING event that have momentum within  $3\sigma$  of the truth momentum.

The reconstructed track purity is shown in Figure 4.10 on the right. This is the fraction of all reconstructed tracks whose momentum is within  $3\sigma$  of the truth momentum. At higher  $p_T$  values the purity falls to about 80%. This means that at these higher  $p_T$  values, where the cumulative total of tracks from 5000 central HIJING events is small, about 20% of the tracks are fake tracks caused by mis-reconstruction of one of the very plentiful low momentum tracks. It should be emphasized that the tracking efficiency for these high momentum tracks is excellent - the reduction of track purity at the higher momenta is entirely due to the addition of a few spurious tracks.

The track purity at high momentum can be improved by better constraining the  $z$  location of the hits in the outer tracker, which has 9.6 mm long strips, by adding one or two layers to the tracker whose only purpose is to improve the pattern recognition. These can be either strips that have larger pitch but are much shorter in the  $z$  direction (say 2 mm) or, alternatively, long strips with small pitch that are tilted (stereo strips). We are presently considering the addition of such a layer to station S0 to reduce the fake track rate.

We note that the tracking results presented here were obtained using the silicon tracker in



standalone. For the Upsilon measurement, the decay electrons will also deposit a large signal in the EMCal, and the addition of this extra space point for the electron tracks is expected to eliminate fake tracks as a factor in the Upsilon measurement.

The DCA track resolution was shown earlier in Figure 4.5, which shows the DCA resolution obtained in central HIJING events with the silicon tracker when the inner tracker is two layers of reused PHENIX pixels. A similar plot where the inner tracker is three layers of a MAPS based detector was shown in Figure 4.6.

The momentum resolution achieved for single pions is shown in Figure 4.11. The momentum resolution at low  $p_T$  is critical for the Upsilon program, where we require  $\Delta p_T/p_T$  of about 1.2% for electrons of  $< 10$  GeV/c to achieve the needed mass resolution. Good momentum resolution at high  $p_T$  is dictated by the requirements for the measurement of fragmentation functions, as discussed in section 4.1. The momentum resolution achieved with the silicon tracker is well within those requirements.

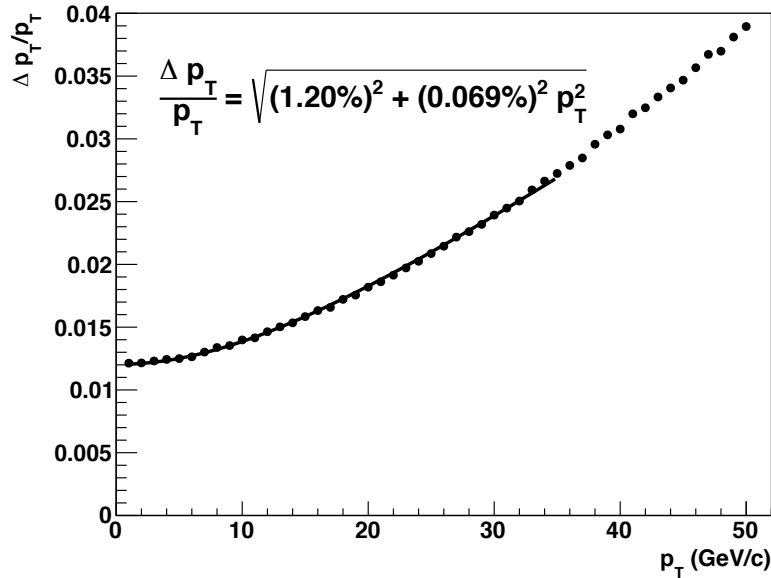


**Figure 4.11:** Momentum resolution of the silicon tracker for single pions.

The Upsilon mass spectrum is obtained using single simulated Y(1S), Y(2S) and Y(3S) thrown into  $\pm 1$  unit of rapidity, with Z-vertex selected randomly from a range of  $|z| < 10$  cm. The results are illustrated in Figure 4.12, where the yields of the three states correspond to those expected in a 10 week  $pp$  run. The mass spectrum is shown for the outer silicon tracker combined with the reused PHENIX pixels as the inner tracker (left) or with a three layer MAPS based inner tracker (right). As expected, the inner tracker option has essentially no effect on the mass resolution, but reduces the radiative tails somewhat. The observed mass resolution of 94 MeV exceeds our specification of  $< 100$  MeV.

The reduction of mass in the silicon strip tracker that results from using the FPHX chip has two important consequences. The first, already discussed, is that the tracker becomes



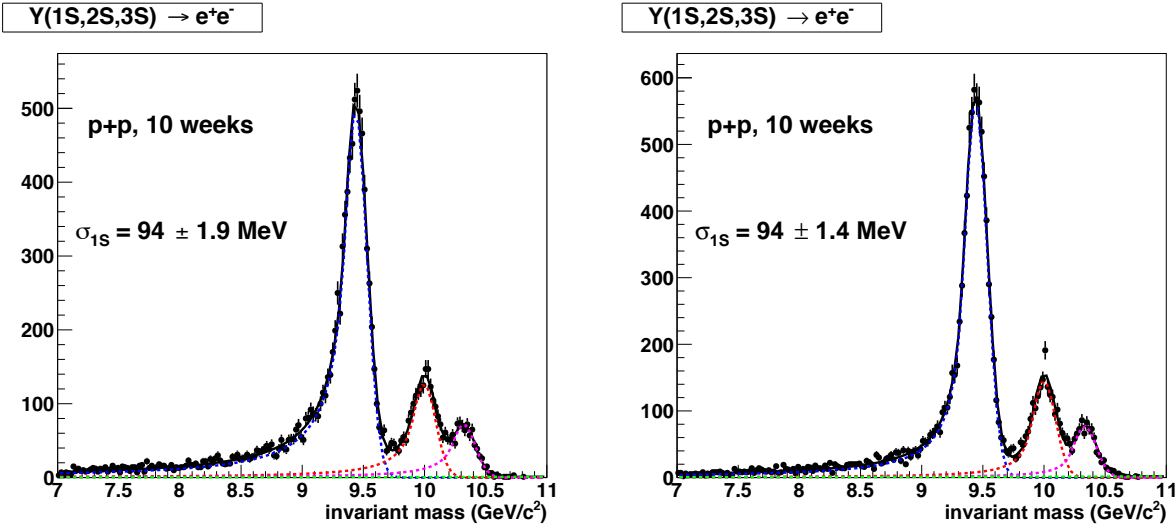


**Figure 4.12:** Mass spectrum of the three Upsilon states, with Crystal Ball fits. The yields correspond to 10 weeks of  $pp$  running. Left: The mass spectrum with the reused PHENIX pixels as the inner tracker (the configuration in Table 4.2). Right: The mass spectrum with the three layer MAPS based inner tracker option as the inner tracker.

more compact, and thus cheaper. The second is that the lower mass of the tracker reduces radiative energy loss for the Upsilon decay electrons, which in turn reduces the loss of electron tracks due to large radiative loss events. This results in an improved acceptance for the Upsilon measurement. For the reference design used in the MIE, where the higher power SVX4 chip was used, when simulated Upsilon's were thrown into  $\pm 1$  unit of rapidity 38% were reconstructed inside a mass window of 7-11  $\text{GeV}/c^2$ . The smaller material budget associated with the use of the FPHX chip raises that fraction to 41%.

Simulations of the response of the EMCal and HCal to electrons and hadrons indicate that a hadron rejection of 90 can be achieved at an electron detection efficiency of 70% using the calorimeters alone. All of our estimates of Upsilon yields in central Au+Au collisions are based on that single track electron efficiency. We have made some estimates of the background expected for the Upsilon measurement using a fast simulation based on pion yields measured in central Au+Au collisions by PHENIX. The fast simulation constructs combinatorial background by randomly mixing mis-identified hadrons, electrons from open heavy flavor, and electrons from Drell Yan. It also estimates the correlated di-electron background from open heavy flavor and Drell Yan, again based on PHENIX di-electron measurements in central AuAu collisions. The resulting signal plus background mass spectrum for the Upsilon's in the 0-10% centrality bin in one year of AuAu running is shown in Figure 4.13 on the left. The same spectrum after subtracting the combinatorial background using event mixing is shown on the right in Figure 4.13.

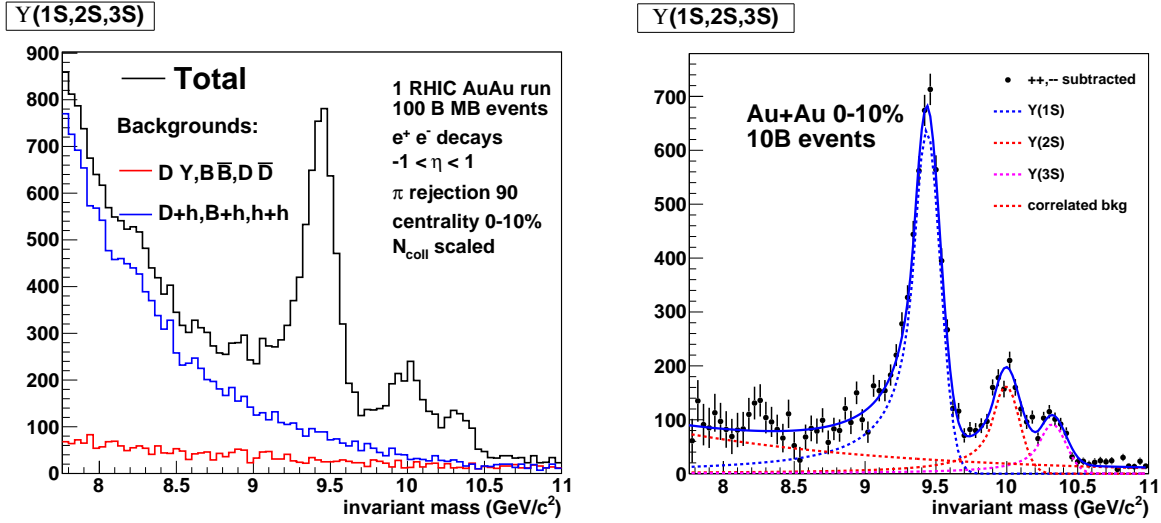


**Figure 4.13:** The mass spectrum expected in the 0-10% centrality bin from 1 year of AuAu running. The background is estimated using a fast simulation based on measured pion and electron yields from PHENIX.

#### 4.6.3 Silicon Strip Tracker Design Details

The silicon strip tracker consists of 3 stations, as shown in Figure 4.7. The S0 and S1 stations each consist of two layers which are separated by 1cm in the radial direction. Both layers (a and b) have fine pitch in the azimuthal direction. Adjacent sensor modules in azimuthal angle are staggered in radius and offset in azimuth relative to each other for hermeticity. Shown in Figure 4.14 is the 3D CAD design of the S1 station.

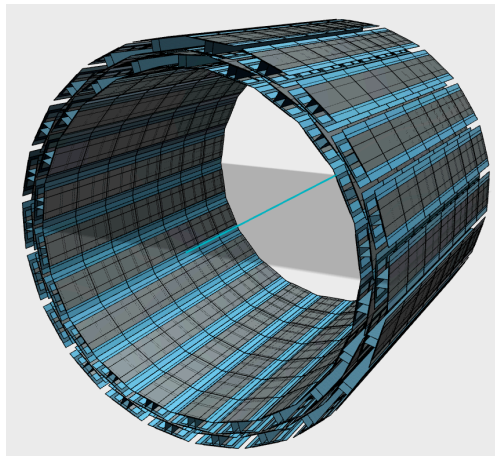


**Figure 4.14:** CAD drawing of the silicon strip tracker S1 layer. In order to minimize the dead area, every other sensor modules are staggered.

### Strip sensors

Each sensor is divided into cells of 9.6mm (in the beam direction)  $\times$  7.68 mm active area, and each cell consists of 128 strips of  $58 \mu\text{m} \times 9.6 \text{ mm}$ . As illustrated in Figure 4.15, the active area of S2, S1, and S0 silicon strip sensors are segmented into  $12 \times 10$ ,  $6 \times 10$ ,  $2 \times 10$  cells, respectively. Readout lines run perpendicularly to the longitudinal strip direction. For the S1 and S2 sensors, the readout line connects multiple strips in different cells to reduce the channel count. 1 channel in the S2 sensor reads 6 strips, in the S1 sensor it reads 3 strips, and in the S0 sensor it reads 1 strip. Thus the readout hit information does not distinguish the origin of the hit among multiple cells separated by 7.68 mm (one block). The offline reconstruction algorithm will distinguish the correct cell by requiring a good  $\chi^2$  for tracks fitted to all layers simultaneously. The probability of misidentifying the cell is low due to the expected low occupancy in the S1 and S2 sensors. The expected channel occupancy is  $\sim 0.2\%$  in S1 and  $0.1\%$  in S2 even in central Au+Au collision.

The top and bottom blocks of cells are read out upwards and downwards, respectively. At the edge of the sensor, the readout lines are connected to readout pads which are aligned to match the FPHX chip pattern as shown in Figure 4.16.

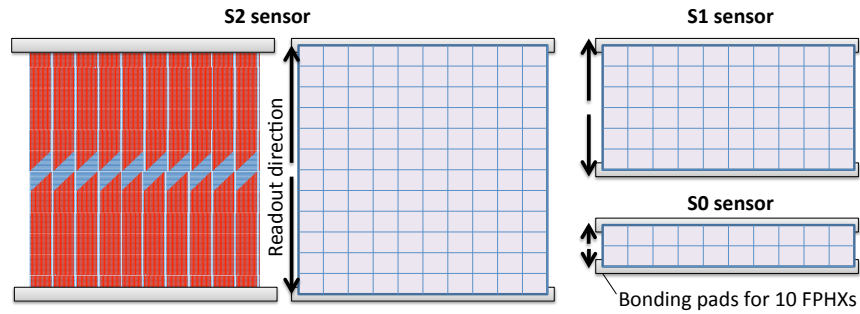


**Figure 4.15:** Illustration of S2, S1, and S0 silicon strip sensors. The active areas are segmented into  $12 \times 10$ ,  $6 \times 10$ ,  $2 \times 10$  cells, respectively.

This mechanical drawing of the S1 sensor is designed by HPK for the standard thickness  $320 \mu\text{m}$ . The breakdown voltage is to be  $>250\text{V}$ , and fully depleted voltage is to be less than  $100\text{V}$ . The bias resistance is 5 to  $15\text{M}\Omega$  per strip.

### Strip HDI

The high density integrated (HDI) circuit is designed by Inoue Material Company in Japan. The company is one of two major companies producing commercial flexible printed circuits (FPI) in Japan. Taking advantage of the R&D work carried out for the FVTX readout design for FPHX chips, the HDI design for the silicon tracker for sPHENIX follows the original FVTX design. In particular, the electric structure is designed to be an exact copy of the FVTX HDIs. As shown in Figure 4.17, the layer structure is basically the same as that of

S1

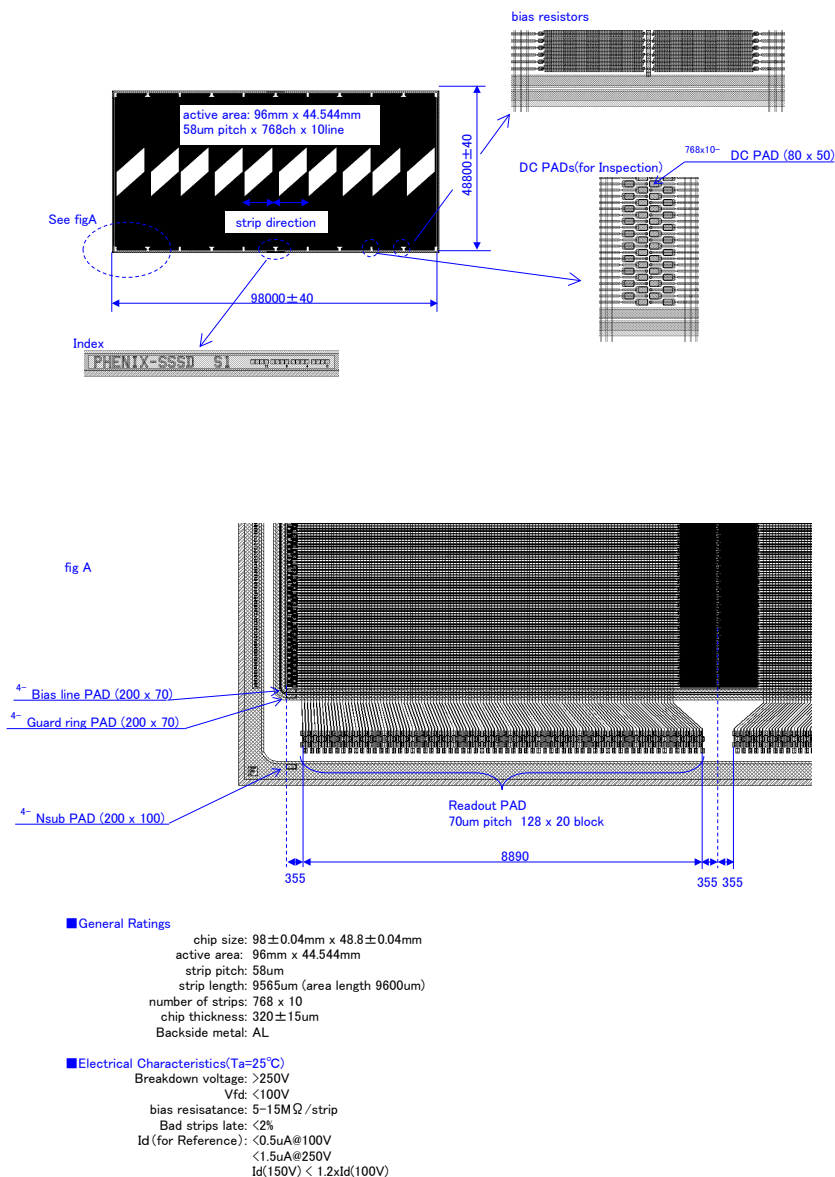


**Figure 4.16:** The mechanical drawing of the S1 sensor designed by HPK.

the FVTX. For example, the grounding layers are assigned to the surface on purpose for noise performance. This is a lesson from the R&D work. However, the HDI still needs to be re-designed for the sPHENIX silicon tracker because the shape is different due to the design difference between the disk (FVTX) and barrel (sPHENIX) type silicon trackers.

The HDI is trapezoidal in shape for the FVTX in the sensor region, while the sPHENIX version has a rectangular shape, as shown in Figure 4.18. The wire pitch is  $50\mu\text{m}$ , which is a less technologically challenging design than the  $40\mu\text{m}$  employed for the HDI readout of the FVTX. This technology choice is allowed because the barrel Si tracker for sPHENIX has fewer space constraints. We emphasize here that the HDI is designed with a well established technological choice, and there will be minimal changes from the original FVTX design.

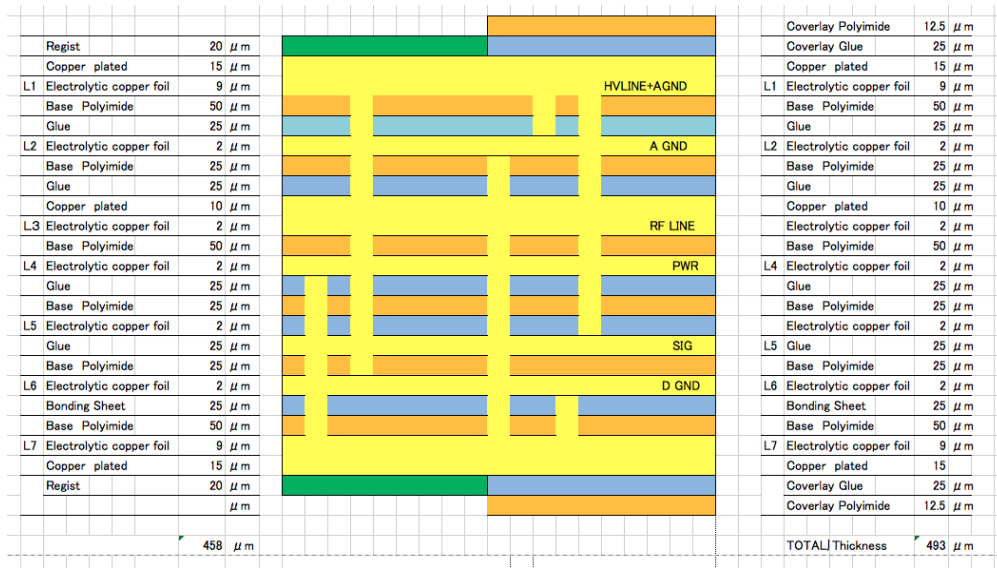


**Figure 4.17:** The 8 layers structure of the HDI for S1 layer.

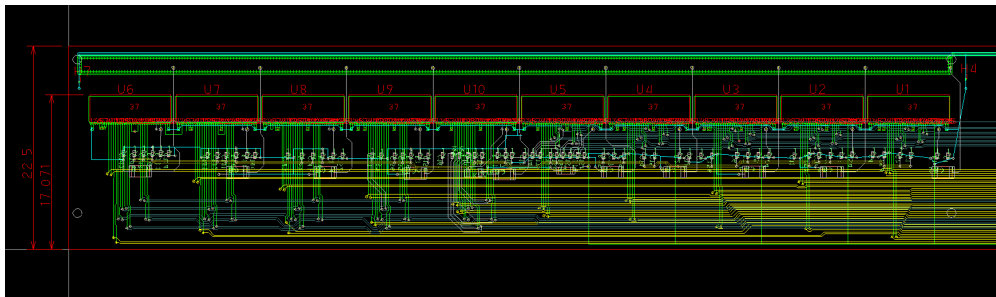


**Figure 4.18:** The circuit drawing of HDI for S1 layer drawn by Inoue Meterial Co.

### Strip sensor module

The silicon module consists of the strip sensors and the HDI. They are to be assembled by Hayashi Seimitsu Kogyo (HSK) Company. Their factory is located in Chiba prefecture, which is right next to Tokyo. HSK assembled the pixel detector that was built by RIKEN for PHENIX. The prototype HDI design for the S1 sensors was incorporated with HSK engineers to avoid possible technical difficulties in the assembly process. Shown in

Figure 4.18 is the 3D CAD drawing of the S0 strip sensor module. The flexible printed circuit (FPC) represents the HDI. Because of the top and bottom readout structure of the sensors, the HDIs are glued on to both ends of the silicon sensors. In order to reduce the amount of material, the two HDIs are completely separated and not connected. As recommended by the consulting HSK engineers, their relative alignment will be done during the assembly process.

The flexibility of the prototype HDI design is under discussion. The rigidity of the HDI depends on the mechanical structure of the support, which is one of the major differences from the FVTX. The rigidity will be optimized in the ladder integration stage by the choice of glue type.

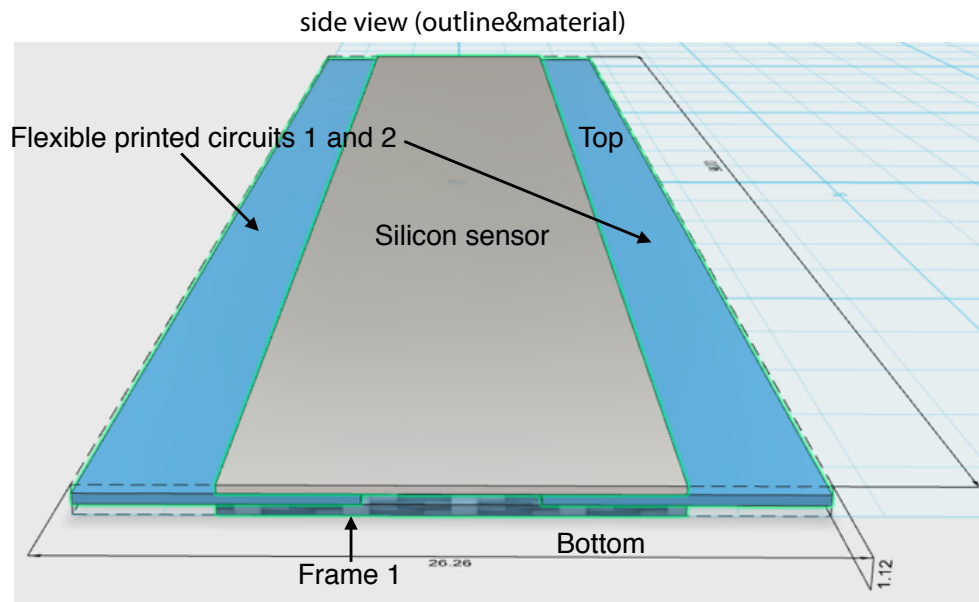


**Figure 4.19:** The CAD drawing of the Silicon module for S0 layer.

#### Stave (cooling)

The stave is mainly composed of the carbon fiber pipe for the air cooling. Shown in Figure 4.20 is the 3D CAD drawing of the cooling pipe made of multi-layered carbon fiber sheets.

#### Ladder

Shown in Figure 4.21 is the 3D CAD drawing for the S0 ladder. The carbon fiber cooling pipe is placed just below the silicon sensors. The main heat source of the silicon module is the FPHX chip, which is located at the tip of the silicon sensors. Thus the location of the cooling pipe is not immediately under the main heat source. The major reason for

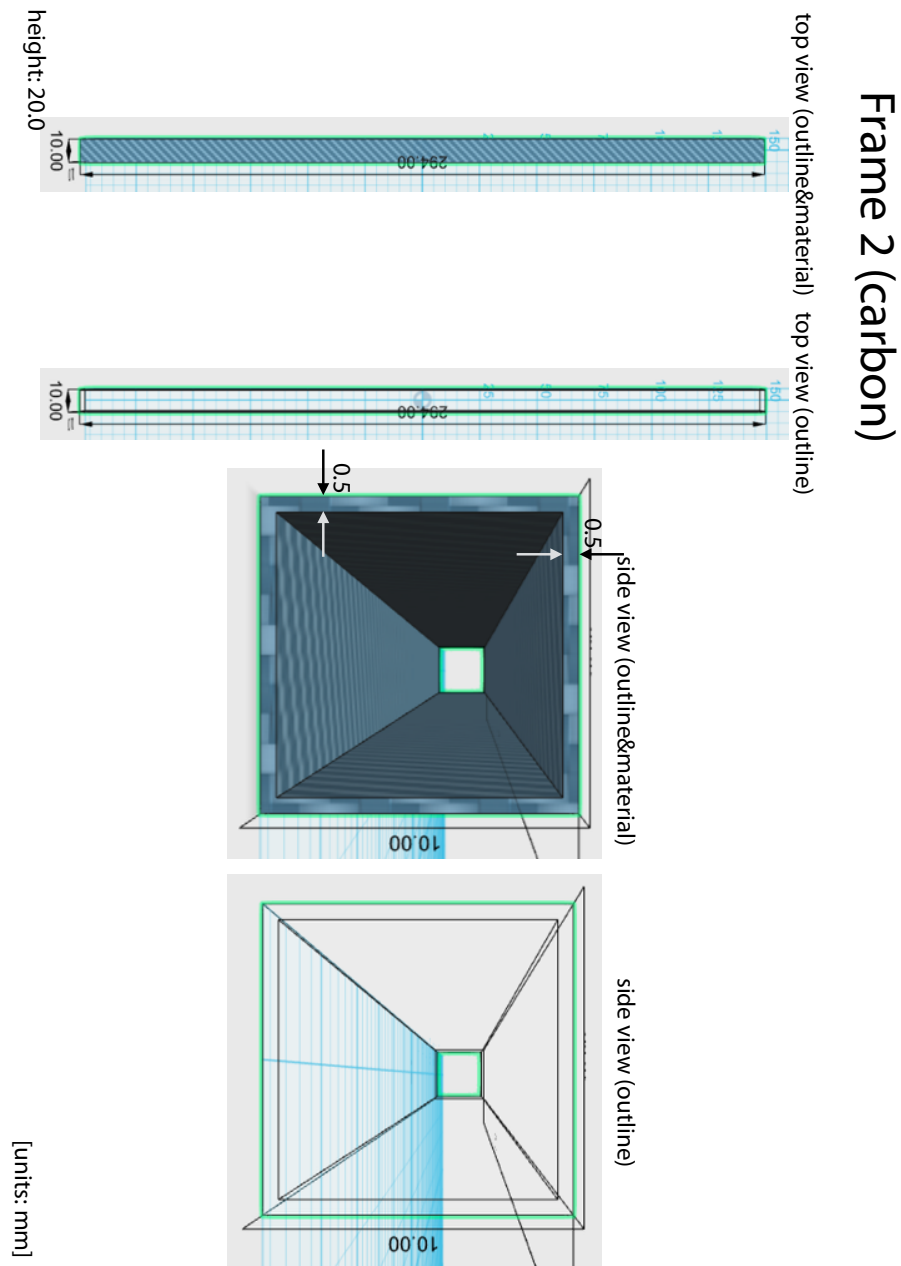


**Figure 4.20:** The CAD drawing of the carbon fiber cooling pipe for S0 layer. The dimension is given in mm.

this design originated from the spacial constraints between adjacent ladders. The current design is intended to minimize the offset between staggered adjacent ladders, since it would be unavoidable to increase the offset if the cooling pipe was aligned just below



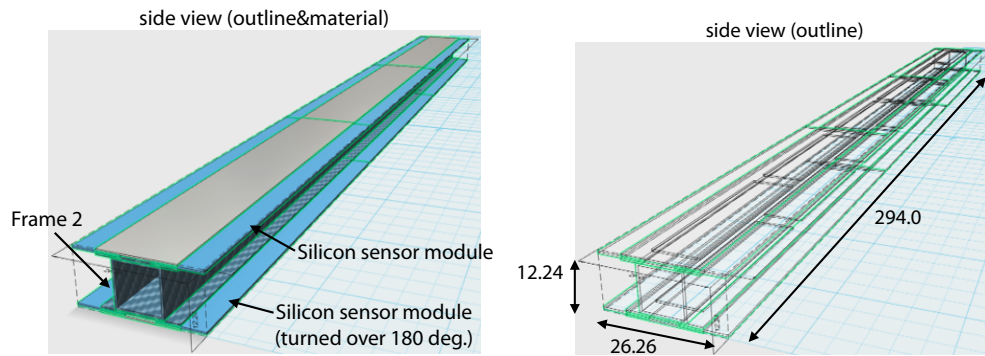


**Figure 4.21:** The CAD drawing of the ladder for S0 layer. The dimension is given in mm.

the FPHX chips, and increasing the offset would result in a larger radius of the staggered layer, and in covering a larger area. The heat conductance of the carbon fibers is good, but the location of the cooling pipe will be optimized during the R&D process. Three sensor modules are glued on the cooling pipe, lined up longitudinally in a row, as shown in Figure 4.21 on both the top and bottom of the cooling pipe.

#### 4.6.4 Justification of Design Choices

The momentum resolution is limited by multiple scattering in the middle (S1) layer, and thus by the amount of material in S1. Additionally the radiative tails on the Upsilon mass peaks are reduced if the total amount of material in the tracker is reduced. The design choices being pursued to minimize the material budget are as follows.

- Using air cooling instead of liquid cooling
- Using a  $240\mu\text{m}$  thickness for the silicon sensor instead of  $320\mu\text{m}$ .

As discussed in the previous section, the choice of the FPHX chip results in smaller heat generation, allowing air cooling, and this helps to reduce the material budget. If  $240\mu\text{m}$  thick silicon sensors demonstrate satisfactory performance, then their use will reduce the material budget for the silicon sensor by 25% relative to the standard thickness of  $320\mu\text{m}$ . The  $240\mu\text{m}$  thick sensor is known to draw larger dark current, and it is still in the development stage.

The cost of the readout is greatly reduced by combining signals across multiple blocks in the azimuthal direction, without widening the strip pitch. In this way the momentum resolution is not sacrificed while reducing number of readout channels.



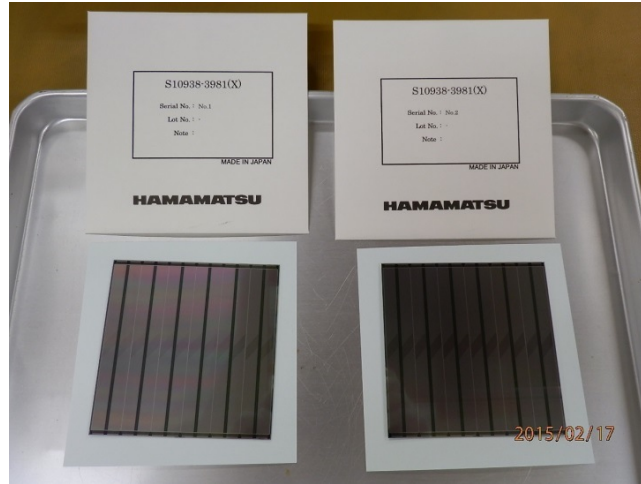


Figure 4.22: The prototype silicon sensors for the S2 layer.

#### 4.6.5 Silicon Tracker R&D

##### Overview

R&D for the silicon strip layers has been under way at RIKEN since 2014. The first prototype of the S2 sensor was made in 2014, and in 2015, we are focusing on the design of the silicon sensors and HDIs, and on the production of the prototype module for the S1 layer. The prototype module testing is expected to start at RIKEN in early 2016.

##### Sensor Prototype

The silicon strip outer tracker consists of the three sub-detectors, i.e., S0, S1, and S2. In 2014, five prototype silicon sensors for the S2 detector were made and delivered to RIKEN, as shown in Figure 4.22. The prototype AC coupled sensors, fabricated by Hamamatsu Photonics K.K. in 2014–2015, have a thickness of  $320\ \mu\text{m}$  and an active area of  $96 \times 92.16\ \text{mm}^2$ , and  $128 \times 24$  readout channels.

According to quality assurance tests by Hamamatsu in March 2015 there were no bad strips or channels on either of the prototype sensors. The full depletion bias voltage was  $V_{\text{fd}} \approx 50\ \text{V}$  and the breakdown voltage  $V_{\text{breakdown}}$  was larger than  $250\ \text{V}$ . This performance met the requirements for the S2 detector

For the S1 detector, we would like to have a smaller total material budget so as to achieve good momentum resolution. Thus we considered silicon sensors with thicknesses of  $240\ \mu\text{m}$  or  $320\ \mu\text{m}$ . A sensor with a thickness of  $240\ \mu\text{m}$  has 25 % less material than the  $320\ \mu\text{m}$  sensor, but it draws 2–3 times more dark current.

We are now making the first prototypes of the S1 sensor. Eight prototype silicon sensors for

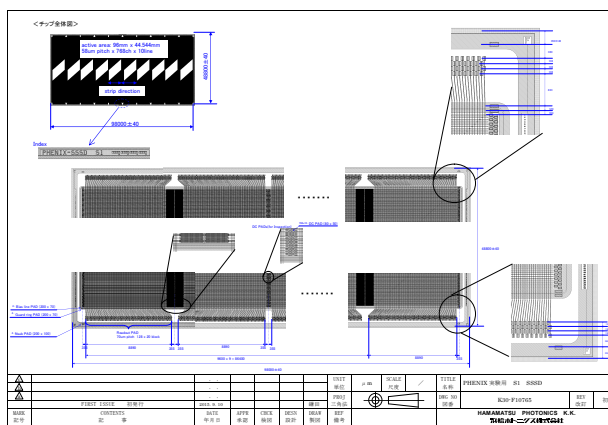


**Figure 4.23:** Layout for the silicon sensor for the S1 detector.

the S1 detector will be produced at Hamamatsu Photonics in December 2015, four sensors will have a thickness of  $240\ \mu\text{m}$  and the other four sensors will have a thickness of  $320\ \mu\text{m}$ . The  $320\ \mu\text{m}$  sensors will be delivered in November 2015, and the  $240\ \mu\text{m}$  sensors will be delivered in December 2015. They will be inspected at RIKEN in early 2016. Figure 4.23 shows the layout of the prototype silicon sensor for the S1 detector.

## HDI prototype

The design of the HDI for the outer tracker has taken into account 1) the effects of both common mode and differential mode noise, 2) the desire to minimize the geometrical size, and 3) the desire to limit the material budget. The second point is very important for the S0 and S1 detectors, since these detectors must be made compact for installation into a tiny space. The third point is especially important for the S1 detector where effects of multiple scattering are most significant. Thus we started the HDI R&D by putting a higher priority on the S0 and S1 detectors compared with the S2 detector.

The current design of the HDI for the S1 detector has seven layers of flexible printed circuits and has dimensions of  $30\ \text{mm}\ (\text{W}) \times 500\ \mu\text{m}\ (\text{H})$ . The length of the HDI in the beam direction varies from 10 cm to 40 cm, depending on its location in the ladder. The size of the HDI is well below the geometrical requirements. The prototype HDI has a thickness of approximately 0.5 % of a radiation length on average. The seven layers of flexible printed circuits have been designed with a special emphasis on a reduction of any unwanted microstrip antenna, and on good impedance matching even at  $\sim 40\ \text{cm}$  distant from the FPHX readout chip. Production of the prototype HDIs for the S1 detector will be performed by Yamashita Materials Corporation and will be ready for further assembly at the end of 2015.

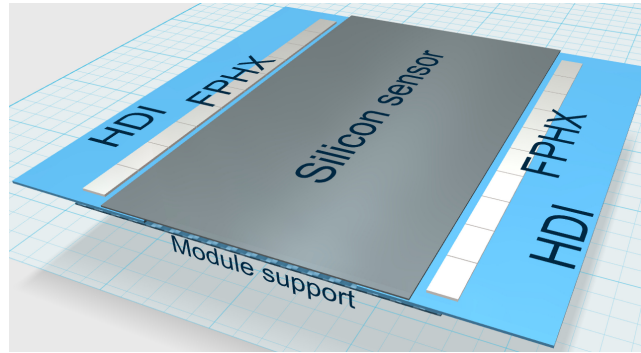


**Figure 4.24:** Layout for the silicon sensor module for the S1 detector.

### Silicon Module Assembly

One silicon sensor, two HDIs with ten FPHX chips for each, and one support frame are assembled into a silicon module as shown in Figure 4.24. In the assembly, the bonding of the FPHX chips to the silicon sensor and their attachment to the two HDIs are performed as well. Hayashi watch-works co., Ltd, who have experience producing the PHENIX VTX detectors, will be employed for the assembly of the prototype module.

### Silicon Module Test Plan

The first prototype module for the S1 detector will be tested at RIKEN. Since the sPHENIX outer tracker uses essentially the same electronics as the PHENIX FVTX detector, namely the FPHX readout chip and front-end circuits. The test bench at RIKEN that was originally setup for the high multiplicity trigger development for the FVTX detectors can be used again to test prototype sensor modules, with minor modifications in the readout configuration. The test is planned in 2016 spring and summer.

### Ladder Prototype

A schematic view of the prototype ladder for the S1 detector is shown in Figure 4.25. The ladder consists of the hollow carbon frame and silicon modules to be attached to the top and bottom of the hollow frame. The design of the prototype ladder is ongoing. Important design considerations are the capability of air-cooling the FPHX chips, and the mechanical vibration of the ladder due to air-blowing inside the frame itself.

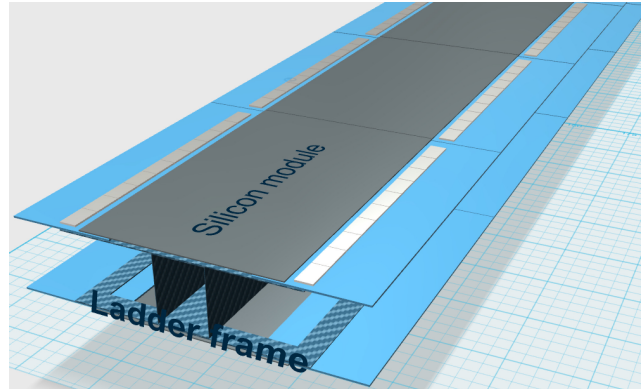


**Figure 4.25:** Layout for the silicon sensor ladder for the S1 detector.

## 4.7 TPC option

### Detector Description

The TPC design follows the classical cylindrical double-sided TPC layout used in several other experiments, with a central membrane electrode located at the middle of the interaction region dividing the TPC into two mirror-symmetric volumes, as shown in fig. 4.26.

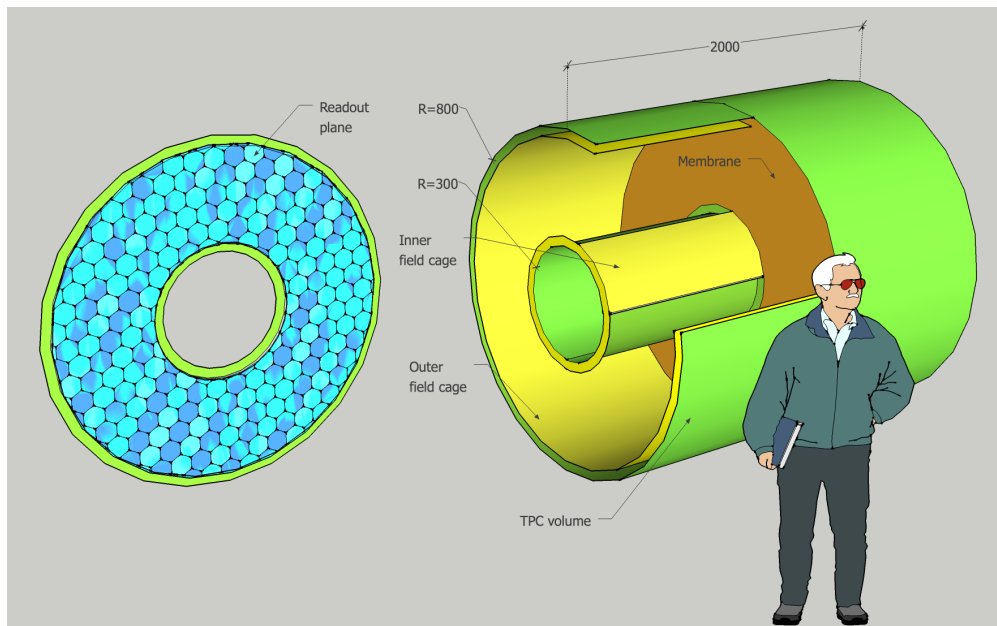


**Figure 4.26:** Schematic layout of TPC main elements.

In each such volume the readout plane is located on the endcap inner surface, facing the gas volume. The electric field, transporting primary ionization to the readout plane is

formed by the membrane electrode set to the highest voltage bias on one side and by the the readout plane at ground potential on the other. The electrical drift field is constrained by the field cage along the inner and the outer cylindrical surfaces of the TPC.

The two mirror-symmetric parts of the TPC form a common gas volume filled with the gas mixture, which transports primary ionization to the readout plane on each TPC endcap surface. The same gas that transports primary ionization also serves as the medium for the amplification elements located in front of the readout planes. These amplification elements are built based on several layers of micropattern gaseous detectors.

Other TPC subsystems directly related to the main volume are the channel readout system; high voltage distribution systems for the drift field and for the amplification elements; gas circulation, control and purification system; TPC calibration systems. Operation and readout of different service subsystems requires a TPC slow control system.

The exact specifications will require additional R&D work to finalize. Nevertheless, it is appropriate to demonstrate an “existence proof” in the form of a design that would match and exceed all necessary performance parameters. Because of the extensive R&D used to establish, in great detail, the operational principles for the ALICE TPC Upgrade project, this example makes for a very effective initial model. In the coming discussion, we use the ALICE upgrade plans and R&D results to show that an implementation along these lines would work for sPHENIX. In the later discussion, we give more detail on how these parameters are likely to be even further optimized for our application. As such, even though we present exact figures here, these should be considered as exact figures of a “strawman design.”

Parameter	Value	Unit	Comment
Gas enclosure	$<30 \rightarrow 80$	cm	
Active volume	$30 \rightarrow <80$	cm	
Length	$\pm 80$	cm	$ \eta  < 1$
Pad Size	$1.2 \times 10$	$mm^2$	45 radial segments
Channel Counter	$123700 \times 2$		
Avalanche Technology	Quadruple GEM		Same as ALICE upgrade design
Gas gain	2000		Same as ALICE
Field Cage Central Potential	32,000	V	$400 \frac{V}{cm}$ , conservatively high

#### 4.7.1 Results

Analytic results and full GEANT simulation results are in excellent agreement, however the analytic results lend insight into which terms in any design limit the momentum resolution. At the lowest momentum, the material term will dominate favoring the TPC-

based design. At the highest momentum, the position resolution term will dominate, favoring the Silicon-based design.

The analytical and semi-analytical calculations use Table 4.2 for the silicon strip tracker and the table below for the TPC to characterize the detector geometry and material.

layer	radius (cm)	Thickness % $\chi_0$	$\frac{\Delta L}{L}$	$c_{ms}$ (mrad)	$\sigma_{ms}$ (mrad)
VTX 1	2.7	1.3	0.95	1.8	1.7
VTX 2	4.6	1.3	0.92	1.8	1.7
air	15	0.1	0.73	0.03	0.02
Field cage	30	1.0	0.55	1.12	0.5

**Table 4.4:** Table showing the input parameters used to characterize the hybrid TPC tracker for the analytic and semi-analytic momentum and mass resolution calculations.

Option	$\sigma_{ms}$	$\sigma_{det}$	$\sigma_{det}^\theta$	$\sigma_\theta^{ms}$
Silicon	0.011	0.00057	0.0012	0.0031
Hybrid	0.0066	0.00105	0.0011	0.0025

**Table 4.5:** Extended Glückstern parameters for each tracking option.

Figure 4.27 shows an overlay of multiple results for the silicon tracking design (reuse of PHENIX silicon pixels plus new silicon strips). Note that this figure plots only the transverse momentum component. The black dots are a full GEANT simulation and the blue lines are analytic calculations. The solid blue line is a first-principles calculation of the result using the Glückstern formula. Despite the fact that the formula is derived assuming that the detector material is uniformly distributed throughout the tracking volume, the agreement is excellent. The dashed blue line is a modest improvement to the fit wherein the functional form was held fixed, but the material thickness and position resolution were allowed to vary as free parameters. The light blue line in this figure indicates the contribution of the position resolution term alone, showing that the resolution in this detector design is nearly entirely dominated by the multiple scattering term. Thus, improved performance (in momentum resolution, mass resolution, and pattern recognition) could be achieved for the silicon tracker only by increasing the tracking radius or lowering the material budget, and not from improving the position resolution.

Figure 4.28 shows a comparison of the analytical results for the momentum resolution for the silicon tracker and the TPC-based option. Note that this plot shows the full momentum resolution (not merely the transverse component), different from the result in Figure 4.27.

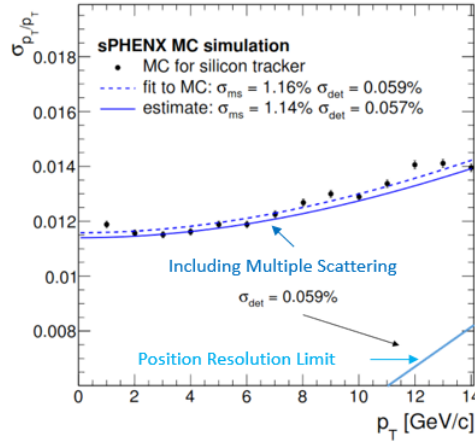


**Figure 4.27:** Transverse momentum resolution of the silicon tracking detector design with the reused pixels. Black dots are from a full GEANT4 simulation. The dashed blue line is a free fit to the Glückstern formula, whereas the solid blue line is a first-principles prediction using the material list. The light blue line shows the contribution from position resolution alone, demonstrating that the baseline design is entirely multiple-scattering limited.

Solid lines indicate the result at  $\eta=0$  and are thereby the same as the result from the prior figure (*i.e.* where  $p_t = p$ ). The dashed lines indicate the result averaged over tracks across the full aperture  $|\eta| = \pm 1$ . The TPC is considered in two different ways: standalone as indicated in pink and with a vertex constraint as indicated in red. At the very lowest momentum, the TPC standalone results are better than those including a vertex constraint since these do not suffer from the multiple scattering limits of the entrance window, beam pipe, and vertex detector. At higher momentum, using the vertex constraint improves the TPC-alone result due to the increased lever arm of the measurement. Clearly, during a physics analysis, one would use a properly weighted average of these two calculations, so that that the lower envelope of these results should indicate the detector system's ultimate performance.

Considering first the  $\eta=0$  results (left panel, solid lines), we see that the hybrid TPC design provides superior performance until  $p_T = 10 \frac{\text{GeV}}{c}$  beyond which the silicon tracker solution is better. However, when averaged over the full aperture (dashed lines), the hybrid solution has superior performance over the entire plotted range (out to  $14 \frac{\text{GeV}}{c}$ ) pushing the momentum at which the silicon performance becomes superior out to  $\sim 17 \frac{\text{GeV}}{c}$ . The relevant range for decay electrons from the Upsilon is roughly  $4 - 10 \frac{\text{GeV}}{c}$ .

The right hand panel of Figure 4.28 shows the full momentum resolution of the various designs as a function of  $\eta$  for discrete momenta 1, 3, 5, 7, and  $9 \frac{\text{GeV}}{c}$ .

Figure 4.29 shows calculations for the TPC-hybrid option on reconstruction of the  $Y(1s, 2s, 3s)$  states. The black dots are the result of a full GEANT calculation (described in detail later in the chapter). These results can be compared to those shown in the black solid histogram, which is the result of the semi-analytical calculation that uses the Glückstern

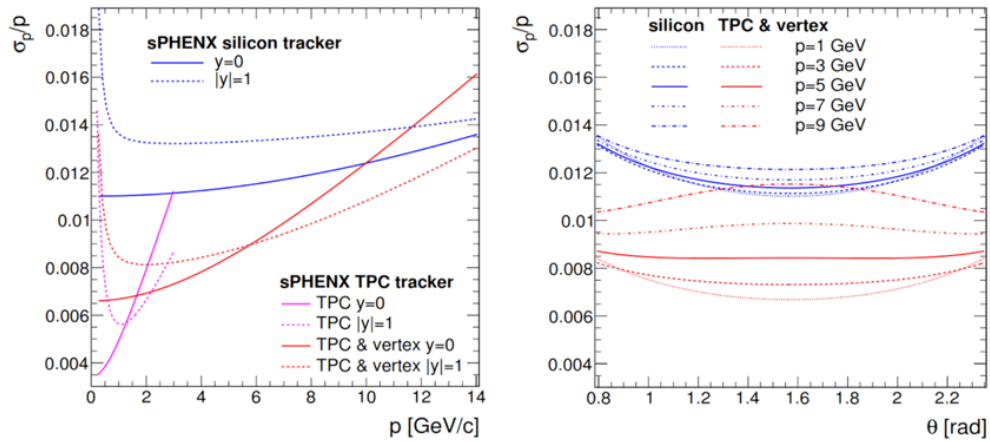


**Figure 4.28:** Momentum resolution of the baseline sPHENIX tracker and the hybrid TPC option. Solid lines in the left panel are for  $\eta=0$  ( $p_T = p$ ), dashed lines are averaged over the entire aperture.

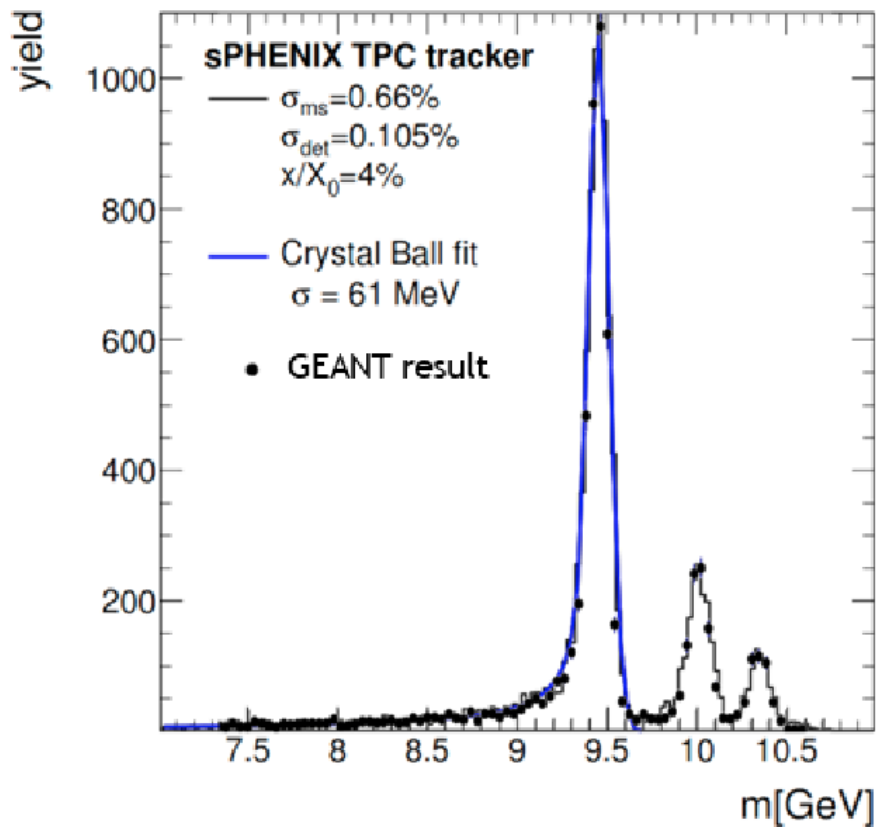


**Figure 4.29:** Simulated Mass Resolution for the Upsilon states. Black dots are the results from GEANT simulations. The black histogram is the result of the semi-analytic calculation. Blue curves are free fits to the  $\Upsilon(1s)$ .



formula generalized to 3D, with the Bremsstrahlung after-burner applied. Finally, the blue curves show the result of a free fit to the so-called “Crystal Ball” function that is used to extract the gaussian width of the  $Y(1s)$  state. As one would expect based upon the previous results, the TPC-hybrid solution produces a peak width  $\sim \frac{2}{3}$  that of the silicon tracker option.

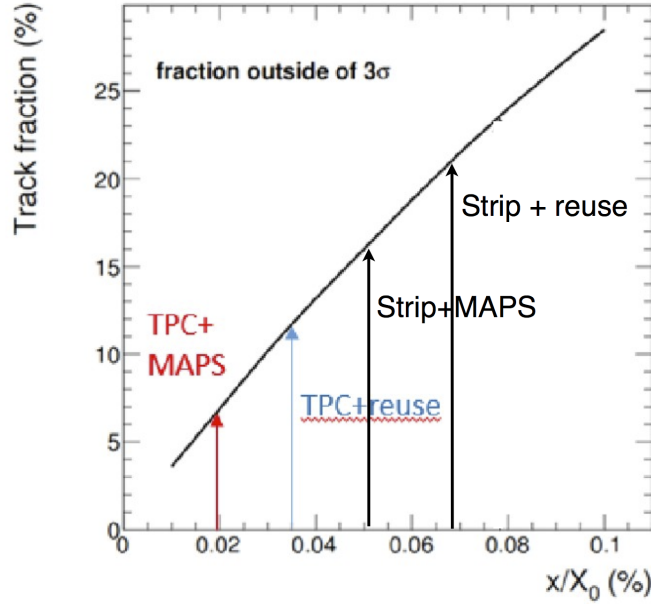


**Figure 4.30:** Statistics loss of Upsilon's due to Bremsstrahlung.

It is found that not only are the shapes of the mass resolution plots different in the two options, but for the same running period the yield is better for the thinner option. This effect is quantified in Figure 4.30. Here we quantify the loss in statistics due to Bremsstrahlung driving counts outside the  $3\sigma$  momentum window. The loss for  $\frac{x}{X_0}=6.8\%$  (the silicon strip and reused pixels option) is 21% of single tracks, meaning a pair loss of 38%. As indicated in the figure, these losses will be smaller as the detector gets thinner, with pair losses of 29% for the silicon strip and MAPS pixel detector, 23% for a hybrid solution with TPC and reuse of PHENIX pixels, and 12% for a hybrid solution with a TPC and MAPS detectors of thickness equal to that being constructed for the ALICE ITR upgrade.

#### 4.7.2 TPC Simulations

The TPC simulations performed target a realistic representation of the cluster size and two-hit resolution based on design parameters *which are consistent with those described in the*

previous section. Thus far the effects of space charge have not been included, but *the effects of space charge should be within the tolerances of already working TPC experiments*.

GEANT4 is used to record energy deposits in a cylindrical volume of gas. In the results shown below, the volume was filled with Argon ("G4\_Ar") in order to simulate the  $dE/dx$  of the T2K gas used in the ILC TPC prototype. The energy deposits are recorded in discrete radial regions of the cylindrical volume. For each region, a Poissonian random number of ionization electrons are produced along the track trajectory according to measured values of the average ionization per energy deposit for the simulated gas. Each electron is then randomly diffused in 3 dimensions according to measured values in the gas with a desired electric field *see table below*. The average diffusion is then added in quadrature with a  $300\ \mu\text{m}$  diffusion to emulate diffusion during the amplification stage of readout.

The  $r - \phi$  readout is simulated using a plane of rectangular pads. Each electron adds to a 12-bit ADC for each pad directly in proportion to the number of diffused electrons reaching the pad (gain fluctuations are not currently simulated). For the  $z$  direction, the analogue timing response is not simulated but rather each electron is placed into a time "bin" with width corresponding to  $\sqrt{12}$  times the expected width of the shaper pulse. If anything the two-hit resolution in the  $z$  direction is pessimistic in the current simulation.

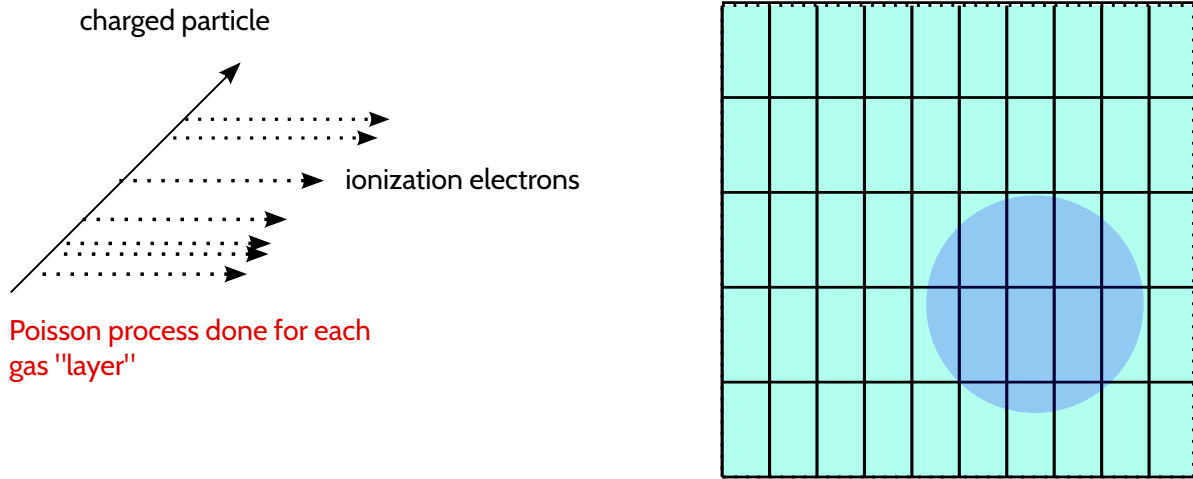


**Figure 4.31:** schematic illustration of electrons drifting to the pad plane in the TPC simulation (pad size not drawn to scale)

After the pad ADC has been recorded in each time bin, clustering is performed to group pad,time-bin pairs into 3-dimensional detector hits to be passed to the track-finding algorithm. In the current simulation, clustering is performed independently for each pad,time pair corresponding to a given radial pad index. This is done for simplicity, but the pad length in the direction corresponding to radial measurement is much larger than the typical electron diffusion so not much generality is lost in this simplification. Figure 4.31 shows the readout and clustering process schematically.

In addition to the TPC, the two reused PHENIX pixel inner layers are included in the

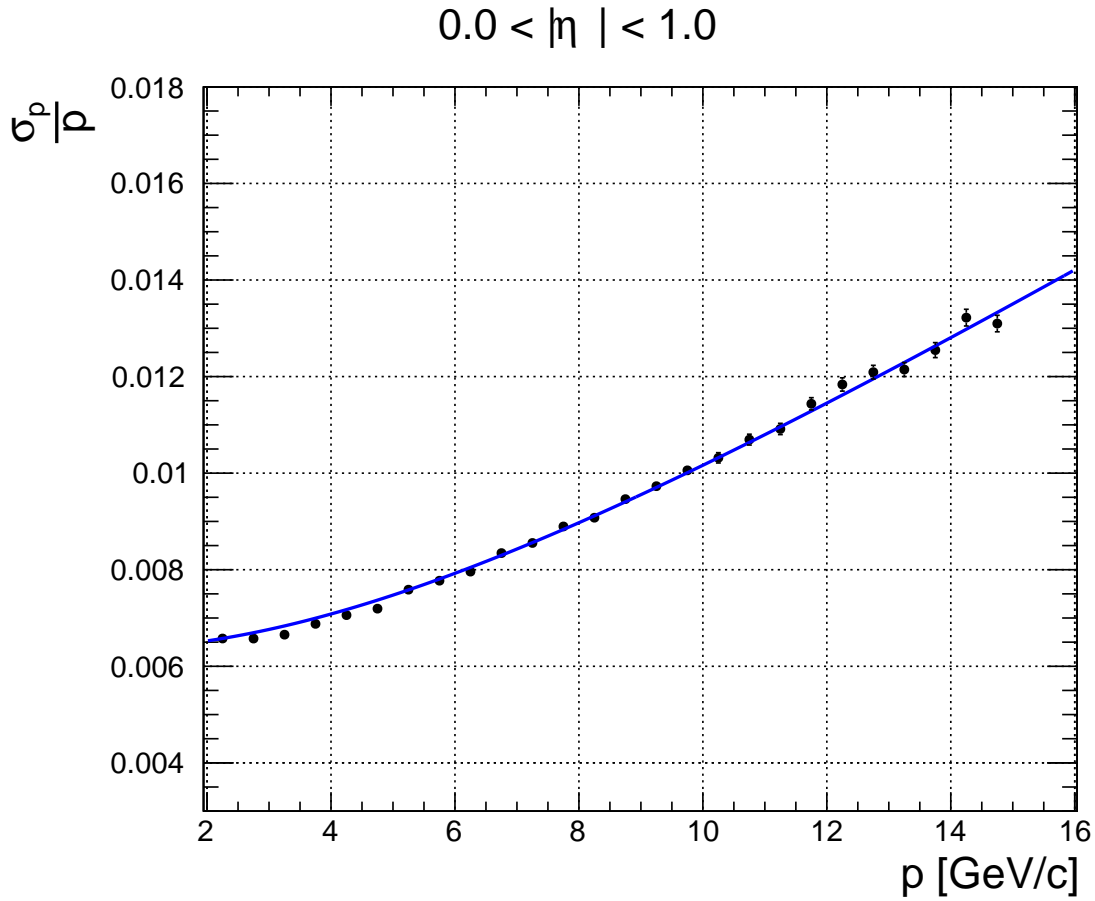


**Figure 4.32:** comparison of the momentum resolution of the simulated TPC with an analytic calculation in one unit of pseudorapidity

tracking setup. The clustering is performed on the silicon hits as in the silicon simulation.

Finally, the clusters are passed to a hough-transform-based algorithm for pattern recognition and fit with a Kalman filter. The momentum resolution achieved is compared to an analytic calculation for the particular TPC simulated in Figure 4.32. The mass resolution for single Upsilon's of the 1S, 2S, and 3S states along with an analytic calculation given the TPC parameters is shown in Figure 4.33.

### 4.7.3 TPC Design Details

#### TPC readout plane

The TPC readout plane is the most composite and multifunctional TPC element. On the inner side of the TPC volume the readout plane is subdivided into conductive readout elements (pads) connected to the electronic readout channels sitting on the opposite side

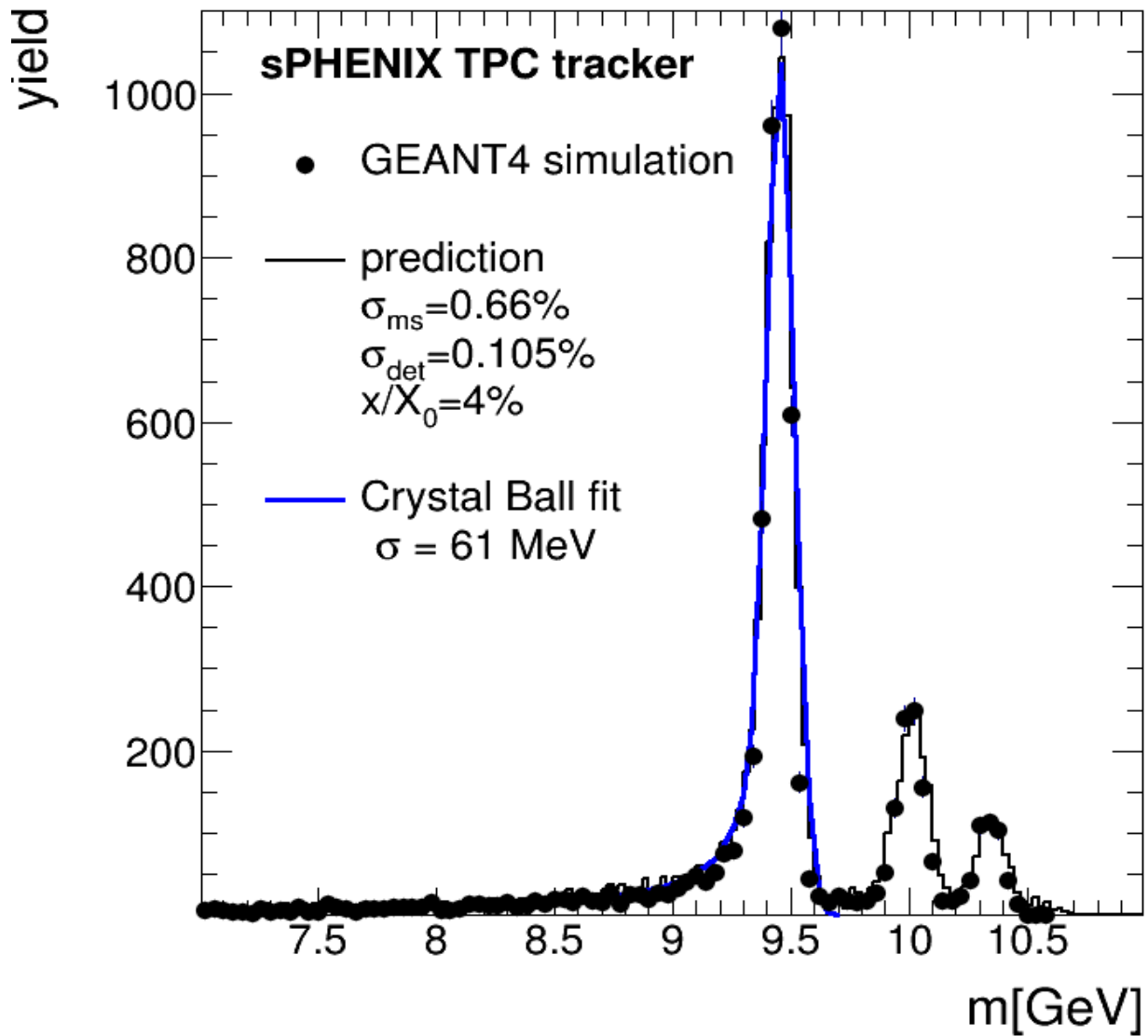


**Figure 4.33:** Upsilon 1S, 2S, and 3S resolution for the simulated TPC along with an analytic calculation

of the plane. The amplification element that receives primary ionization and multiplies it to the level suitable for the electronics is directly coupled to the readout plane on the inner side of the TPC volume. The readout plane also handles some additional communications like high voltage, calibration and other services. The electronic and mechanical design of the readout plane is a multi parametric task that involves matching the performance of almost all TPC subsystems.

The pad structure of the readout plane is considered to be formed by concentric circular rings of pads spanning between the innermost and outmost TPC radii as schematically shown in fig. 4.34. The radial pad size is  $\sim 1$  cm. The pads will have a so-called "chevron"

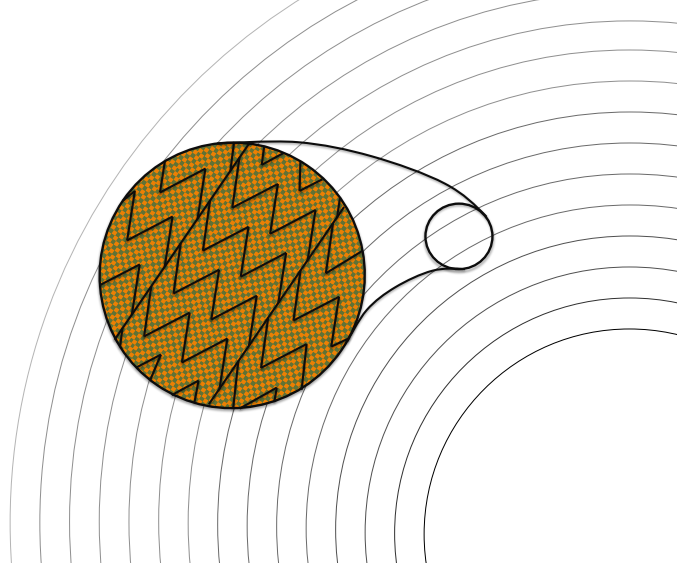


**Figure 4.34:** Schematic layout of the TPC pad rows and chevron pads.

shape that enforces charge sharing between the neighboring pads for the most precise determination of the hit azimuthal position. The transverse dimension of the pads is compatible with the size of the avalanche determined by electron diffusion during both the drift and avalanche stage. The best position resolution will result from designing the diffusion to be primarily from the gas stage, with little diffusion from the drift.

Although it has been shown that the “straw model” resulting in  $\sim 250,000$  pads will result in excellent performance, the actual number of pad rows, size and shape of the pads, are subject to further optimization during the R&D period.

The TPC amplification element is based on several layers of Gas Electron Multiplier (GEM) detectors. Traditional Multi-Wire Proportional Chamber (MWPC) technology is not considered because it a) cannot provide desired  $r\phi$  resolution of  $100\ \mu\text{m}$  and b) the MWPC requires gating to stop ion back flow, and that significantly limits the data taking rate.

Four GEM layers are considered in the current scheme of the amplification element. Each GEM will provide gain in the range of typically a few thousand, suitable for the readout electronics considered for the TPC. The gain range is driven by two competing factors. Higher gains will improve the signal:noise and improve  $\frac{dE}{dx}$  results, but will also increase the Ion Back Flow (IBF). ALICE intends to run at a gain of 2000 with SAMPA chip readout. ALICE results also demonstrate high stability of GEM operation in the environment of high energy heavy ion collisions.

The amplification element is shown in fig. 4.35. Besides providing gas amplification suitable for the electronics, the element also has two other functions.

First, the transverse size of the ionization cloud arriving at the readout plane from the drift volume is defined by the gas diffusion and by the longitudinal (w.r.t. to the drift direction)

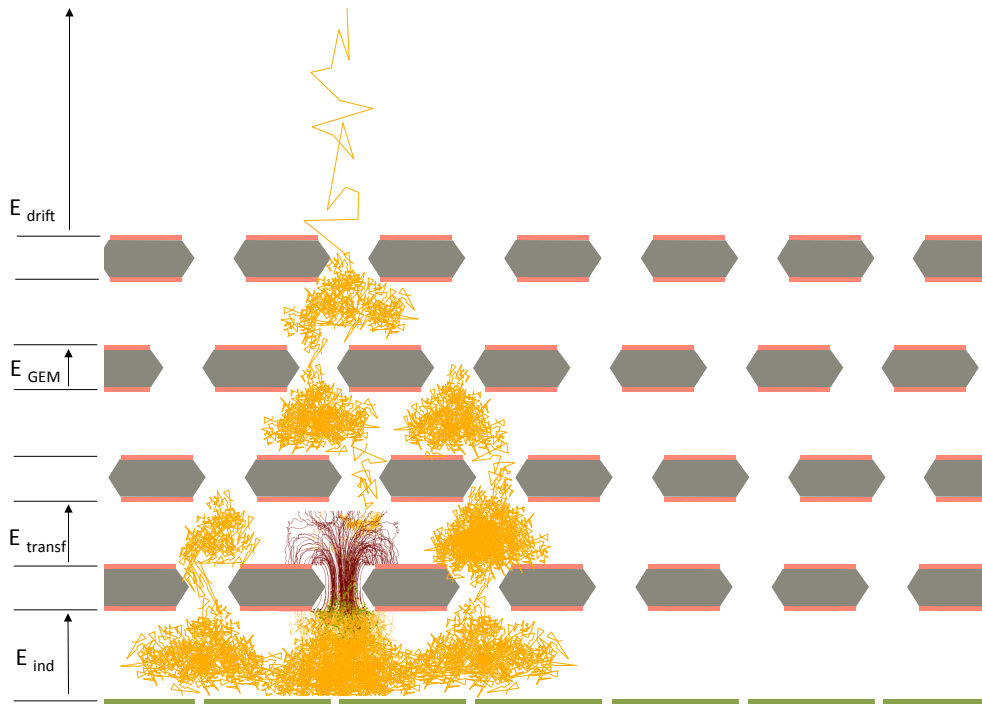


**Figure 4.35:** Schematic view not to scale of the readout element built with four layers of GEMs. Yellow lines show electron paths, brown lines show the ion paths for one single hole (simulation).

magnetic field. As shown in later sections, a strong magnetic field limits transverse diffusion significantly. Some diffusion will, however, be necessary to spread the signal charge across multiple electrodes. By using several layers of GEM, an effective “hole-misalignment” diffusion term is introduced. Often the hole patterns on the individual GEMS (where holes make equilateral triangles) are rotated by 90 degrees to avoid large regions of accidental hole alignment (Moire pattern). ALICE plans to not only change the orientation of the holes layer-by-layer, but also their spacing.

Second, the most important task for operating the TPC at high rates is to suppress the Ion Back Flow (IBF) that leads to build up of space charge in the drift volume of the TPC and, as a result, to the distortion of the primary ionization arrival point onto the readout plane. Some ions are created by the tracked particles ionizing the gas in the TPC volume, but most ions come from the avalanches in the GEM layers. The second contribution is larger by several orders of magnitude (the gas gain factor) than the first contribution. The number of ions arriving from lower (closer to readout plane) GEM layers is higher than from the upper layers. Properly configuring electric fields inside and between the GEM layers can significantly suppress the second contribution by redirecting ions to drift towards the back planes of the upper GEMs, as shown in fig. 4.35. Recent studies made by the ALICE collaboration and shown in fig. 4.36 demonstrate a dependence of the IBF on

the charge measurement resolution at constant gas gain. These results show that the IBF

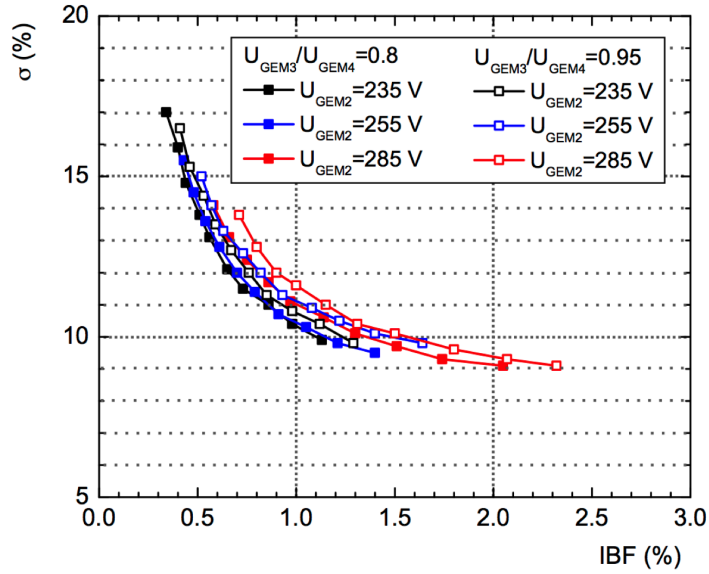


**Figure 4.36:** Ion Back Flow in ALICE.

can be reduced to  $\approx 2\%$  for a charge determination resolution of approximately 12%. This is considered to be an acceptable level for operating the ALICE detector.

### TPC field cage

The basic function of the TPC field cage is to provide a uniform drift field from the central membrane to the detector modules at each end. This field cage is traditionally defined by a series of conducting rings held at uniformly decreasing potential by a precision-matched chain of resistors. The field cage is then surrounded by a gas enclosure. Both for safety considerations and to avoid stray electric fields in neighboring detectors, the gas enclosure is usually grounded. Figure 4.37 shows the configuration found on the outer shell of the STAR TPC. Both the field cage and the gas enclosure are made structurally rigid using a hex cell honeycomb sandwich structure.

The field cage electrodes are made as a double-layer of staggered rings, one facing the operating gas and the other embedded in the field cage wall. The latter ring serves to shape the field and minimize nonuniformities in the drift volume. Dry nitrogen gas flows through the 5.7 cm gap, exceeding by slightly more than a factor of two the "rule of thumb" gap dielectric strength of  $1 \frac{kV}{mm}$  when operating at a central potential of 27 kV. Although in STAR the inner gas enclosure is skipped (exposing the field cage strips to outside air and stressing inner detectors with electric field) in the sPHENIX application we have more than enough room between the inner silicon pixels and the TPC active volume for an inner

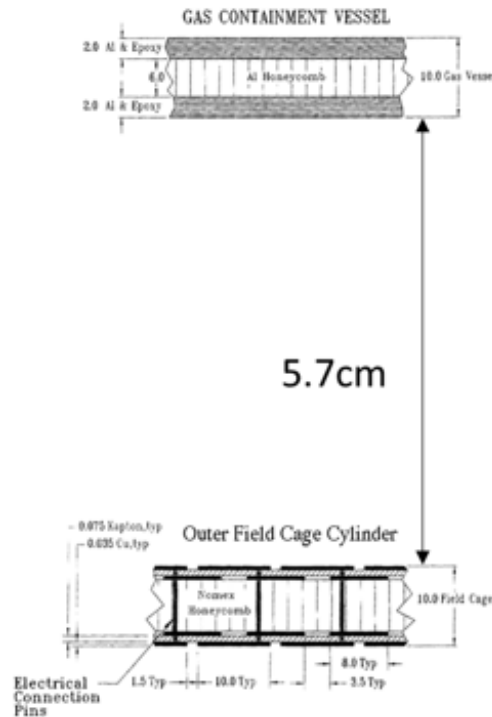


**Figure 4.37:** Scale drawing of the outer field cage and gas enclosure for the STAR TPC.

gas enclosure. Scaling to an identical safety factor as used by STAR, we would require a  $5.7\text{cm} \frac{34\text{kV}}{27\text{kV}} = 7.2\text{cm}$  gap.

An “air” gap of this size would be undesirable for the outer TPC wall since it would limit the active volume and degrade the momentum resolution. Because the TPC is followed by the EMCAL, we can safely afford to solve the field issue using a solid of high dielectric strength. The concern over this solution is two-fold. First, the dielectric field strength of common materials is found to reduce with time in a variety of materials as shown in Figure 4.38. Much of this variation (*e.g.* FR4) is dominated by micro-gas bubbles within the material which can carbonize over time. Secondly, dependent upon material, solid material high voltage gaps, can be subject to permanent failure during a discharge event or over-time corona current.

Material Type	Max. Operating Temperature (°C)	T/G °C	Voltage (V/mil) Note 1	Aged rating (V/mil)	W°C/m
FR4	105-130	160	800	300/150	0.21
FR4 Hi-Temp.	130-150	170	800	300/150	0.22
BT Epoxy	140-160	180	1300	600/400	0.40
Polyimide	150-190	200	900	700/500	0.25
HVPE*	180-200	210	3000 to 7000	3000/2000	0.28

\*HVPE is a trademark of Sierra proto express.

**Figure 4.38:** Dielectric strengths of various common circuit card materials, reproduced from figures by Sierra Proto Express, a Palo Alto-based circuitry company specializing in high voltage circuit card for both terrestrial and satellite applications.



sPHENIX is working with the Sierra Proto Express company to develop a robust solid core solution for the outer field cage that would maximize the reliability and longevity of the device. Although a multi-material, layered ultimate design is likely, the table below shows the required thicknesses for safety factors of 3X and 5X in the design assuming a single material type and neglecting contributions other than the insulator itself. Calculations here use the worst-case aging estimates from Sierra for each material type. These initial calculations seem promising, meaning that the "air gap" solution is presently considered only as a fallback option. If the solid option realization has a sufficiently small radiation length, it can also be considered for the entrance window, thereby simplifying the design.

Material	$\chi_0$ (cm)	Volt/mil	3X Safety	5X Safety
FR4	16.76	150	1.72 cm (10.3% $\chi_0$ )	2.88 cm(17.2% $\chi_0$ )
Kapton	28.58	500	0.52 cm (1.8% $\chi_0$ )	0.86 cm(3.0% $\chi_0$ )
HVPF	28.57	2000	0.13 cm (0.45% $\chi_0$ )	0.22 cm(0.75% $\chi_0$ )

The endplates of the TPC will likely be shaped in a "spoke" pattern and house either 6 gain stage modules on each end or 8 gain stage modules. The 6-module solution provides the largest live area and least material that could disturb future upgrade plans. The 8-module design would use smaller GEMS and thereby involve a moderately reduced risk.

### TPC gas

The choice of gas is a critical design criterion for the TPC as this choice affects the potential of the central membrane, single point resolution, multiple scattering, and positive ion feedback. Currently, the largest effort has been put into considerations of the so-called "T2K" gas and the "ALICE" gas. The characteristics of these two gasses are summarized in Figure 4.39.

The T2K gas has exceptionally low diffusion ( $50 \frac{\mu m}{\sqrt{cm}}$ ) at a rather low drift field of ( $\sim 120 \frac{V}{cm}$ ). At 85 cm of drift, the central membrane would only require a voltage of  $\sim 10$  kV. It is also a "fast gas" with a drift velocity at minimum diffusion of  $\sim 60 \frac{\mu m}{nsec}$  and thereby a full TPC drift time of 14  $\mu sec$ . Furthermore, T2K gas is near a velocity plateau, thereby relaxing the constraints on field uniformity. Conversely, the ALICE gas has a significantly higher minimum diffusion ( $\sim 150 \frac{\mu m}{\sqrt{cm}}$ ) and lower drift velocity ( $22 \frac{\mu m}{nsec} \rightarrow 34 \mu s$ ). Recently ALICE added  $N_2$  to the mix which slightly increases the drift speed as noted earlier.

The naive assumption favors low diffusion, high speed, and a velocity plateau making the T2K gas an apparent winner. But for our application, further consideration is required. Since we will likely be using MPGD-style avalanche, we **rely** upon the diffusion of the charge to spread the avalanche across the pads. To achieve a sigma of  $\frac{1}{2}$  pad-width =  $500 \mu m$ , would require at least 1 meter of drift length. In the ALICE gas, this level of diffusion is achieved after only 10 cm of drift. Furthermore, since the slow shaping time of the SAMPA chip (190 nsec) is significantly longer than the charge collection time in either gas, the

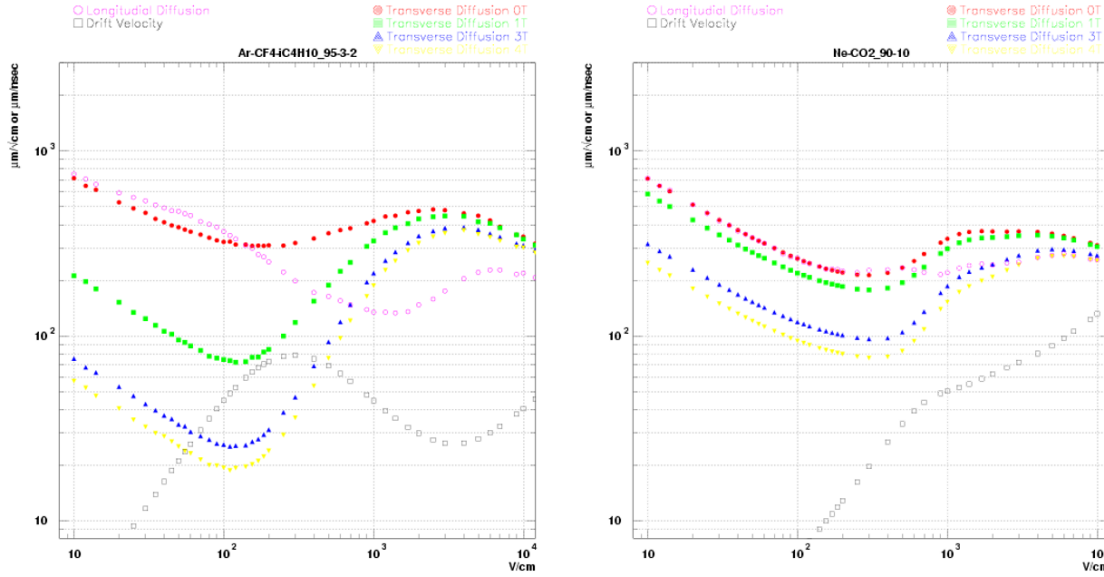


**Figure 4.39:** Comparison of the electron transport properties of T2K gas ( $Ar:CF_4:iC_4H_{10}$  95:3:2) and ALICE gas ( $Ar:CO_2$  90:10).

effective voxel occupancy of T2K gas is more than twice that of ALICE gas. For heavy ion collisions with embedded high momentum Jets, this might be a significant limiting factor to the detector performance. Furthermore a significant limiting factor for TPC operation at high rate is ion feedback. Selecting a light dominant noble gas (*e.g.* Ne instead of Ar) can increase the ion mobility by factors approaching 10X. STAR (Ar-based) is dominated by space charge from the primary ionization. After upgrade ALICE will have positive ion feedback from the ungated avalanche stage, but not from the primary beam. To first approximation, if we were to use an Ar-based (low ion mobility) gas we would encounter both the primary ionization load and the ion back flow load.

As stated earlier, we have concentrated this far on T2K gas and ALICE gas as two extreme choices. Figure 4.40 shows two different Neon-based gas choices with difference choices of quench ( $CF_4$  vs.  $CH_4$ ). Both of these combinations have a reasonably flat velocity curve near the diffusion minimum and would require a rather low central membrane potential ( $\sim 10$  kV), reasonable drift velocity, and a diffusion value that is enough to ensure good charge sharing for all drift lengths. Among the parameters plotted here, both would appear to be superior to the ALICE gas, with the edge going to the  $CH_4$  mixture. This last one is effectively the STAR gas with the argon swapped for Neon.

An additional, but critical parameter regards the ion mobility in the TPC gas. Positive ion transport through a gas follows the form:

$$v_{ion\ drift} = KE \quad (4.5)$$

where K is the ion mobility (typically in units of  $\frac{cm^2}{Volt \cdot sec}$ ) and E is the applied electric field. Since the prior expression is dependent upon the number density of the gas, it is frequently

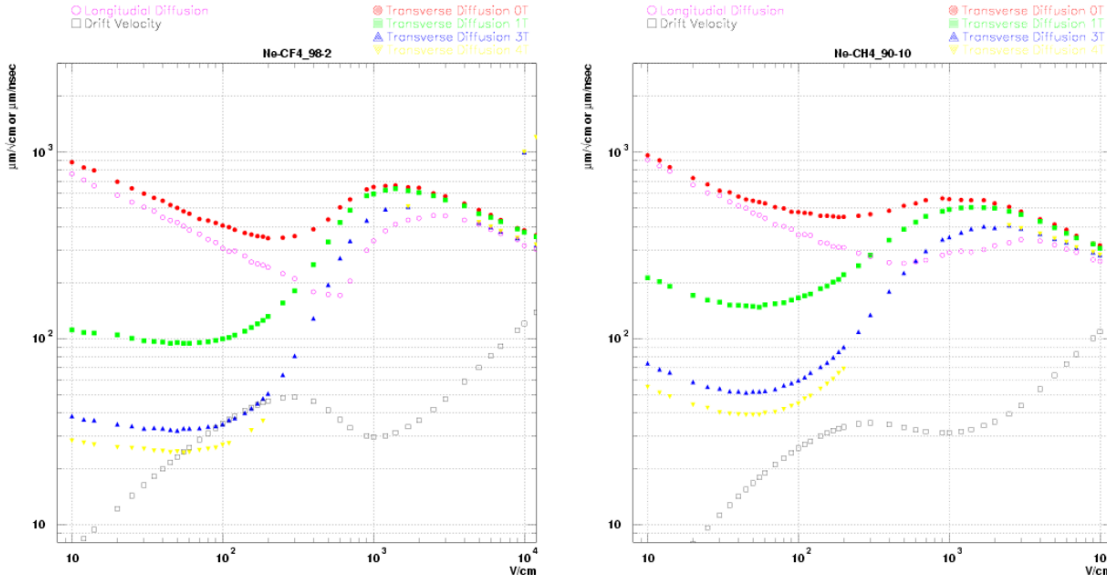


**Figure 4.40:** Alternative gas choices that may be better compromises for sPHENIX.

rewritten in terms of a reduced mobility  $K_0$  and a field/number density  $\frac{E}{N}$  in units of the Townsend (Td). For reference, room temperature gasses have 1 Td equating to  $E = 250 \frac{V}{cm}$ . Although the ion mobility does indeed vary with applied field, it is typically flat until  $\sim 10$  Td, which is far in excess of any drift field we would consider for the TPC. Therefore, the ion velocity will be proportional to the applied electric field, which should be as high as possible to minimize space charge effects.

Ion velocity in mixed gasses is a well understood phenomenon and follows Blanc's Law for which:

$$\frac{1}{K_{TOT}} = f_1 \frac{1}{K_{11}} + f_2 \frac{1}{K_{22}} \quad (4.6)$$

in exact analogy to resistors in parallel. This was shown for Argon mixtures in 1977 by Charpak and Sauli and measured more recently for neon mixtures as illustrated in Figure 4.41. Since the TPC gas is likely to be dominated by the noble gas component, it is interesting to compare the ion mobilities for three pure noble gases as shown in the table below.

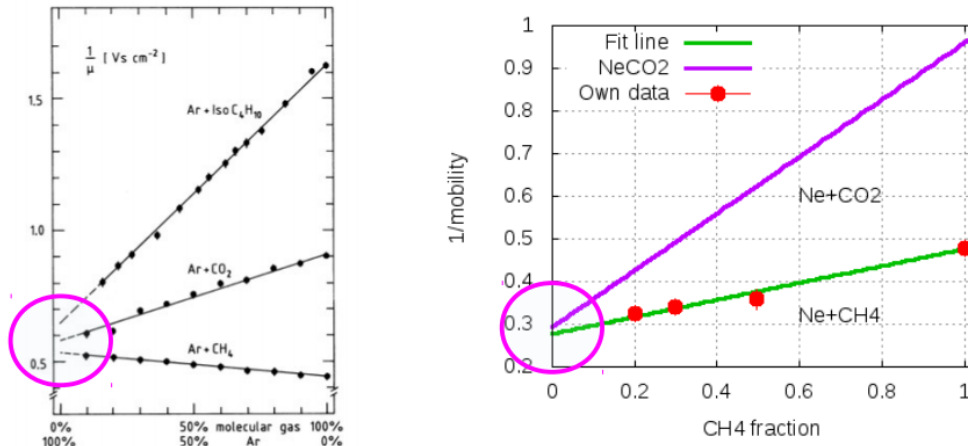


**Figure 4.41:** Inverse ion mobility as a function of gas fraction demonstrating Blanc's Law.

Gas	$K \left( \frac{\text{cm}^2}{\text{Volt} \cdot \text{sec}} \right)$	$v_D \left( E = 130 \frac{\text{V}}{\text{cm}} \right)$	$v_D \left( E = 400 \frac{\text{V}}{\text{cm}} \right)$
Ar	1.51	196	604
Ar-CH <sub>4</sub> 90:10	1.56	203(STAR)	624
Ar-CO <sub>2</sub> 90:10	1.45	189	582
Ne	4.2	546	1680
Ne-CH <sub>4</sub> 90:10	3.87	503	1547
Ne-CO <sub>2</sub> 90:10	3.27	425	1307(ALICE)
He	10.2	1326	4080
He-CH <sub>4</sub> 90:10	7.55	981	3019
He-CO <sub>2</sub> 90:10	5.56	722	2222
T2K	1.46	190(ILC)	584

It is clear that the space charge issues in STAR and ALICE are of an entirely different nature. In STAR, the ion mobility is low enough that the positive argon ions from the primary charge generate track distortions. In ALICE, both the noble gas choice (Ne instead of Ar) and the high drift field, dramatically reduce the distortions due to the space charge from the primary ionization. After upgrade, ALICE will struggle primarily with the ion back flow from the amplification stage. For sPHENIX, we should choose to avoid corrections from both these contributions and therefore we are driven toward Ne or He as the noble gas, and the use of a strong drift field.

## TPC fab

Because of the size of the TPC, the fabrication of all parts could, in principle, be accomplished at any of our collaborating institutions worldwide. That said, it would nonetheless be simplest if the field cage assembly was done locally, with smaller parts made around the world. This model proved quite effective in building the PHENIX Hadron Blind Detector,

wherein the individual parts were manufactured at the Weizmann Institute of Science in Israel, and the assembly was accomplished at Stony Brook University.

Because of the need to maintain active area to the largest radius, our designs for the TPC field cage and gas enclosure will be biased toward the thinnest of robust designs. Thus, the STAR and ILC field cage designs are the most appropriate as models for our work. Those devices were manufactured using large mandrels upon which layers of flexible circuit card and honeycomb were applied. Each mandrel is designed to release by "collapsing" to smaller radius after the TPC shell is cured, thereby releasing the shell. The completed shells are then outfitted with aluminum spoke-like end caps and a central membrane to form the completed field cage. We intend to design the field cage to safely hold the highest potential currently under investigation (ALICE gas  $\sim 37$  kV).

The open ports between the spokes of the end caps will be filled with "mechanical blank" modules to allow the field cage to become gas tight during the prototyping stage. This will allow full testing of the high voltage stability of the field cage without any of the gain stage modules in place.

During the prototyping stage, single items of the prototype gain stage module will be built. Because of the finite size of these units, there is a list of institutions that are capable of prototype construction, including Weizmann, Stony Brook, BNL, Yale, Wayne State, and UT. All of these institutions have past experience in the PHENIX HBD construction, or in the ongoing construction of the inner TPC layers for the ALICE upgrade. We envision two full sized prototypes whose design is driven by results from our ongoing TPC gain stage R&D, which has been funded by the EIC R&D program. As described below, we have already garnered extensive experience in multiple gain stage technologies, as well as a number of clever readout scheme applications.

The so-called "pre-production prototype" will be the third and final stage of full sized prototype construction. Barring any discovered deficiencies, "production" would involve the manufacture of the remaining gain stage modules as well as spare units. As with the prior work, it is likely that much of this effort will take place "off site" from the location of the field cage itself, with working modules shipped via clean, dust-free packaging.

## TPC Electronics

The TPC is assumed to have 30 cm inner radius and 80 cm outer radius, resulting in a cross-section in the radius direction of  $5500 \text{ cm}^2$  ( $\equiv 550000 \text{ mm}^2$ ) per side. With the pad size of  $6 \text{ mm}^2$ , there are  $\sim 90\text{k}$  readout channels on each side, or  $\sim 180\text{K}$  channels in total.

The ALICE TPC at the LHC is to read out continuously at 50 kHz in Pb+Pb collisions, a reasonable match to requirements at RHIC. Figure 4.42 shows the block diagram of signal processing based on the ALICE TPC upgrade electronics. Starting from the end of the signal processing chain, the Data Control System (DCS) and online farm is the computer system where the data are stored and processed for analysis. The LTU provides the timing

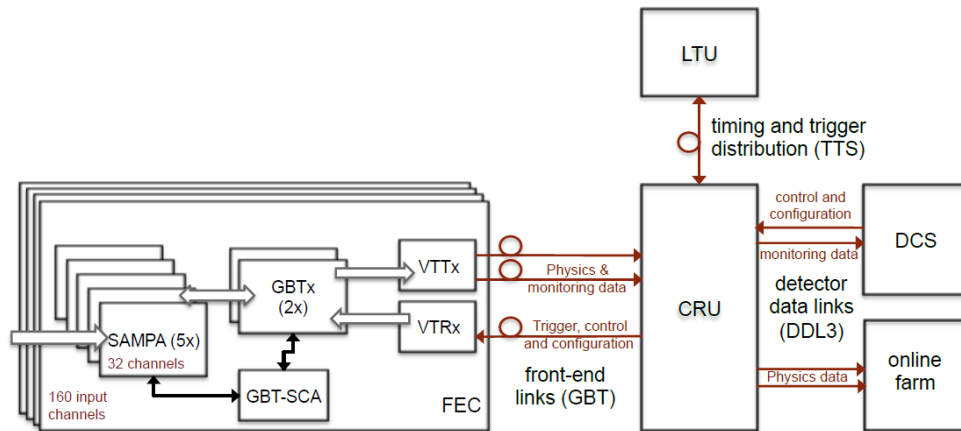


**Figure 4.42:** Block diagram of signal processing for ALICE TPC upgrade

and trigger signal to the Common Readout Unit (CRU), which is the post-processing system where some online calibrations and event reconstruction are performed.

The Front End Card (FEC) consists of SAMPA chips which amplify and shape the analog signals and digitize them. The DSP (data processing unit) is also on the chip. This formats the digital data into a data packet (it also performs baseline suppression, i.e., zero-suppression of the raw data). The packet is then sent to GBTx followed by VTTx. They convert the data packet into optical signals. In the PHENIX case, DCM-II is defined as the destination of the data to be sent optically. Since, we don't perform calibration or reconstruction online, we wouldn't need CRU as long as the data format for DCM-II is simple enough that the DSP can fully handle it.

The block diagram of the SAMPA chips is shown in Figure 4.43. In the ALICE design, there

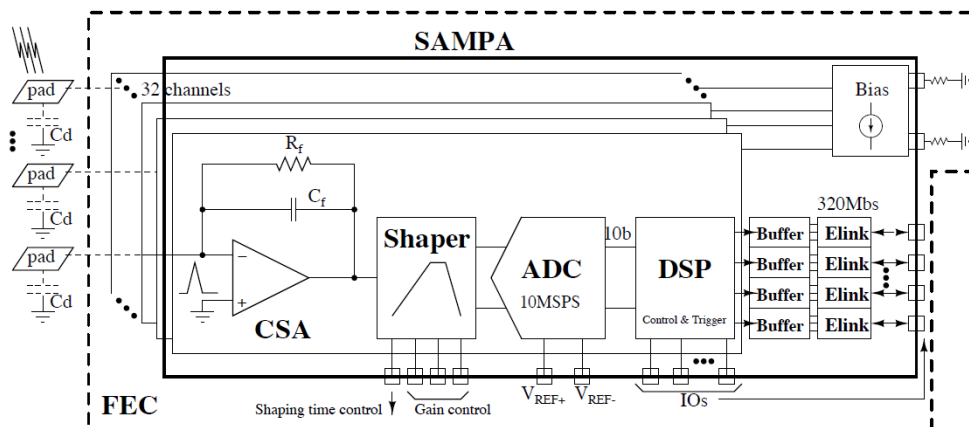


**Figure 4.43:** Block diagram of ALICE SAMPA chip

will be 5 SAMPA chips multiplexed by 2GBTx ASICs. One SAMPA chip accepts 32 inputs, therefore one FEC can process 160 inputs. The ALICE TPC will have 121 FECs per readout

segment module. The TPC will be equipped with 18 segments in each side, 36 segments in total. It should be noted that the simple math using the number of FECs, segments and channels per FEC doesn't give the 550K channels of electronics that ALICE claims to need. We don't discuss this here, since it is not relevant for the estimation of our needs for electronics. We show the FEC block diagram designed by the ORNL group in Figure 4.44, and the actual connection scheme to the TPC in Figure 4.45. The cables from TPC to the

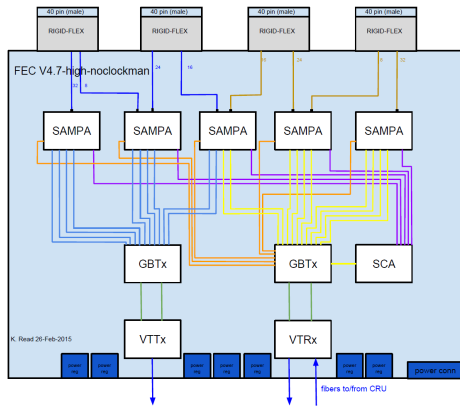


**Figure 4.44:** Conceptual Board Schematics of ALICE TPC FEC

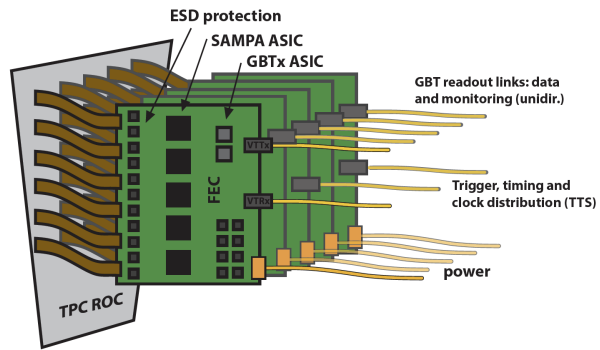


**Figure 4.45:** Installation image of ALICE TPC FEC to TPC

FECs are part of the connector on the FECs. So, we don't need to prepare additional signal cables for this purpose. Therefore, once the FEC is designed and fabricated with the optimal form factor that fits to the TPC, the only remaining off-board parts are power supplies and their cables, and optical fibers to DCM-II. The power supply that ALICE chose is Wiener PL 500 F12. One power supply can take care of two readout segments, which is 242 FECs as shown in the diagram in Figure 4.46. ALICE needs 18 of them + 1 spare, but we need only 6 of them + 1 spare. The picture of the power supply itself is shown in Figure 4.47. We learned that the cables for connecting the FECs and the power supplies are provided by CERN, and the cost is not known. We have to estimate the cost ourselves for our TPC case, but we expect that the cost is negligibly small compared to the FECs or the power supplies themselves.

Based on the difference between the number of channels between the ALICE case and our case, without taking the contingency into account, the cost for 200k channel electronics for our TPC will be ~\$2-2.2M. There is still uncertainty on the time scale on the SAMPa chip development, and this will affect our FEC development. If the SAMPa chip development will be significantly delayed, we may consider taking the old ALICE TPC electronics scheme; design the FECs with PASA and ALTRO chips, which basically splits the functions to be integrated into the SAMPa chip. Another concern is the optical readout module. ALICE uses a rad-hard optical module which is a common device throughout the LHC experiments. sPHENIX could use a commercially available optical module if it meets the requirements for the radiation conditions at RHIC. We will investigate this option because it would likely reduce the cost.



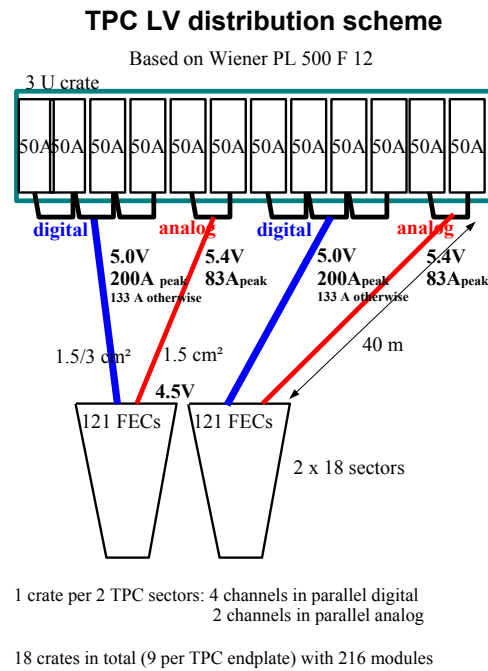


**Figure 4.46:** Diagram of power supply for ALICE TPC FEC



**Figure 4.47:** Power Supply module, Wiener PL 500 F21, employed for ALICE TPC electronics.

### TPC cooling and cabling

Our cooling requirements for the TPC electronics will be significant. Although we are only cooling  $\frac{1}{2}$  as many channels as ALICE, these channels are distributed over only  $\frac{1}{10}$  as much surface area. Therefore the power required from our cooling plant will be smaller overall, but we will need to design for very effective heat transfer to the cooling lines.

Figure 4.48 shows the configuration of the cooling plant currently in use by the ALICE



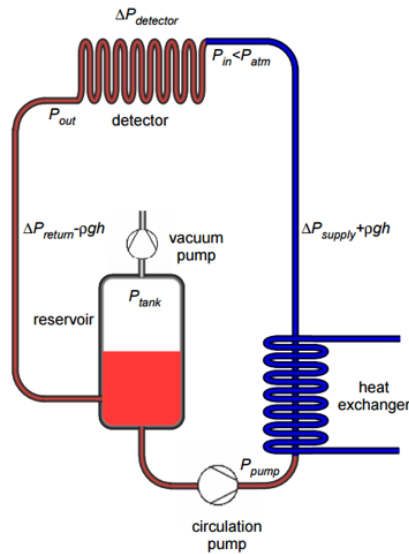


**Figure 4.48:** Diagram of the cooling plant in use the the ALICE TPC. The cooling plant is an under pressure system so that any leak results in gas bubbling into the coolant rather than coolant dripping into the detector.

experiment. The key feature of this cooling plant is that the coolant is delivered at pressures below one atmosphere so that in the event of a leak, gas is introduced into the coolant rather than coolant introduced into the gas. The ALICE resistor chains dissipate a significant amount of power (8W in each of 4 resistor bars). Higher power in the resistor chain is driven by the need for robust performance in the face of stray currents due to nearby ionization. Although the track density in sPHENIX and ALICE are very similar, the charge load onto the ALICE TPC frame is much higher. Among STAR, ALICE, and ILC, only ALICE water cools their resistor chain. Since our power dissipation will be the least of these three applications, we are safest to not water cool the resistor chain, and thereby preclude from the outset the risk of water leaking into the chamber.

The cable plant for the TPC includes a pair of shielded coaxial high voltage leads whose diameter will be under  $\frac{1}{2}$ " (e.g. Dielectric Sciences 2125: 100 kV;  $\varnothing$  0.4"). Each sector will receive bias for the GEMstack as 8 independent voltages. The readout cards, will receive DC power input, optical connections for slow control and optical connections for data output. To the extent possible, this significant cable plant will be localized so as to align with the end cap spokes, to minimize the radiation depth for the end cap detector systems.

#### Pixel/TPC installation and calibration

The assembly order for sPHENIX specifies that the "Tracker Barrel" assembly will be inserted from the end after the calorimeters have already been installed onto the magnet. Although the utility of all the sPHENIX calorimeters leading into the Electron-Ion Collider era is clear, the tracking situation is less clear. This distinction is one of the reasons why

multiple tracking solutions are currently under consideration. The TPC/MAPS solution is currently considered as the optimal choice for the EIC due both to minimal radiation length and excellent hadron-ID capability at low momentum. However, to retain future flexibility and simple upgrade capability, the tracking systems, regardless of inner details, will be mounted to an external space frame. This space frame will carry the load of the tracking detectors, and define the so-called Tracker Barrel.

TPC calibration will be achieved using a laser system, similar in philosophy to that used by STAR and prototypes for the ILC. Because the work function of aluminum is low, a UV flash will release electrons. Both the STAR TPC and the ILC TPC prototype used a pattern of aluminum applied to the central membrane to produce these reference tracks. The pattern used by STAR consists of lines shown in Figure 4.49, whereas that of the ILC was a pattern of dots. The laser system will not only provide an initial reference calibration, but can be fired at regular intervals (PHENIX fires their EMCAL laser at 1 Hz) during data collection to provide a continuous calibration of the drift velocity and space charge distortions. Gain calibrations can be roughly estimated using cosmic rays, but final calibration will use collision data.



**Figure 4.49:** Photograph of the central membrane of the STAR TPC. The pattern of Aluminum strips is used to release electrons via laser flash as a calibration signal.

### Justification of Design Choices

The basic geometry of the sPHENIX TPC is driven by several factors. As is typical for cylindrical collider detectors, the division between the "barrel" acceptance and future endcap upgrades is located at  $\eta = \pm 1$ , as enforced by the existing BaBar coil. The radial

extent of the TPC is driven differently on the outside and inside surfaces. Both the inner and outer walls will have two layers:

- The "field cage" defines the active volume of the detector.
- The gas enclosure defines the physical size of the detector and its coupling to other parts of the spectrometer.

At the outer radius, the location of the gas enclosure is defined by the surrounding systems. Currently the EMCAL inner radius is 90 cm. Furthermore, we envision adding some hadron ID capability as we upgrade the spectrometer for use at the future electron-ion collider. Some devices (e.g. the BaBar DIRC or ALICE-like HMPID) would fit within 10 cm and so we currently constrain the outer TPC gas enclosure to  $r = 80\text{cm}$ . The outer radial extent of the tracking volume itself will depend upon the exact design of the field cage and would then be less than 80cm.

Contrarily, the inner radius is defined by the inner tracking volume. Possible interference between the TPC inner gas enclosure and a 2-3 layer vertex pixel detector is a loose constraint. The driving factor in locating the TPC inner field cage is the radius at which the TPC begins to track with high efficiency. Currently we are taking the inner field cage radius to be 30 cm. This figure is a compromise between being safely outside of the vertex detector, maximizing the length of the measurement, and experiencing particle densities similar to those at the inner portion of the ALICE TPC.

The pad size, gas choice, avalanche technology, gas gain, and central potential of the TPC are facets of a single optimization problem necessary to define the best design. Furthermore, these parameters must be correctly matched to the electronics by having the charge collection time less than the amplifier shaping time. All of this must be optimized not only for momentum resolution but also excellent two-particle response for closely spaced tracks. Despite this complexity, we can constrain the design well enough to demonstrate its feasibility in at least one incarnation.

The driving characteristic of the TPC performance is that it should have momentum resolution sufficient to cleanly separate the  $Y$  1s, 2s, and 3s states. As shown in the discussion on simulations, mass resolution performance exceeding that of the specification is achieved through forty radial measurements, each of  $\sigma \sim 120\text{ }\mu\text{m}$ . Pixels of full-width  $a$ , measure position with a resolution of  $\sigma = \frac{a}{\sqrt{12}}$  (less than  $\frac{a}{3}$ ). Charge division between neighboring cells of pitch  $a$  typically measures position to better than  $\frac{a}{10}$ . Thus, an appropriate pixel size is 1.2 mm around the azimuth and 1 cm in radius. This leads to a total channel count summed across both readout ends below 250,000.

Traditionally, TPC devices were described as "low rate" detector elements, as defined by the long single event collection time and the need for "gating" to prevent positive ion buildup within the TPC gas volume. Both of these arguments have become obsolete in recent years. Traditional calculations assumed that an event would be lost if a second event occurred within the readout time. If we were to use the "slow" gas of the ALICE

detector ( $Ne - CO_2$  90-10;  $v_d = 30 \frac{\mu m}{ns}$ ), an 80 cm drift would correspond to a full drift time of  $26 \mu sec$ . At a 15kHz collision rate, this would put a second event in the readout time window with a probability of  $\sim \frac{1}{3}$ . In recent years, it has been realized that because the TPC measures trajectory by time, it is naturally able to distinguish overlaid events via their apparent displaced event vertex. As an example, the ALICE upgrade is designed to have their TPC, with more than  $80 \mu s$  drift time, measuring collisions at rates up to 50 kHz! The key to this revolution is the development of electronics that dismisses the concept of a single event and instead simply reads out the TPC continuously over time. The net result for sPHENIX is that by using this same readout principle, for all reasonable gas choices, the "speed" of the gas will never be an event rate limiting factor. Gas speed requirements are bracketed by the competing goals of minimizing particle pileup within an event (wherein slower is best) and minimizing event pileup (wherein faster is best). The advent of continuous readout electronics shifts the balance away from faster gasses and toward slower gasses.

The second consideration is "gating" the TPC. Avalanche of the primary charge necessarily produces a large quantity of positive ions. Introduction of all these ions into the TPC volume would distort the electric field to the point that the TPC could no longer function. Because drift speeds of ions are dramatically slower than electron drift speeds, the time to neutralize these ions generates a "dead interval" for the TPC. Although schemes for fast flush of the positive ions have been developed, most of the R&D on TPC readout currently involves using Micro Pattern Gas Detectors (MPGD) as these can be configured to reject  $\sim 99\%$  of the positive ions, allowing the TPC to remain live at all times.

Figure 4.50 shows the characteristics of the  $Ne - CO_2$  gas mixture used by ALICE. The best single point resolution is achieved by using a drift field that simultaneously minimizes the diffusion and also resides at a plateau in drift velocity. No such plateau exists for  $Ne - CO_2$  and so the operating conditions for this gas would be defined merely by the diffusion, implying a drift field of  $400 \frac{V}{cm}$ , with a transverse diffusion of  $150 \frac{\mu m}{\sqrt{cm}}$ , longitudinal diffusion of  $220 \frac{\mu m}{\sqrt{cm}}$ , and drift velocity of  $30 \frac{\mu m}{nsec}$ . Note that these values are not read off the graph, but taken from ALICE wherein they have also added 5%  $N_2$  to the gas mixture to improve voltage stability. Note also that the lack of plateau in drift velocity requires the TPC to have a highly uniform electric field, thereby placing tight constraints on the field cage design.

Traditional wire chamber TPC designs image the positive ion cloud around the wire onto a segmented pad plane. Thus, the spread of the charge as compared to the pad segmentation is controlled by the wire-to-pad gap. Using MPGD readout, the electron cloud itself must be spread wide enough to allow for charge sharing among multiple pads for every avalanche. This is an extreme challenge for ALICE because of their large pad size ( $\sim 4mm$  in azimuth). Their saving grace is the large amount of diffusion due to the long drift distance and purposeful "hole misalignment" among the GEM-based avalanche scheme. For sPHENIX, the job is simpler. Accounting for a hole-induced charge spread of  $\sim 400 \mu m$ , we can add this in quadrature to the diffusion induced charge spread to find that charge

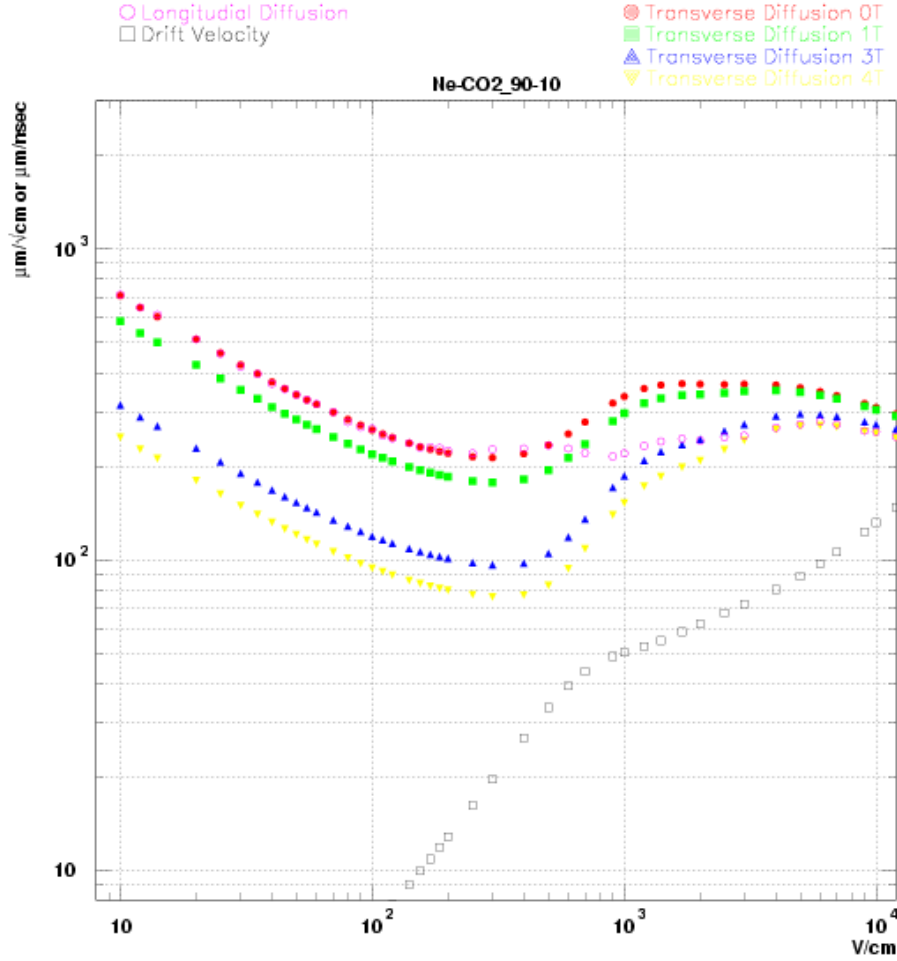


**Figure 4.50:** Calculated drift characteristics of  $Ne - CO_2$  gas (same as used by ALICE).

clouds will have width in the range  $400 \mu m < \sigma < 1400 \mu m$ , which is ideally matched to the proposed segmentation. Furthermore the longitudinal diffusion will induce a time spread in the farthest signal ( $\frac{\sigma_{long}}{v_d}$ ) of less than 70 nsec. The SAMPA chip is designed with a minimal shaping time of 190 nsec, meaning that our signals will have the same characteristic shape independent of drift length (an ideal feature). Finally, as shown in the later sections we are considering a chevron or “zig-zag” shape for our pads which should not only improve the resolution beyond  $\frac{a}{10}$ , but also ensure good charge sharing for all avalanches, including the narrowest we envision.

Although we have shown that “ALICE gas” would have performance that would satisfy all design criteria, it is likely that further study will reveal even better choices. A more detailed discussion of other gasses is included below.

#### 4.7.4 TPC Tracker R&D

##### Overview

R&D for the development of new gas-based detectors is very active around the world. In addition to the aforementioned efforts on upgrades to ALICE and design of the TPC for the ILC, both ATLAS and CMS have taken new gas detector designs to an advanced stage. The principle development has been the invention of the Micro Pattern Gas Detector or MPGD. Both of the two basic MPGD technologies (GEM from Sauli and  $\mu$ MEGA from Giomataris) had successful applications in the COMPASS experiment. The PHENIX HBD pioneered a very unique GEM application using evaporated coatings of CsI to create a large area gaseous UV photon detector. ATLAS plans include large ( $1 \times 2 \text{ m}^2$ )  $\mu$ MEGA chambers and CMS plans to use large GEM chambers as part of their upgrade to higher luminosity running.

Several years ago, BNL began hosting the EIC R&D program, which has had active participation from many institutions with diverse historical backgrounds. Much of the EMCAL R&D work discussed in later chapters was performed under the guise of the so-called "Calorimeter Consortium" from within the EIC R&D program. The calorimeter consortium features leading contributions from both STAR (UCLA) and PHENIX (BNL) institutions. Even prior to the formation of the calorimeter consortium, the "Tracking and PID Consortium" (aka RD6) formed and also featured broad support from institutions with varied historical backgrounds: Stony Brook (PHENIX), BNL (PHENIX), Yale (STAR), University of Virginia (JLab: Hall A), and Florida Institute of Technology (CMS). All these institutions are also members of the CERN RD51 Collaboration which is dedicated to the development and advancement of MPGD technology. Furthermore, our Yale collaborators have been central figures in the R&D leading to the designs utilized for the ongoing ALICE TPC upgrade.

In this section, we will give an overview of the relevant R&D that we have conducted to date and an outlook for how this research will continue toward the development of the TPC detector. This discussion will necessarily be an incomplete summary of RD6, since that research has broader goals beyond TPC development (forward planar GEM trackers, GEM-based RICH, ...).

##### Recent R&D Efforts

BNL and Yale maintain joint custody of an apparatus designed to characterize gas properties as shown in Figure 4.51. Electrons liberated by either a laser source (measured time  $\rightarrow$  measured velocity) or  $^{55}\text{Fe}$  photon conversion (known energy) follow the vertical drift tube and generate signals at the base (mostly via GEM-induced avalanche). Some of the results from these measurements are summarized in Figure 4.52. Most of these measurements focus on Ne-based mixtures, as is appropriate for a TPC in heavy ion collisions where space

charge is a concern. Among the many results, the  $Ne - CH_4 - CO_2$  mixture is especially intriguing since it not only exhibits a long plateau in drift velocity as a function of field, but it is among the gasses with the lowest probability of charge attachment.

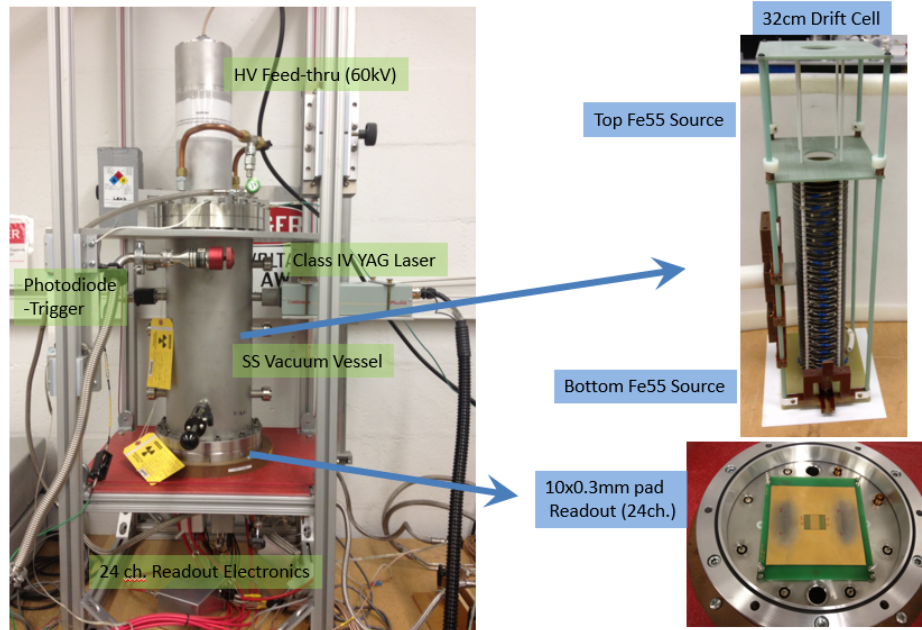


Figure 4.51: Apparatus used to measure electron drift velocities and electron attachment.

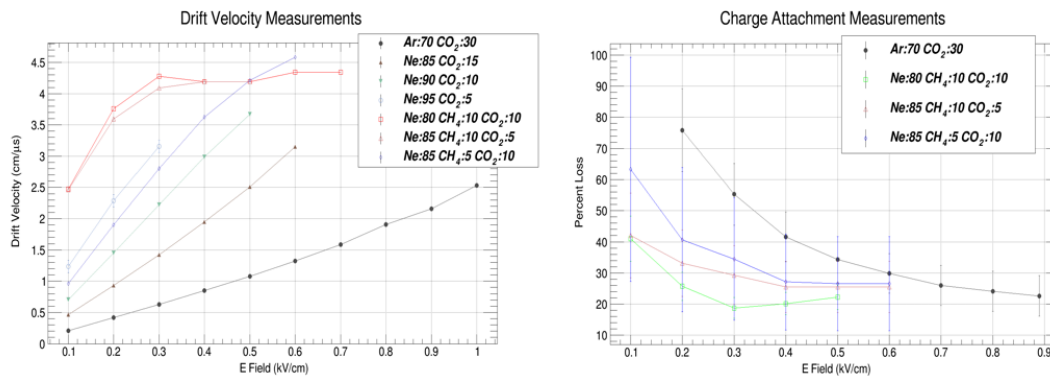
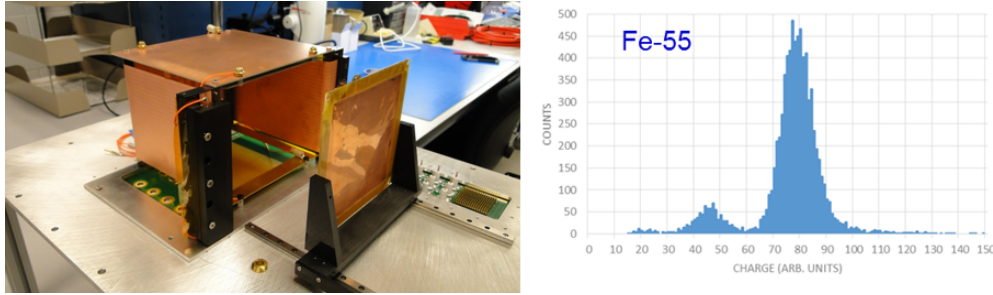


Figure 4.52: Results for drift velocity and electron attachment in a variety of gasses.

These gas results and **extensive** ANSIS field calculations lead to the design of the small prototype TPC shown in Figure 4.53. This TPC has a unique feature in that it combines the typical drift volume of all TPCs with a wire-mesh wall on the particle exit face of the cube. Behind the wire mesh is a CsI GEMstack that will allow this "TPC/HBD" hybrid device to measure not only the trajectory (momentum),  $\frac{dE}{dx}$  (hadron ID), but even the generation of cherenkov light (electron ID). The result on the right shows that this device has excellent energy resolution ( $\frac{dE}{dx}$ ) since the width of the  $^{55}Fe$  peak is not significantly broader than the statistical fluctuations intrinsic to the primary charge. This prototype is not only used to



test possibilities for cherenkov light detection, but it is additionally used to evaluate the performance of various options for the readout plane segmentation.



**Figure 4.53:** Photograph of the TPC/HBD prototype along with a measurement of the  $^{55}\text{Fe}$  energy deposit spectrum.

The TPC prototype is presently equipped with a readout pattern similar to that described in Figure 4.34. This shape of pads significantly improves the position resolution of the device at the cost of a small, but correctable differential non-linearity. The result shown in the upper left corner of Figure 4.54 shows the comparison between the reconstructed position of a precise ionization source and that reconstructed by charge sharing. The regular structure of this correlation, with a period equal to the pad pitch is an indication of the level of differential non-linearity induced by the chevron design. By quantifying the difference between the true position and that from the reconstruction as a function of the reconstructed position, we determine the correction that must be applied to data. The result of applying this correction improves the measurement to a precision of  $\sigma = 99 \mu\text{m}$ , exactly as needed for the final TPC device.

The item of central and critical importance in designing the TPC will be handling the Ion Back Flow (IBF). MPGD-based gain stages (along with streaming electronics), are the principle advance that make a TPC into a high collision rate device. These techniques are new and require extensive R&D. Although ALICE considers the R&D phase of their TPC upgrade (up to the stage of technology choice) to be complete, our R&D plan allows us time to improve further upon these plans and benefit from their experience. Figure 4.55 shows a schematic of the Yale apparatus used to perform the ion back flow measurements. This particular figure shows the configuration used to measure the so-called "hybrid gain stage" solution that features a microMEGA plane preceded by a two stage GEMstack.

Figure 4.56 shows the results for IBF as measured for the hybrid gain stage. The vertical axis denotes energy resolution, the sigma for the main  $^{55}\text{Fe}$  peak over its mean. This measurement is lower-limited to the natural width of just below 10%, driven by the statistics of the primary ionization. The horizontal axis shows the level of ion back flow measured at a gain of 2000. Nearly all gases behave in the same manner, tracing out a banana shaped curve. The reason for this shape is simple. In any multi-stage avalanche process, statistical fluctuations in the first stage of amplification generate the limiting resolution. Therefore making the initial GEM gain as high as possible yields the best energy resolution. That said, ions resulting from the first stage of avalanche are perfectly



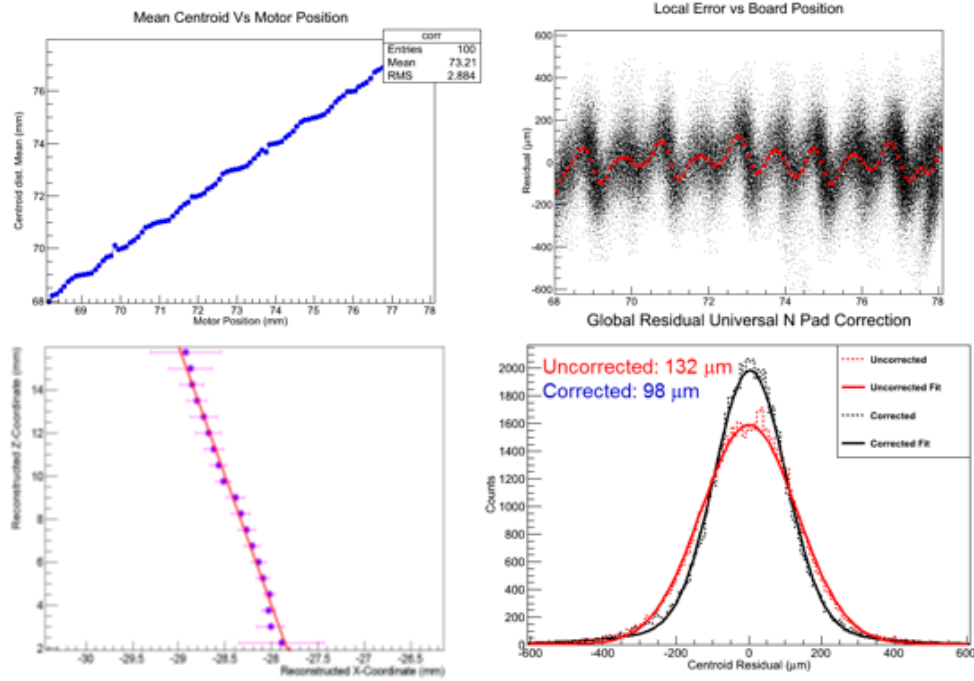


**Figure 4.54:** Measurements of the differential non-linearity of chevron pad response and demonstration of the resolution achieved after correction.

coupled back into the TPC volume. The band is formed by smoothly changing the fraction of the gain carrier by the first GEM; high gain in the first GEM optimizes resolution, while low gain in the first GEM optimizes IBF. It is worth noting that these results are, in fact, significantly better than the final design chosen by ALICE. Because the running conditions might drive the balance between energy resolution and ion feedback to different optimal points (e.g. optimize  $\frac{dE}{dx}$  resolution for EIC and optimize IBF for Au+Au collisions), it might be worthwhile to adopt a HV solution similar to ALICE wherein the voltage is supplied separately to each side of each GEM, allowing run-time decisions about the operating point along the banana curve.

Another intriguing option for dealing with IBF involves re-inventing the gating grid rather than eliminating it. A typical gating grid involves a single wire or mesh plane whose voltage decides whether it is transparent to both electrons and ions or opaque to both. Because of the very slow drift speed of the ions, the minimum time for the grid to be off after recording an event is often multiple hundreds of microseconds! Howard Weiman has proposed a new grid style in which the grid has many layers and the ion clearing time is not set by the full depth of the grid, but rather by the distance to the nearest layer. Using such a grid, one would leave it open for a significant time (until it filled with ions) and then briefly dump the ions prior to opening again. Initial estimates of such a structure indicate that it could nearly entirely eliminate ion back flow at the cost of a "duty cycle" of 80-90%. Using Garfield and ANSYS calculations, we have simulated designs for such a grid using both multiple wire planes and multiple mesh planes. These results are shown

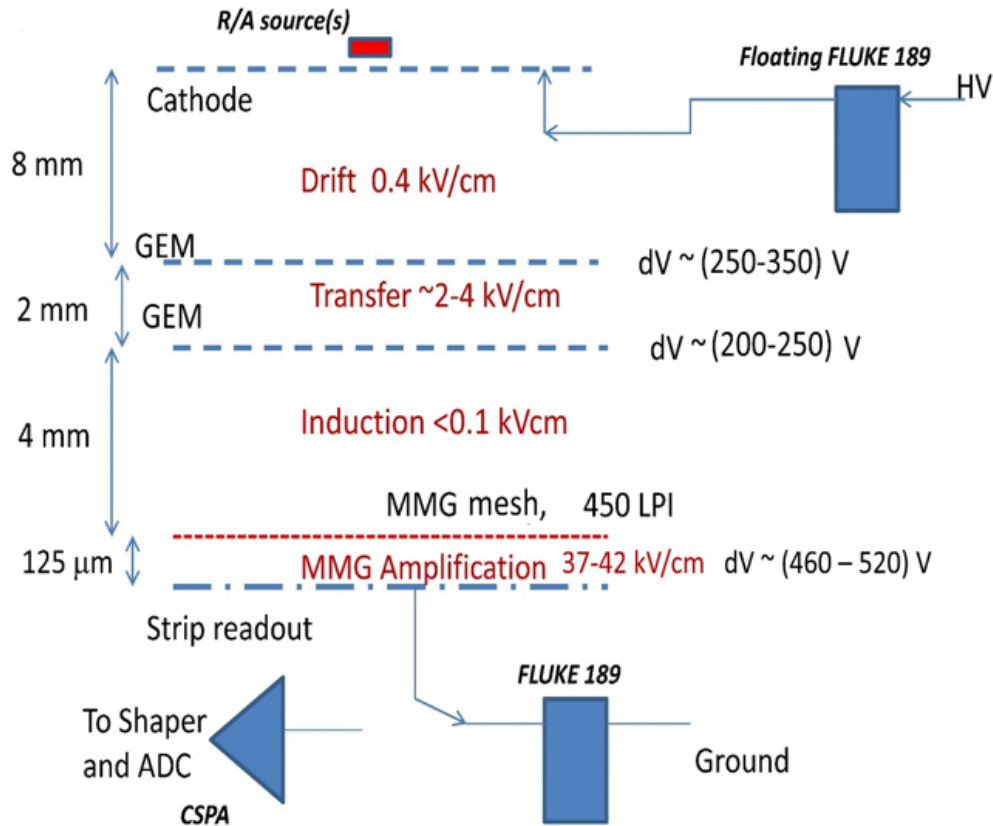


**Figure 4.55:** Ion back flow measurements for the ALICE upgrade were made by the Yale group (collaborators through EIC R&D) not only for the quad-GEM solution, but also for other alternative readout schemes. This figure shows their apparatus as setup for measurements of a hybrid gain stage utilizing two GEMs followed by a microMEGA.

in Figure 4.57. Indeed, the ion clearing time is reduced to 10's of microseconds, but there is a long tail due to ions starting in low field areas within the grid structure. The net result with the currently calculated grid design exhibits a long tail, meaning that more clever designs would be necessary to achieve an IBF of exactly zero, characteristic of old-style gating grids.

Although PHENIX collaborators who worked on the PHENIX HBD, have gained extensive experience with GEM avalanche devices, these GEMs were roughly the same size as a standard sheet of paper. Challenges are certain as GEMstacks become larger. Shown in Figure 4.58 is a picture of the GEM chamber that we took to test beam in October 2013. At the time, this device (designed and built by our U. Va. colleagues) was among the largest GEM chambers yet built. At that same test beam an equal sized chamber designed and built by our Fla. Tech. colleagues was tested as well. Both chambers worked flawlessly with the U. Va. chamber producing a resolution below  $80 \mu\text{m}$ . Note below, the new ideas from WIS, will be investigated for "tiling" a large area with self-supporting GEMstack structures.

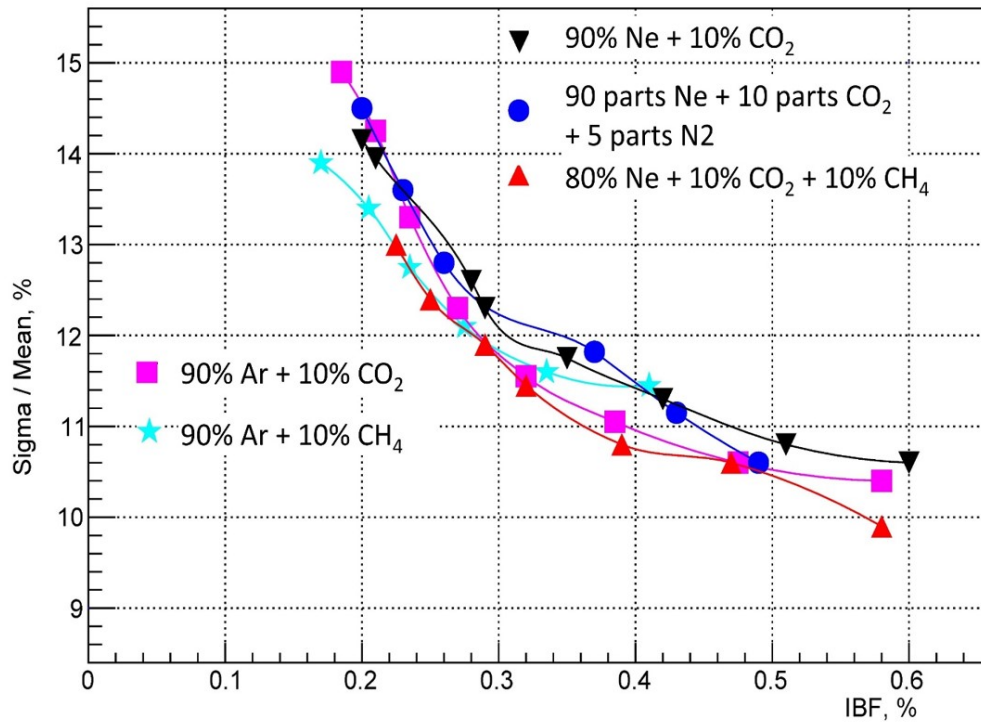


**Figure 4.56:** Resolution of the hybrid gain vs ion back flow percentage.

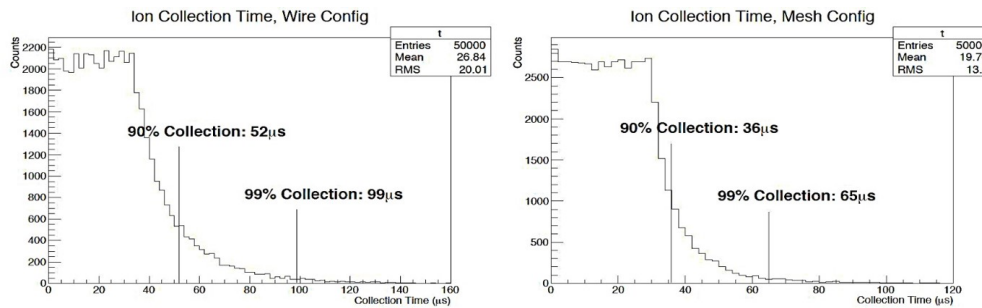


**Figure 4.57:** Ion clearing times in the stacked grid scheme.

### TPC electronics R&D plan

Currently, we are following the R&D plan for ALICE TPC electronics, namely, prototype version 1, pre-production prototype and the final production. The first version prototype should meet the schedule for second prototype of TPC development with which we should do the beam test with high multiplicity events.

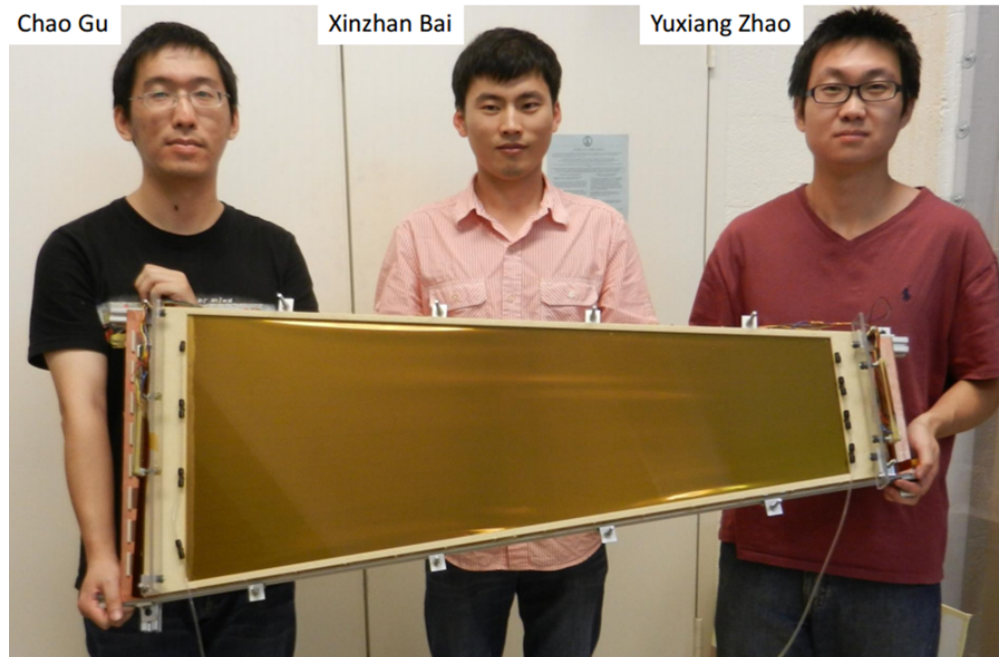


**Figure 4.58:** The RD6 GEM detector shown here is among the largest GEM chambers yet built. It was tested at Fermilab test beam and yielded a position resolution of better than  $80\ \mu\text{m}$

### Steps to Project Completion

As compared to previous TPC devices used in heavy ion experiments, the sPHENIX TPC will be quite small. The STAR TPC has a radius of 2 meters, ALICE has a radius of 2.5 meters and sPHENIX will have only an 80 cm radius. Because the device is shorter than an average person, a variety of simplifications in the construction will result. Although, many of the typical issues are simpler to address than they were for the larger devices, there are nonetheless challenges. The principle design challenges involve maximizing the active volume in such a small device and developing a robust gain stage.

Both STAR and ALICE use an “air” gap ( $N_2$  for STAR and  $CO_2$  for ALICE) as the principle voltage gap between the high voltage center of the field cage and the protective ground shield. A principle advantage of an air gap is that the overall material thickness is minimal. In sPHENIX, we propose to use an air gap on the inner surface where the material budget is critical, but use a well designed solid gap (polyimide or  $FR_4$ ) on the outer gap where material budget is less of an issue, but active area is at a premium.

Although a significant R&D program (including research from ALICE and sPHENIX institutions) has shown in bench tests and beam tests the viability of the quad-GEM approach, it has yet to be realized in a working device. Furthermore, experience shows that scaling a small area GEM detector to full size can be fraught with difficulty. For these reasons we have embarked on a conservative plan to lead us through the prototyping

stages to full detector development with minimal risk.

## 4.8 Alternative technologies

The high multiplicity environment created by heavy ion collisions has driven technical solutions for tracking inside a radius of 1 meter toward two solutions, silicon and Time Projection Chambers. sPHENIX is considering both options as detector systems that could deliver the performance necessary to meet the sPHENIX physics objectives. Alternate established tracking solutions such as Multiwire Proportional Chambers or straw tubes are not suitable for the charged track densities that will exist inside the detector at  $R \leq 80$  cm during heavy ion running. However, though practical considerations drive us toward either an all-silicon or hybrid Si-TPC solution, there are still technical choices to be determined within both solutions. For instance, silicon sensors come in a number of forms, pixel, strip and pads, and within each sensor form there is a variety of implementations. The number of layers of pixels versus the number of layers of strips, the type of pixel or strip sensor, the geometric configuration of each sensor layer, and the electronics readout solution all have to be considered and optimized. Likewise with the compact Time Projection Chamber there are a number of important technology choices to be considered for the readout plane, gas enclosure and readout electronics. The choice of TPC gas and the method for TPC calibration also require study and a certain amount of R&D.

### Alternate TPC readout plane options

As discussed previously, we are currently investigating a list of possible alternate technologies for the readout plane. These alternatives include both the possibility of changing a classic gating grid to implement a prompt flush for positive ions (possibly resulting in a TPC with zero ion back flow, at the cost of adding a “duty cycle”) and variations of the scheme for the MPGD-based gas amplification stage. Already discussed is the ongoing work to implement a hybrid  $\mu$ MEGA/GEM detector that would benefit from the superior ion back flow characteristics of the  $\mu$ MEGA and achieve remarkable stability by lowering the  $\mu$ MEGA gain requirements via the assistance of the GEMstack.

A unique suggestion has been tested at WIS. In this case, small self-supporting hexagonal GEM stacks were developed that could be used to populate any large surface. These devices would feature the robust performance of smaller GEMs while still maintaining a nearly hermetic acceptance. The first results with the prototypes show high mechanical rigidity of the elements, not affected by the transfer electric fields.

Besides providing nearly hermetic acceptance the modular solution requires a large number of small GEMs that allow one to reduce the overall cost of the readout plane, but more importantly such an approach benefits from a very stringent quality control at the production stage that insures high gain and residual ion backflow uniformity across the

area of the reaction plane.

# Chapter 5

## Electromagnetic Calorimeter

### 5.1 Physics Requirements

The EMCal performance is central to the direct photon and upsilon measurements and it is also a key component, along with the hadronic calorimeter, of the calorimetric jet reconstruction. In this section the photon and upsilon requirements for the EMCal are discussed.

Direct photons and their correlation with jets are a unique probe of partonic interactions in the QGP. Photons can be the result of a hard scatter (for example  $gq \rightarrow \gamma q$ ). The photon, not carrying color charge, does not interact strongly with the QGP and thus provides a direct measure of the momentum transfer of the hard scatter itself that is accessible in the final state. This is in contrast to dijet systems where both jets interact strongly with the QGP. Direct photon measurements in heavy ion collisions are limited by the rate of the photon production and the efficiency and purity with which the photon can be identified. Therefore, the main requirements on the EMCal from photon measurements are on the size of the acceptance and the contamination of the photon candidate cluster by energy deposited near the photon from the underlying event. As illustrated in Fig. 1.21, the photon/ $\pi^0$  discrimination is not a driver of the calorimeter performance at the momenta of interest at RHIC.

The goal is to have the detector resolution and segmentation be compatible, rather than the intrinsic limitations on the electron cluster reconstruction due to the underlying event background in a central heavy ion event. A typical cluster size (a 3x3 tower array) contains about 340 MeV of underlying event energy in the EMCal (see Fig. 5.25). Using a typical Y-electron cluster of 5 GeV and the underlying event blurring to set the magnitude of the energy resolution leads to required resolution of approximately  $\Delta E/E \leq 15\%/\sqrt{E}$ .

For the Y, the EMCal requirements are driven by the need to reject hadrons by a matching condition between the track momentum and the EMCal energy. Hadrons misidentified as electrons will lead to an increased combinatoric background in the Y mass distribution. The

desire is to optimize the electron identification efficiency with respect to the pion rejection by the calorimeter energy matching condition. As in the photon case, central Au+Au collisions are the most challenging environment and drive the detector specifications. The physics requirement is to be able to have sufficient statistical precision to measure the suppression of the three  $Y$  states separately.

## 5.2 Detector Design

### 5.2.1 Design Requirements

The design requirements for the sPHENIX electromagnetic calorimeter are based on the physics requirements described in the previous section. The calorimeter will play a major role in both the measurement of jets and single photons out to high  $p_T$ , as well as identifying and measuring the energies of the electrons from  $Y$  decays. In addition, the calorimeter must fit inside the BaBar magnet and allow space for the tracking system that will reside inside the calorimeter. The calorimeter should also be as compact as possible in order to minimize the overall size and cost of the hadronic calorimeter. The basic detector design requirements can be summarized as follows:

- Large solid angle coverage ( $\pm 1.1$  in  $\eta$ ,  $2\pi$  in  $\phi$ )
- Moderate energy resolution ( $\leq 15\%/\sqrt{E}$ )
- Fit inside BaBar magnet
- Occupy minimal radial space (short  $X_0$ , small  $R_M$ )
- High segmentation for heavy ion collisions
- Minimal cracks and dead regions
- Projective (approximately)
- Readout works in a magnetic field
- Low cost

The requirement for large solid angle coverage is driven by the need to accumulate high statistics for measuring jets and single photons out to the highest  $p_T$  possible in an unbiased way using full jet reconstruction over the entire central rapidity region. The requirement for the energy resolution is determined by achieving the best resolution possible consistent with the contribution to the energy resolution from the underlying event in central heavy ion collisions. The energy from the underlying event also requires the tower size to be



small ( $\sim 1 R_M^2$ ) in order to minimize the background contribution for measuring the jet energy or the electron energy from  $Y$  decays. This then also determines the minimum inner radius of the calorimeter and the required level of segmentation. The current design places the inner radius of the calorimeter at 90 cm and has a segmentation of  $0.025 \times 0.025$  in  $\Delta\eta \times \Delta\phi$ , which leads to  $96 \times 256 = 24,596$  towers over the full rapidity and  $\phi$  range. Figure 5.1 shows the energy deposition in the sPHENIX calorimeter system as a function of the geometric position in the detector. In Figure 5.25, this is quantified in terms of the distribution of energy in single calorimeter towers and in  $3 \times 3$  tower sums for central Au+Au HIJING events. The average energy for the tower sum is  $\sim 340$  MeV.

The requirement for minimal gaps and dead regions is driven by the need to measure jets over a large solid angle with good uniformity. Gaps are particularly undesirable since they can lead to missing energy for the electromagnetic component of the shower.

Projectivity in two dimensions (2-D proj.) is desired for the upsilon program. With the one dimensionally projective (projective in  $\phi$  only, or 1-D proj.) calorimeter, the pion rejection at fixed electron efficiency degrades with increasing  $|\eta|$ , as electrons enter the calorimeter at increasing angles. The resulting shower is spread through a larger number of towers (Figure 5.22) and thus has higher contributions from the underlying event overlapping with the cluster, blurring the electron/hadron separation. At 70% electron efficiency the pion rejection degrades from a factor of 100 in the two dimensionally projective case to 60 for  $0.7 < |\eta| < 0.9$  (see the discussion of Figure 5.27). This results in an increase in the combinatoric background and a corresponding decrease in the statistical power of the upsilon measurements from that shown in Figure 1.18

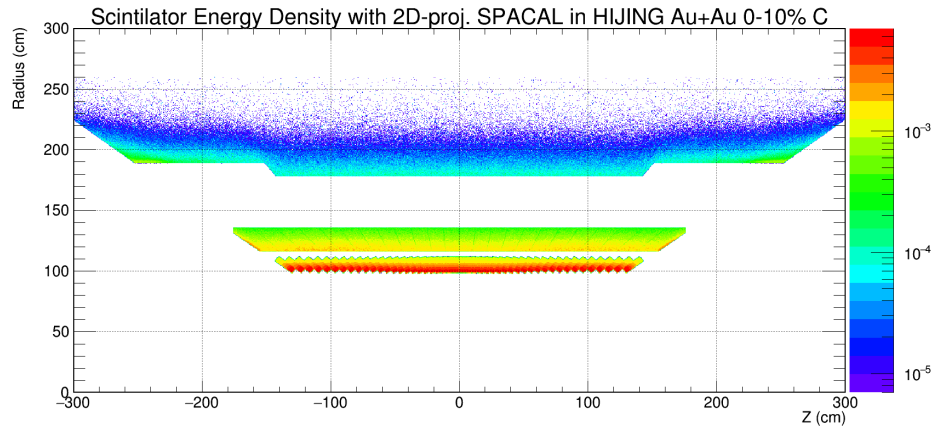


**Figure 5.1:** Visible energy density in the sPHENIX calorimeter systems in central Au+Au collisions. The electromagnetic calorimeter at radius of  $\sim 100$  cm observes a high amount of background energy density, which is quantified in Figure 5.25 in a later section. Each block of the EMCal consists of two towers in the  $z$ -direction.

The technology chosen for the EMCAL utilizes an absorber consisting of a matrix of

tungsten powder and epoxy with embedded scintillating fibers (W/SciFi), similar to the SPACAL design that has been used in a number of other experiments [128, 129, 130, 131, 132]. In order to work inside the magnetic field, the readout will utilize silicon photomultipliers (SiPMs), which provide high gain and require minimal space. The readout will digitize the SiPM signals and also provide a trigger for high energy electrons and photons. The W/SciFi absorber matrix was developed at UCLA and has been tested several times in test beams at Fermilab [133, 134]. The matrix is formed by preparing an assembly of 0.47 mm diameter scintillating fibers, held in position by a set of metal meshes. The nominal center to center spacing of the fibers is 1.0 mm. The fiber assembly is encapsulated in a mixture of tungsten powder and epoxy, which is compacted by vibration and/or centrifuging to achieve a density  $\sim 10 \text{ g/cm}^3$ . This results in a sampling fraction  $\sim 2.3\%$  with a radiation length  $X_0 \sim 7 \text{ mm}$  and a Molière radius  $R_M \sim 2.3 \text{ cm}$ .

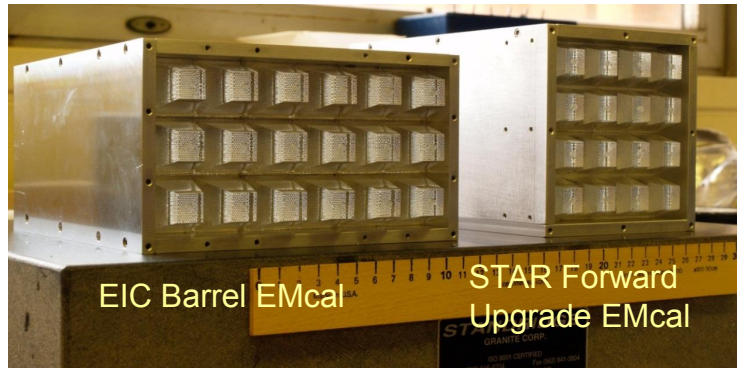


**Figure 5.2:** Prototype W/SciFi calorimeters tested at Fermilab in 2014. The detector on the left consists of semi-projective modules and the one on the right consists of non-projective modules

Figure 5.2 shows two prototype W/SciFi calorimeters that were tested at Fermilab in 2014. The one on the left, which was designed to test a barrel calorimeter for EIC, consisted of modules that are projective in one dimension (1D projective), and the one on the right, which was designed to test a forward upgrade calorimeter for STAR, consisted of non-projective, rectangular modules. Figure 5.3 shows the energy resolution and linearity measured for the semi-projective prototype at three different effective rapidities ( $\eta = 0.0, 0.3$  and  $0.9$ ). The fits show that the resolution is  $\leq 12\%/\sqrt{E}$  at all rapidities and that the response is linear up to 12 GeV. The small change in slope for the different rapidities can be explained by the detector having a slightly increased sampling fraction at shallower impact angles.

The design of the EMCal is being developed with the use of simulations, tests of individual calorimeter components, development of a complete mechanical design, and the construction and evaluation of several prototype calorimeters that will be studied along with the hadronic calorimeter in a series of beam tests. These various efforts of the EMCal design are described in the sections below.

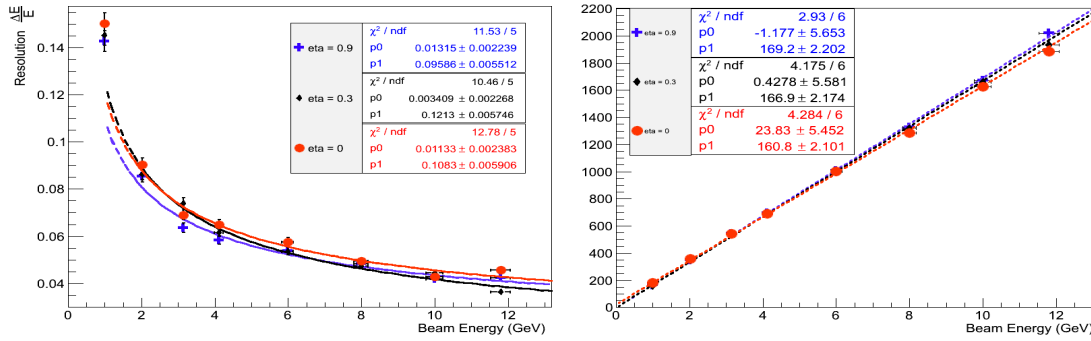


**Figure 5.3:** Test beam results for the semi-projective prototype calorimeter. Left: Energy resolution for three different effective rapidities ( $\eta = 0.0, 0.3$  and  $0.9$ ). Right: Calorimeter response as a function of electron beam energy.

## 5.2.2 Module and Sector Design

The EMCal will consist of 64 sectors ( $32 \text{ azimuthal} \times 2 \text{ longitudinal}$ ) that are supported by the inner HCal. Each sector will subtend  $11.2 \text{ deg}$  in  $\phi$  and cover  $1.1$  units in  $\eta$ . They will be supported by rails that will be used for installing each sector one at a time and will allow removal of any sector for service or repair. Each sector will contain 384 towers that will be constructed from blocks of  $2 \times 2$  towers. Four blocks will be joined together to form a modules consisting of  $2 \times 8 = 16$  towers. Twenty four of these modules will then be used to form a sector. Table 5.1 gives the key parameters for the EMCal.

The current design assumes that all of the EMCal towers are projective in both  $\eta$  and  $\phi$  (i.e., 2D projective) such that they point back to the collision vertex. However, since the collisions are distributed longitudinally with a  $\sigma \sim \pm 10 \text{ cm}$ , the towers do not have to be perfectly projective. We envision that each  $2 \times 8$  module will be oriented to be approximately projective back to the nominal vertex position.

Figure 5.4 shows the design of an EMCal sector. Each module forms a slice in  $\phi$  that gradually tilts along the  $z$  axis in order to project back to the vertex at larger rapidity. The four  $2 \times 2$  blocks within a module are epoxied together and the modules are placed side by side in order to minimize any dead material. The blocks are attached to a support plate at the back using small screws. The plate is then attached to the rail system which is mounted on the inner surface of the Inner HCal. The entire sector is enclosed in a thin walled ( $\sim 1 \text{ mm}$  thick) stainless steel box that provides overall support and light tightness. Figure 5.5 shows a cross section of the sector showing the location of the absorber, the light guides, front end electronics and cabling. The towers are read out from the front, inner radius. This allows access to the electronics from inside the magnet through a removable cover on the sector enclosure.

Parameter	Units	Value
Inner radius (envelope)	mm	900
Outer radius (envelope)	mm	1161
Length (envelope)	mm	$2 \times 1495 = 2990$
tower length (absorber)	mm	144
Number of towers in azimuth ( $\Delta\phi$ )		256
Number of towers in pseudorapidity ( $\Delta\eta$ )		$2 \times 48 = 96$
Number of electronic channels (towers)		$256 \times 96 = 24576$
Number of SiPMs per tower		4
Number of towers per module		$2 \times 8 = 16$
Number of modules per sector		24
Number of towers per sector		384
Number of sectors		$2 \times 32 = 64$
Sector weight (estimated)	kg	326
Total weight (estimated)	kg	20890
Average sampling fraction		2.3%

**Table 5.1:** Key parameters of the EMCal

### 5.2.3 Module Construction

The EMCal will require a total of 24576 towers, in 6144 blocks, each of which contains  $2 \times 2$  towers. The manufacturing of such a large number of blocks is at an industrial scale, and we expect that these blocks can best be manufactured by a commercial company utilizing mass production techniques and industrial level quality control. The company we hope that will be able to produce these blocks for us is Tungsten Heavy Powder (THP) [135], which is the company that has supplied the tungsten powder for all of the modules we have built so far. In addition, THP has been involved in an R&D program with us for more than a year to develop the technology for mass producing these blocks, which has been very successful. They are continuing to work with us to develop their manufacturing process to improve the quality of the modules in terms of consistency, uniformity, minimizing dead material, improving the optical quality of the finished fiber ends and reducing the production costs. We hope that this will lead to a situation where THP will be able to produce all of the modules for the calorimeter in a cost effective way and within the time frame required for constructing the detector.

We are also developing the capability to produce modules at the University of Illinois at Urbana-Champaign (UIUC). The Nuclear Physics Group at UIUC has significant production capabilities and expertise in producing detector components of this type. They have, in fact, built a similar tungsten-scintillating fiber calorimeter in the past in connection with the g-2 experiment [136]. They have also been closely involved with the R&D to produce our prototype modules and could also be in a position to produce the modules needed for the calorimeter if needed. We feel that having these two manufacturing options at this

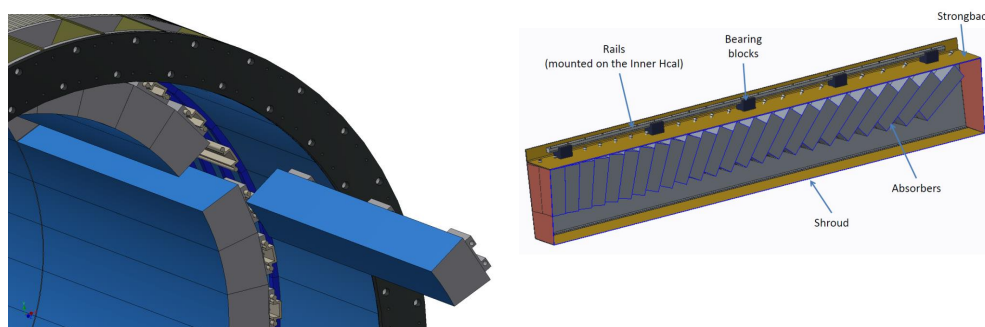


**Figure 5.4:** Left: EMCal sector showing installation on the Inner HCal. Right: Mechanical detail of an EMCal sector

stage of the project provides sufficient flexibility and possible options for the future.

The SPACAL blocks that were developed at UCLA are 2-tower blocks that are tapered in one dimension (1D projective), as shown in the Figure 5.6. The procedure used at UCLA to construct these blocks consists of the following steps:

1. Place 5 mesh screens together to form a flat stack
2. Drop fiber segments halfway through the screens to form a fiber/screen assembly
3. Separate the screens
4. Place the assembly into a mold, incrementally tilting the screens to produce the taper in one direction
5. Pour W powder into the mold and vibrate to compact
6. Infuse epoxy into the W/fiber matrix using vacuum to insure uniformity

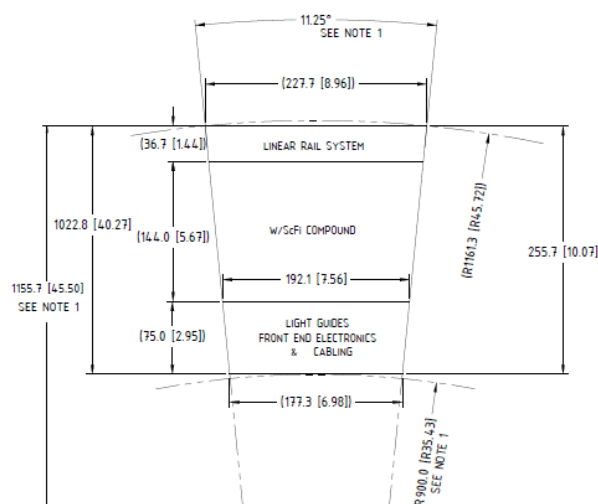


**Figure 5.5:** Cross sectional drawing of an EMCal sector.

Figure 5.7 shows some of the components used to form the block, including the tungsten powder, brass screen, and fiber/screen assembly loaded into a SPACAL module mold, and Table 5.2 lists some of the properties of the materials used.

In order to further develop the techniques for producing the W/fiber blocks, groups from BNL, UIUC, and THP all produced blocks according to the UCLA 1D projective design. This resulted in a number of improvements and in devising ways to make the process of forming the blocks more efficient, reliable and cost effective. Tungsten Heavy Powder produced a number of blocks and used a centrifuging method to compact the powder, which resulted in blocks with densities  $\sim 10.6 \text{ g/cm}^3$ . Figure 5.8 shows several blocks produced by THP. Figure 5.9 shows the light output from three of these blocks measured with cosmic rays. Figure 5.10 shows the measured light output from one of the same blocks (number 2) read out through a light guide with 4 SiPMs, again with cosmic rays. The blocks have shown a steady improvement in light yield since THP has been developing their process and the last module produced had a light yield equivalent to the original UCLA modules.

In parallel with this effort, the BNL and UIUC groups also explored ways to produce 2D projective blocks. Requiring the fibers to taper at different angles in two dimensions is more complicated. The procedure for filling the mold with tungsten powder and infusing it with epoxy is the same for 1D or 2D tapered blocks, but positioning the fibers in the screens and then into the mold with the desired 2D taper is more difficult. We have developed two different methods for this procedure using different types of metal screens. One is to use a set of screens with gradually changing hole patterns that achieves the double taper. Figure 5.11 shows a drawing of the overlapping screens. The holes near the center align but are misaligned towards the edges. Using CAD design tools and rapid prototype

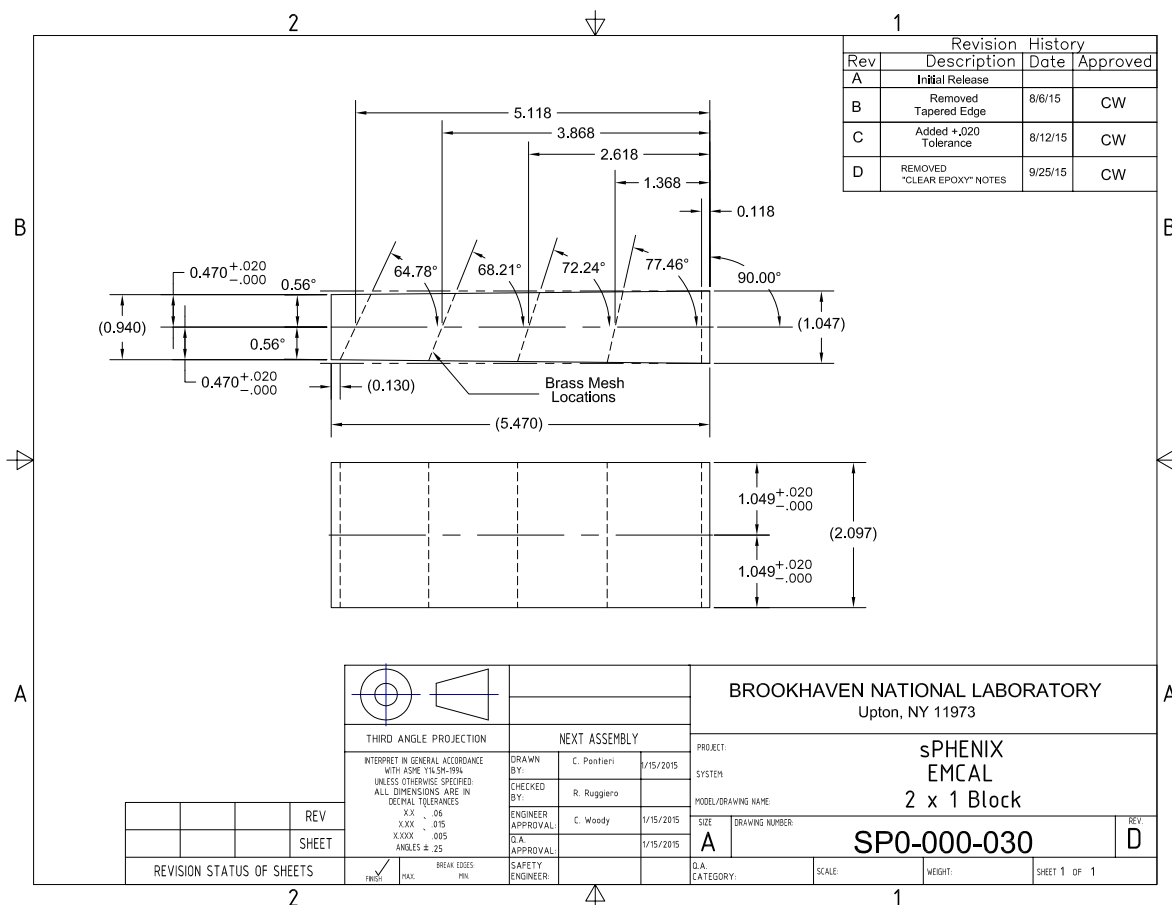


**Figure 5.6:** Technical drawing of the SPACAL block 2 tower, 1D projective block

printing, we developed fixtures to improve the process of loading fibers into the meshes. We have so far developed these molds and fixtures to produce single tower 2D blocks and we are continuing to refine the design of the molds and fixtures to improve the quality and consistency of the blocks produced.

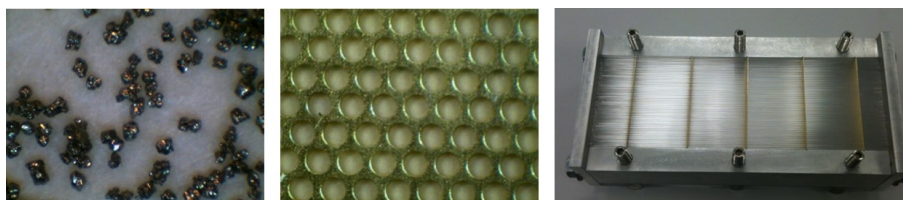


**Figure 5.7:** Magnified photo of Technon 100 mesh powder (left), etched brass fiber positioning mesh (center), and fiber/mesh assembly in open mold (right).



Material	Property	Value
Tungsten powder	THP Technon 100 mesh	
	Particle size	$\leq 100 \mu\text{m}$
	bulk density (solid)	$\geq 18.50 \text{ g/cm}^3$
	tap density (powder)	$\geq 11.25 \text{ g/cm}^3$
	purity	$\geq 99.9$ percent W
Scintillating fiber	impurities ( $\leq 0.1$ percent)	Fe, Ni, O <sub>2</sub> , Co, Cr, Cu, Mo
	Kuraray SCSF78 (blue)	
	fiber diameter	0.47 mm
	cladding	single
	core material	polystyrene
	cladding material	polymethylmethacrylate
	emission peak	450 nm
	decay time	2.8 ns
	attenuation length	$\geq 4.0$ m
Epoxy	Epo-Tek 301	
	pot life	1-2 hours
	index of refraction	1.519 at 589 nm
	spectral transmission	$\geq 99\%$ at 382-980 nm

**Table 5.2:** EMCal module component materials

The other method we have explored to produce 2D tapered blocks is to use a set of thin wire frames that are tilted at two different angles to position the fibers. When the wire frames are placed together, the fibers can be easily inserted through the frames. The frames are then separated and held at the appropriate angles in the mold to achieve the 2D taper. Figure 5.12 on the left shows a fiber assembly formed by the tilted wire frames inside the mold. The wire frame method could also be used to cast 2 blocks simultaneously in a "bow-tie" arrangement as shown in Fig 5.12 on the right. Figure 5.13 shows some examples of 2D projective modules produced at BNL.

The quality of the end surfaces of the fibers is important for the performance of the calorimeter blocks since it directly affects the light output. A clean cut and polished end with minimal fiber damage is required to maximize the scintillation light collection from the blocks. In the UCLA design, the blocks have a clear epoxy region (i.e., no tungsten powder) at each end so that when the ends are machined, tungsten powder is not embedded into the surface of the fibers. However, this requires two extra gluing steps in forming the blocks. UIUC has developed a process to diamond-cut and polish the tungsten powder-epoxy material with minimal damage to the surface of the fibers, thus eliminating the need for the clear epoxy region and simplifying the manufacturing process. Figure 5.14 shows an example of the surface quality that can be achieved with this procedure.



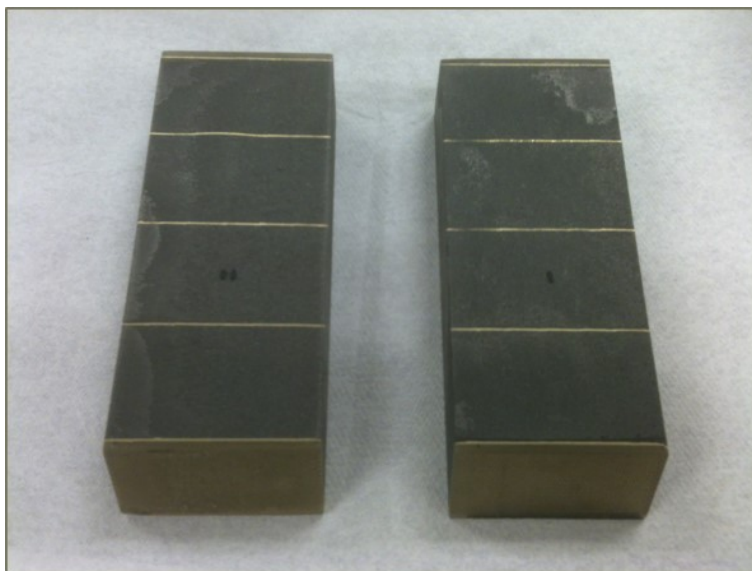


**Figure 5.8:** 1D projective blocks produced by THP.

#### 5.2.4 Light Guides

Light guides will be used to optically couple the optical sensors to the readout surface of the calorimeter blocks. Each light guide will define a readout tower. The surface area of a single tower is  $19.8 \text{ mm} \times 19.8 \text{ mm} = 392 \text{ mm}^2$ , while the combined active area of the 4 SiPMs is  $4 \times (3 \text{ mm} \times 3 \text{ mm}) = 36 \text{ mm}^2$ . The initial design for the light guide is a modified version of the SPACAL light guide, shown in Figure 5.15, which is a simple trapezoidal shape, with a height of 25 mm, to couple the 2 areas. These light guides are machined acrylic which has good optical transmission above 400 nm. The lightguides will be epoxied to the absorber blocks as shown in Fig 5.16. Silicone cookies will be used to optically couple the SiPMs to the lightguides. Initial measurements of these light guides, coupling a prototype W/fiber calorimeter block to photomultiplier tube, show an efficiency of 71 percent.

#### 5.2.5 Sensors

The photosensor selected for the EMCal is the Hamamatsu S12572-015P SiPM, or Multi Pixel Photon Counter (MPPC), described in detail in the Electronics - 7.1 Optical Sensors section of this document. This device will be used for both the HCal and EMCal. The EMCal will use a 2x2 arrangement of 4 SiPMs per tower, passively summed into one preamp/electronics readout channel. The 4 SiPMs will be gain-matched (selected) and will share a common bias voltage.

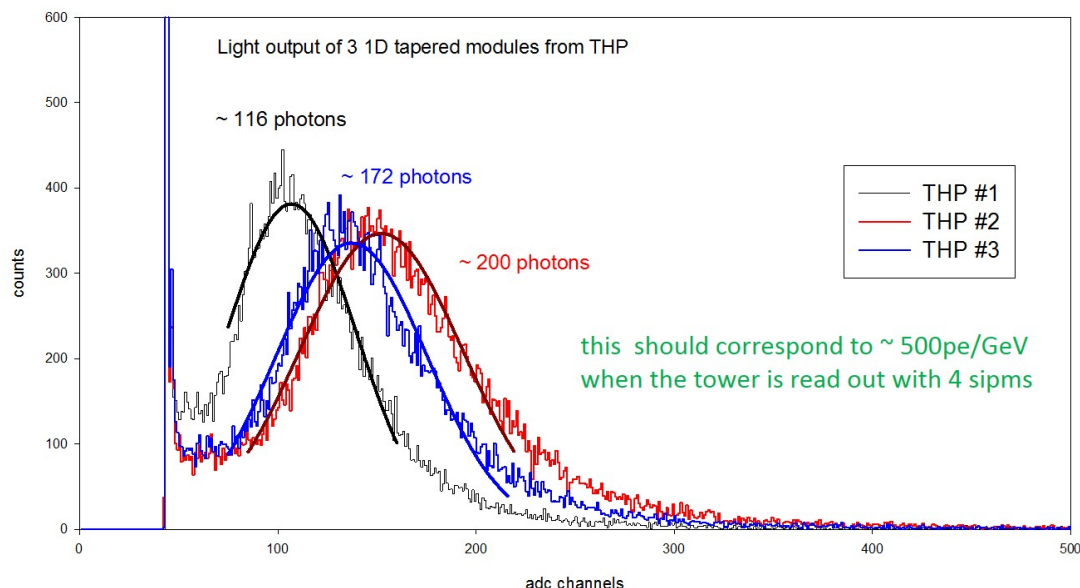


**Figure 5.9:** Measured light output from first THP produced blocks. Read out directly coupled to a 2" PMT, cosmic ray trigger. Converted to photons using pmt QE = 0.20.

### 5.2.6 Electronics

The readout electronics for the EMCal consists of the analog front end, slow controls, digitizers and power distribution system. The EMCal Preamp Board consists of an  $8 \times 2$  array of preamplifier circuits that are laid out to match the geometry of the light guides. The Preamp Boards are mounted directly to the light guides. The analog signals from each of the four SiPMs associated with an EMCal tower are passively summed into one readout channel. The analog sum signal is amplified with a common-base transistor amplifier, shaped with a 30 ns peaking time and driven differentially to digitizer electronics located near the detector. The analog signals are digitized with a Flash ADC operating at 6 times the beam crossing (BCO) frequency and stored in a digital pipeline with a 40 BCO latency. Upon receipt of a Level-1 (L1) trigger, the digital wave form is transferred to a readout buffer capable of buffering up to 5 events for readout to the data acquisition system via a high speed optical link. The digitizer boards also compute trigger primitives which are transmitted to the Level-1 trigger system through independent optical fiber links. Full details of the calorimeter electronics can be found in Chapter 7.

### 5.2.7 LED Calibration

Pulsed LEDs (450 nm), mounted on the SiPM side of the preamp PCB, and projecting light into the lightguides, will be used to calibrate the detector channels and monitor gain drift.

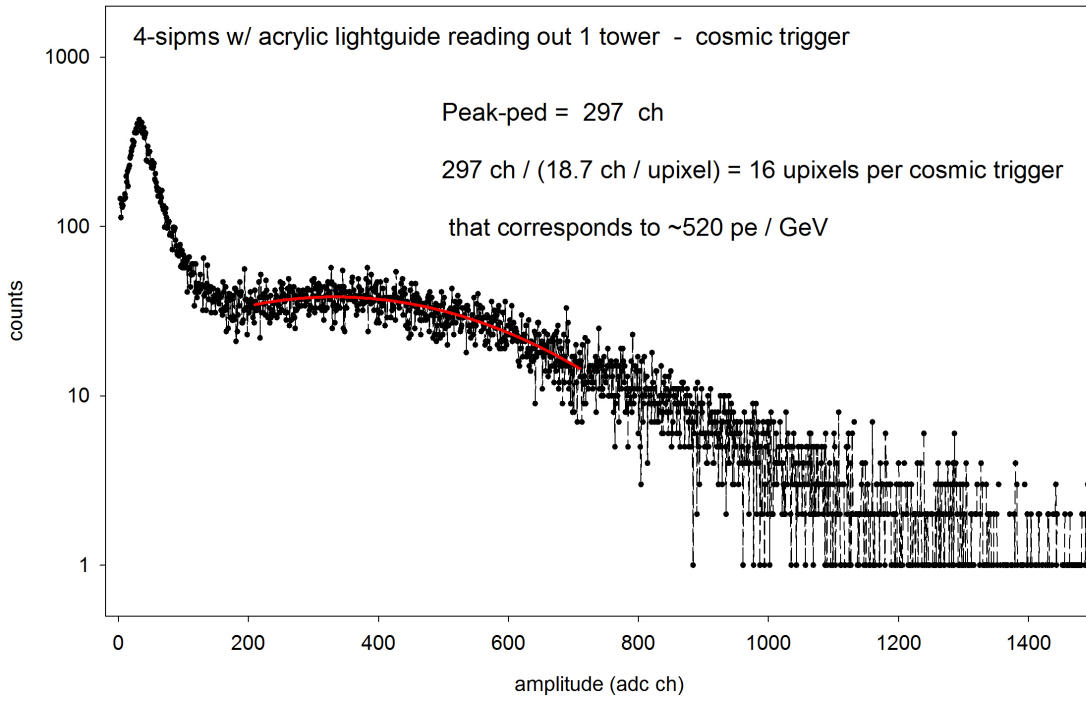


**Figure 5.10:** Measured light output from a THP produced block, read out through light guide with 4 SiPMs, cosmic ray trigger. The four summed sipms have a total of  $4 \times 40,000 = 160,000$  micropixels, which establishes the upper end of the dynamic range.

## 5.3 Simulations

### 5.3.1 Introduction

Both the 2D and the 1D SPACAL designs have been implemented in detail using the sPHENIX analysis framework and GEANT4. The 1D implementation allows for verifying the simulation with existing test beam data. A large set of calorimeter simulations has been run with the aim of defining design goals and quantifying detector and physics performance. The basic features of the simulation setup are as follows:

- Both the 1D and 2D projective EMCal designs are implemented in a full detector simulation of sPHENIX. The structure of the SPACAL in simulation is detailed to each of the 20M fibers (including core and cladding) to properly study the shower sampling.
- The simulation is based on GEANT4 v4.10 [137] with the QGSP\_BERT\_HP physics list.
- The default GEANT4 Birks correction model for scintillation light production [137]

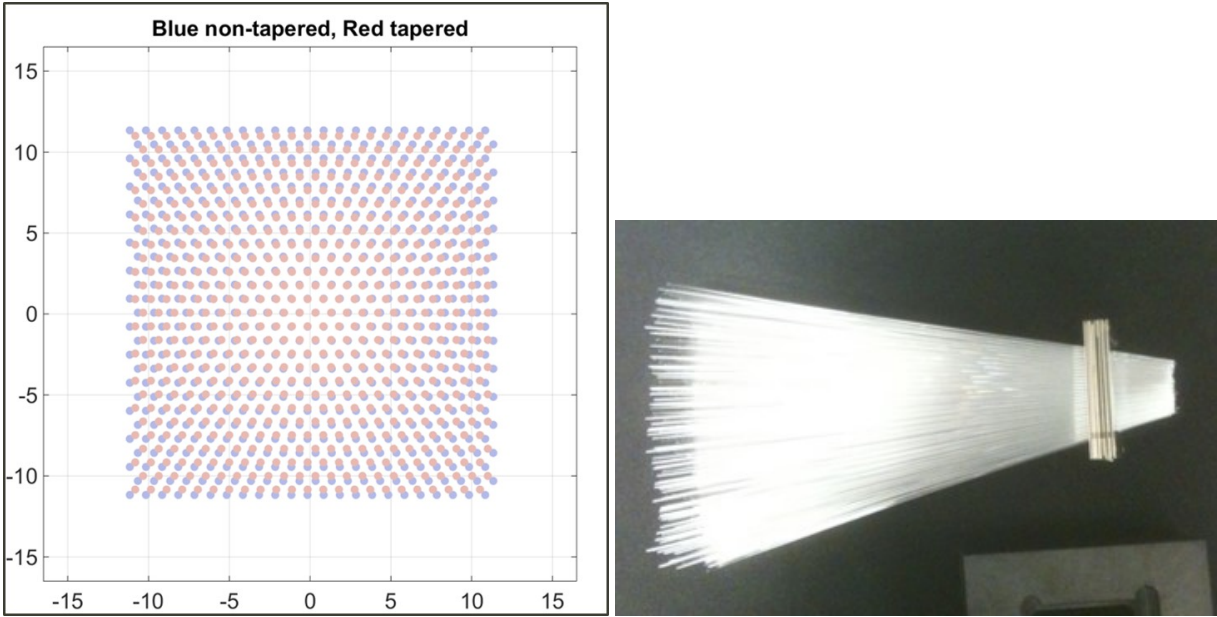


**Figure 5.11:** Drawing of overlaid screens (left), and photo of fibers threaded through spaced screens for 2D tapered module production (right).

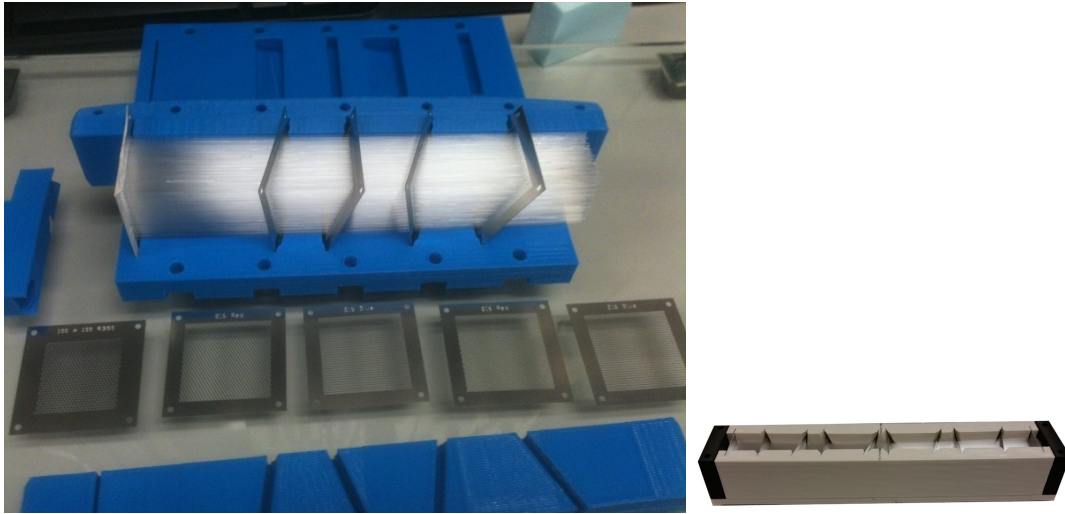


**Figure 5.12:** Wireframe and fiber assembly in open mold (left), "bowtie" arrangement for 2 block production (right).

with Birks constant  $k_B = 0.0794 \text{ mm/MeV}$  [138] is implemented.

- The mean number of photoelectrons per GeV of total energy deposit is 500. The observed number of photoelectrons follows a Poisson distribution.
- The pedestal width is taken to be 8 photoelectrons with a zero-suppression of 16



**Figure 5.13:** 2D tapered block production at BNL: 3D printed mold (left), filled mold, connected and ready to infuse epoxy (center), 2D tapered modules produced at BNL (right).

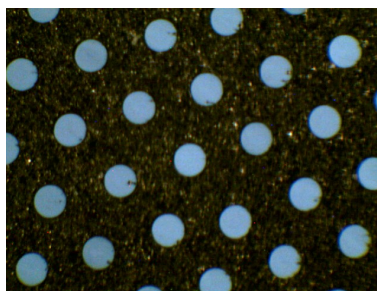


**Figure 5.14:** The diamond cut end of a tungsten powder/fiber/epoxy block, cut with the UIUC-developed technique.

photoelectrons per EMCal tower, based on the experience of the EIC eRD1 beam test with the SPACAL [133].

- The sPHENIX offline analysis framework is used to handle the conversion of the ADC value to measured energy, group towers into EMCal clusters, and match with tracks.

Event displays for a single tower and full EMCal are shown in Figure 5.17 and 5.18, respectively.

### 5.3.2 Verification of Simulation

The simulation was verified with data from the EIC eRD1 beam test of the 1D projective SPACAL prototype [133]. As shown in Figure 5.19, the simulation and data agree reasonably well for three choices of beam energies:

- The measured energy resolution for electron showers is reproduced in simulation within 10%.
- A 10% contribution of muons is expected in the test beam with a “non-electron”



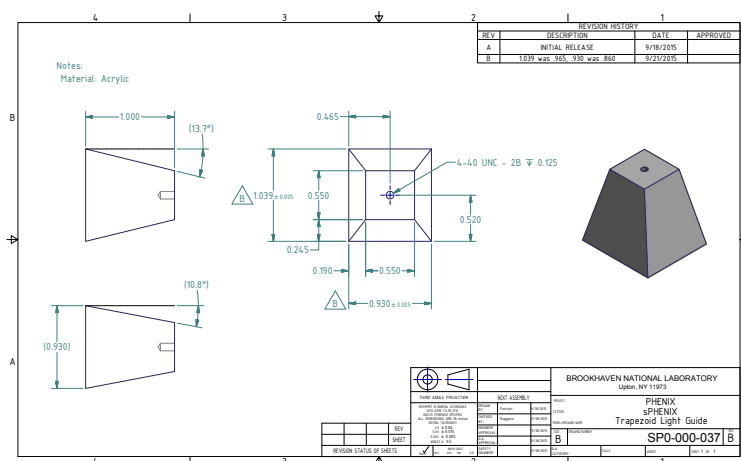


**Figure 5.15:** Preliminary design for EMCal light guides.

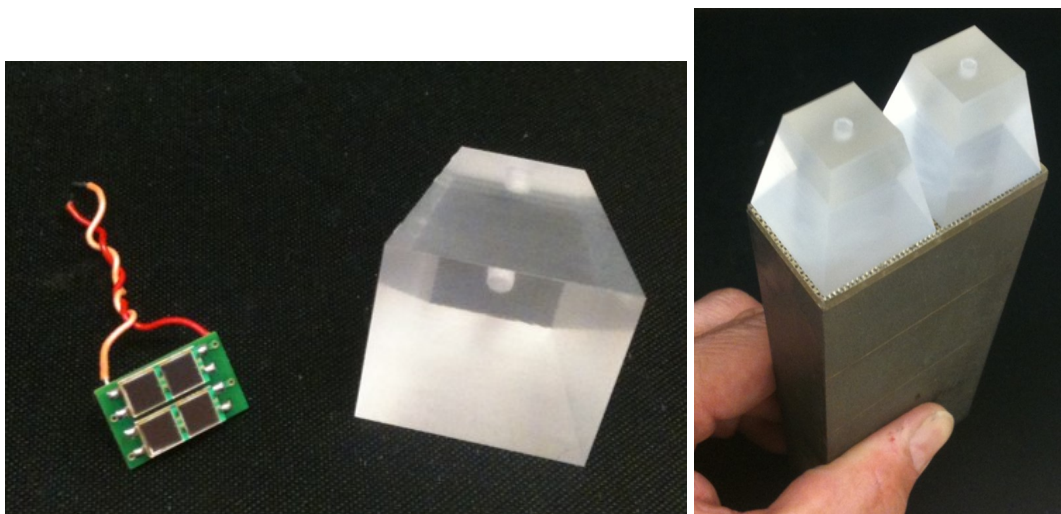


**Figure 5.16:** Four-SiPM pcb and SPACAL acrylic lightguide (left), lightguides on SPACAL block (right). In the current design, the sipms will be mounted on a larger pcb with preamps and electronics. The sipms will be positioned to accomodate the mounting hole in the light guide.

Čerenkov cut. Likewise a small amount of electrons and other beam background are suggested by the data.

- The simulated hadronic shower response is consistent with data within a factor of 2 across all energy bins.

Even though good agreement has already been achieved with default tuning of the simulation, further improvements can be made:

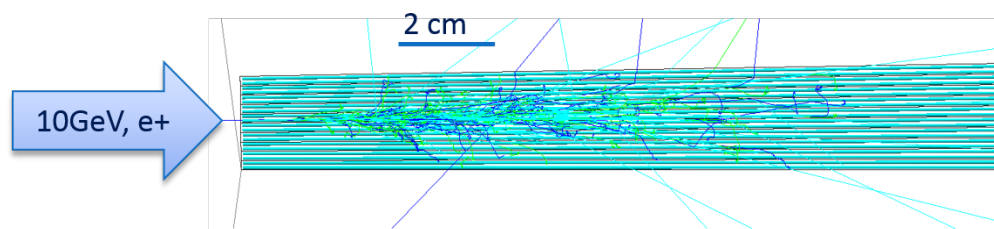


**Figure 5.17:** Event display of a 10 GeV positron shower in a single SPACAL tower. Scintillation fibers as embedded in the module are also shown, while the absorber material is not displayed.

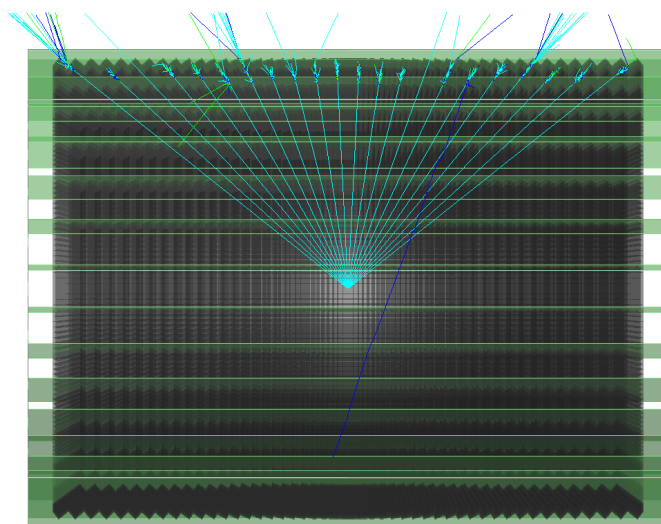


**Figure 5.18:** Simulation display of a half cut view of the 2D projective EMCal. The SPACAL modules (2x8 towers each) are display in gray; the stainless steel enclosure box is displayed in green.

- The Birks constant for the fiber core material can be tuned. Preliminary tests showed that a higher Birks constant than the one found by the CALICE experiment [139] can significantly improve the agreement for the hadronic shower component.
- Implementation of fiber-to-fiber light collection efficiency variations. This should reduce the difference in energy resolution at the high energy side.
- Comparison to data from a planned future beam test of the sPHENIX prototype (planned for 2016).

### 5.3.3 Sampling Fraction

In the W-epoxy and scintillator fiber structure, only energy deposition in the core of fiber is visible via detection of scintillation light, which represent a small fraction of the total shower energy. The sampling fraction is around 2.4% as shown in Figure 5.20 with two choices of typical showers: 4 GeV electrons as typical  $\Upsilon$  decay products; and 24 GeV photons as typical for  $\gamma$ -jet measurements. The higher energy showers are sampled with lower sampling fraction as the shower moves deeper into the calorimeter, where the fibers have larger spacing due to the projectivity.

### 5.3.4 Lateral Shape of Showers

To study the property of EM shower in the W-epoxy and scintillator fiber structure, the lateral extension of the EM shower is quantified in Figure 5.21, by histogramming all scintillator GEANT4 hits with their distance to the projection of the incoming 4 GeV electrons (as typical  $\Upsilon$  decay products in the central pseudorapidity). The Molière radius is about 2 cm in order to contain 90% of the EM shower. A  $3 \times 3$  EMCal tower-cluster contains about 95% of the EM shower. For pion showers in the EMCal, which the calorimeter system is designed to reject, the same  $3 \times 3$  EMCal tower-cluster contains about 50% of the shower energy, which helps to improve the efficiency of the  $E/p$  cut. The inner hadron calorimeter (HCal) immediately behind the EMCal is used to catch the tails of the pion shower in order to veto hadrons. A  $3 \times 3$  inner HCal tower-cluster can contain 60% of the energy of the pion shower tail. These simulation served as a guild line for the choice of tower size for both EMCal and inner HCal, as the choice of tower segmentation is optimized for the shower containment in  $3 \times 3$  tower-clusters, and a finer towering structure would not significantly improve the clustering.

The shower size is also quantified using towers of 1-D and 2-D SPACAL as shown in Figure 5.22. For a 2-D projective SPACAL, despite the fact that the towers are shifted along the longitudinal direction (as illustrated in Figure 5.1 and 5.4), a circular distribution of towers for the EM shower is observed around the track projection for both central and forward pseudorapidity. This leads to a round-shaped cluster with a minimal number of towers necessary to contain an EM shower. In comparison, a shower in the 1-D projective SPACAL is spread into multiple towers along the polar direction, which leads to an elongated cluster covering more towers, as quantified in the right panel of Figure 5.22.

### 5.3.5 Single EM Shower Performance

The linearity and energy resolution for photon clusters as simulated through the full sPHENIX detector and analysis chain are presented in Figure 5.23 and 5.24.

For sPHENIX  $\gamma$ -jet measurements, the photon clusters were simulated with the full



sPHENIX detector, which produces an energy resolution better than  $\sim 14\%/\sqrt{E}$  as shown on the left side of Figure 5.23. For the 1D projective SPACAL, the energy resolution improves as the photon shifts toward forward rapidity and the shower deposits more energy at a smaller radius and becomes better sampled.

For possible use of the calorimeter in a future EIC experiment with a much thinner tracking detector, the single electron resolution without the sPHENIX silicon tracker was also simulated as on the right panel of Figure 5.23. The electron energy resolution is better than  $\sim 12\%/\sqrt{E}$ , which benefits from the bending of low energy electrons in the magnetic field and radially shallower showers compared with photons.

As shown in Figure 5.24, the linearity for both SPACAL options is better than 3.5%, as defined as the relative deviation from  $E_{\text{reco}}/E = 1$  at the maximum photon energy of  $E = 50$  GeV. The linearity is improved to better than 2.0% when photons are in the forward rapidity direction, where the SPACAL becomes thicker along the path of the photon, and therefore lower back-leakage occurs. The 1D projective SPACAL yields better linearity, since the variation of the fiber density and the sampling fraction along the depth of the shower is lower.

### 5.3.6 Occupancy

The occupancy in central Au+Au collisions (the highest background event) is illustrated in Figure 5.1 and quantified in Figure 5.25. For a typical  $3 \times 3$  EMCal tower-cluster in the 2-D projective SPACAL, the mean background energy is 340 MeV. For the 1-D projective SPACAL at forward rapidity, a significantly larger underlying event (about 550 MeV) would be included in a cluster since electron showers would spread into more towers (as illustrated in the right panel of Figure 5.22). Meanwhile, this background presents a large tail extending to higher energy, which leads to a challenge of rejecting hadron shower for electron-ID as the logarithmically dropping hadron shower tail is shifted up in energy by this background.

### 5.3.7 Electron Identification

One key function of the EMCal is to identify the electron/positron tracks within the hadron background for the  $Y$  measurement. The energy of the electron/positron from the  $Y$  decay range from 2-10 GeV, with averages of 4.8 GeV in the central pseudorapidity to 5.7 GeV in the forward direction ( $0.7 < \eta < 0.9$ ). The primary method of electron-identification (eID) is to match the measured track momentum with the measured cluster energy in the EMCal. Furthermore, the inner hadron calorimeter can improve the eID by vetoing track candidates with a large leakage behind the EMCal. For each track, cluster energy information from both the EMCal and inner HCal is analyzed using a likelihood method, by comparing the observed cluster energy with the EMCal-HCal two-dimensional probability distributions

extracted from template samples of pure electrons and hadrons. By selecting tighter or looser cuts, the hadron rejection versus electron efficiency curves can be mapped out for each combinations of track rapidity, track momentum and SPACAL configurations.

The reference electron identification performance is shown in Figure 5.26 in the single particle simulations (expected performance in  $p+p$  collisions) and 5.27 in the most central Au+Au collisions (top 0-10% in centrality). These reference eID performance curves are simulated with a 1-D projective SPACAL fiber structure. Then hits in Geant4 can be grouped around the track projection into clusters in order to estimate the performance for the 2-D projective SPACAL, or grouped radially in order to estimate the performance for the 1-D projective SPACAL. The cluster energy is sum over all energy deposition in the fiber core (prior to the Birks correction model for scintillation light production [137]), which is then scaled to the measured energy in the calorimeter with a scaling constant of  $1/(\text{sampling fraction})$ .

In these reference studies, the 2-D projective SPACAL provided better than 100:1 pion rejection at 95% efficiency for 4 GeV electrons in  $p+p$  collisions (Figure 5.26), and better than 90:1 pion rejection at 70% efficiency for 4 GeV electrons in the most-central Au+Au collisions (left panel of Figure 5.27). These pion rejection and electron efficiency values has been used to for the estimates of the  $Y$  in our reference design. We also estimate that if a 1-D projective SPACAL is used, the pion rejection at large pseudorapidities will be reduced due to the larger cluster size necessary to contain the EM-shower, as shown in the right side of Figure 5.27.

Significant simulation effort has also been invested into updating these projections with a realistic setup of the SPACAL as shown in Figure 5.18, including incorporating the support/enclosure structures and the longitudinal offsets of the modules, and improved shower simulation (including the Birks scintillation model [137], photon fluctuations, and pedestal widths, which are crosschecked with test beam results as shown in Figure 5.19. When compared with the reference performance, preliminary results show improved eID performance with the suppressed hadron response in the default GEANT4 Birks scintillation model.

### 5.3.8 Dynamic range

The dynamic range required for the ADC system is studied by comparing the maximum energy deposition in a tower to the pedestal width. For a 50 GeV photon shower, a maximum of 22k photoelectrons were observed in a single tower as shown in Figure 5.28 (assuming a high pixel count SiPM). To encode this maximum photoelectron count down to the pedestal noise of 8 photoelectrons, a 12-bit ADC is required. The EMCal electronics, which provides a 14-bit ADC, will satisfy this requirement.

### 5.3.9 Trigger Performance

The performance of possible electron triggers for selecting di-electron  $Y$  decays in high-luminosity  $p+p$  running in sPHENIX has also been investigated. These triggers are based on energy sums in the electromagnetic calorimeter, and have been examined with a full event PYTHIA8 and GEANT4 simulation of the whole sPHENIX detector. 2D projective SPACAL towers were collected into sliding tower windows made from  $4 \times 4$  towers via a trigger logic emulator ( $\Sigma_{4 \times 4}[E_{\text{Tower}}]$ ). As one leading design of the trigger electronics, the top 8-bit ADC value for each tower was used in the sum in order to conserve trigger data bandwidth. The distribution of largest energy sums in minimum bias PYTHIA events was used to determine the rejection factors for the trigger. The efficiency for  $Y$  events was determined using a cut on largest energy sums in PYTHIA events, which contain at least one  $Y(1S)$  particle that decayed into di-electrons and was reconstructed by the full tracking detector to be within an invariant mass window of  $M_{Y(1S)} \pm 200 \text{ MeV}$  ( $M_{Y(1S)} \pm 2\sigma$ ).

Figure 5.29 summarizes the performance of such an electron trigger by simultaneously plotting the rejection factor for minimum bias events and the efficiency for  $Y$ 's as a function of the minimum energy required in the electromagnetic calorimeter tower windows using both the full ADC bit-width and the top 8-bit truncated ADC information. In particular, the vertical gray band in the figure at  $\Sigma_{4 \times 4}[E_{\text{Tower}}] = 4.3 \text{ GeV}$  gives an example of a choice of minimum threshold energy in  $4 \times 4$  windows for which the rejection factor is better than  $\approx 5 \times 10^3$  while maintaining an  $Y$  efficiency of 98% in both ADC bit-width choices. This demonstrates the feasibility of an electron trigger for the Upsilon program in high-luminosity  $p+p$  data-taking.

## 5.4 Prototyping and R&D

A number of tests of the W/SciFi SPACAL design have already been carried out by the UCLA Group [133, 134] and some of the results are shown in 5.3. The modules studied in those tests were 1D projective modules. We plan to carry out a series of new tests to study similar 1D modules produced both at THP and UIUC in order to compare their performance with those produced at UCLA. We will construct a new prototype consisting of an array of  $8 \times 8$  towers consisting of  $1 \times 2$  1D projective blocks, where half of the blocks were produced at THP and the other half at UIUC. We plan to carry out these tests at Fermilab in the spring of 2016 in conjunction with a new HCAL prototype. Later next year we plan to build another  $8 \times 8$  tower prototype consisting of 2D projective blocks and test these modules along with the HCAL prototype reconfigured to correspond to a larger rapidity section of the calorimeter. Following these tests and the analysis of the test beam data, we will construct a full scale pre-production prototype that will correspond to one full EMCAL sector and test this in the beam at Fermilab.

## 5.5 Alternative Technologies

A number of alternative designs for the electromagnetic calorimeter have been considered.

The BaBar experiment had a CsI electromagnetic calorimeter which is available to a new experiment. Clearly, it is a good match mechanically to the BaBar solenoid, occupying radial space from about 90 cm to the inner radius of the cryostat, but its segmentation, Moliere radius, and time resolution are not well suited to RHIC heavy ion operation. The Moliere radius of the CsI(Tl) is 3.8 cm compared to about 2.2 cm of the proposed calorimeter, limiting the segmentation possible at the radius that the electromagnetic calorimeter could be deployed, and the segmentation reflects that, with the barrel divided into 48 rings of 120 crystals, compared to the proposed 96 rings of 256 calorimeter elements. CsI(Tl) is a relatively slow scintillator, with an average decay time of about  $1\mu\text{s}$ , which would effectively integrate over 10 or more RHIC crossings. Despite the attractiveness of redeploying an elegantly engineered and executed detector, it is not suitable for use at RHIC as part of a barrel calorimeter.

Other crystal calorimeter options are attractive, in particular  $\text{PbWO}_4$ , as used in the CMS electromagnetic calorimeter. Lead tungstate crystals are fast, have a short radiation length (8.9 mm), and can give excellent energy resolution. If they could be produced in a timely fashion at a reasonable cost, they would be satisfactory. However, there are very few sources of crystals in the world, and the cost of growing them is high, resulting in crystal costs of \$5/cc to \$10/cc, compared to a material cost for the SPACAL of  $\sim \$1.50/\text{cc}$ .

The CDF and D0 experiments were surveyed for possible calorimeter components. Aside from the logistical challenges of extracting the desired components, the size and mechanics do not appear to be practical to redeploy either inside or outside the BaBar solenoid.

A lead-scintillator “shashlyk” calorimeter similar in design to the PHENIX and ALICE calorimeters was considered. The tooling for the construction of the ALICE calorimeter is still available, and the performance of these designs has been extremely satisfactory both in PHENIX and ALICE. Depending on the sampling fraction, the Moliere radius can be tuned to give adequate segmentation, but with lead absorber, fitting a depth of at least 18 radiation lengths requires a radial extent that precludes any part of the hadronic calorimeter (or second longitudinal segment of the electromagnetic calorimeter) inside the cryostat. Use of tungsten absorber in a “shashlyk” design was investigated. This would reduce the Moliere radius and make the design very competitive with a tungsten SPACAL. However, due to the difficulties of working with metallic tungsten and the number of holes needed in the absorber plates, this solution would require considerable development, and a potentially lengthy process of prototyping and testing.

A tungsten scintillating fiber “accordion” calorimeter was also considered, which would have a similar Moliere radius, radiation length and sampling fraction as the W/Scifi SPACAL. A prototype calorimeter of this type was in fact built and tested. However, due to the difficulty of forming the tungsten accordion plates and controlling their tolerances

at reasonable cost, this option was also rejected in favor of the W/Scifi SPACAL.

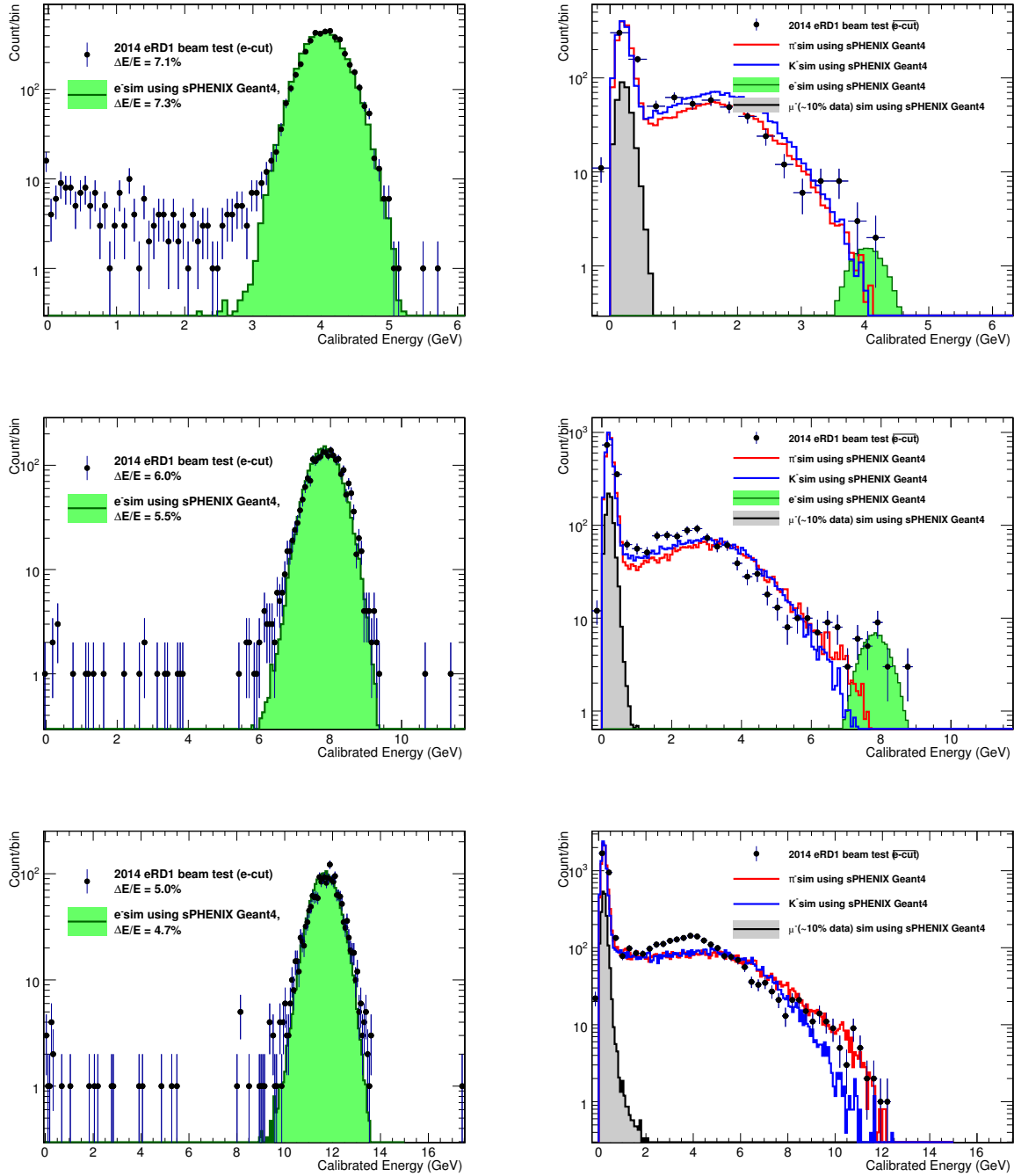


**Figure 5.19:** Comparison of the eRD1 beam test data and sPHENIX GEANT4 simulation for three choices of beam energies: 4.12 GeV (top), 8.0 GeV (middle) and 12.0 GeV (bottom). The left column data (black points) are with an electron requirement based on a beam Cherenkov detector, and the right column with a non-electron requirement. Curves represent simulated electrons (green), pions (red), kaons (blue) and muons (black).

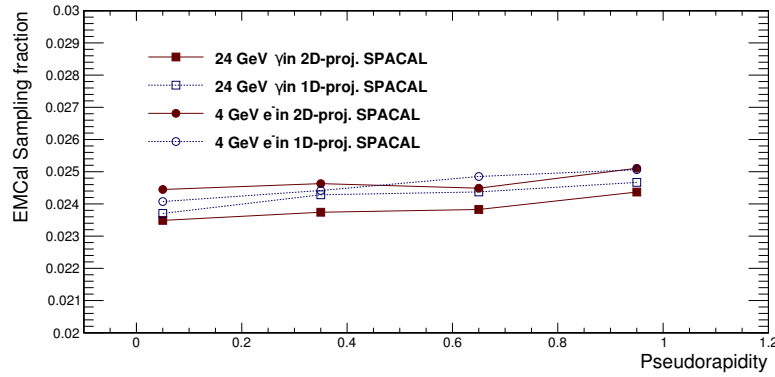


**Figure 5.20:** The sampling fraction of the 1D and 2D projective SPACAL as a function of pseudorapidity. Two energy ranges were chosen: the circles represent electron showers at 4 GeV, which is a typical energy for  $\gamma$  measurements; the squares represent photon showers at 24 GeV, which is a typical energy for  $\gamma$ -Jet measurements.

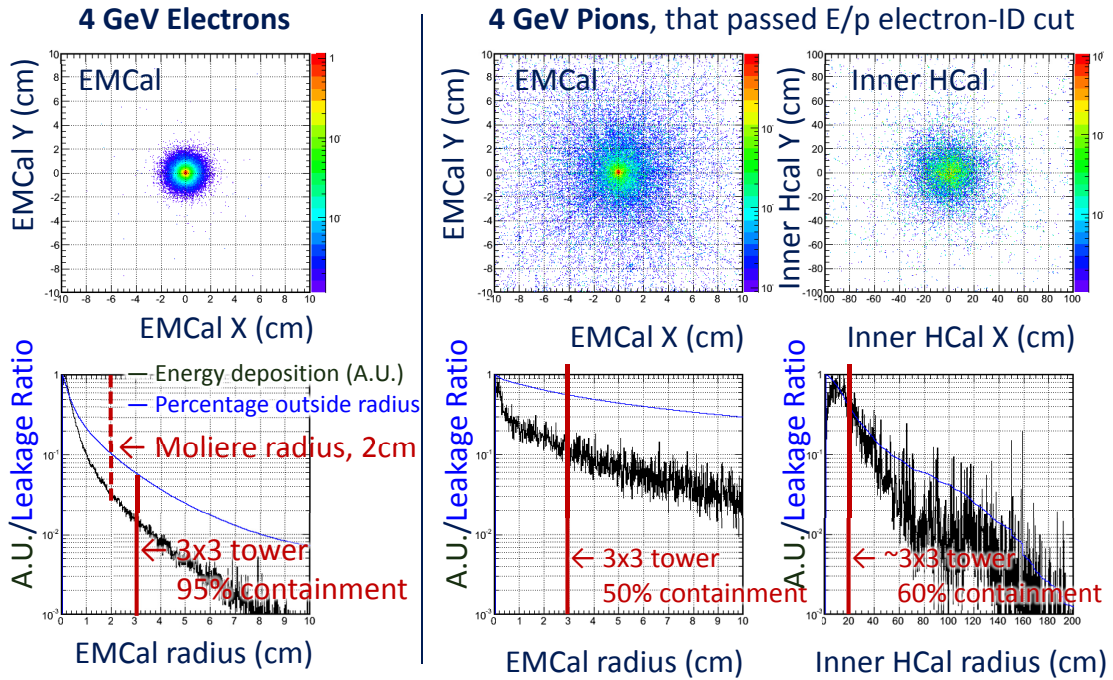


**Figure 5.21:** The lateral expansion of 4 GeV electron showers in the EMCal (left column), which is compared with 4 GeV negatively charged pion showers in the EMCal (middle column) and in the inner HCal (right column). The center,  $(X, Y) = (0, 0)$  cm, denotes the projection of the electron track. Then the energy deposition of all scintillator hits in GEANT4 is histogrammed versus the lateral distance from the track projection. The top row shows the energy deposition density in the 2-D lateral dimension, and the bottom row shows the energy density (black) and the shower leakage ratio (blue) vs. lateral radial distance.

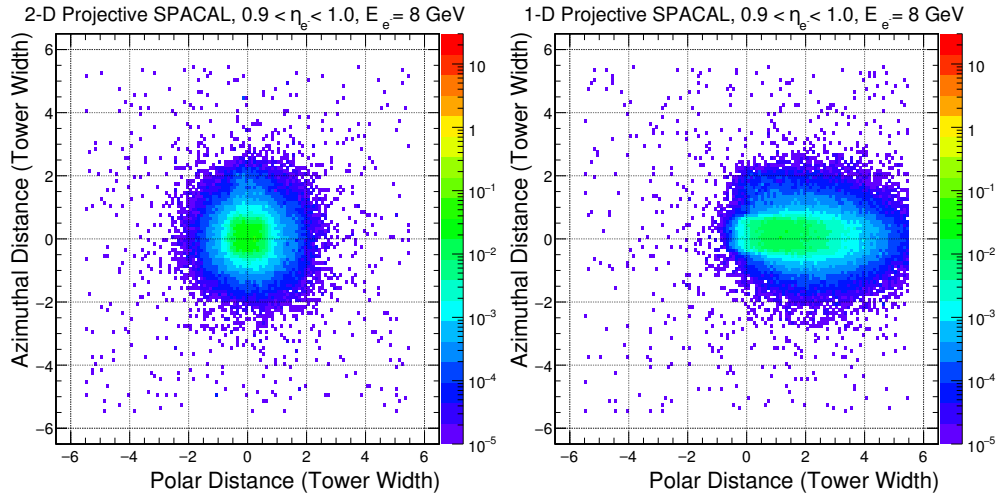


**Figure 5.22:** For very forward pseudorapidity, the lateral distribution of 8 GeV electron showers as observed in the 2-D projective (left) and 1-D projective (right) SPACAL towers. The polar (X-axis) and azimuthal (Y-axis) distances are defined as the distance between the tower and the electron track projection, in the unit of tower width.

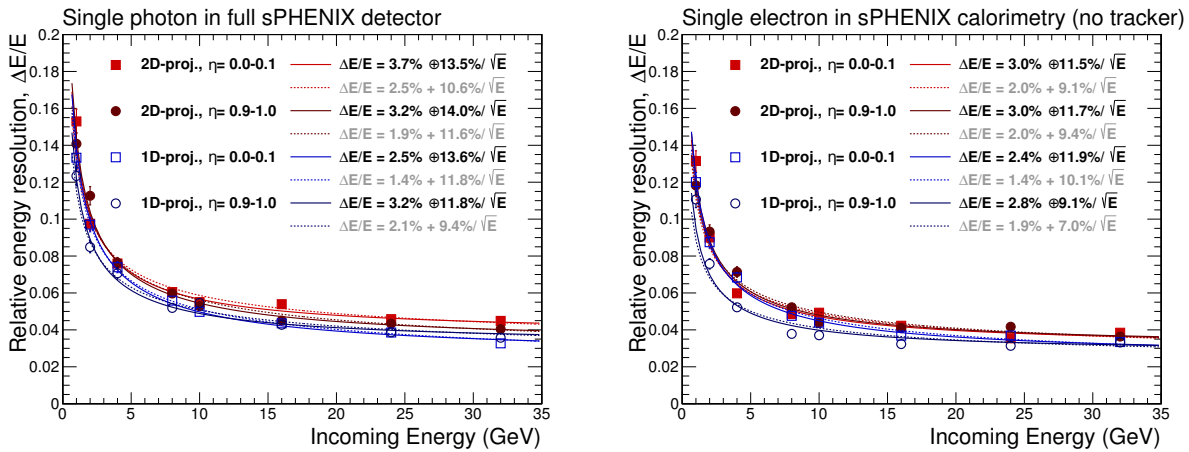


**Figure 5.23:** Left: the energy resolution for single photon clusters as reconstructed with the fully simulated sPHENIX detector, right: the energy resolution for single electron clusters as reconstructed with the sPHENIX calorimeters only (no silicon detector before EMCal). Two formulas were used to fit the resolution points: a quadratic sum of linear and statistical terms (solid line) and a linear sum of the two (dash line). Both 1D (blue curves and open points) and 2D (red curves and closed points) SPACAL options are presented.



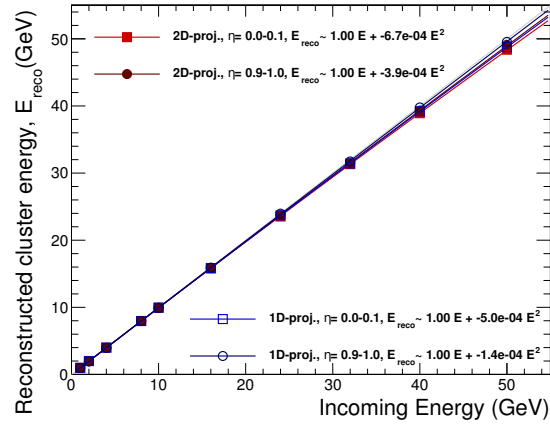


**Figure 5.24:** Linearity for single photon clusters as reconstructed with the full sPHENIX detector simulation and analysis chain. The linearity is calibrated for each pseudorapidity region to 1 at the low energy end, while the non-linearity towards the high energy end is quantified via a quadratic fit.

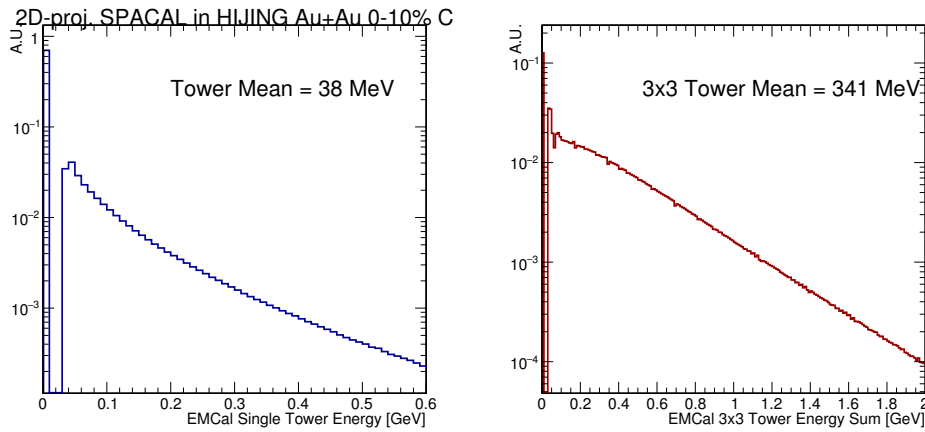


**Figure 5.25:** a) Energy per tower ( $\sim 1R_M^2$ ) for central Au+Au HIJING events, b) Mean energy for a  $3 \times 3$  EMCal tower-cluster. The 2-D projective SPACAL configuration is shown here.

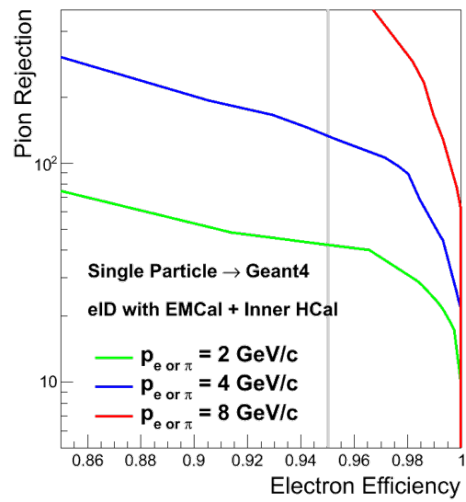


**Figure 5.26:** Pion rejection vs. electron identification efficiency for a single particle simulation for the 2-D projective SPACAL, which represents the performance for  $p+p$  and EIC collisions.

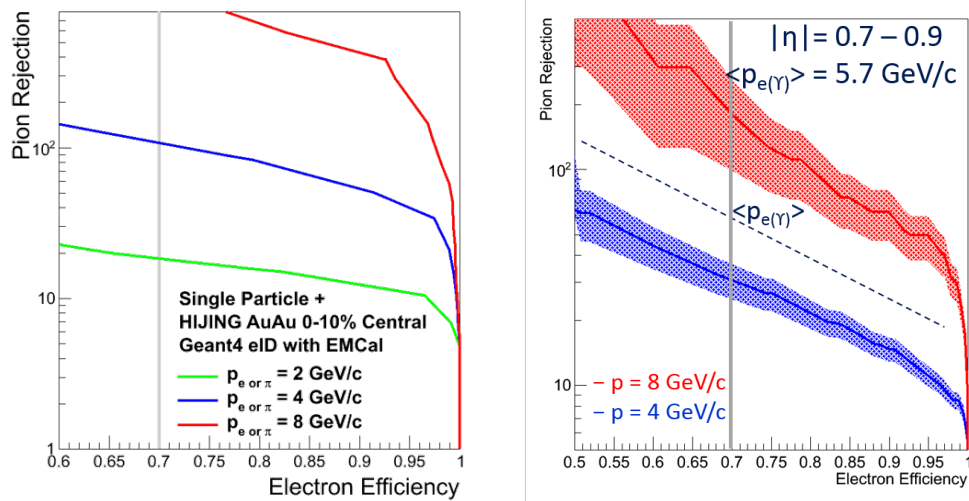


**Figure 5.27:** The pion rejection vs electron identification efficiency for the 2-D projective (left) and 1D-projective (right) SPACAL in central Au+Au collisions (0-10% central).

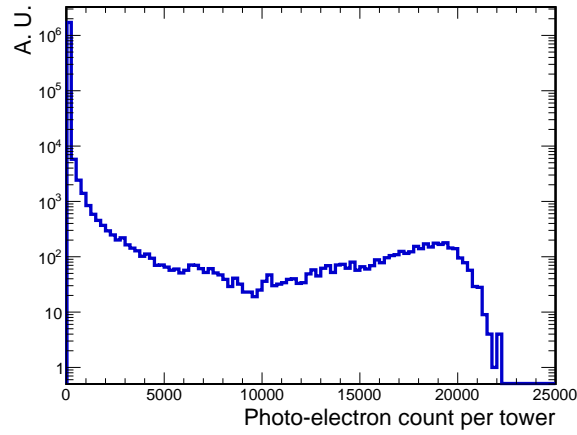


**Figure 5.28:** Number of photoelectrons per tower for 50 GeV photons as the maximum energy shower targeted by this calorimeter system. To encode the maximum photoelectron count down to the pedestal noise level, a 12-bit ADC is required.

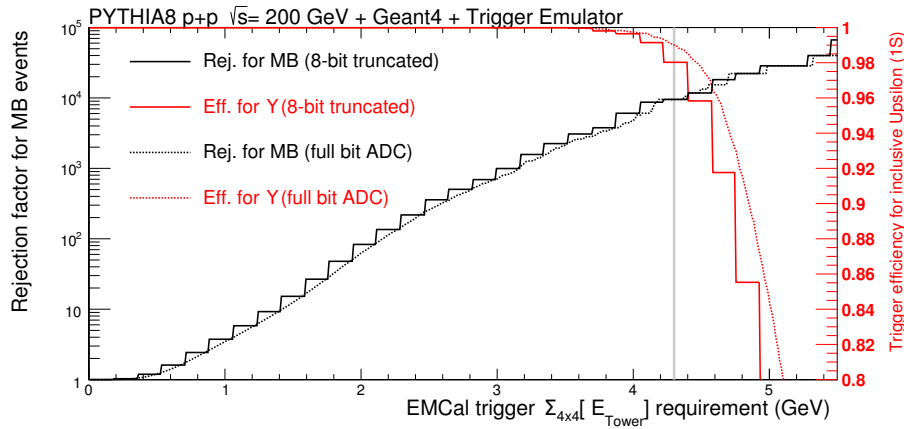


**Figure 5.29:** Rejection factor and efficiency for an Y-electron trigger, which requires some minimum amount of energy in a 4x4-tower of the 2D projective SPACAL ( $\Sigma_{4 \times 4}[E_{\text{Tower}}]$ ). Results are shown for a full PYTHIA and GEANT4 simulation of the detector response. The rejection factor for minimum bias  $p+p$  events (black lines) and the efficiency for Y (red lines) are plotted as a function of the required energy  $\Sigma_{4 \times 4}[E_{\text{Tower}}]$ . For the dashed lines, full bit-width ADC values were used in the trigger sum, while the solid line shows trigger performance when only the top 8-bit ADC information is used.



# Chapter 6

## Hadronic Calorimeter

The hadronic calorimeter or HCAL, essential for measurements of jets, is a steel-scintillator sampling calorimeter with two longitudinal segments, one inside the magnet and one outside the magnet. The outer hadronic calorimeter also serves as the flux return of the solenoid and supports the solenoid and the detector components inside the solenoid. This chapter describes the reference design of the detector, simulation results obtained with it, prototype detector components, and progress toward the development of a complete detector design.

### 6.1 HCAL Requirements and Overview

The performance requirements for the sPHENIX HCAL are driven by the physics requirements related to measuring jets in relativistic heavy ion collisions and the need to realize the HCAL in an efficient, cost-effective manner.

A uniform, hermetic acceptance is required between  $-1.1 < \eta < 1.1$  and  $0 < \phi < 2\pi$  to minimize the systematic errors associated with missing energy. For similar reasons, the HCAL is required to absorb  $>95\%$  of the hadronic energy, which sets the required depth to 5.5 nuclear interaction lengths. The very modest energy resolution requirement of  $\frac{\sigma}{E} = \frac{100\%}{\sqrt{E}}$  is adequate in heavy ion collisions due to the fact that at low energies the jet energy resolution is dominated by the subtraction of the underlying event and not the energy resolution of the HCAL. However, it is important to limit the non-Gaussian tails of the energy resolution function as knowledge of the tails in the energy response may limit the systematic errors in unfolding the jet spectra.

Key design aspects of the HCAL are determined by the mechanical and practical limitations. To limit civil construction in the 1008 interaction region, it is highly desirable that the sPHENIX detector fit through the existing shield wall opening. In addition, the engineering challenge of supporting the HCAL grows greatly as the radius of the detector increases,

which drives a design that makes use of the outer HCAL as the magnet flux return and drives the placement of the inner HCAL segment inside the magnetic solenoid. For these reasons we have chosen a novel tilted plate calorimeter design, which is described more fully in the following sections.

## 6.2 Detector Design

The design of the hadronic calorimeter has been developed by a program of simulation and prototyping which is continuing to optimize the design. The reference design being optimized consists of two longitudinal compartments of calorimeter, one inside the solenoid, which serves both to measure the longitudinal development of electromagnetic showers thus providing additional discrimination between electrons and hadrons beyond determination of  $E/p$  in the electromagnetic shower, and as the first nuclear interaction length of the hadronic calorimeter. In order to keep cost low, the inner and outer hadronic calorimeter sections are presently envisioned to use designs which are very similar to each other, although obviously some design choices must be adjusted for radial position and to optimize  $e/h$  separation.

The basic calorimeter concept is a sampling calorimeter with tapered absorber plates tilted from the radial direction to provide more uniform sampling in azimuth. Extruded tiles of plastic scintillator with an embedded wavelength shifting fiber are interspersed between the absorber plates and read out at the outer radius with silicon photomultipliers. The tilt angle is chosen so that a radial track from the center of the interaction region traverses at least four scintillator tiles. Each tile has a single SiPM and the analog signal from five of them are ganged to a single preamplifier channel to form a calorimeter tower. Tiles are divided in slices of pseudorapidity so that the overall segmentation is  $\Delta\eta \times \Delta\phi \sim 0.1 \times 0.1$ .

### 6.2.1 Scintillator

The scintillating tiles are similar to the design of scintillators for the T2K experiment by the INR group (Troitzk, Russia) who designed and built 875 mm long scintillation tiles with a serpentine wavelength shifting fiber readout [140]. The MINOS experiment developed similar extruded scintillator tiles. The properties of the HCAL scintillating tiles are listed in Table 6.1.

We have considered two wavelength shifting (WLS) fiber manufacturers: Saint-Gobain (formerly BICRON), product brand name BCF91A [141], and Kuraray, product name Y11 [142]. Both vendors offer single and double clad fibers. The Kuraray single clad fiber was chosen due to its flexibility and longevity which are critical in the geometry with multiple fiber bends. The properties of the HCAL wavelength shifting fibers are listed in Table 6.2

Property	
Plastic	Extruded polystyrene
Scintillation dopant	1.5% of PTP and 0.01% POPOP
Reflective coating	Proprietary coating by surface exposure to aromatic solvents
Reflective layer thickness	50 $\mu$
Wrapping	0.1 mm Al foil followed by one layer of 30 $\mu$ cling-wrap and a 100 $\mu$ layer of black TEDLAR
Attenuation length in lateral (with respect to extrusion) direction	$\sim 30$ mm
Wavelength shifting fiber	Single clad Kuraray Y11
Fiber size	1 mm round
Fiber core attenuation length	$> 2$ m
Optical cement	Epotek 3015

**Table 6.1:** Properties of HCAL scintillating tiles.

Property	
Fiber diameter	1.0 mm
Formulation	200, K-27, S-Type
Cladding	single
Cladding thickness	2 percent of d (0.02 mm)
Numerical Aperture (NA)	0.55
Emission angle	33.7 deg
Trapping Efficiency	3.1 percent
Core material	polystyrene (PS)
Core density	1.05 g/cc
Core refractive index	1.59
Cladding material	Polymethylmethacrylate (PMMA)
Cladding density	1.19 g/cc
Cladding refractive index	1.49
Color	green
Emission peak	476 nm
Absorption Peak	430 nm
Attenuation length	$> 3.5$ m
Minimum bending radius	100 mm

**Table 6.2:** Properties of Kuraray Y-11 (200) wavelength shifting fibers.

The scintillator emission spectrum and the fiber absorption spectrum are shown in Figure 6.1. The fiber routing was designed so that any energy deposited in the scintillator is

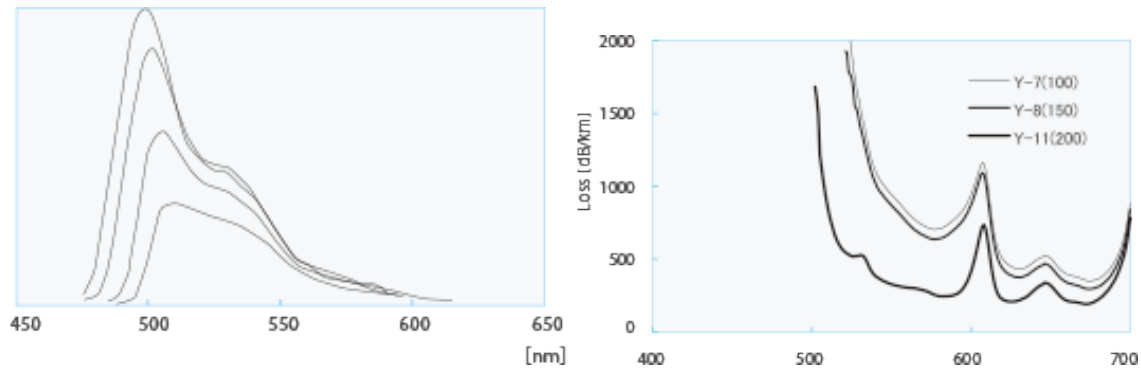


**Figure 6.1:** Y-11 (200) WLS fiber emission spectrum (left) and transmission loss (right).

within 2.5 cm of a WLS fiber, and the bend radius of any turn in the fiber has been limited to 35 mm based on T2K and our own empirical experience with test tiles.

The two ends of a fiber are brought to the outer radius of a tile where a small plastic holder carries a  $3 \times 3$  mm SiPM at 0.75 mm from the end of the polished fibers. The 0.75 mm gap is filled up with optical quality silicon (Dow Corning-3145 RTV). With this arrangement, we estimate that about 80% of the light can be collected from the fiber.

The inner and outer HCAL each require 12 different shaped tiles (both calorimeters are north-south symmetric).

### 6.2.2 Inner HCAL

The inner HCAL occupies a radial envelope bounded by 50 mm clearance inside the solenoid cryostat and the outer radius of the electromagnetic calorimeter. The skin on the inner radius provides support for the electromagnetic calorimeter and the HCAL, and rings at either end carry the load to the Outer HCAL.

Table 6.3 shows the basic mechanical parameters of the Inner HCAL reference design. The major components are 320 stainless steel absorber plates and 7680 scintillating tiles which are read out with SiPM's along the outer radius of the detector. The detector would be built in 32 modules, which would be wedge-shaped sectors containing 2 towers in  $\phi$  and 24 towers in  $\eta$  equipped with SiPM sensors, preamplifiers, and cables carrying the differential output of the preamplifiers to the digitizer system on the floor and upper platform of the detector. Figure 6.2 shows the arrangement of absorber plates in a sector (two towers in  $\phi$ ) with 10 scintillator tiles sandwiched between stainless steel absorber plates. The Inner HCAL modules are to be bolted together with spacers maintaining the 8.5 mm gap between plates for inserting the scintillator tiles. The plates would be assembled into mechanically complete modules at the steel vendor, at BNL, or at a collaborating institution. In parallel, scintillating tiles would be prepared with their SiPM's and LED flasher and tested with radioactive sources or cosmic rays before installation into the Inner



Parameter	Units	Value
Inner radius (envelope)	mm	1157
Outer radius (envelope)	mm	1370
Length (envelope)	mm	$2 \times 2175 = 4350$
Material		310 Stainless Steel
Number of towers in azimuth ( $\Delta\phi$ )		64
Number of tiles per tower		5
Number of towers in pseudorapidity ( $\Delta\eta$ )		24
Number of electronic channels (towers)		$64 \times 24 = 1536$
Number of modules (azimuthal slices)		32
Module weight (estimated)	kg	900
Number of towers per module		$2 \times 24 = 48$
Absorber plate thickness at inner radius	mm	10.2
Absorber plate thickness at outer radius	mm	14.7
Total number of absorber plates		$5 \times 64 = 320$
Tilt angle (relative to radius)	°	32
Scintillator thickness	mm	7
Gap thickness	mm	8.5
Size of tower at outer radius (approximate)	mm	132
Sampling fraction at inner radius		0.078
Sampling fraction at outer radius		0.060

**Table 6.3:** Design parameters for the Inner Hadronic Calorimeter.

HCAL modules. A potential assembly sequence for the Inner HCAL modules is shown in Figure 6.3.

The SiPM's on the tiles in a tower must be matched, because we plan to provide the same bias voltage on all five of the SiPM's in a tower. This should be possible by sorting the SiPM's according to the manufacturer's measurements. The SiPM sensors, preamplifiers, and cables are arranged on the outer circumference of the Inner HCAL, with cables exiting the two ends of the modules. Interface board mounted at the ends of the modules monitor the local temperatures and leakage currents, distribute the necessary voltages, and provide bias corrections for changes in temperature and leakage current. The current design plan is shown in Figure 6.4.

The Inner HCAL is designed to be inserted as a complete unit into the solenoid cryostat, and access to the on-detector electronics and cables would require the EMCAL to be removed and the Inner HCAL to be removed from its position inside the solenoid cryostat. Therefore, it is important that the Inner HCAL on-detector electronics be thoroughly tested and burned in before completing the assembly of the detector in the magnet.

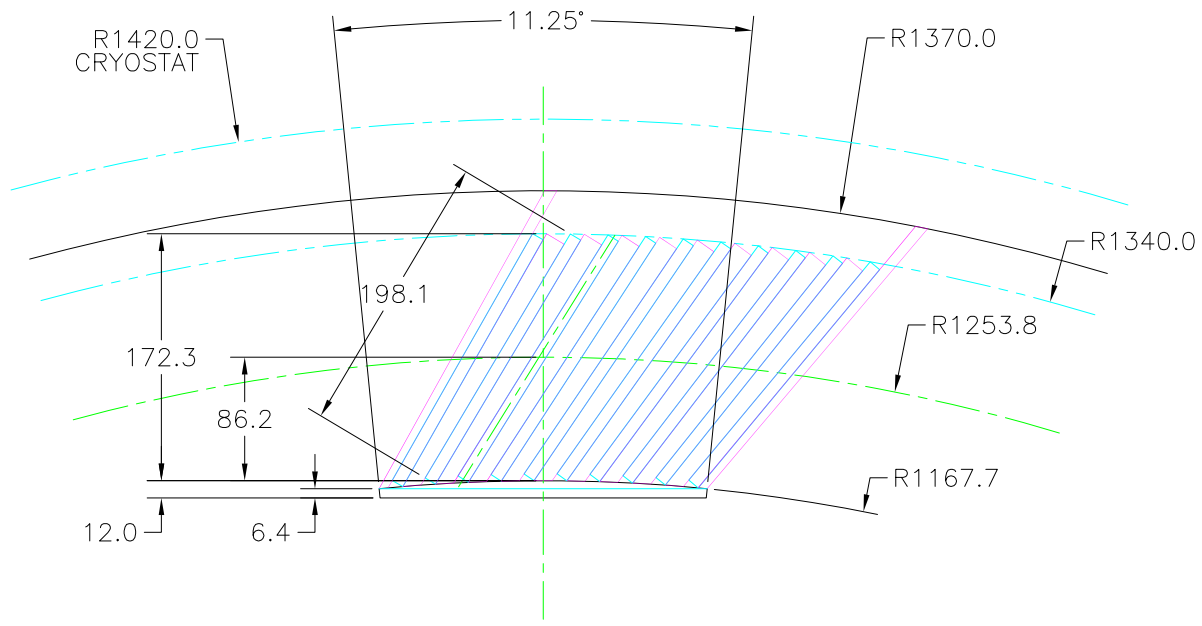


**Figure 6.2:** Transverse cut of an Inner HCAL module, showing the tilted tapered absorber plates. Light collection and cabling is on the outer radius at the top of the drawing.

### 6.2.3 Outer HCAL

The concept for the Outer HCAL is similar to the Inner HCAL. However, since the absorber occupies considerably more radial space in order to have a minimum thickness of  $5.5\lambda_I$ , a smaller tilt angle is needed to preserve the “4 crossing” geometry. Table 6.4 summarizes the major design parameters of the Outer HCAL, which is illustrated in Figure 6.5.

The Outer HCAL can serve as the flux return of the solenoid since the absorber plates are planned to be single long plates running along the field direction.

The Outer HCAL SiPM sensors and electronics are to be arranged on the outer circumference of the detector.

### 6.2.4 Electronics

#### Light Coupling

Experience in constructing the first prototype demonstrated the difficulty of working with a large number of fragile 1 mm fibers which need to be coupled to SiPM's outside the active volume of the detector. The next prototype will have a single SiPM on every tile in a tower (thus, a tower will have 5 SiPM's instead of one). Design work on a new SiPM mounting fixture that will allow a single SiPM to be coupled to the the fibers from a tile

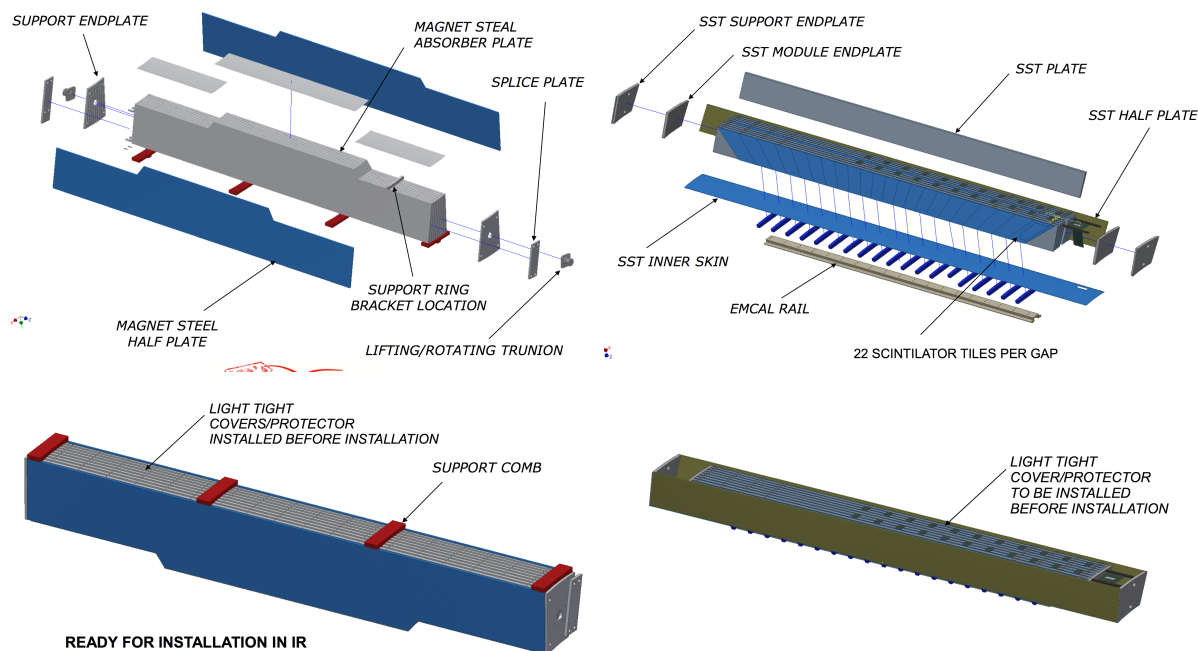


**Figure 6.3:** Assembly of inner HCAL modules.

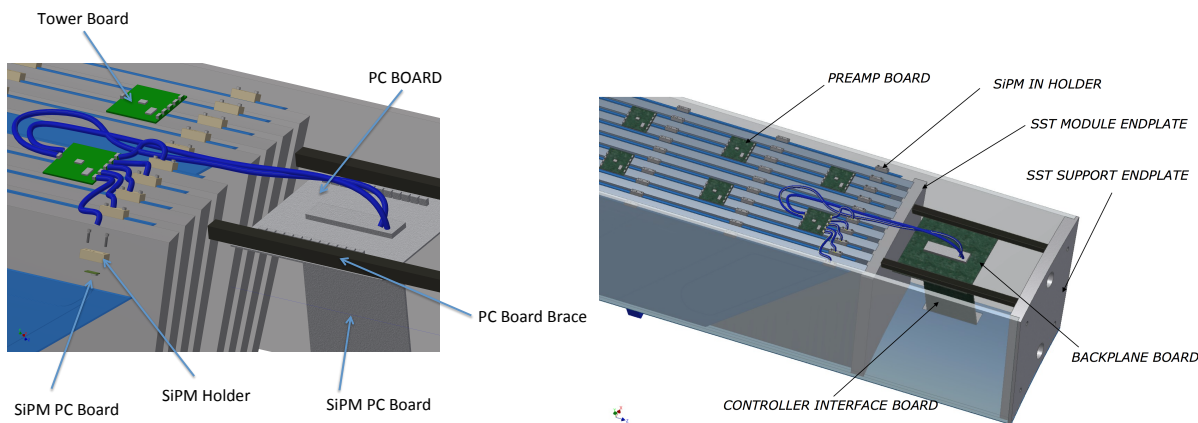


**Figure 6.4:** The current design for electronics and cable routing from inner HCAL sector. The SiPM holders are mounted directly on the end of the tile with a single preamplifier/shaper/driver board mounted nearby. An Interface Board at the end of the sector, provides power and bias voltage distribution and local monitoring.

and can be printed using a 3-D commercial printer and is shown in Figure 6.6. This design will allow for a simpler attachment of the SiPM with reduced risk to damaging the fibers.

Parameter	Units	Value
Inner radius (envelope)	mm	1820
Outer radius (envelope)	mm	2685
Length (envelope)	mm	$2 \times 2175 = 4350$
Material		1006 magnet steel
Number of towers in azimuth ( $\Delta\phi$ )		64
Number of tiles per tower		5
Number of towers in pseudorapidity ( $\Delta\eta$ )		24
Number of electronic channels (towers)		$64 \times 24 = 1536$
Number of modules (azimuthal slices)		32
Module weight (estimated)	kg	900
Number of towers per module		$2 \times 24 = 48$
Absorber plate thickness at inner radius	mm	10.2
Absorber plate thickness at outer radius	mm	14.7
Total number of absorber plates		$5 \times 64 = 320$
Tilt angle (relative to radius)	°	12
Scintillator thickness	mm	7
Gap thickness	mm	8.5
Size of tower at outer radius (approximate)	mm	132
Sampling fraction at inner radius		0.037
Sampling fraction at outer radius		0.028

**Table 6.4:** Design parameters for the Outer Hadronic Calorimeter.

## LED Calibration System

In order to monitor changes in relative gain between scintillator panels in the HCAL, the design incorporates an LED calibration system. The sPHENIX LED Calibration System is integrated into the Slow Controls system to eliminate additional cabling and circuitry on the detector. The Timing System generates a calibration logic pulse whose leading edge is used to initiate a pulse of light in one or more UV LEDs located on the light collection optics on the detector. This logic pulse is connected to the front panel of the sPHENIX Slow Controls Crate Controller which drives it onto the Slow Controls Crate standard VME P1 backplane. The Slot Controller logic in any of up to sixteen such controllers then determines whether or not to pass this pulse on to the Interface via its differential data output line. Prior to passing the pulse to the Interface the Slot Controller sets the Interface Pulse Enable Mask register to enable selected LEDs to be driven. The pulse leading edge then triggers a one-shot multivibrator which is set to produce a fixed length pulse to a driver which drives the LED. Figure 6.7 shows a block diagram of the LED pulser system.

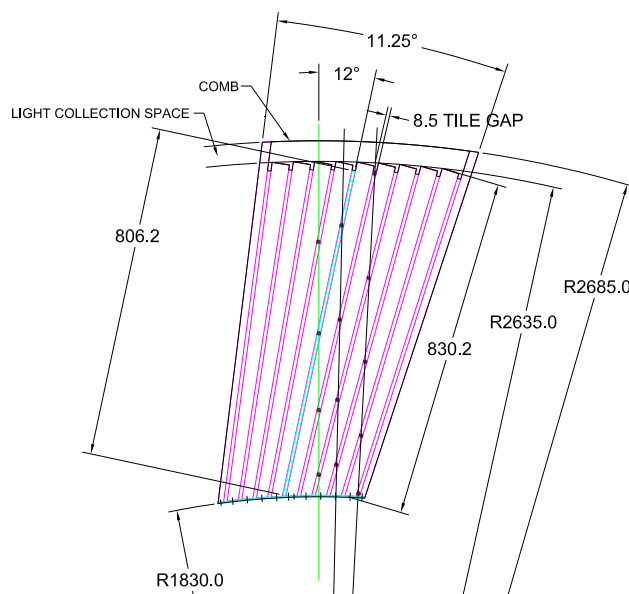


**Figure 6.5:** Transverse cut of an Outer HCal module, showing the tilted tapered absorber plates. Light collection and cabling is on the outer radius at the top of the drawing.

### 6.2.5 Calibration

A preliminary plan for calibration of the detector has been developed which relies on the LED pulser system for tracking short term gain changes caused by temperature compensation of the SiPM's and increased leakage current caused by radiation damage. A switchable high gain amplifier output with sufficient gain to see minimum ionizing particles has been provided, and the concept will be tested in beam and bench tests.

### 6.2.6 Mechanical Design

The current design concept for the Outer and Inner Hadronic calorimeter subsystems relies on load transfer scheme where the tilted stainless steel plates in the Inner HCal and steel plates in the Outer HCal form the primary structural members for transferring loads. The concept further requires the Inner HCal to support the EMCal and the Outer HCal must support the Inner HCal and the superconducting solenoid magnet independently. The Inner HCal is comprised of 32 independent sectors joined at its longitudinal ends by stainless steel rings, to integrate the sectors into a single entity which is installed inside and through the solenoid magnet and mounted to the Outer HCal by mounting rings on either end. The Outer HCal sectors are joined at their longitudinal ends by steel splice plates between adjacent sectors into a single unit, which is mounted on the Central Platform. The reference design for the Inner and Outer HCal support structure is shown in Figure 6.8.

Validation of this mounting scheme has been demonstrated using finite element modeling

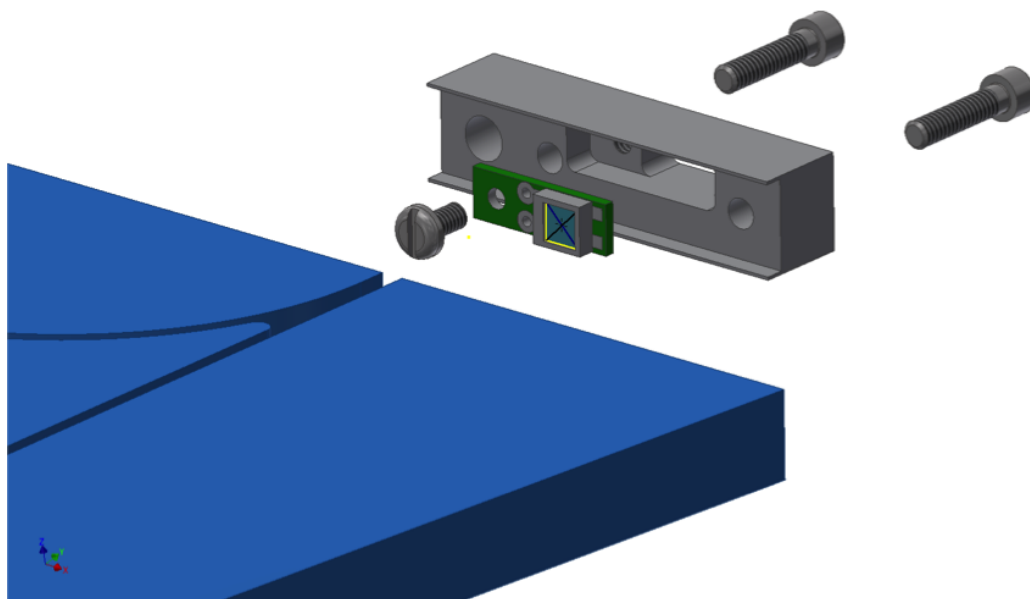


**Figure 6.6:** Design of the small plastic fixture coupling the fiber to an SiPM.

and analyses to calculate the stresses and displacements of the design concept. Analyses of the Inner HCal structure with and without EMCal loads has been performed and an example of the results is shown in Figure 6.9, showing that the final assembly deformation is within the tolerance necessary to be certain that scintillator tiles are not compressed. Similarly, analyses of the Outer HCal structure and multiple Inner HCal installation concepts have been performed to validate the concepts.

## 6.3 Simulations

### 6.3.1 Simulation Framework

A series of GEANT4 simulations of the combined EMCal + HCAL calorimeter system have been performed in order to characterize the basic, fundamental performance of the baseline system and to demonstrate the effect of design choices on the performance of the calorimeter system. Figure 6.10 shows an example event display of a 10 GeV pion shower in the GEANT4 Monte Carlo.

The simulations of the HCAL are based on the GEANT4 simulation toolkit[137]. It provides physics lists - pre-defined collections of physics processes suitable for different

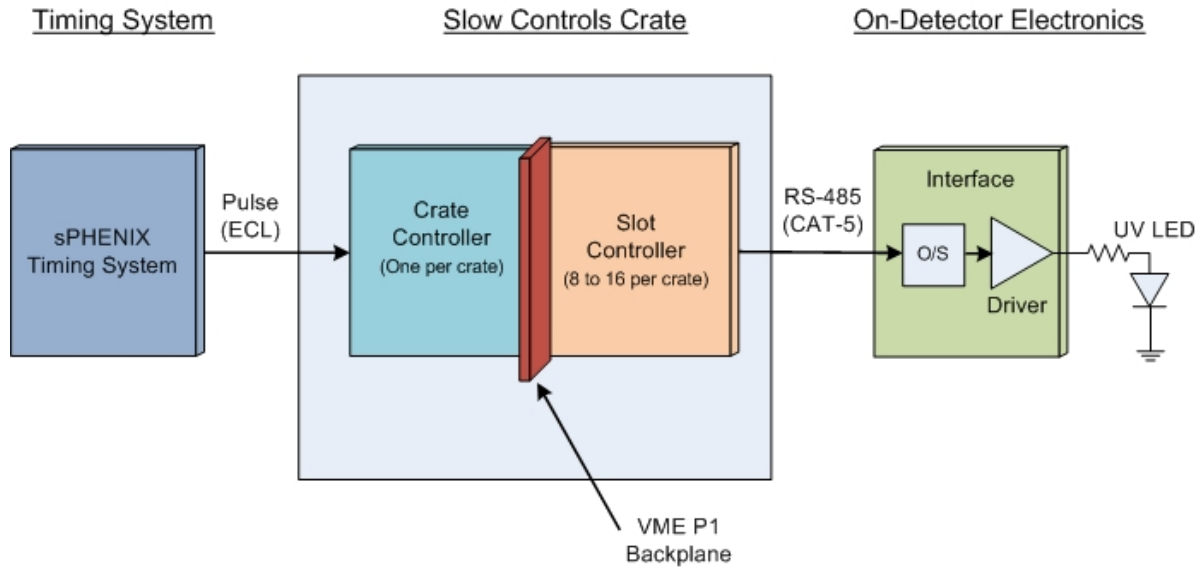


**Figure 6.7:** Design of the LED calibration system.

applications. We selected the QGSP\_BERT\_HP list which is recommended for high energy calorimeter simulations and is employed by CMS and ATLAS. This list incorporates a high precision neutron tracking package for low energy neutrons which is necessary for realistic calorimeter simulations. Birks law is applied to the ionization energy deposited in the scintillator to account for saturation effects. Magnetic field maps for the BaBar magnet have been imported from OPERA calculations. The magnetic field map in the region of the outer HCAL takes its geometry into account with the field concentrated in the steel plates and the scintillators in a field free region.

The superconducting magnet is simulated with the proper location and material of the cryostat. All simulated tracks which reach a layer 10 cm outside the outer HCAL are aborted and their energy recorded to yield an estimate of the leakage from the back of the outer HCAL. The energy deposited in the absorber is recorded. This information is used to calculate the sampling fraction.

The implementation of the hadronic calorimeters is highly configurable. This allows for the investigation of different design choices (inner and outer radius, plate tilt angle, gap size for scintillator, scintillator thickness, pseudo rapidity coverage, and so on). The single particle simulations were done using fixed momenta with a random pseudo rapidity in ranges of 0.1 and random azimuthal emission angle. The vertex was randomized along the beam axis within  $\pm 10$ cm.

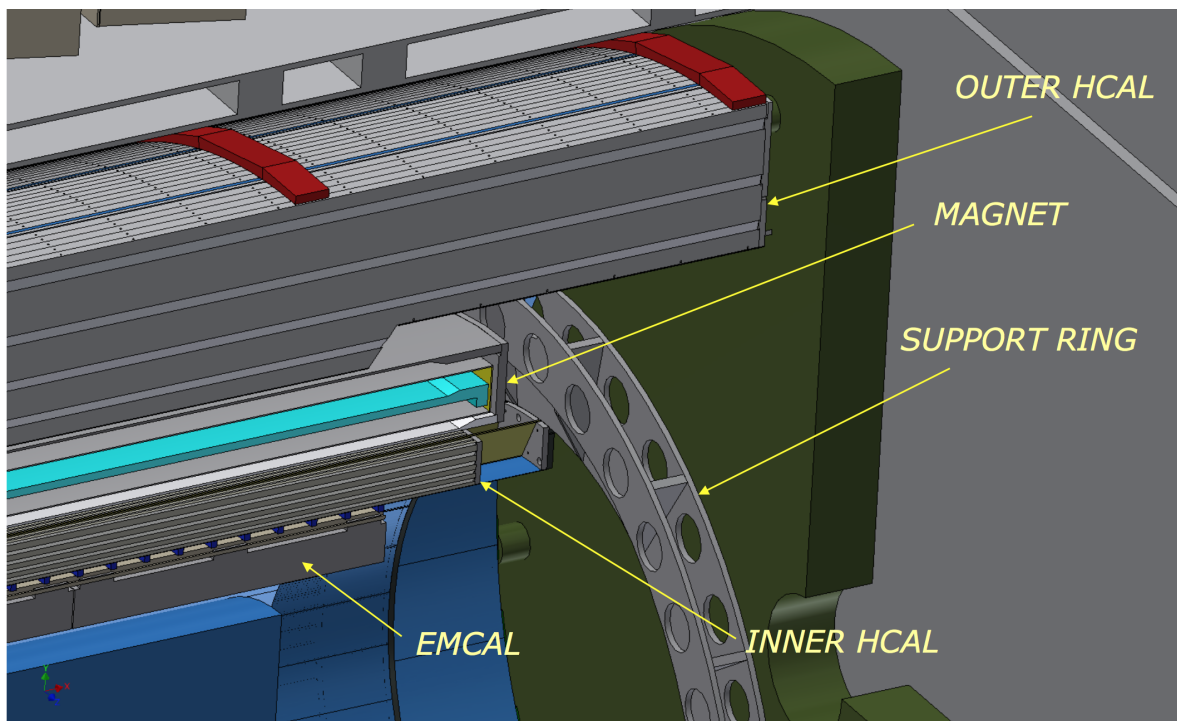


**Figure 6.8:** Inner and Outer HCAL with support structure.

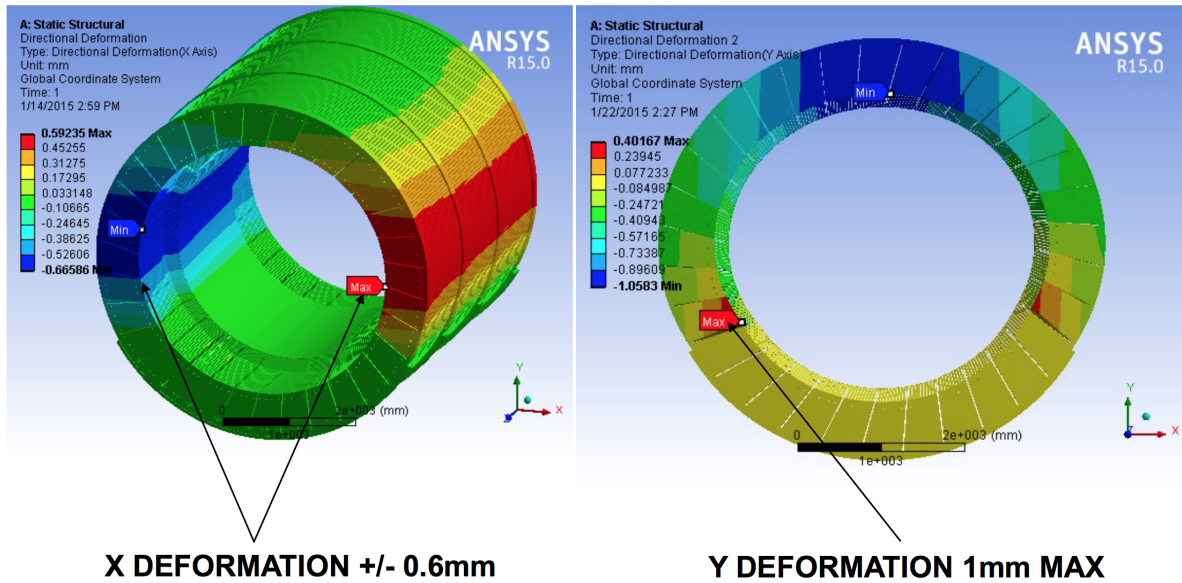
### 6.3.2 Single Particle Simulations

In the sections that follow, we describe a set of single-particle GEANT4 simulations designed to elucidate the effect of design choices on the calorimeter systems performance. It should be noted that while in general the GEANT4 simulations show a better energy resolution than is anticipated in the real device, particularly at low energies, we are not predicting the ultimate performance but rather comparing the variation between designs from a reference design.

The simulations described in this section focus on a limited set of key configurations:

- A "reference" configuration of the sPHENIX calorimetry system, as described in this document. In particular, the inner HCAL tilt angle is 32 degrees and the outer HCAL tilt angle is 12 degrees.
- A variety of tilt angles in the inner and outer HCAL to study the effect of the tilt angle on calorimeter performance.
- A configuration in which a compensating correction is introduced to account for the variation of the sampling fraction in the inner and outer HCAL as a function of depth.





**FINAL ASSEMBLY DEFORMATION IS WITHIN TOLERANCE**

**Figure 6.9:** Results of finite element analysis of Outer HCAL after final assembly, showing the maximum deformation of the structure.

For each configuration we characterize the performance of the calorimetry system by both the Gaussian and non-Gaussian components of the energy response.

For the tilt angle studies, the angles were chosen to correspond to the number of scintillator crossings a ray from the vertex will encounter in passing through the inner/outer HCAL compartments. Zero crossings corresponds to the steel and scintillator plates oriented radially (no tilt). The sPHENIX reference configuration corresponds to four crossings, see Figure 6.11.

Large numbers of crossings (large tilt angles) can change the effective depth of the HCAL system in units of nuclear interaction length. Using the material scan function in GEANT4, the interaction length,  $\lambda_0$ , of the calorimeter system was measured as a function of  $\eta$  and tilt angle (see Figure 6.12). The simulation includes the EMCal, inner HCAL, magnet and outer HCAL, which contribute roughly 13%, 17%, 3% and 67% of the total path length respectively. (Due to the modular structure of the detectors, there is some variation in the value of  $\lambda_0$  as a function of  $\phi$ . Figure 6.12 shows the mean value at each  $\eta$  position.) The change in slope as a function of  $\eta$  results from the shape of the outer HCAL scintillator tiles shown in Figure 6.13. The variation in the effective depth between one to four crossings is rather small. However, by 10 crossings the interaction length of the calorimeter system is reduced significantly. The effects of this are evident in the energy resolution and leakage characteristics of the calorimeter system, as discussed in the following sections.

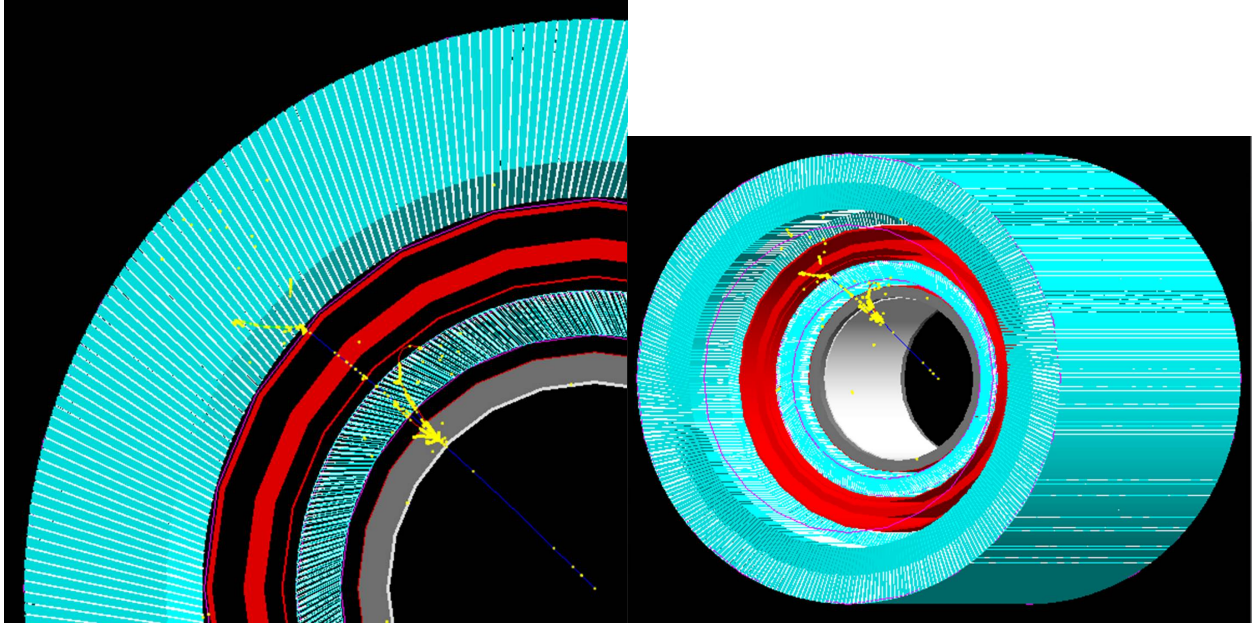


**Figure 6.10:** GEANT4 event display of a 10 GeV  $\pi$  shower in the sPHENIX calorimeter system.

### 6.3.3 Baseline Performance

Figure 6.14 shows the energy resolution of the combined sPHENIX calorimetry system for negative pions from 1-50 GeV for different  $\eta$  selections. This plot was generated by first measuring the average sampling fraction in the EMCal, and inner and outer HCAL, by summing the energy deposited in both the scintillator and absorber material in the Monte Carlo. The energy deposited in the scintillator was modified according to a Birks factor correction. The average sampling fractions were measured using the  $>10$  GeV shower samples for  $\eta = 0.30$  and were measured to be 2.4%/6.7%/3.5% in the EMCal/inner HCAL/outer HCAL, respectively. Using the average sampling fractions, the summed energy in each compartment was corrected and combined to yield the calorimeter response. No towering or clustering algorithms were applied, but all energy was summed, as we were interested in study the intrinsic response of the calorimeter due only to its geometry. It is important to note that this will result in an energy resolution that will be better than what can be achieved in a realistic detector, but in the studies that followed we wanted to be sensitive to potentially quite small changes in the performance of the device as we changed design parameters, and not have small changes hidden by additional sources of fluctuations. Of course, it will need to be determined if design variations result in improvements that will still be meaningful in a realistic detector configuration.

The resolutions shown in Figure 6.14 are taken from the  $\sigma$  of a Gaussian fit to the calorimeter response at each energy. In general the energy response is fit quite well by a Gaussian with small deviations in the tails, which is quantified further below. Please note that the energy resolution shown is the energy resolution for the combined sPHENIX calorimeter system

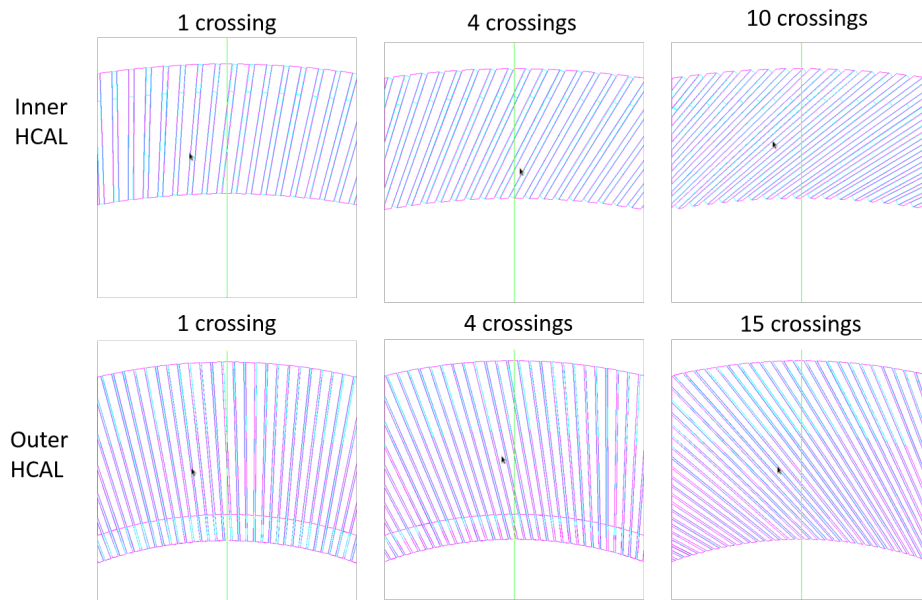


**Figure 6.11:** GEANT4 visualizations of the inner (top row) and outer (bottom row) HCAL geometry for different crossing values. A crossing value of four is the reference configuration, corresponding to tilt angles of 36 and 12 degrees, respectively, in the inner and outer HCAL engineering drawings.

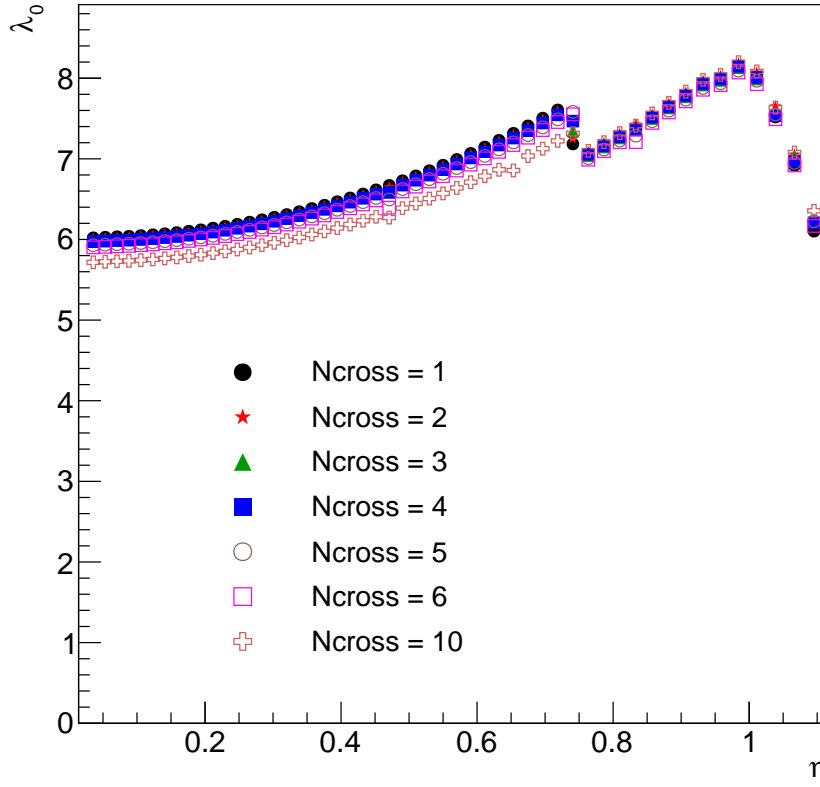
in simulations, combining the EMCal and inner and outer HCAL section, and not just the resolution of the HCAL alone.

Figure 6.15 shows the energy linearity of the combined sPHENIX calorimetry system response for negative pions from 1-50 GeV for different  $\eta$  selections. While the response is quite linear, the actual slope varies slightly as a function of  $\eta$ .

In order to characterize the non-Gaussian component of the calorimeter response, the Gaussian fit used to determine the resolution was used as a comparison to count the overall fraction of events that were above and below  $2\sigma$  of the Gaussian fit mean. If the fit were perfectly Gaussian, these fractions should be constant at 2.5% of the total each for the high and low side statistic. Figure 6.16 shows the non-Gaussian tails metric for negative pion showers for the reference sPHENIX design.

As can be seen in Figure 6.16, two features are clearly evident. The first is a high-side tail at low energies that becomes consistent with a Gaussian response for higher energy showers. We believe that this arises from the granularity of the sPHENIX inner HCAL and an  $e/h$  ratio that deviates from unity, combined with fluctuations in the development of the hadronic shower. Simulations show that events in the tail correspond to over-sampling (compared to the average) of the energy in the scintillator in the inner HCAL.

An opposite effect is observed in the development of a low-side tail in the energy response at high energies, with a characteristic pattern as a function of  $\eta$ . This low-side tail originates from events that shower later in the sPHENIX calorimetry system, leaving most of their



**Figure 6.12:** GEANT4 calorimetry material scan in nuclear interaction lengths vs. pseudorapidity for a variety of crossing angle configurations.

energy in the outer HCAL. These events results in a low-side tail for two reasons, First, the sampling fraction of the HCAL compartments decreases with depth because the steel plates grow in thickness while the scintillator panels are constant thickness. Second, for these events leakage of energy out the back of the calorimeter is a significant effect. As can be seen in Figure 6.12 the thickness of the calorimeter grows as a function of  $\eta$ , which results in the strength of the low-side tail decreasing as a function of  $\eta$ .

#### 6.3.4 Tilt Angle Studies

The tilt angle of the inner and outer HCAL is a key design parameter. While the presence of a magnetic field during normal operation of sPHENIX will prevent particles from channeling down the scintillator tiles, some tilt angle should be chosen to maintain performance during zero field calibration running. The chosen tilt angle should optimize performance as much as possible with mechanical constraints, and be consistent with readout requirements. The tilt angle should be be overly large as a large tilt angle decreases

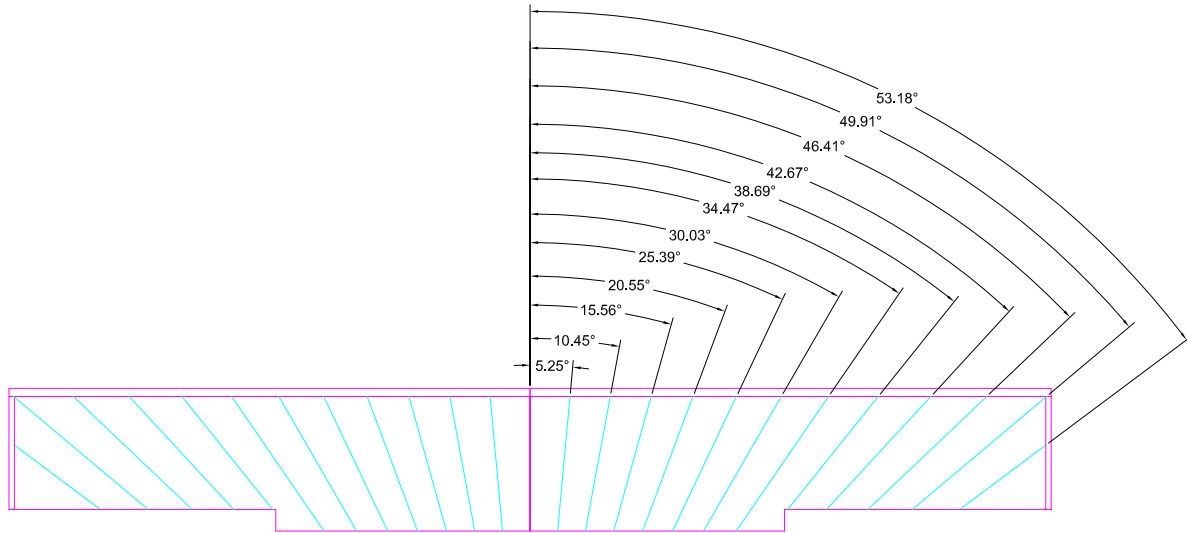


**Figure 6.13:** Scintillator tiles in a layer of the Outer HCAL.

the effective depth of the calorimeter system (see Figure 6.12). In addition, the effective sampling fractions in the inner and outer HCAL sections also vary with the tilt angle.

For this study, crossing configurations of 0,1,2,3,5,6 and 10 crossings were chosen for the inner and outer HCAL (see Figure 6.11). Note that both the inner and outer HCAL tilt angles were varied at the same time due to constraints in the Monte Carlo, and the inner and outer HCAL tilts are opposite of each other. The Gaussian and non-Gaussian energy response was characterized as described in previous sections, and is plotted in Figures 6.18, 6.19 and 6.20. For clarity, we plot the variation of the energy resolution at a single energy (24 GeV) in Figure 6.18. To highlight the behavior of the low- and high-side non-Gaussian tails, we plot the metric at 2 GeV (Figure 6.19) and 50 GeV (Figure 6.20).

As can be seen in Figures 6.18, 6.19 and 6.20 the character of the energy response is not a strong function of the tilt angle of the inner and outer HCAL segments. There is some advantage to avoiding a small tilt angle to avoid channeling in zero field running, and a large tilt angle tends to make the calorimeter less deep, increasing leakage and the low-side tail in the energy response at high energies. Based on these, the choice of tilt angles based on four crossings is consistent with the required performance.

### 6.3.5 Sampling Fraction Variation

Finally, we examine the effect of the sampling fraction variation as a function of depth in the inner and outer HCAL compartments. As noted previously, the steel plates in each section widen with radius while the scintillator panels maintain a constant thickness, resulting in a reduced sampling fraction as shown in Figure 6.21. The goal of this study is to investigate if degrading the light response of the tile to even out the sampling fraction as



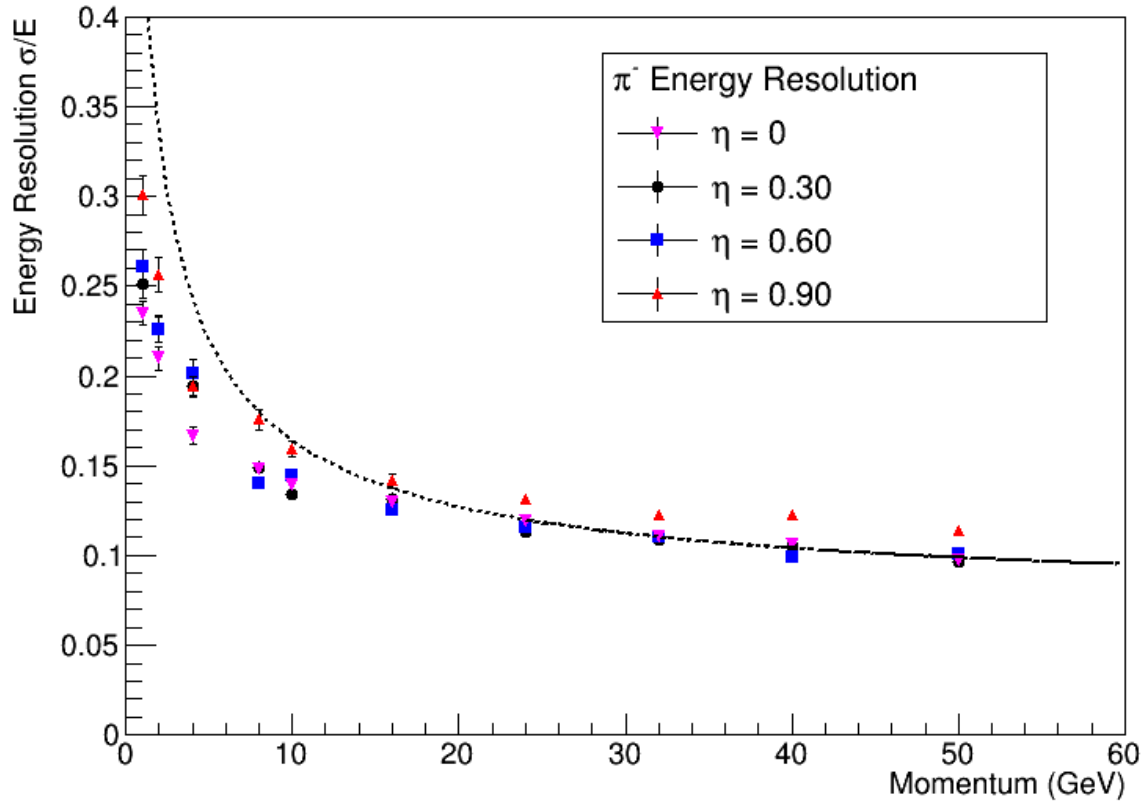


**Figure 6.14:** Combined calorimeter energy resolution from GEANT4 simulations of the EMCAL and inner and outer HCAL for negative pions. The dashed line is a fit to the  $\eta = 0$  data points above 16 GeV corresponding to  $\frac{\sigma}{E} = \frac{46\%}{\sqrt{E}} \oplus 7.4\%$ .

a function of depth would improve the energy response of the calorimetry system (albeit with a corresponding loss of light)

Using the results from Figure 6.21, a correction was applied to the energy response as a function of depth along the scintillator tile to decrease the response at inner radii. This correction was applied at the GEANT4 step level, and can be thought of as grading the light yield of the tile from the inner to out radius with, for example, and varying coating in the tile surface.

With this correction in place, new effective sampling fractions were extracted from the Monte Carlo for the inner and outer HCAL, which can now be seen to be independent of depth in the inner and outer HCAL (see Figure 6.21). The energy response is then calculated using the new sampling fractions, and changes in the energy resolution and non-Gaussian response from the baseline design (without the light yield correction) are shown in Figures 6.22 and 6.23.

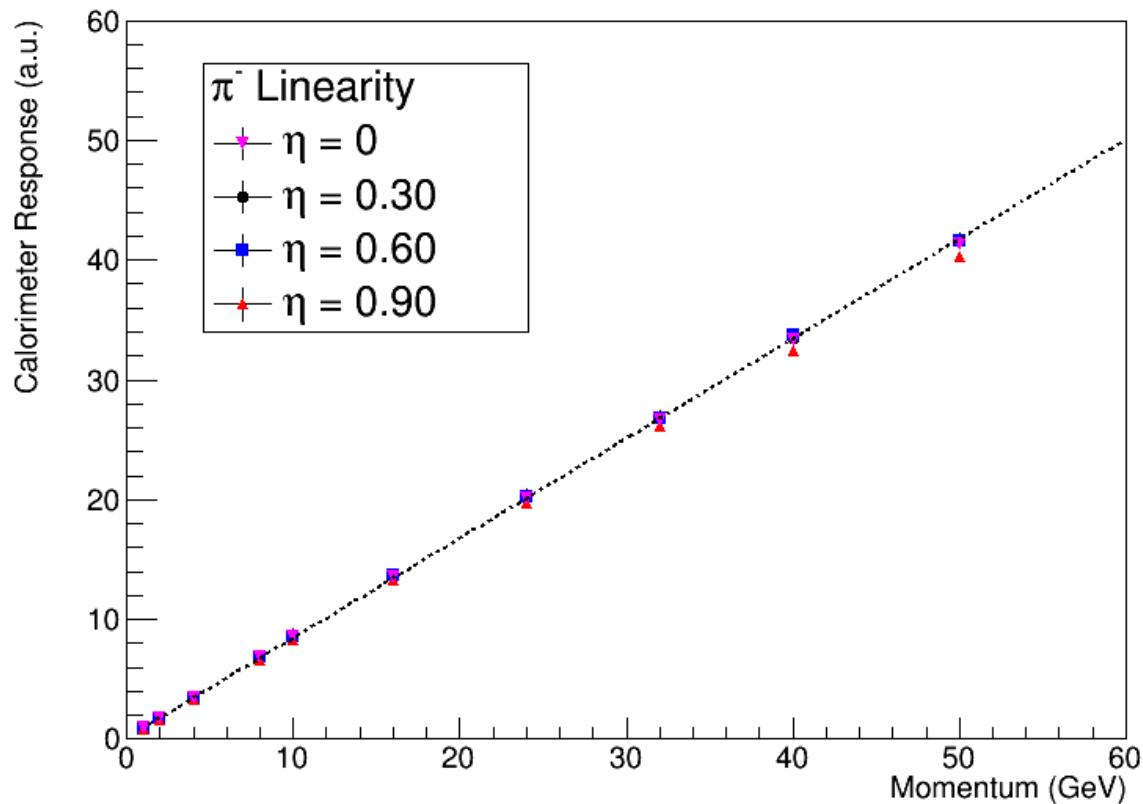


**Figure 6.15:** Linearity of the sPHENIX calorimetry system response for negative pions as a function of pion momentum and different  $\eta$  selections. The line is a linear fit to the  $\eta=0$  data points.

From Figure 6.22 we can see that a small improvement in the energy resolution (0.5% absolute) is achieved with the light yield correction. In addition, Figure 6.23 shows a modest improvement in the low-side tails at high energy, at the expense of slightly enhanced high-side tails. However, both of these changes are quite small and would likely be lost in a realistic device when towering and clustering are included. Therefore, from this study we conclude that variation in the sampling fraction as a function of depth in the sPHENIX HCAL system is not a significant contributor to either the energy resolution or the non-Gaussian tails in the energy response.

### 6.3.6 HCAL Dynamic Range

The maximum energy deposited in Inner and Outer HCAL towers has been calculated with the GEANT Monte Carlo for 50 GeV protons (Figure 6.24) to check that the dynamic range of the amplifier and digitizer are sufficient for measurements over the full range of

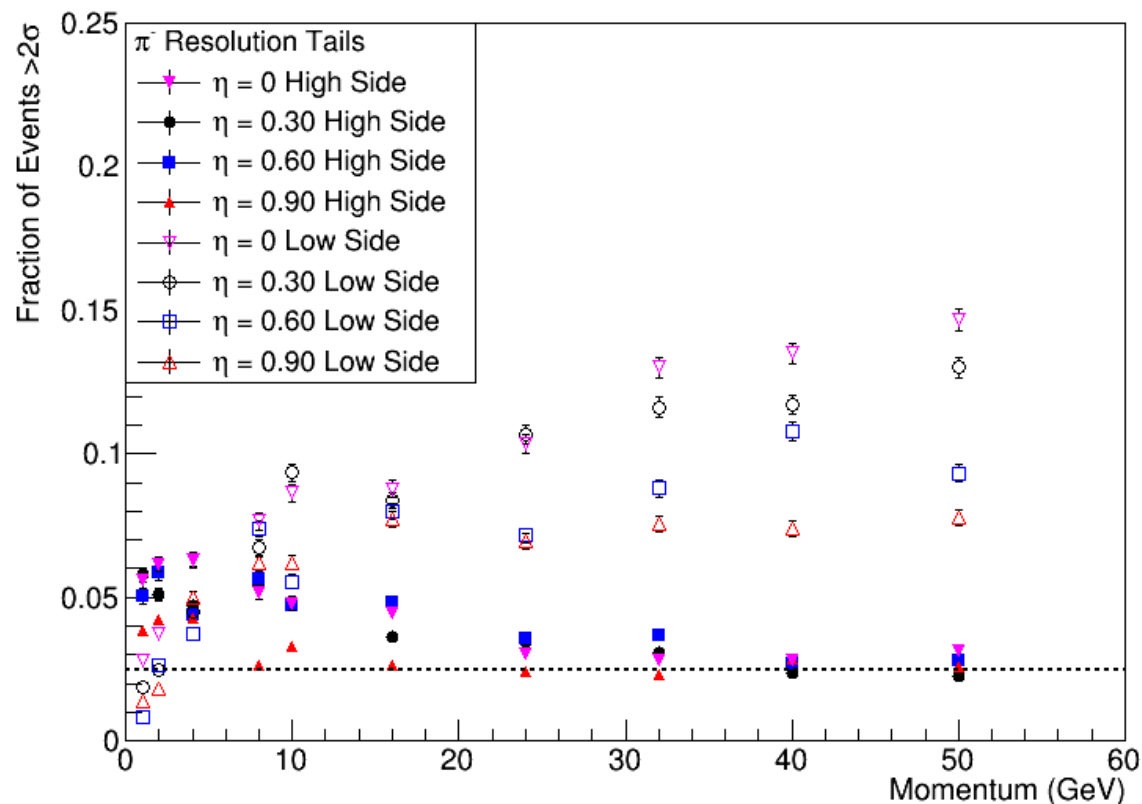


**Figure 6.16:** Behavior of non-Gaussian tails in the energy resolution function from GEANT4 simulations of the EMCAL and inner and outer HCAL for negative pions. The dashed line at 2.5% would characterize a purely Gaussian response.

energies.

## 6.4 Prototyping and R&D

### 6.4.1 Results from HCAL Prototype Test Beam

A beam test of an early HCAL prototype was performed at the test beam facility at Fermilab National Accelerator Laboratory (FNAL) in February of 2014. The results of this study sheds light on the fundamental understanding of the performance of a tiled-tile hadronic calorimeter which includes the energy resolution, signal linearity and the  $e/h$  ratio.

The HCAL prototype consisted of two segments: inner HCAL (H1) and outer HCAL (H2). Both H1 and H2 have 16 layers of steel plates and scintillator tiles as shown in Fig. 6.25. Figure 6.25 also shows photos of the grooved scintillator sheets used in the prototype. The



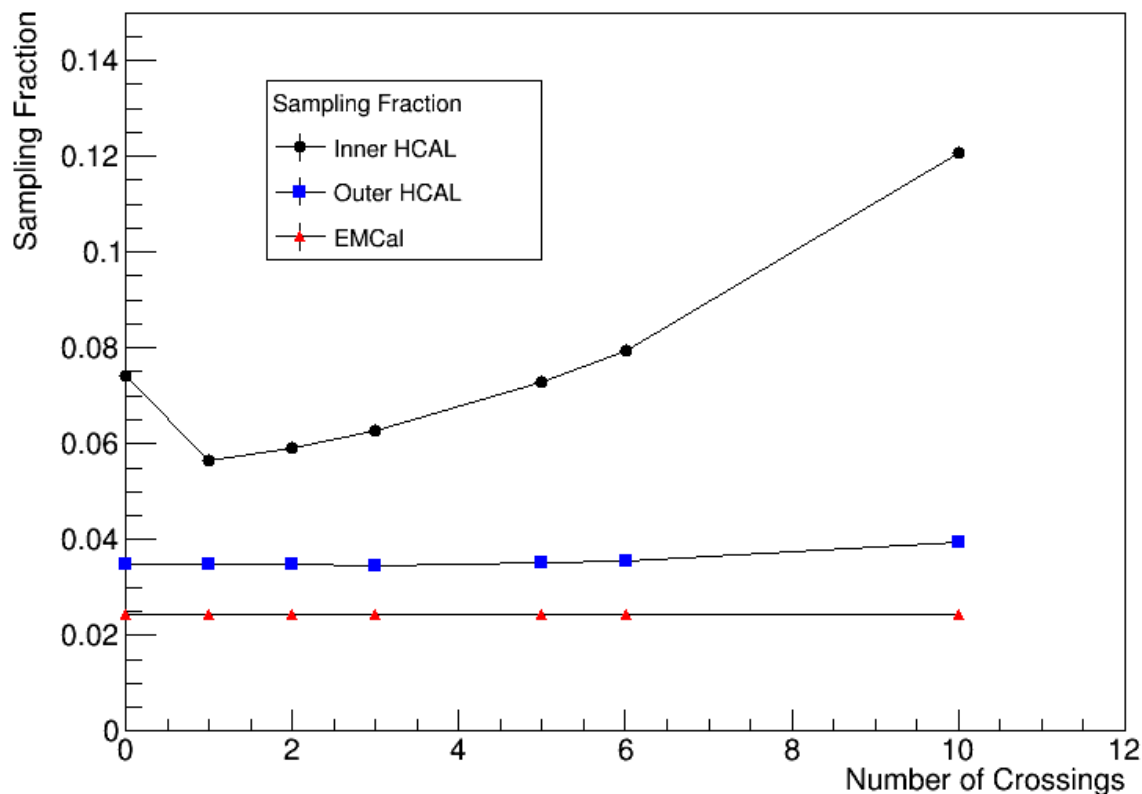


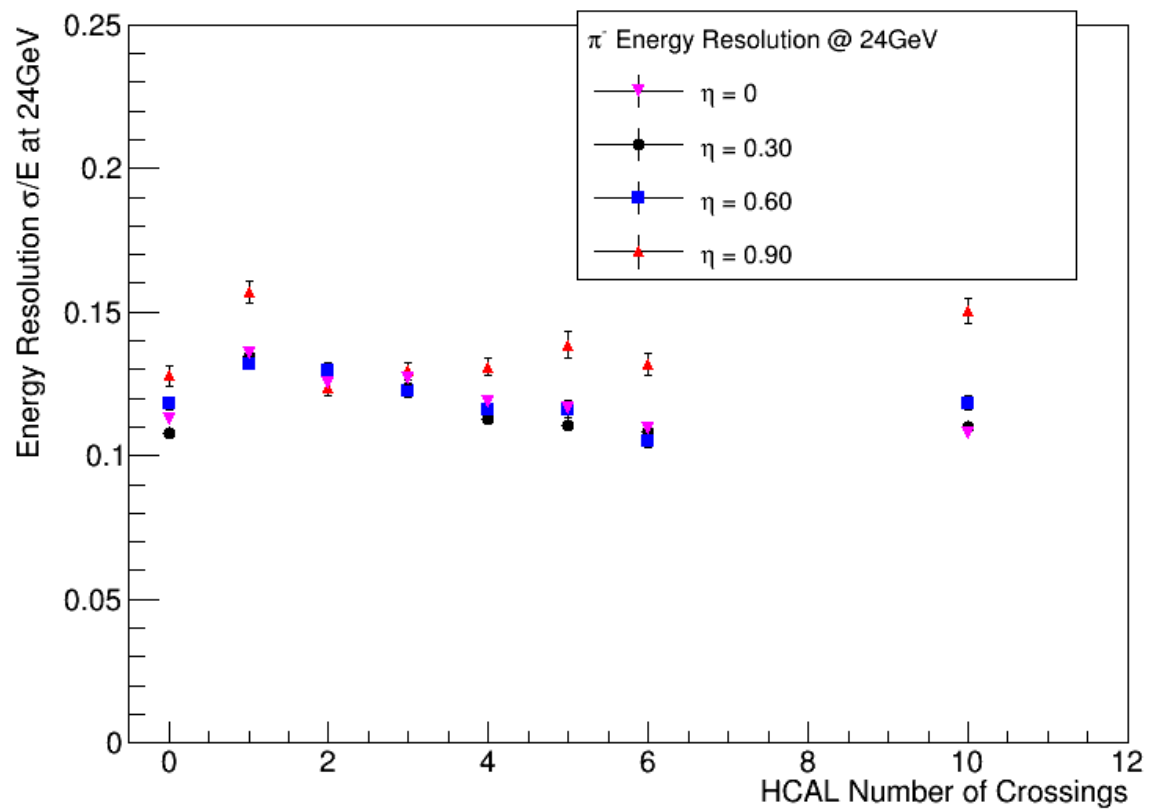
**Figure 6.17:** Variation of the EMCal and inner and outer HCAL sampling fractions as a function of number of crossings in the inner and outer HCAL.

steel plates and scintillator tiles in H1 and H2 are tilted in opposite directions to avoid particle channeling.

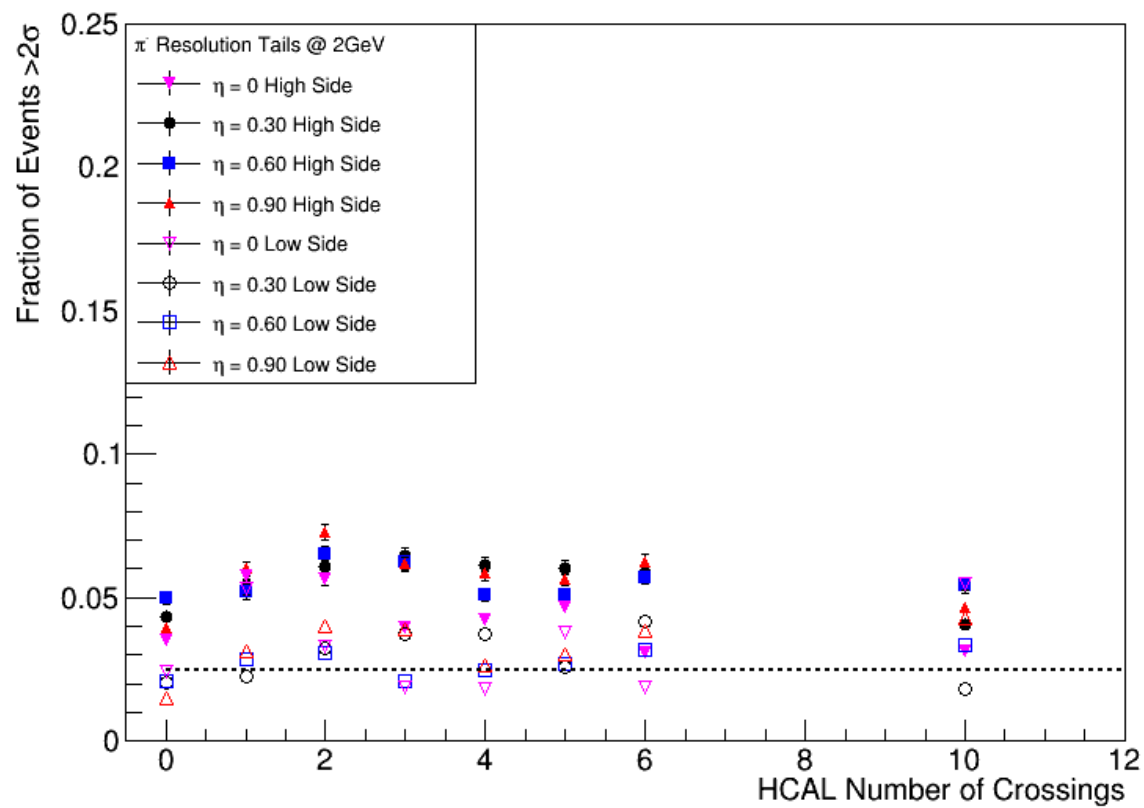
The entire HCAL prototype measured 1.2 m x 1.7 m x 1.3 m and weighed about 8,000 lbs mounted on a support structure. The prototype and support structure was built and assembled at Brookhaven National Lab by the PHENIX Tech Team.

Figure 6.26 shows the HCAL prototype mounted on a movable lift table which can be moved horizontally along the z-axis (perpendicular to the beam) and vertically along the y-axis. One could also rotate the HCAL prototype about the z and y axis. Four scintillator paddles were used (two at the top and two on bottom) as the cosmic ray trigger.

Test beam data were recorded with beam energies ranging from 4 GeV to 60 GeV for normal detector configuration (28.5 inches in height and no rotation about x and y axis). We also took HCAL data by moving it vertically to different heights together with a few selected rotational angles at 30 GeV beam energy. In total, 142 k events were recorded with nominal detector configuration with beam energies between 4 and 60 GeV, and 254 k events were recorded in various detector height and rotation with 30 GeV beam.



**Figure 6.18:** Gaussian energy resolution as a function of crossing angle for 24 GeV pions.



**Figure 6.19:** Non-Gaussian tails to the energy response as a function of crossing angle for 2 GeV pions.

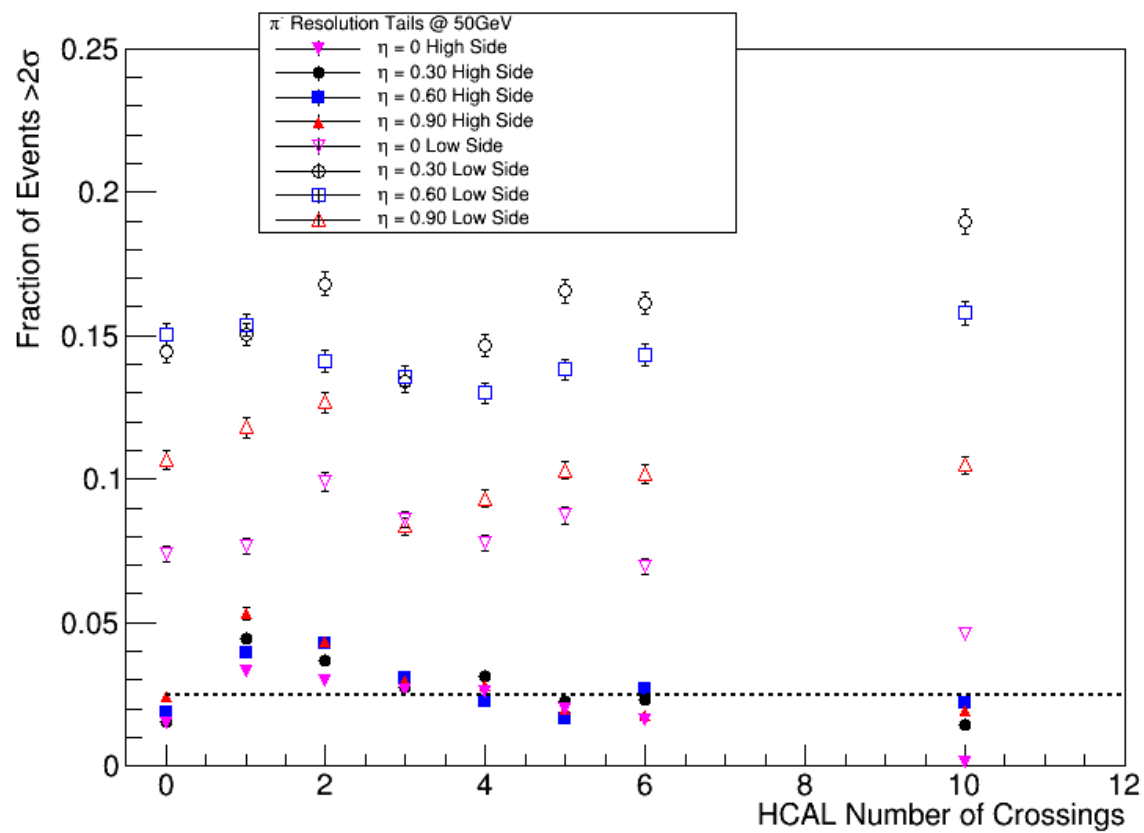


**Figure 6.20:** Non-Gaussian tails to the energy response as a function of crossing angle for 50 GeV pions.

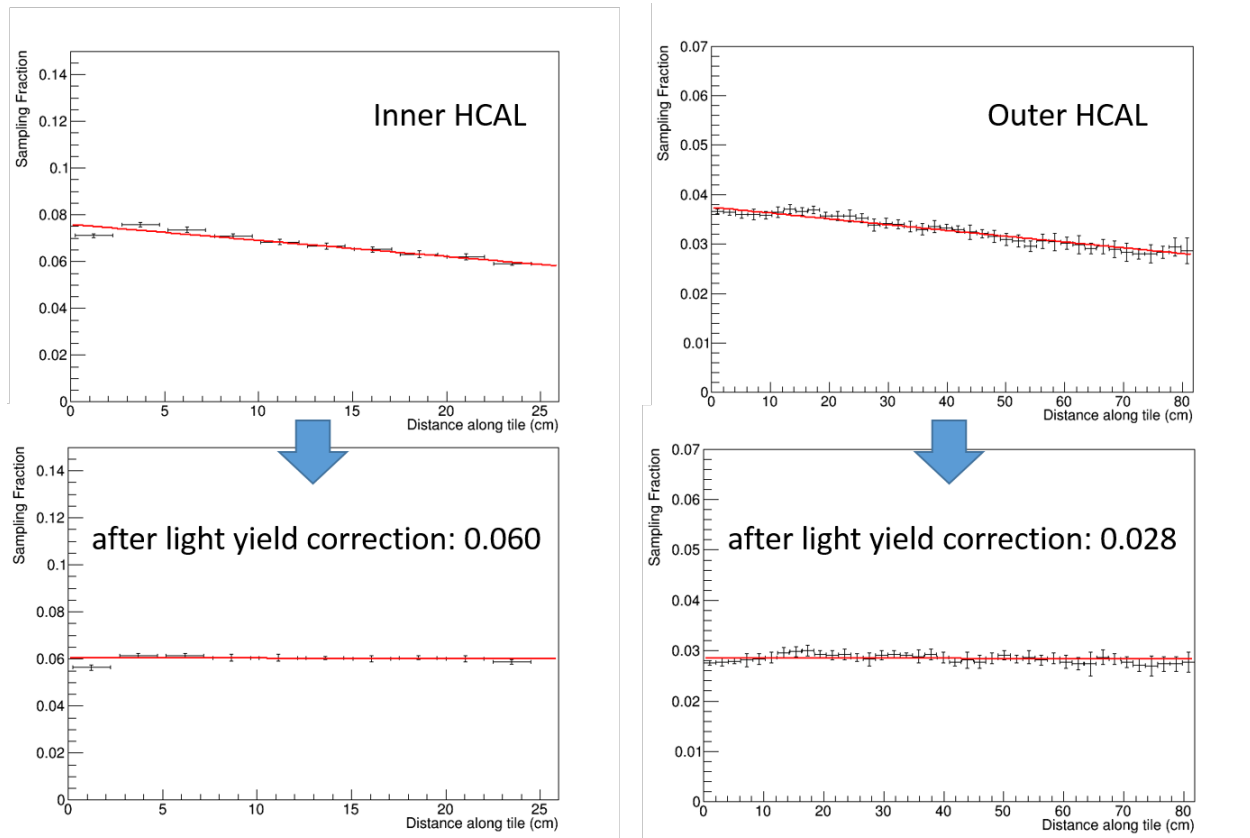


**Figure 6.21:** TOP ROW: Sampling fraction in the inner (left) and outer (right) HCAL from GEANT4 simulations as a function of depth along the scintillating tiles, showing the decrease in the sampling fraction as a function of depth in each HCAL compartment. BOTTOM ROW: Sampling fractions in the inner and outer HCAL after the light yield correction has been applied, resulting in a uniform sampling fraction as a function of depth along the tile.

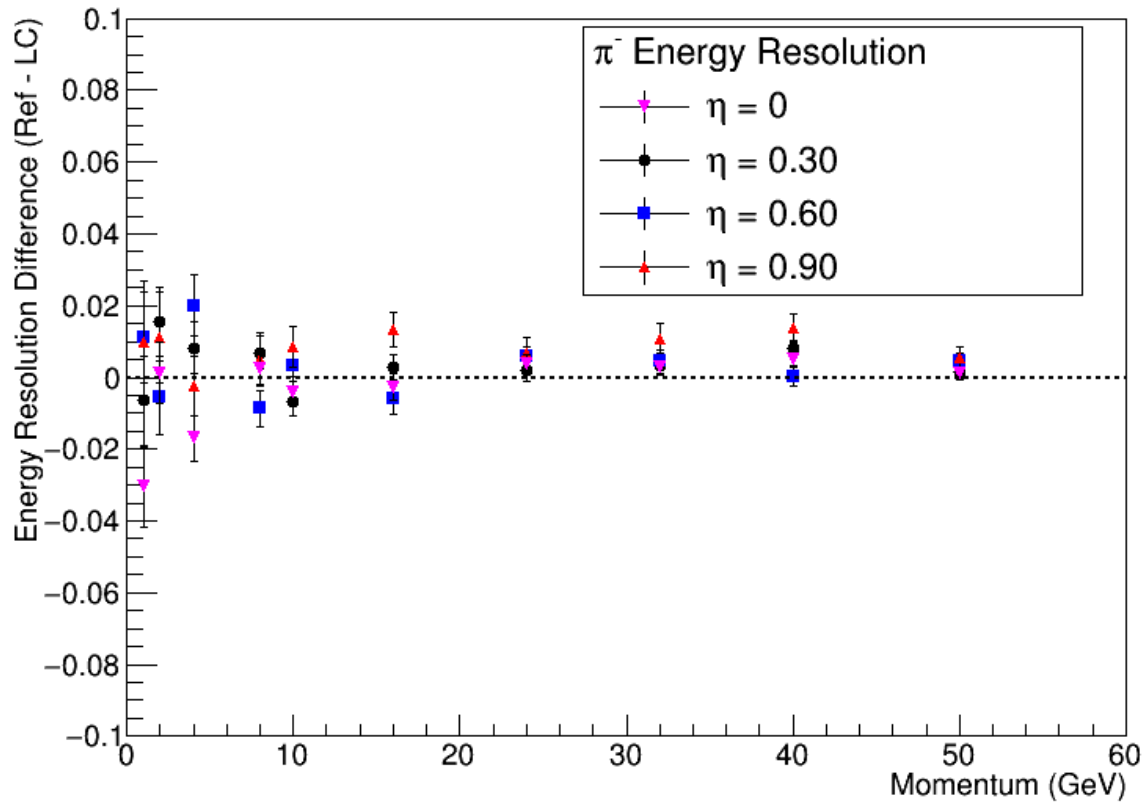


**Figure 6.22:** Point-by-point comparison of the energy resolution of the baseline sPHENIX calorimetry design with the inclusion of a light yield correction to even out the sampling fraction in the inner and outer HCAL. The baseline energy resolution is shown in Figure 6.14. A positive value indicates improvement in the resolution with the light yield correction.

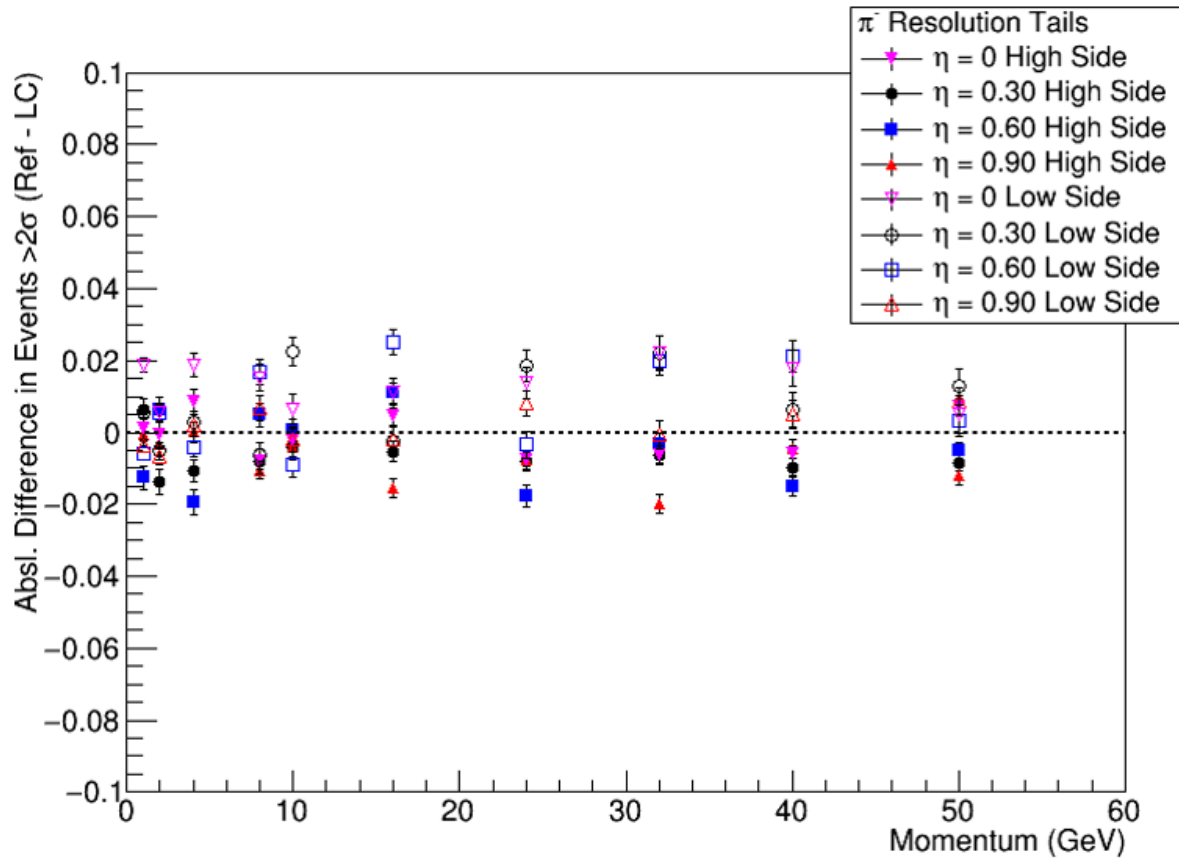


**Figure 6.23:** Point-by-point comparison of the non-Gaussian tails in the baseline sPHENIX calorimetry design with the inclusion of a light yield correction to even out the sampling fraction in the inner and outer HCAL. The baseline non-Gaussian tails are shown in Figure 6.16. A positive value indicates improvement in the non-Gaussian tails with the light yield correction.

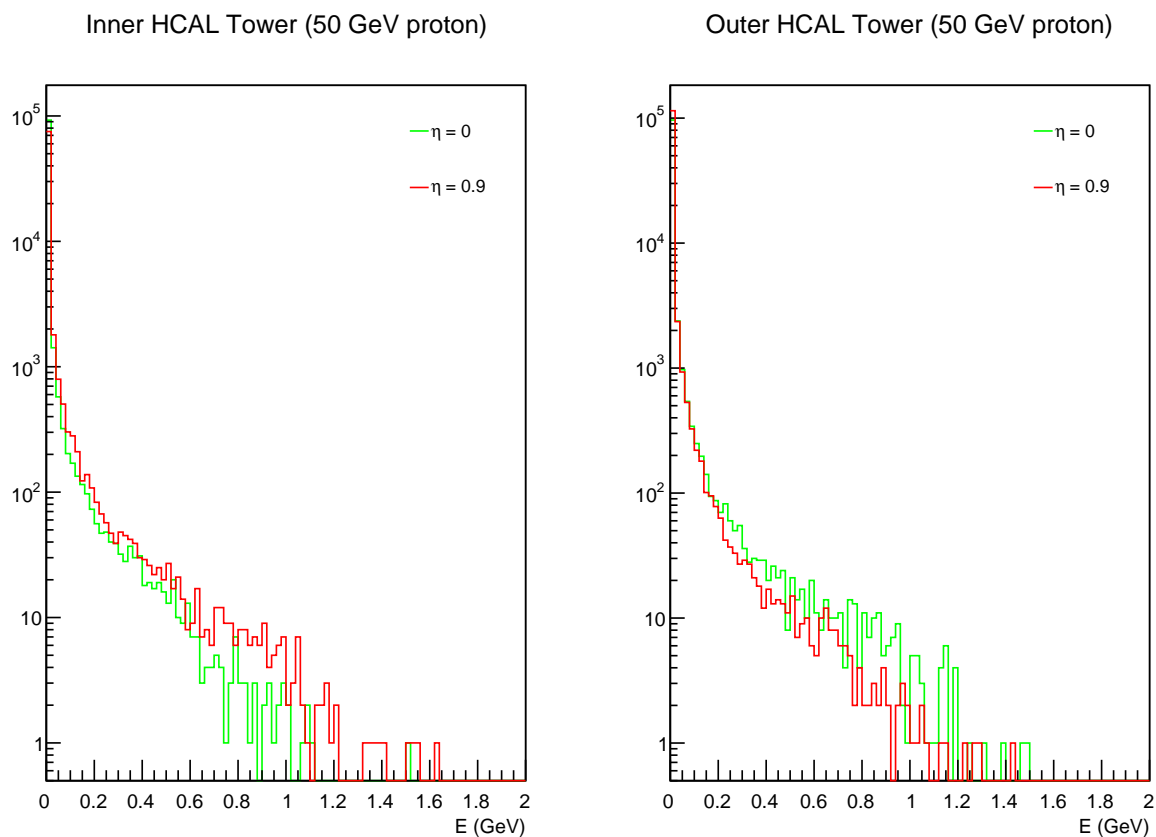


**Figure 6.24:** Calculated energy deposited in scintillator tiles in HCAL towers from 50 GeV protons in towers at two pseudorapidities.

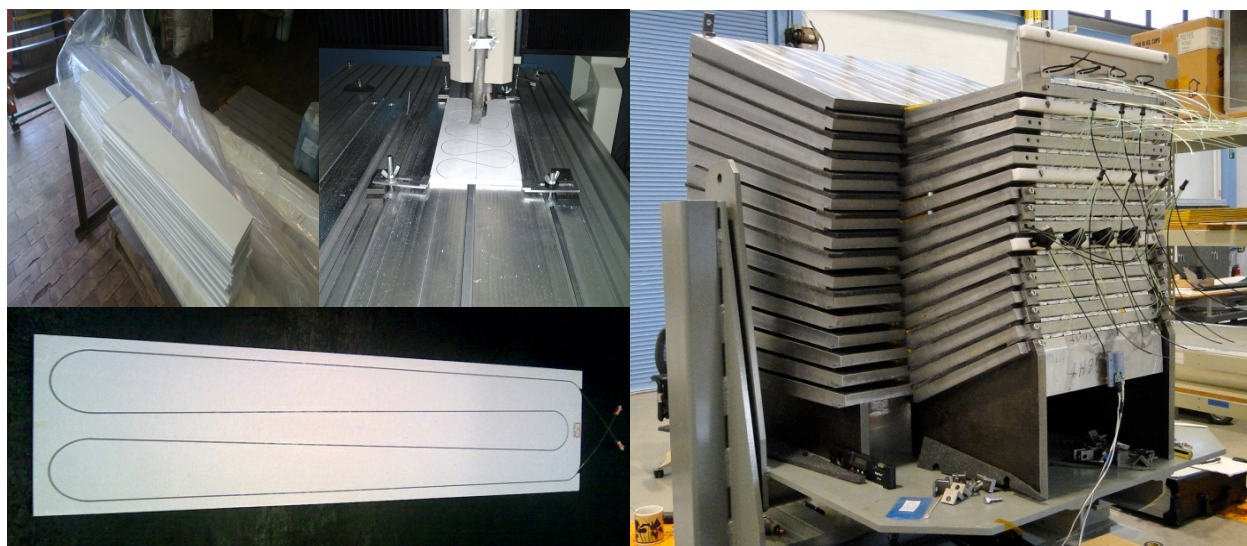


**Figure 6.25:** Scintillating tiles with embedded wavelength shifting fibers (left panel) and the HCAL prototype calorimeter (right panel).



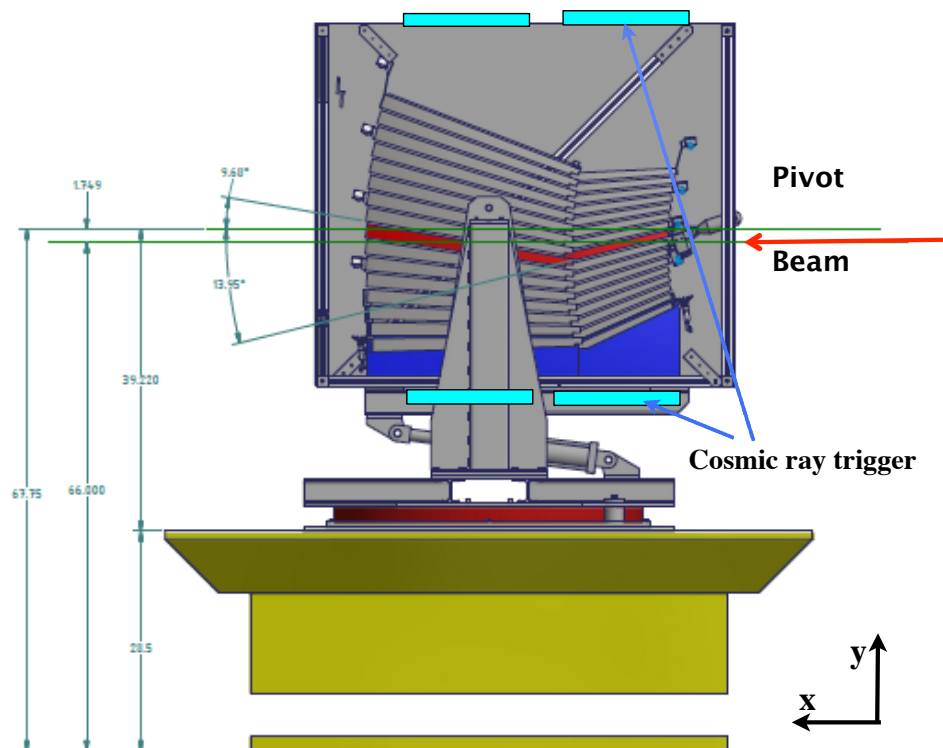


**Figure 6.26:** Side view of the layout of the HCAL prototype detector at the FNAL test beam facility. The beam enters from the right as indicated by the red arrow.

Energy Resolution, Linearity and  $e/\pi$  Ratio

Using the reconstructed energy spectra based on the calibrations using cosmics, we were able to determine the calorimeter energy resolution and its linearity. The results are shown in Fig. 6.27 and 6.28, respectively. The fractional energy resolution is fitted with the “standard” functional form (i.e., a stochastic term plus a constant term)

$$\frac{\sigma}{E} = \frac{a}{\sqrt{E}} \oplus b, \quad (6.1)$$

where  $a$  and  $b$  are the stochastic and constant contributions to the resolution, respectively.

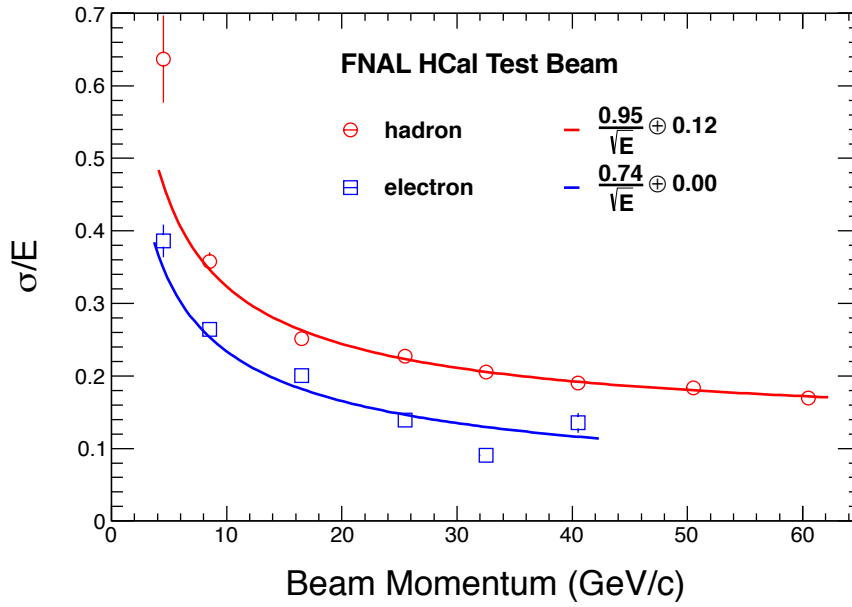


**Figure 6.27:** sPHENIX HCal prototype energy resolution for pions and electrons obtained from the FNAL test beam data.

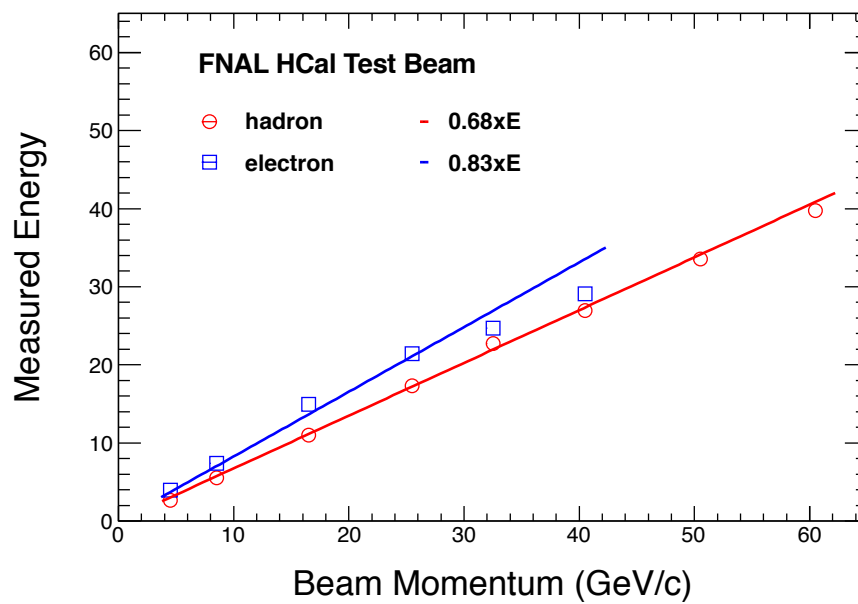


**Figure 6.28:** sPHENIX HCal prototype energy linearity for pions and electrons obtained from the FNAL test beam data.

From the reconstructed energy spectra, the  $e/\pi$  ratio is calculated as follows

$$e/\pi = \frac{\langle E_e \rangle}{\langle E_\pi \rangle}, \quad (6.2)$$

where  $\langle E_e \rangle$ , and  $\langle E_\pi \rangle$  are the reconstructed mean energy for electron and pions, respectively. And the  $e/h$  ratio is then determined by fitting  $e/\pi$  distribution with formula:

$$e/\pi = \frac{e/h}{(e/h)f_{\pi^0} + (1 - f_{\pi^0})}, \quad (6.3)$$

where  $f_{\pi^0} = k \ln(E)$  is the average fraction of electromagnetic energy in the hadronic shower, and  $k = 0.11$ .

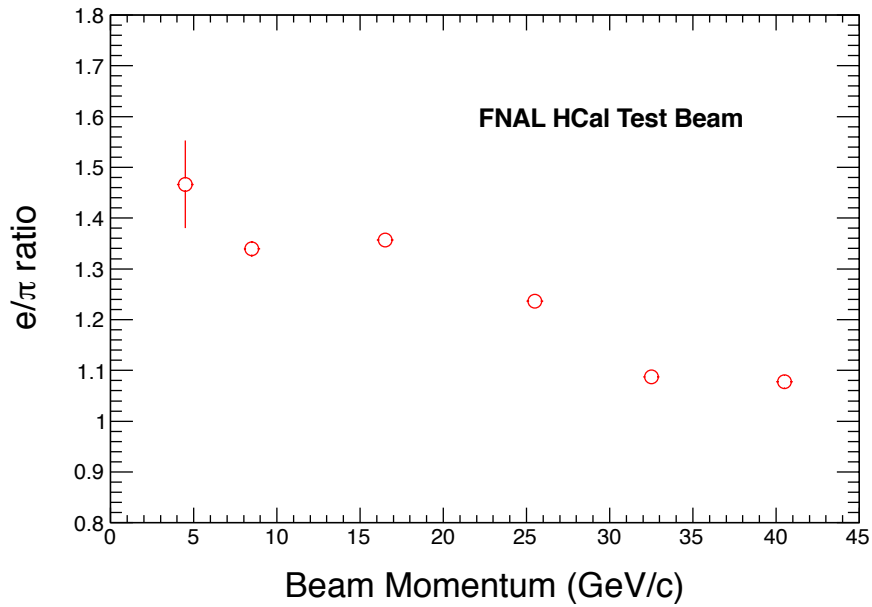


**Figure 6.29:**  $e/\pi$  ratio of the HCal prototype.

#### Comparison with GEANT4 Simulation

We have compared the test beam results with the results from the GEANT4 simulations. Figure 6.30 shows the energy resolution comparison between data and the GEANT4 simulation. Figure 6.31 shows a comparison of the  $e/\pi$  ratio between data and simulation.

#### 6.4.2 Scintillator Tile Testing

At the present time there are two major scintillator tile testing efforts underway within the sPHENIX HCAL groups. One effort, centered at BNL, is focused on understanding the

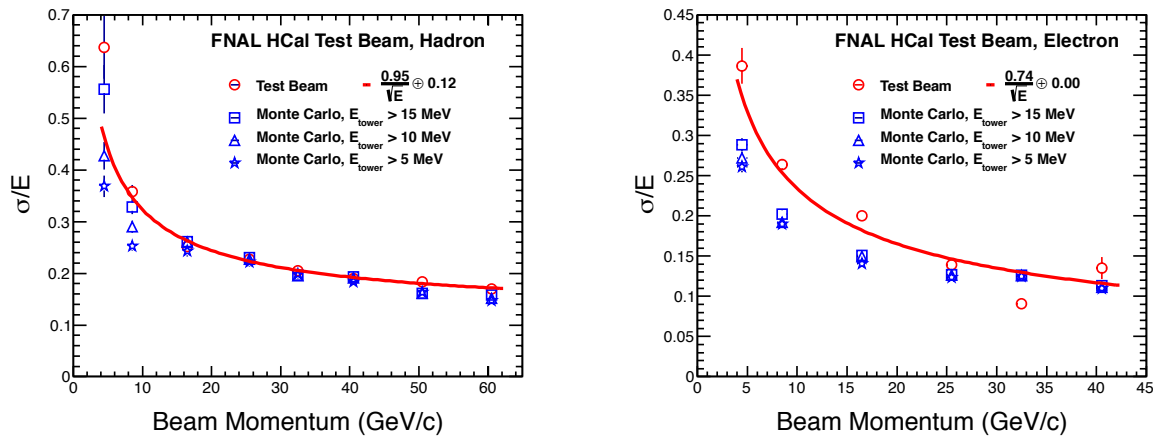


**Figure 6.30:** Comparison of the energy resolution for pions (left panel) and electrons (right panel) between test beam data and the GEANT4 simulation.

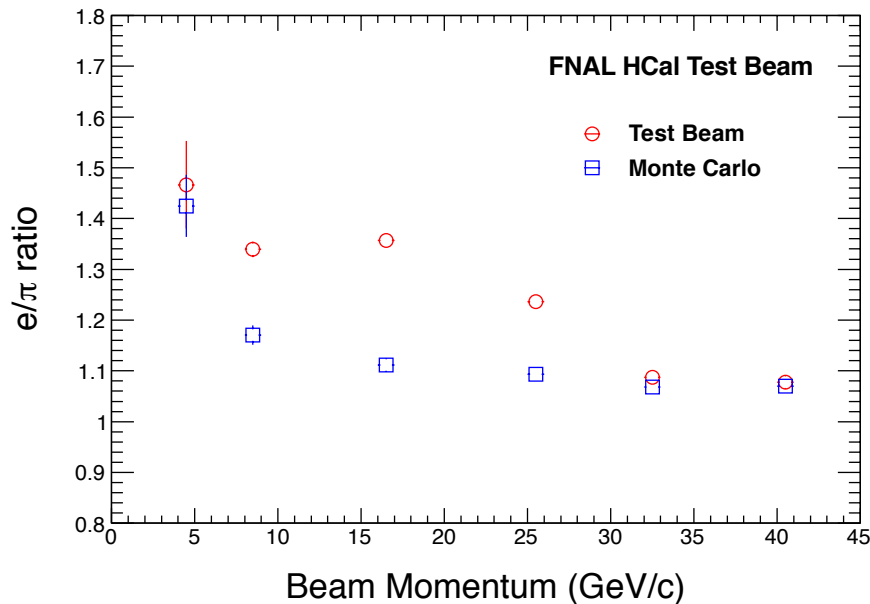


**Figure 6.31:** Comparison of the  $e/\pi$  ratios evaluated from test beam data and the GEANT4 simulation.

light yield in the scintillator tiles and characterizing the performance using cosmic rays. A second effort at the University of Colorado, Boulder, also has the capability to test HCAL scintillator tiles with cosmic rays. In addition, the UC Boulder group has also developed an automated test stand that allows scintillator tiles to be scanned with a radioactive source. The ultimate goal of these efforts will be to characterize the tile light yield and correlate the cosmic test results with the results from a source scan. As a source scan can

be accomplished in a substantially smaller amount of time, this will enable a fast quality assurance on the HCAL tiles used in module production.

A third tile testing effort is ramping up at Georgia State University. Because of that large scale of the HCAL and the large number of scintillating tiles involved we believe that developing expertise at multiple sites will allow important crosschecks.

### 6.4.3 Future test beam efforts

Building on the success of the first sPHENIX calorimetry prototype, we plan to construct a second prototype for testing in the FNAL test beam in 2016. The prototype will consist of a full calorimetry section of the detector, including EMCal and inner and outer HCAL prototypes, as well as a mockup of a section of the magnet solenoid.

Testing of the prototype will proceed in two stages. In the first stage, planned for the spring of 2016, the prototype will be configured with scintillator tiles as we intend to use for midrapidity in the sPHENIX detector. The goals of this test beam will include characterization of the light yield of the full detector for hadronic showers, as well the energy response and calibration procedure using cosmic rays and the LED gain monitoring system. The readout system for the calorimeter will use prototype sPHENIX readout electronics.

In the second phase of the prototype beam test, scheduled for fall 2016, the calorimeter will be configured in manner that mimics the high-rapidity configuration of sPHENIX. The goals for the second phase will be to understand the performance characteristics of the calorimeter in a high-rapidity configuration.

# Chapter 7

## Calorimeter Electronics

The sPHENIX reference design for electronics is based on a common electronics design for both the EMCal and HCal detectors using off the shelf components. This approach will reduce the overall cost and minimize the design time for the electronics. The reference design uses multiple Silicon Photomultipliers (SiPMs) as the optical sensors. Signals from the SiPMs associated with a single tower in the calorimeters are passively summed, amplified, shaped and differentially driven to digitizer boards located in racks near the detector. The differential analog signals are received by 64 channel digitizer boards and digitized by a 14 bit ADC operating at 6 times the beam crossing frequency sampling rate. Upon receipt of a Level-1 (L1) trigger signal, the digitized data is transmitted to the PHENIX DAQ. A block diagram of the calorimeter electronics is shown in Figure 7.1.

**ADC System Block Diagram**

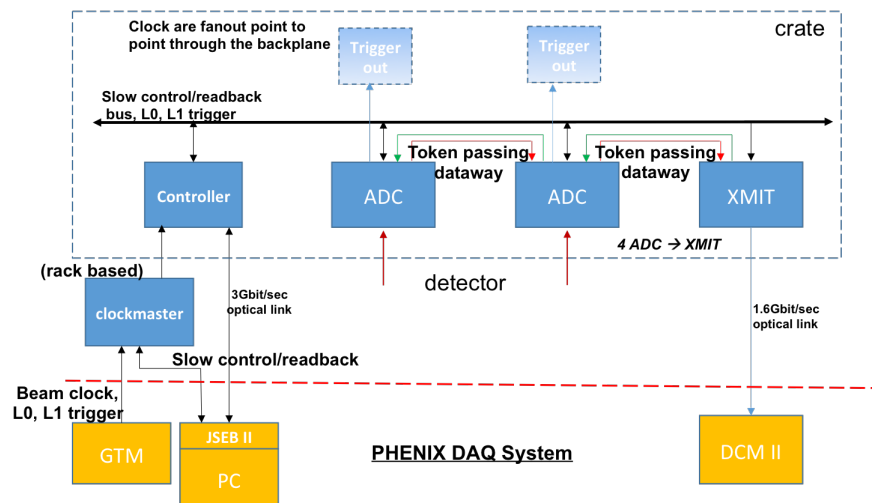


**Figure 7.1:** Block diagram of a ADC system

The technical specifications for the calorimeter electronics are set by physics requirements

and the performance characteristics of the calorimeters are summarized in Table 7.1. For the EMCal, The expected energy range for photons is expected to be 1 GeV to 50 GeV. For a 1 GeV photon incident on the center of an EMCal tower, 80% of the energy will be deposited in the central tower with 20% of the energy shared among the 8 surrounding towers. This implies a minimum energy of 25 MeV and a dynamic range of  $10^3$  to cover the range of expected energy deposition in a single tower of the EMCal. The total number of electronics modules required for the EMCal and HCal readout are summarized in Table 7.2.

**Table 7.1:** Technical Specifications for the Calorimeter Electronics.

Component	Requirement	Specification
Optical Sensor	Pixel Size	$15 \times 15 \mu m^2$
	Dynamic Range	$10^4$
	PDE	25%
	Gain	$10^4$
	Pixels/GeV: EMCal	1600
	Pixels/GeV: HCal	
Amplifier/Shaper	Gain	100 mV/pC
	Signal-to-Noise	10:1
	Peaking time	30nSec
Digitizer	Signal Polarity	Positive
	Resolution	14 Bit
	Maximum Sampling Frequency	65 MHz
	Latency	40 BCO
	Multi-event Buffering	5 Events

## 7.1 Optical Sensors

The compact nature of the EMCal and HCal detectors and the location of the EMCal and Inner HCal being inside the 1.5T solenoidal field require that the optical sensors be both physically small and immune to magnetic effects. A device with large gain is also desirable in order to reduce the demands on the performance specifications of the front end analog electronics. For both the electromagnetic and hadronic calorimeters, silicon photomultipliers (SiPMs) are being considered in the reference design for optical sensors. SiPMs have the advantage that there are immune to magnetic fields, have large gain and are small in size.



**Table 7.2:** Electronics Component Count.

EMCal Front End Electronics	SiPMs	98304
	Preamplifier Channels	24576
	Preamplifier Boards	1536
	Interface Boards	384
	Controller Boards	64
	Controller Board Crates	4
	Crate Controllers	4
HCal Front End Electronics	SiPMs	15360
	Preamplifier Channels	3072
	Preamplifier Daughter Boards	3072
	Interface Boards	128
	Controller Boards	16
	Controller Board Crates	2
	Crate Controllers	2
Digitizer Electronics Electronics	Signal Cables	1728
	Digitizer Boards	432
	XMIT Modules	118
	Controller Boards	28
	Crates	28

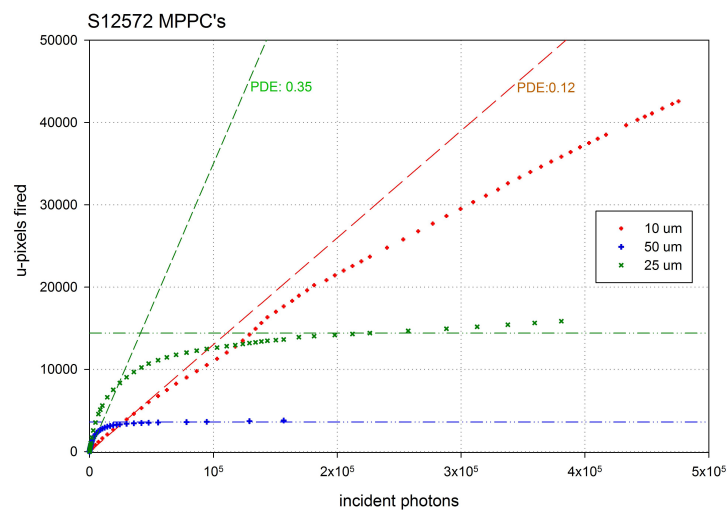
### 7.1.1 Device Characteristics

Devices of varying sizes and pixel counts from several manufacturers have been evaluated in context of the sPHENIX calorimeter optical sensor requirements. The devices evaluated and their properties are summarized in Table 7.3. SiPMs are inherently limited in their dynamic range by the number of micropixels in the device, as shown in Figure 7.2. Due to the digital nature of the SiPM, the usable dynamic range is significantly less than the total number of micropixels. Each micropixel fires once per event regardless of how many photons hit it. Distributing the incident light uniformly across the active area maximizes the useful range, but for large signals it is still limited by optical saturation, that is more than one photon hitting the same micropixel. While increasing the number of micropixels would increase the dynamic range, there are trade-offs in that more micropixels typically means lower gain and lower photon detection efficiency, PDE.

In order to achieve the required dynamic range, a device with a large number of micro-cells is required, which limits the number of devices that meet the technical specifications for the optical sensors. Hamamatsu has a number of devices with high pixel counts, high gain, and good PDE which meet the sPHENIX technical requirements. For both the electromagnetic and hadronic calorimeters the reference design is based on the Hamamatsu S12572-33-015P

**Table 7.3:** Properties of SiPMs Studied. (Data collected from manufacturers datasheets).

manufacturer	model	$\mu$ -cell size ( $\mu\text{m}$ )	active area ( $\text{mm}^2$ )	$\mu$ -cells count	gain ( $\times 10^5$ )	PDE (%)	Idark (nA)
Hamamatsu	s10931-025P	25	3x3	14,400	2.75	20	100
	S12572-010P	10	3x3	90,000	1.35	10	15
	S12572-015P	15	3x3	40,000	2.30	25	20
	S12572-025P	25	3x3	14,400	5.15	35	80
	S12572-050P	50	3x3	3,600	12.5	35	350
SensL	MicroFC30020	20	3x3	10,998	10	24	85
	MicroFC30035	35	3x3	4,774	30	31	250
	MicroSL10050-x13	50	1x1	3,600			
AdvanSiD	ASD-SiPM3S-P-50	50	3x3	3,600	25	22	2000
KETEK	PM3350	50	3x3	3,600	80	50	260
Excelitas	C30742CERH-50-3-1	50	3x3	3,600	15	30	700
	C30742CERH-25-1-1	25	1x1	400			

**Figure 7.2:** Optical saturation in Hamamatsu S12572 MPPCs. 10 $\mu\text{m}$ , 25 $\mu\text{m}$ , and 50 $\mu\text{m}$  micropixels

MultiPixel Photon Counters (MPPC). The device is a  $3 \times 3 \text{ mm}^2$  device with 40K pixels each  $15 \times 15 \mu\text{m}^2$  in size. A photograph of the device is shown in Figure 7.3 and a technical drawing is shown in Figure 7.4. The properties of this device are summarized in Table 7.4. Any SiPM device will have an intrinsic limitation on its dynamic range due to the finite number of pixels, and with 40K pixels, this device has a useful dynamic range of  $\sim 10^4$ .

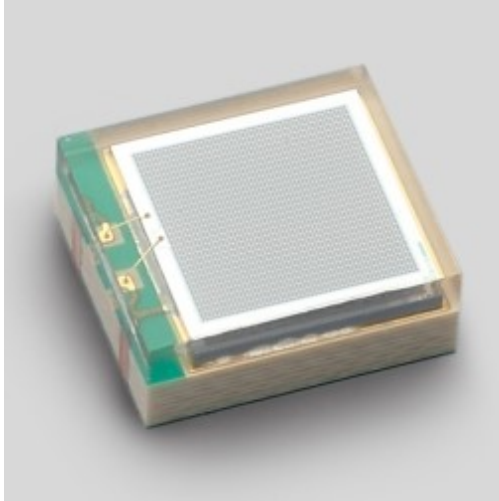


**Figure 7.3:** Hamamatsu S12572 MPPC (SiPM). The device is  $3 \times 3 \text{ mm}^2$  with 40,000 pixels  $15 \mu\text{m}^2$ .

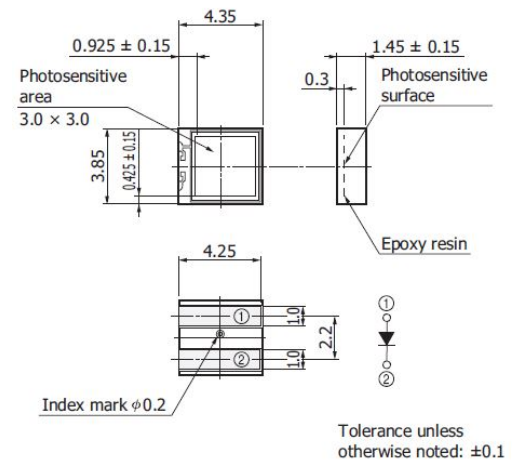


**Figure 7.4:** Hamamatsu S12572 MPPC surface mount package dimensions.

However, the optical saturation at the upper end of the range is difficult to correct for as the device response deviates from linearity as the number of activated pixels approaches the total number of pixels in the device, so the effective pixel count is significantly less than 40K. With a PDE of  $\sim 25\%$  it should therefore be possible to adjust the light level to the SiPM using a mixer to place the full energy range for each tower ( $\sim 5 \text{ MeV}$ – $50 \text{ GeV}$ ) in its useful operating range. For example, if the light levels were adjusted to give 10,000 photoelectrons for 50 GeV, this would require only 200 photoelectrons/GeV, which should be easily achieved given the light level from the fibers entering the mixer.

The performance of a SiPM is affected by temperature of the device. SiPMs show an increasing dark current and a diminishing gain with increasing temperature. Figure 7.5 shows the dependence of gain on temperature for different SiPMs and the dependence of device leakage current on temperature for Hamamatsu S12572 SiPMs of different pixel sizes. The Hamamatsu devices operate in a higher voltage range the devices from other manufacturer (70V vs 30V) and have a steeper temperature dependence. Devices with larger pixel sizes typically have higher gain, but also higher leakage current. The leakage current increases rapidly above  $30^\circ\text{C}$ , suggesting the benefit of operating in  $5\text{--}20^\circ\text{C}$  range. While in principle cooling could be used to mitigate the increased dark current due to radiation damage, the scale of the increase (orders of magnitude) greatly exceeds the potential benefits of cooling (factors of 2) over the temperature range  $0\text{--}40^\circ\text{C}$ . Figure 7.6 shows the leakage current, signal amplitude, and signal noise performance of a S12572-015P SiPM and an sPHENIX preamp as a function of temperature.

Property	
active area	3mm x 3mm
number of micropixels	40,000
micropixel pitch	15 $\mu\text{m}$
geometric fill factor	0.53
package	surface mount
window	epoxy resin
window refractive index	1.55
operating temperature	0-40 deg C
spectral response range	320-900 nm
peak sensitivity wavelength	460 nm
photon detection efficiency (PDE)	0.25
Dark Count Rate (typ)	1 Mcps
Terminal capacitance	320 pF
Gain	230,000
Gain temp coefficient	3500 / $^{\circ}\text{C}$
Breakdown voltage ( $V_{\text{br}}$ )	$65 \pm 10$ V
Recommended Operating Voltage	$V_{\text{br}} + 4$ V
Temp coeffic at $V_{\text{op}}$	60 mV / $^{\circ}\text{C}$

**Table 7.4:** Properties of Hamamatsu S12572-015P MPPC.

### 7.1.2 Neutron Radiation Effects

Silicon photomultipliers have been found to be susceptible to damage from neutron radiation. Matsumura et.al. as part of the T2K collaboration found that exposure to protons resulted in an increase in the device leakage current, increased noise, and reduced single photoelectron resolution [143]. Qiang et.al. of the GlueX experiment has also measured increased leakage current after neutron irradiation [144]. Musienko et.al. of the CMS HB/HE Calorimeter Upgrade also studied radiation damage and worked with manufacturers to develop more radiation-hard SiPMs [145]. Simulations to estimate neutron fluences in the sPHENIX IR based on studies of the current STAR and PHENIX IRs at RHIC [146] suggest that the expected neutron fluence is approximately  $2 \times 10^{10}$  n/cm<sup>2</sup> per Run year. Based on the measurements of increase in leakage current due to neutron damage and the expected neutron rates in the sPHENIX interaction region and number of studies on the impact to SiPM performance in context of the sPHENIX calorimeter requirements have been carried out.

Studies of SiPMs were conducted in the current PHENIX IR during Run 14 and Run 15 to observe the effects of neutron radiation on a sample SiPMs of various pixel size, in the approximate sPHENIX environment. Figure 7.7 shows leakage currents measured from different Hamamatsu devices during Run 15 as a function of fluence. Part of this study done in the PHENIX IR during Run 15 was to investigate whether thermal neutrons were

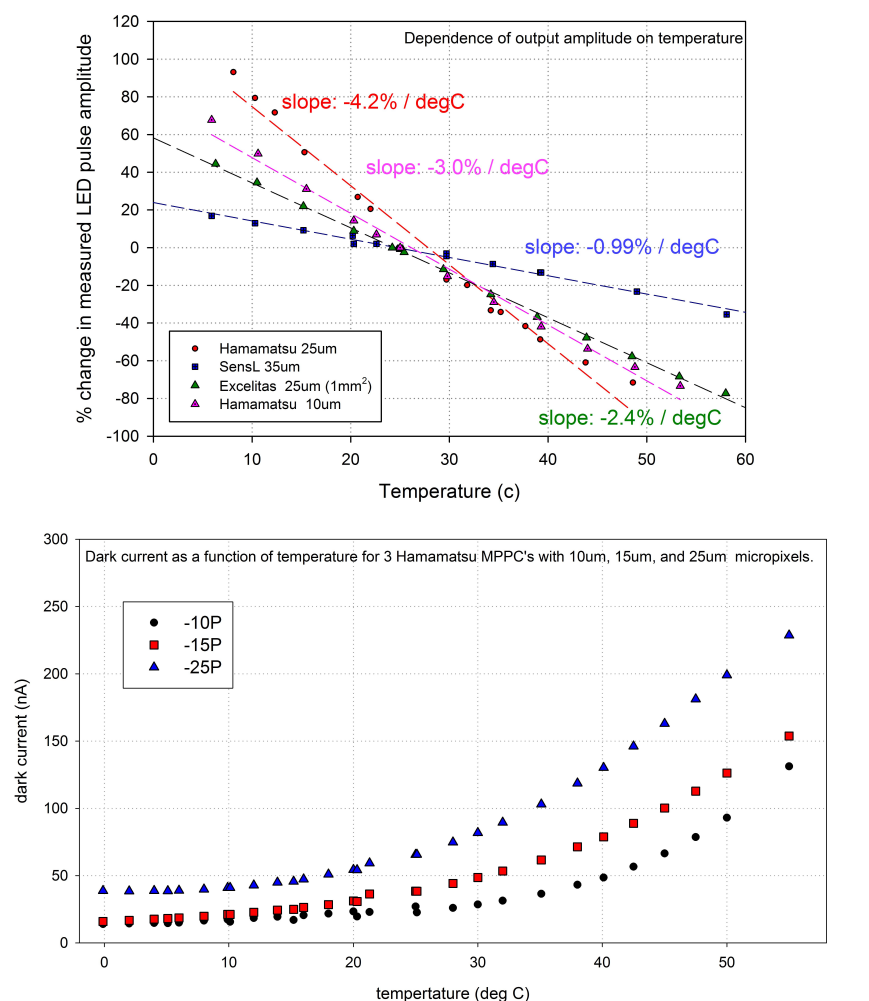


**Figure 7.5:** Percent change in LED signal amplitude vs temperature for Various SiPMs. (top) and Dependence of leakage current on Temperature in Hamamatsu S12572 MPPCs with 10 $\mu$ m, 15 $\mu$ m, and 25 $\mu$ m micropixels (bottom).

causing some of the damage to the SiPMs. Two groups of identical devices, positioned at the same location in the IR, were compared; 2 SiPMs were placed inside a Gadolinium-shielded box to eliminate thermal neutrons, the other 2 SiPMs were left un-shielded. Both groups of SiPMs showed a similar increase in leakage current. There was no obvious difference in the damage to the 2 groups based on the leakage current measurements, suggesting that the observed damage was not caused by thermal neutrons. The data for these devices is included in Figure 7.7.

As a follow-up to the PHENIX IR measurements, with a more controlled, neutron source, we irradiated additional SiPMs at the BNL Solid State Physics Irradiation Facility. A deuterium-tritium neutron source was used to generate 14 MeV neutrons. We exposed the devices to neutrons at a flux rate of  $10^5 \text{ n/cm}^2$ . The SiPMs were characterized before and after irradiation. Figure 7.8 shows a plot of the increasing leakage current versus exposure

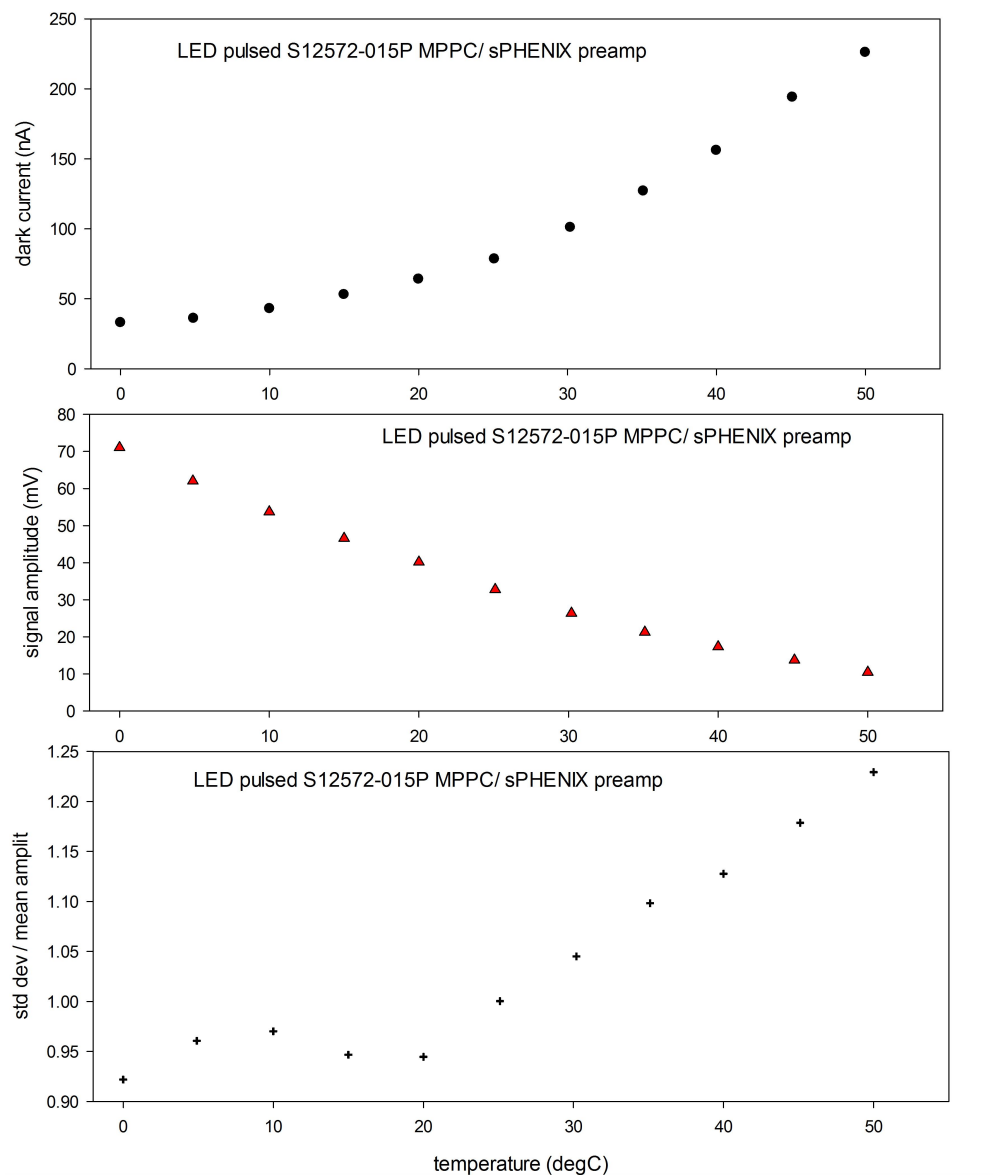


**Figure 7.6:** Performance as a function of temperature - Hamamatsu S12572-015P MPPCs with an sPHENIX preamp. Dark current as a function of temperature (top), signal (LED pulse) amplitude vs temperature (center), and for the LED signal, stddev/mean vs temperature (bottom)

time for the SiPMs tested.

Two additional studies have been done to understand the effects of neutron irradiation on SiPM devices using neutron sources at National Laboratories. In the first, SiPMs were exposed to neutron fluences at the University of Indiana Low Energy Neutron Source (LENS) facility, equivalent to about 2 orders of magnitude higher than what is

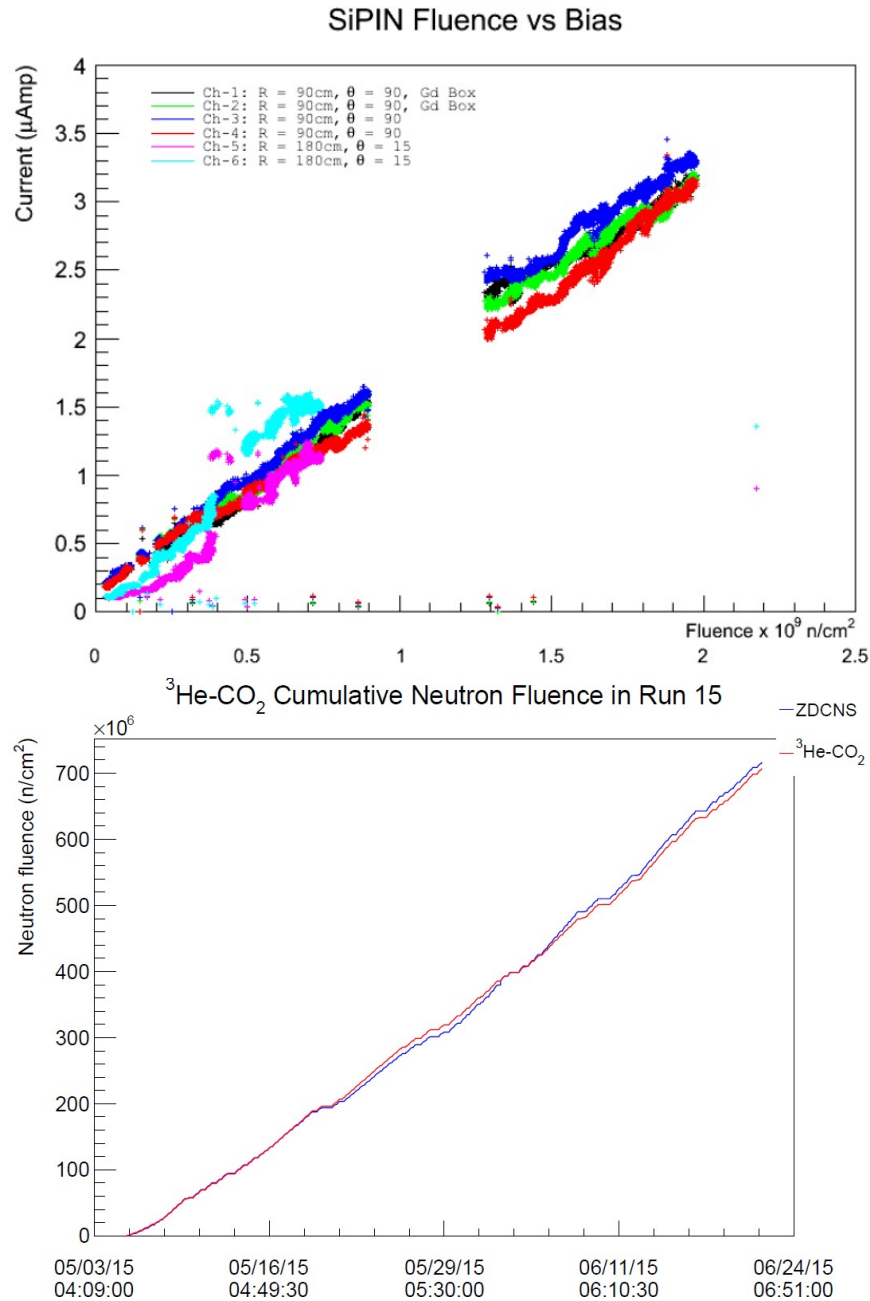


**Figure 7.7:** Sipms in the PHENIX IR during Run 15 p-p running. The devices – Hamamatsu S12572-025P, -015P, and -010P all showed a steady increase in leakage current with cumulative neutron fluence during Run 15.

anticipate over their sPHENIX lifetime at RHIC. These results are shown in Figure 7.9. In the second test, Hamamatsu SiPMs were irradiated at the Los Alamos LANSCE facility to the approximate fluences expected over the expected lifetime in sPHENIX (about  $7 \times 10^{10} \text{ n/cm}^2$ ). The leakage current versus  $V_{\text{bias}}$  curves for the devices before and after irradiation are shown in Figure 7.10. The S12572-015P shows an increase from 50nA to

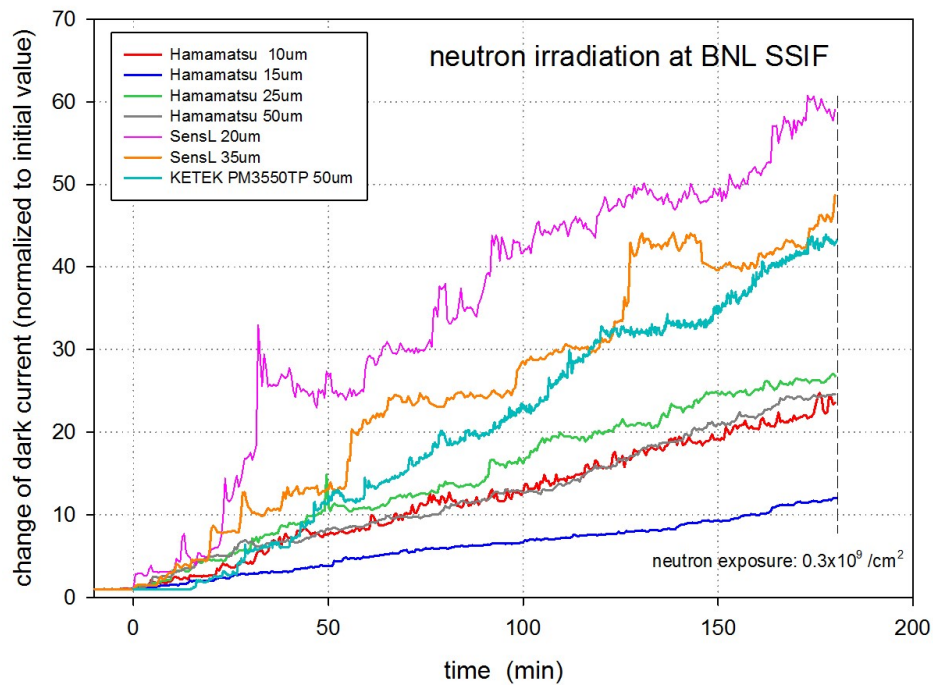


**Figure 7.8:** Various sipms studied at BNL SSGRIF facility. Increasing leakage current vs time during neutron exposure.

250 $\mu$ A at its operating voltage.

In summary the following radiation damage studies of SiPMs have been done:

- PHENIX IR RUN14 (200 GeV Au-Au, h-Au), 2 Hamamatsu -025P SiPMs-about 3 weeks of beam running time.
- PHENIX IR RUN15 (200 GeV p-p, p-Au, p-Al) 30 Hamamatsu -010P, -015P, -025P SiPMs - about 8 weeks of beam running time.
- Neutron generator irradiation studies at BNL SSGRIF SiPMs from Hamamatsu, SensL, AdvanSiD, Excelitas, and KETEK of various  $\mu$ -pixel sizes cumulative exposures to  $10^9$  n/cm<sup>2</sup>.
- Neutron Irradiation studies at Indiana University LENS Facility Hamamatsu -025P MPPCs cumulative exposures up to  $10^{13}$  n/cm<sup>2</sup>.
- Neutron Irradiation studies at Los Alamos (LANSCE) - Hamamatsu MPPCs of various  $\mu$ -pixel size -Cumulative exposures to about  $7 \times 10^{10}$  n/cm<sup>2</sup>.

The STAR collaboration at RHIC has also been studying the effects of neutron damage to the SiPMs that are being used in the STAR FPS detector. In order to understand the



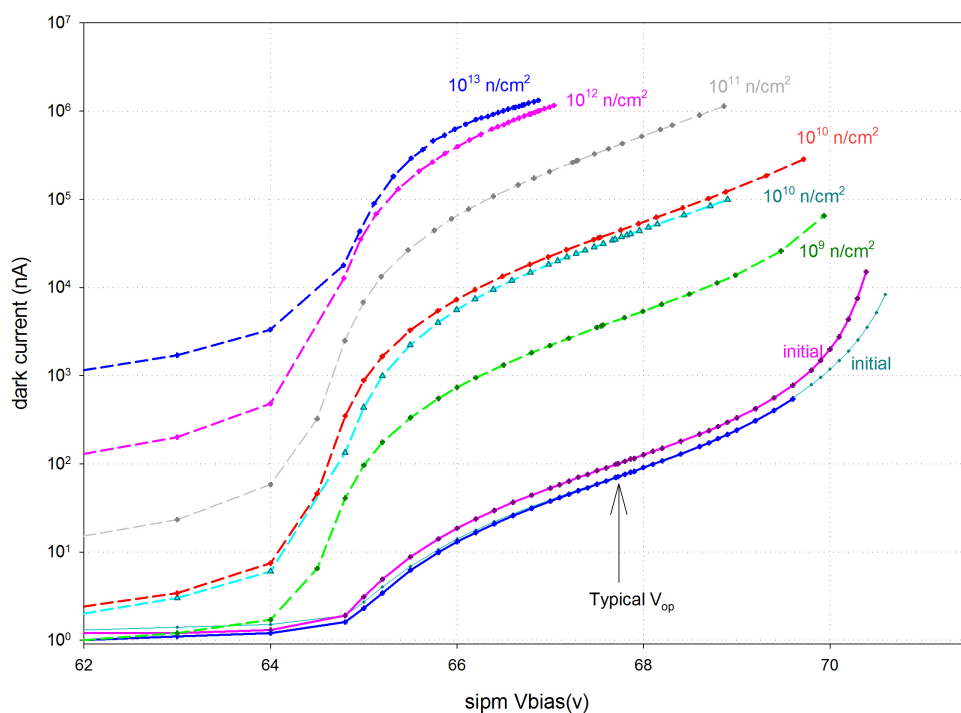


**Figure 7.9:** Neutron damage in Hamamatsu MPPCs exposed at Indiana Univ LENS facility

impact of the increase in the leakage current, they looked at the MIP peak for different data runs taken during RHIC Run 15. Shown in Figure 7.11 is the measured MIP peak in the STAR FPS for 3 runs corresponding to increasing integrated exposures of the SiPMs. As can be observed, there is not appreciable shift in the measured MIP peak indicating that the increased leakage current does not significantly impact the light measurement of the device.

The increase in leakage current due to neutron damage poses a technical challenge for maintaining a constant gain, however, the gain stabilization circuit as described in Section 7.2.2 is designed to compensate for the increased leakage current. While the increase in the leakage current will limit the ability to observe single photo-electron peaks, the leakage current increases that are expected in 3 years of sPHENIX running will not significantly impact the signals that are of interest for sPHENIX, as demonstrated by the STAR MIP peak measurements and are shown in Figure 7.11. As part of the on going R&D effort, studies will continue to understand the impact of the neutron damage in context of the sPHENIX requirements.

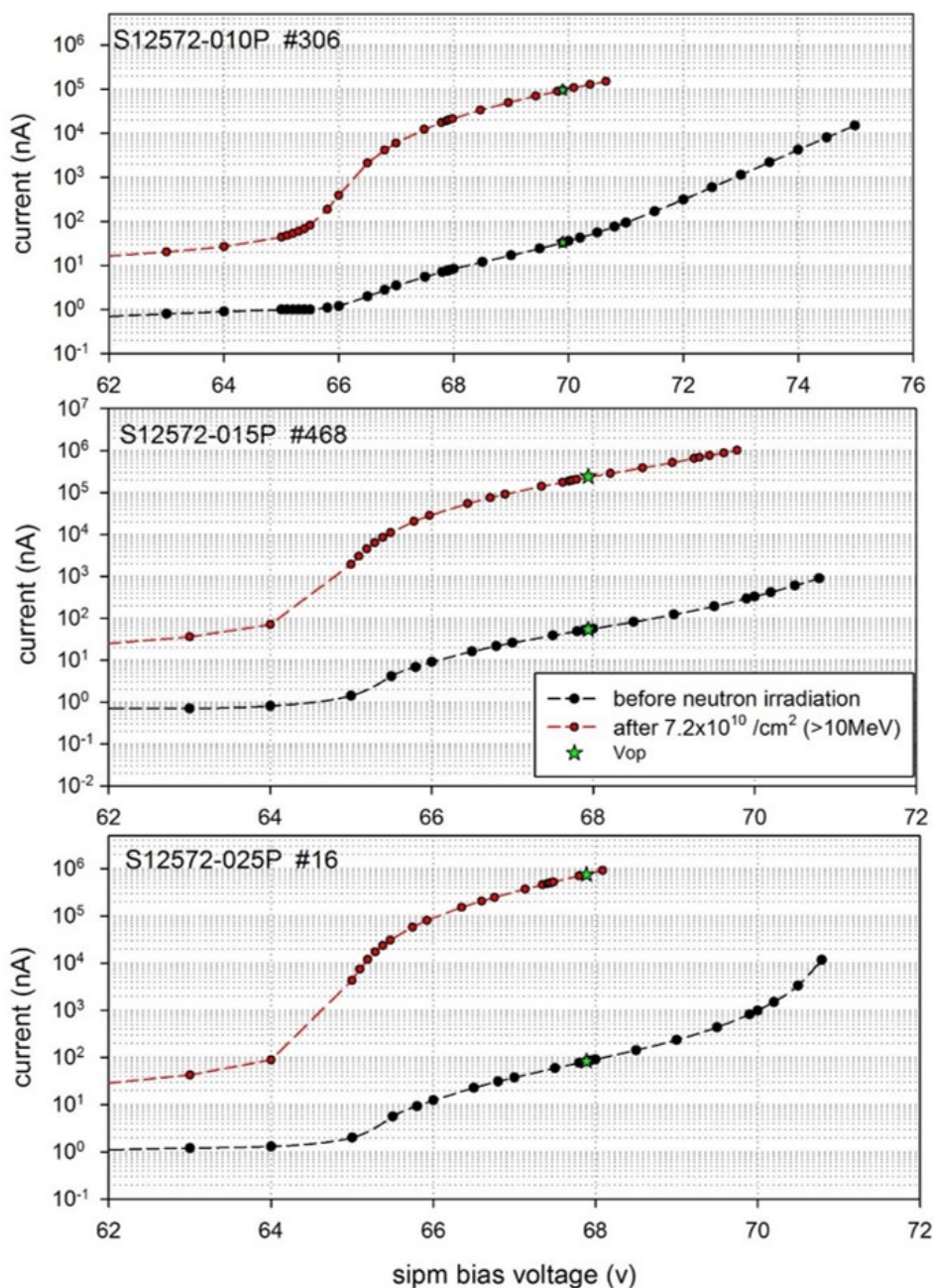


**Figure 7.10:** Neutron damage in Hamamatsu MPPCs exposed at Los Alamos LANSCE facility

## 7.2 Readout Electronics

The readout electronics consists of the analog front end electronics mounted directly on the detector, slow controls, digitizers and power distribution systems located in racks near

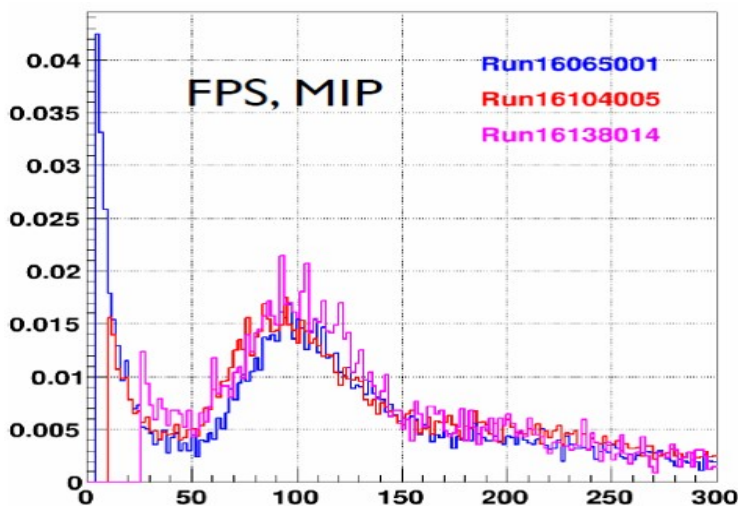


**Figure 7.11:** Radiation damage in Hamamatsu MPPCs exposed at BNL in the STAR FPS during Run 15. MIP peak measured at different times over the course of the run. Despite the significant increase in leakage current, only a small change is seen in the MIP peak amplitude. Vbias across the sipms was kept constant.

the detector. The front end electronics are functionally the same for the EMCal, Inner HCal and Outer HCal, although they will be packaged differently to account for differences in the mechanical design of the detectors. The same digitizer systems are used for both detectors.

A block diagram of the readout electronics for a half sector of the HCal is shown in Figure 7.12. Each of the five tiles that form an HCal tower has a single SiPM mounted on the edge of the tile where the wavelength shifting fiber comes out. The 5 SiPMs for a single tower are connected to an HCal Preamp Board with a shielded cable where the signals are passively summed, shaped and driven to Digitizer Boards that are located in racks near the detector. Mounted on the end of an HCal half sector is an HCal Interface Board which distributes the SiPM bias voltage and low voltage for the preamps for the 24 towers in an HCal half sector, along with current drivers for the LED calibration system and ADCs for monitoring the SiPM temperature, bias currents and voltages. The Interface Boards are connected to a Controller Board via a bi-directional serial link in a nearby crate. The Controller Board transmits to the Interface Board the parameters for the temperature compensation and gain control, LED enables and pulse trigger, and reads back monitoring information from the Interface Board. Each Controller Board is capable of controlling 8 Interface Boards. A Crate Controller communicates with the Controller Boards through parallel bus on the crate back plans. Communications with the slow control system is Ethernet based.

A half sector of the EMCal consists of 384 towers in a  $8 \times 48$  ( $\phi \times z$ ) configuration. To match the mechanical layout of the EMCal towers, the EMCal analog channels are arranged in a  $8 \times 2$  array on a Preamp Board matching the EMCal tower geometry. The SiPMs are

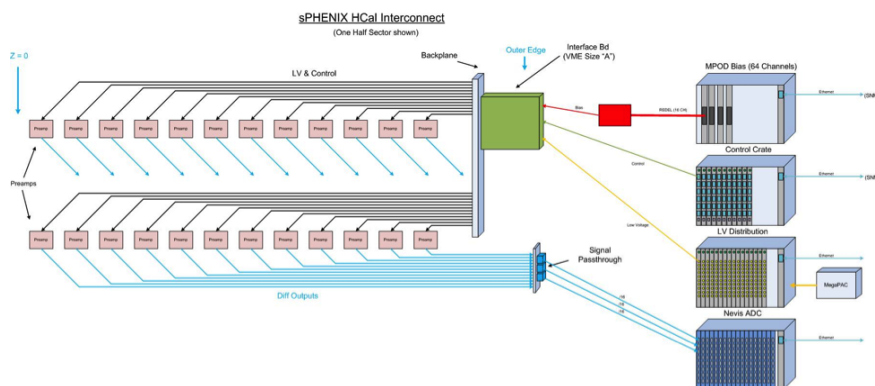


**Figure 7.12:** A block diagram showing the overall design of the HCal electronics for one half sector of the HCal. There are a total of 128 half sectors for the inner and outer HCal combined. Not shown are the connections for the LED monitoring system.

surfaced mounted on one side of the Preamp Board along with thermistors for monitoring the SiPM temperatures and LEDs for calibration and gain monitoring. The preamp and bias components are mounted on the opposite side of the board. The signals from the 4 SiPMs associated with an EMCAL tower are passively summed, amplified, shaped and differentially driven over shielded cable to Digitizer Boards located in nearby racks. Four EMCAL Preamp Boards are connected to an EMCAL Interface Board which distributes the bias voltage and preamp low voltage, LED driver circuits and control and monitoring of power and temperatures. The six EMCAL Interface boards in a half sector are connected with a bi-directional serial connection to a controller board. The EMCAL control system is identical to the HCal control system described earlier. A block diagram of the front end electronics for one EMCAL half sector is shown in Figure 7.13.

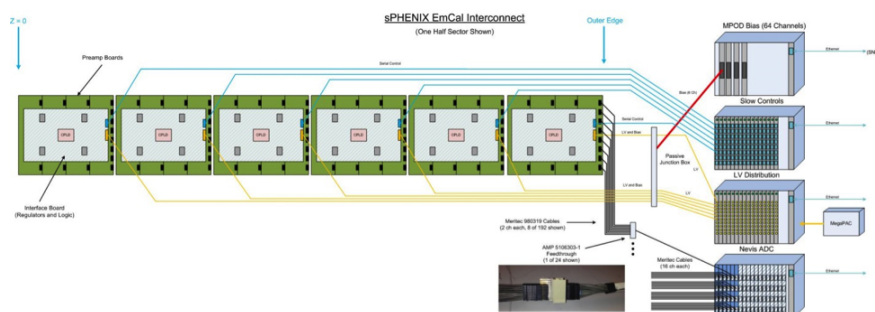


**Figure 7.13:** A block diagram showing the overall design for the EMCal electronics for one half sectors for the EMCal. There are a total of 384 towers per half sector and 32 half sectors for the EMCal.

### 7.2.1 Analog Circuit Design

To improve light collection, four SiPMs will be used in parallel for the EMCal and five for the HCal sections. This paralleling of devices also leads to a total input capacitance into the preamplifier that can exceed 1.5nF. Preamplifier circuits that use feedback to obtain linearity are prone to oscillation due to the significant input pole presented by this source capacitance. Other approaches which amplify signal voltage developed across a source resistor produce nonlinearity due to the inherent dynamic source impedance of SiPMs and an excessively long wave shape. A common-base transistor amplifier (CBA) was chosen to address these concerns. The CBA acts as a transresistance amplifier or current to voltage transformer without the need for feedback. The result is a stable circuit with an input impedance of less than 4 ohms.

A differential output amplifier is required to drive the signals through 10 meter Meritec cables to the inputs of the Digitizer Boards which are located in rack mounted crates near the detector. The shaper/driver is a differential driver amplifier configured as a multiple-pole feedback filter with a corner frequency of 5 MHz which provides a peaking time of 30 nS for ADC sampling at 65 MHz.

The SiPM delivers nominally 37 fC for a single micro-cell fired and the CBA produces an Equivalent Noise Charge of about 43 fC, as shown in Figure 7.14, so the signal to noise ratio is approximately 0.86 at the single micro-cell level. A Minimum Ionizing Particle is expected to produce approximately 35 photoelectrons which would yield 9 micro-cells fired given a PDE of  $\sim 25\%$ .

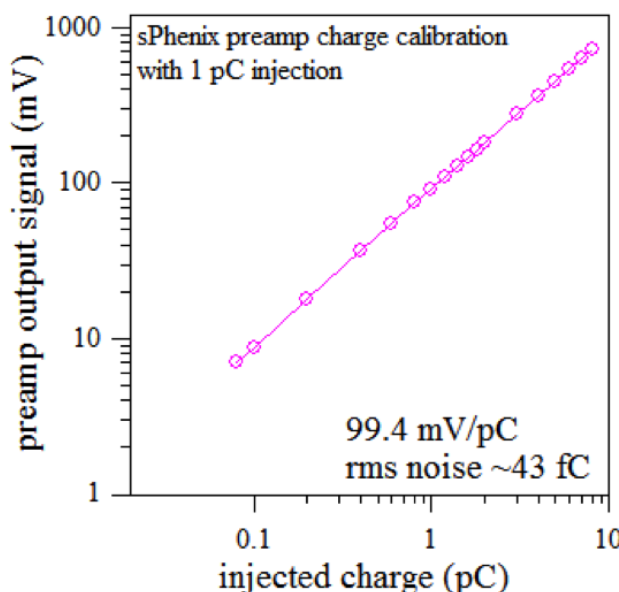


**Figure 7.14:** The response of the common-base transistor amplifier as a function of the injected charge as measured in the lab. The measured RMS noise is  $\sim 43$  fC which matches the charge injected by a single microcell of the SiPM firing.



## 7.2.2 Gain Stabilization

The SiPM reverse breakdown voltage,  $V_{br}$ , is proportional to temperature and increases nominally by  $60\text{mV}/^\circ\text{C}$ . As the SiPM bias increases over  $V_{br}$ , the SiPM begins to operate in Geiger mode with a gain up to  $2.75 \times 10^5$  and is linearly proportional to the bias over-voltage,  $V_{ov}$ . The range of this over-voltage is typically 4 Volts and represents the useful gain range of the device. In order to compensate for temperature variations and maintain a stable gain, a closed feedback loop consisting of a thermistor, ADC, logic and a DAC will be used to adjust  $V_{ov}$  and stabilize the voltage as shown in Figure 7.15. The thermistor is located near the SiPMs and is measured by 16 bit ADC located on the Interface Board. The digitized temperature measurement is transmitted over a serial communications line to a Controller Board located in a rack near the detector where a local processor computes an offset for the bias voltage to correct for temperature variations. The 12 bit correction is transmitted back to the Interface Board where a 12 bit DAC provides an offset voltage to adjust the SiPM bias voltage for the desired gain. Additional corrections can be made to correct for gain variations in SiPMs and correct for increases in leakage current in the SiPMs due to radiation damage.

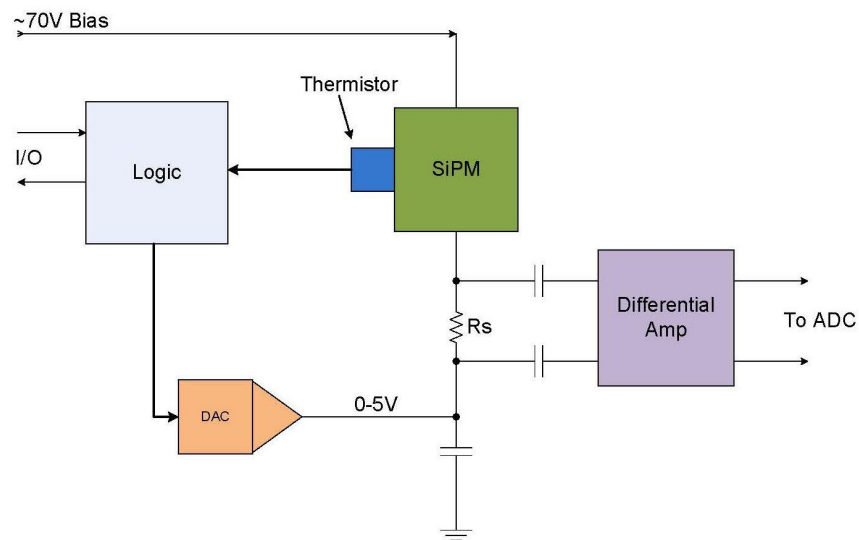


**Figure 7.15:** Block diagram of a temperature compensating circuit for SiPMs

One effect of the increase in leakage current resulting from neutron damage is that voltage drop across the current limiting resistor for the bias supply changes as function of time. In order to compensate for this changing voltage, the bias current for SiPMs in an EMCal or HCal tower is monitored. The measured bias current, combined with the known value of the limiting resistors is used to compute an additional correction to the bias that is added to the bias correction required for temperature variations.

### 7.2.3 Slow Control and Monitoring

The slow control and monitoring for the EMCal and HCal electronics consists of the Interface Board, Slot Controller Board, and Crate Controller Board. The Interface Board mounts directly on the detector, with the Slot Controller and Crate Controller located in a rack mounted crate nearby. A block diagram of the slow control and monitoring system for the EMCal and HCal detectors is shown in Figure 7.16. The Interface Board contains a Xilinx®CoolRunner-II™ CPLD, 16 bit ADC and multiplexers to monitor voltages, leakage currents and temperatures. The CPLD runs a state machine that selects each of the analog channels to be monitored, reads out the associated ADC information and updates the bias DACs when new settings are transmitted to it from the Controller Board. A single Interface Board is capable of monitoring 24 towers for the HCal and 64 Towers for the EMCal. The data is transmitted serially to the Controller Board which is capable of controlling up to 8 Interface boards. A processor on the Controller Board uses the temperatures measured by the thermistors next to the SiPMs to determine the individual DAC settings to correct the bias voltage to compensate for temperature variations and maintain a stable gain. The DAC settings are transmitted back to the CPLD on the interface board and loaded into the appropriate DACs. All digital data is transmitted to the slow control monitoring system via the crate back plane and crate controller.

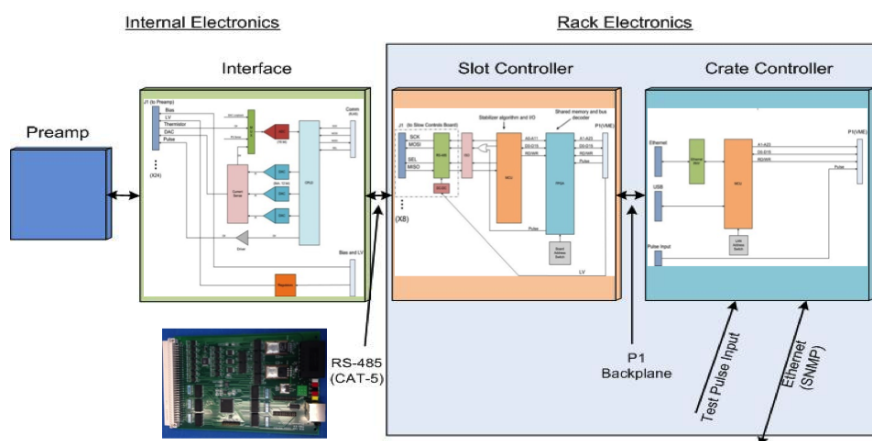


**Figure 7.16:** Block diagram of the slow controls for the calorimeter front end electronics. The inset picture shows a prototype module of the HCal Interface board that will be used on the HCal Beam Test prototype.

### 7.2.4 Digitizers Electronics

One solution to readout the EMCal and HCal is direct digitization of the SiPM signals. The reference design digitizer electronics for sPHENIX is based on the digitizer system built for the PHENIX Hadron Blind Detector (HBD) [147] and modified for the PHENIX Muon Piston Calorimeter (MPC) detector. A block diagram of the Digitizer Module is shown in

Figure 7.17. Differential signals from the preamplifiers are received over a 10 meter Hard Metric cable by an Analog Device AD8132 differential receiver which also serves as the ADC driver. The signals for 8 towers are digitized by an Analog Device AD9257 8 channel, 14 bit ADC operating at 6x the beam crossing clock (BCO). The serialized data from the ADC is received by an Altera Arria V GX FPGA which provides a 40 BCO L1 delay and a 5 event L1 triggered event buffer.

The L1 data from 4 Digitizer Modules are received by an XMIT board using token passing to control the readout from the Digitizer Modules over the back plane. The data is sent by 1.6 GBit optical links using 8Bit/10Bit encoding to PHENIX data collection modules (DCM-IIs). The crate controller interfaces to the PHENIX Granular Timing Manager (GTM) and fans out the 6x BCO, L1 triggers, slow control signals, and test enable signals to the Digitizer and XMIT modules.

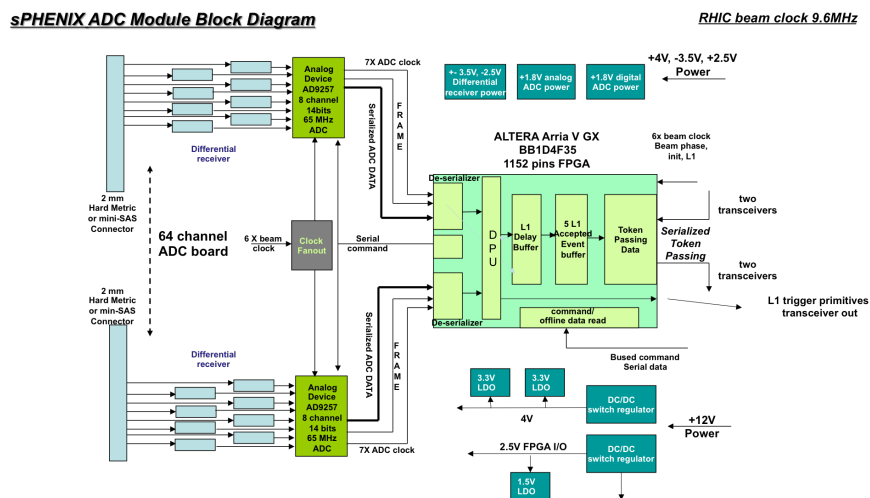


Figure 7.17: Block diagram of the Digitizer Module electronics.

In addition to processing the data for 64 channels, the digitizer board also produces the L1 trigger primitives. For each tower, the 6 samples corresponding to a beam crossing are summed and pedestal subtracted to form an integrated pulse amplitude for the tower. Additional corrections for gain or pedestal shifts can be applied to the integrated signal. The sums from 4 towers forming a  $2 \times 2$  tower array are then summed together to form an 8 bit  $2 \times 2$  patch sum trigger primitive. A total of 16  $2 \times 2$  trigger primitives are formed on each digitizer board every beam crossing. These 16 trigger primitives along with a framing word and header word are transmitted optically using 8b/10b encoding to a trigger processing system located off detector. For a 10 MHz beam crossing frequency, this results in a 1.8Gbit/sec data rate per digitizer board.



## 7.3 Power Systems and Ground

Low voltage power for the analog front end electronics will be provided using bulk supplies and distributed through the second generation PHENIX LV distribution system. The PHENIX LV system is a crate based system which fans out up to 200 low voltage channels which are individually switched and monitored. Control of the system is provided via MODBUS/TCP and client software such as Iconics Graphworx. All low voltage will be locally regulated on the detector. For the digitizers, low voltage power will be supplied by local bulk supplies and DC-to-DC converters located in the crates. Local monitoring of the digitizer voltages will be done using a monitoring system similar to PHENIX monitoring system based on ADAMS modules by Advantech using a MODBUS/TCP interface.

Bias power for the SiPMs will be provided by commercial power supplies such as the WEINER-ISEG system proposed for Hall-D at Jefferson Lab. Bias voltage from single channel of the WEINER-ISEG system is fanned out multiple SiPMs with all the SiPMs for a tower receiving a common bias voltage that has been adjusted for temperature variations and leakage current effects.

Critical to minimizing the noise and maintaining the requirements for the signal-to-noise is a well developed grounding plan. Preliminary work has started on defining such a plan. It is a star grounding plan with the reference point defined near the front end electronics. All electronics will be electrically isolated from the mechanical components of the detector which are separately connected to the experimental ground. All power supplies will have isolated returns decoupling them from the AC power ground. A preliminary grounding plan is shown in Figure 7.18.

## 7.4 Radiation Tolerance

During the past several runs of PHENIX, the radiation levels at several locations in PHENIX interaction region that correspond the approximate locations of where the front end electronics will be located has been measured. The total ionizing dosage (TID) measured per run is dependent on the beam species and energies, but typical values range from 2 kRad to 10 kRad per run with the highest dosage coming during the 510 GeV p+p running periods. While these dosages are several orders of magnitude lower then what is experienced at the LHC experiments, it is still necessary to consider the effects of radiation damage on the front end components. The three areas of concern are the analog devices (amplifiers, DACs and ADCs), the voltage regulators and the CPLD used for temperature compensation, gain corrections and monitoring. For the analog components and regulators, when possible, devices certified as radiation tolerant for CERN LHC applications will be chosen. In cases where devices can not be identified that have been LHC certified, testing will be done to evaluate their radiation tolerance and the impact of failure due to irradiation.

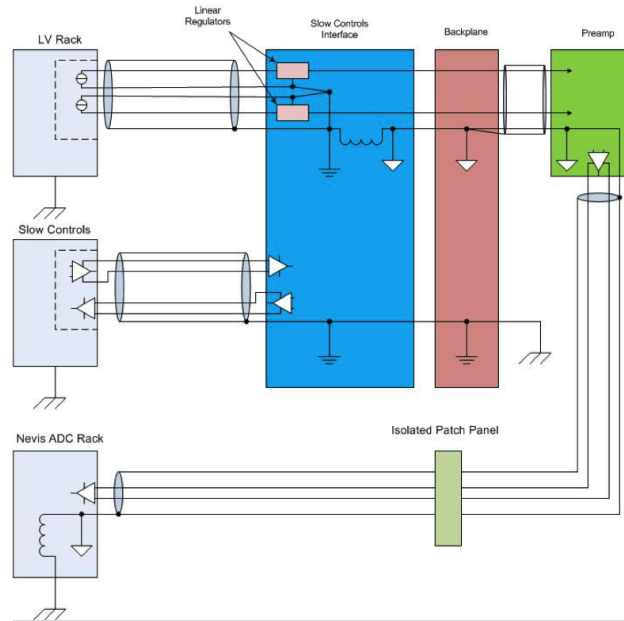


**Figure 7.18:** Preliminary grounding plan for calorimeter electronics which is based on a star grounding configuration. Not shown is the grounding of the mechanical parts of the calorimeters.

In the reference design, the Xilinx®CoolRunner-II™ CPLD technology has been chosen. This device has been tested for radiation effects up to an integrated TID of 22 kRad [148]. There were no Single Event Errors (SEE) observed in the flash memory, allowing the device to be recovered at any time by powering device off and back on. The SRAM cells are sensitive to protons with energies greater than 15 MeV with a MTBF of 11 days in the worst case. The actual MTBF in real applications will be higher since only a small fraction of the Single Event Upsets (SEU) will generate a functional error.

## 7.5 Alternative Technologies

Several alternatives have been considered for the reference design calorimeter electronics. For the optical sensor, avalanche photodiodes (APDs) have been considered. Like SiPMs they are small devices and immune to the effects of magnetic fields. The gain of these devices is significantly less, ( $\sim 50 - 100$ ) compared to SiPMS ( $\sim 10^5$ ) so they would require more demanding low noise, high gain analog front end. However, they do provide better linearity over a larger dynamic range and have shown to be immune to the effects of radiation damage. While the gain of both SiPMS and APDs are temperature dependent, SiPM's have a stronger temperature dependence than APDs (typically  $10\%/^{\circ}\text{C}$  for SiPMS and  $2\%/^{\circ}\text{C}$  for APDs).

A design with the digitizer electronics located directly on the calorimeters near the optical

sensors has also been considered and poses several technical challenges that would need to be addressed. The electronics for the EMCal and Inner HCal would be located in high radiation areas, requiring that all the components (ADCs, FPGAs, LDOs) be radiation hard. The compact location of the electronics would also require additional cooling to maintain a suitable temperature environment for the SiPMs and minimize the leakage current. Finally the location inside the solenoid would limit access to the EMCal digitization electronics to periods of extended shutdown and the inner HCal digitizers would not be accessible after installation in the current reference design. In the current reference design the digitizers are located in racks that are outside the detector behind  $\sim 5\%$  interaction lengths of material. This material provides shielding for the electronics placing it in an area where radiation levels are at a level where radiation hard devices are not required. Located inside racks, the electronics can be air cooled and are easily accessible during short access.

An analog pipeline read design similar to what was done for ATLAS and LHCb has also been considered as an alternative to direct digitization. The challenge of an analog pipeline is providing trigger primitives and maintaining the signal integrity until a trigger is received. ATLAS and LHCb did this using custom radiation hard ASICs which were produced in limited quantities and designed to meet the specific requirements of the experimental data acquisition systems. Using one of these designs would require additional studies on the feasibility of using previously designed chips and the possibility of fabricating additional chips. If it was determined that current chips are not available, then an R&D program to develop a new analog ASIC would be required. It should be noted that the ATLAS upgrade path calls for direct digitization of signals similar to the approach in the sPHENIX reference design.



# Chapter 8

## Data Acquisition and Trigger

### 8.1 Data Acquisition

In this section we detail the architecture of the sPHENIX data acquisition and how to satisfy the requirements to achieve a 15 kHz data accept rate with a livetime greater than 90% in a high-multiplicity environment. The estimates are based on the the RHIC Collider Projections as documented in Ref. [116]. Compared to the luminosity achieved in 2014, we expect an increase of up to about a factor of two of the rates of interaction which take place within a  $z$ -vertex range  $|z| < 10$  cm for Au+Au collisions at 200 GeV. The  $|z| < 10$  cm vertex is inside the coverage of the sPHENIX tracking system. In the case of Au+Au collisions, we expect to record minimum bias triggers mostly (i.e. a simple interaction trigger), and expect to collect in the order of 100 billion events in a typical 22-week running period. There are also selective jet and photon triggers that can sample additional physics from the entire accessible vertex range  $|z| < 30$  cm. In  $p+p$  and  $p+A$  collisions, more selective triggers utilize the EmCal and HCal. Select results from simulation studies are given in the sPHENIX proposal [1].

The sPHENIX reference design consists of the existing silicon pixel detector, new silicon strip detectors, the EmCal, the HCal, and a Beam-Beam Counter, which will provide the vertex determination and the interaction trigger. The readout of these systems closely follows the design of the PHENIX DAQ [149]. The architecture is a fully pipelined design, which allows the next event to be triggered without waiting for the previous event to be fully processed. The existing PHENIX design allows for a depth of 4 such events to be buffered in front end modules before transmission. This multi-event buffering is the key concept to achieve the design event rate of 15 kHz while preserving livetime.

Table 8.1 shows a breakdown of the expected data sizes per subsystem. The estimate for the readout of the calorimeters is based on 6 samples from each channel, and assumes an occupancy of 25% for the EmCal (estimated from HIJING Monte Carlo and plausible expectations for pedestal noise), and 100% for the HCal and the BBC. The estimate for the

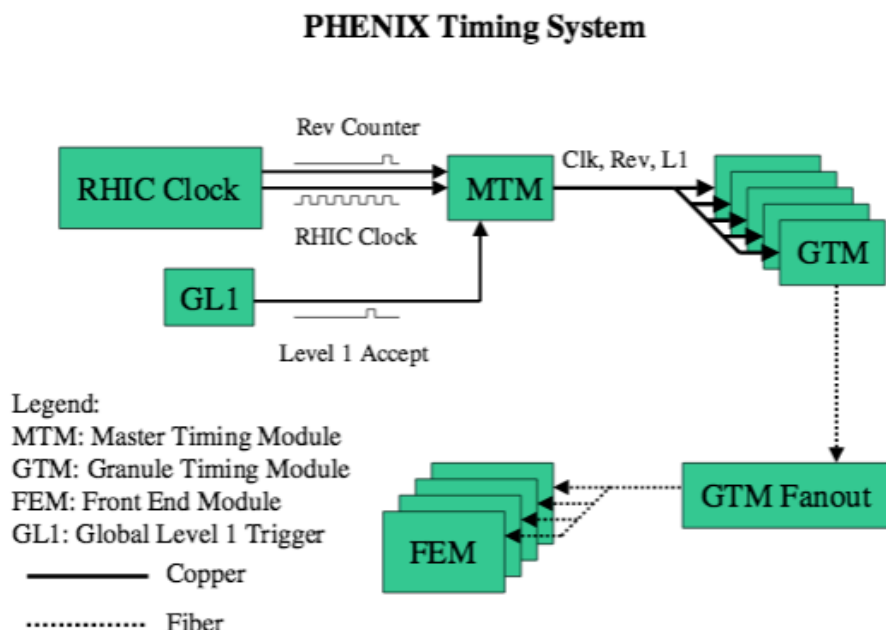


**Figure 8.1:** Schematic view of the trigger and front-end system. The Global Level 1 provides the trigger to the Master Timing System, which is then distributed to the granule timing modules, which provide the subsystem-specific trigger signals and timing to the Front-End Modules.

**Table 8.1:** Counts of channels, fibers, and readout components for the subsystems from the reference design. The last column is the estimated data size from that subsystem per event in Au+Au collision at 200 GeV. In the case of the VTX, the only subsystem that has been in use previously, the data are from the Au+Au part of the PHENIX Run 14, scaled for full azimuthal coverage and smaller radial positions.

subsystem	channels	occupancy	data size (kbytes)
EmCal	24,576	25%	150
HCal inner	1,536	100%	100
HCal outer	1,536	100%	100
VTX	4,700,000	n/a	55.5
BBC	512	100%	3.5

VTX-pixels, the only detector that has been used previously, is derived from data from the PHENIX Run 14, where the pixel configuration consisted of two layers at 25 and 50 mm radius, respectively, with 10 and 20 ladders. In sPHENIX, the pixel layers will be at 24 and 44 mm, with a total number of 36 ladders. The average data size of approximately 42 kbytes per minimum bias event in Run 14 200 GeV Au+Au is scaled by 36/30 to account

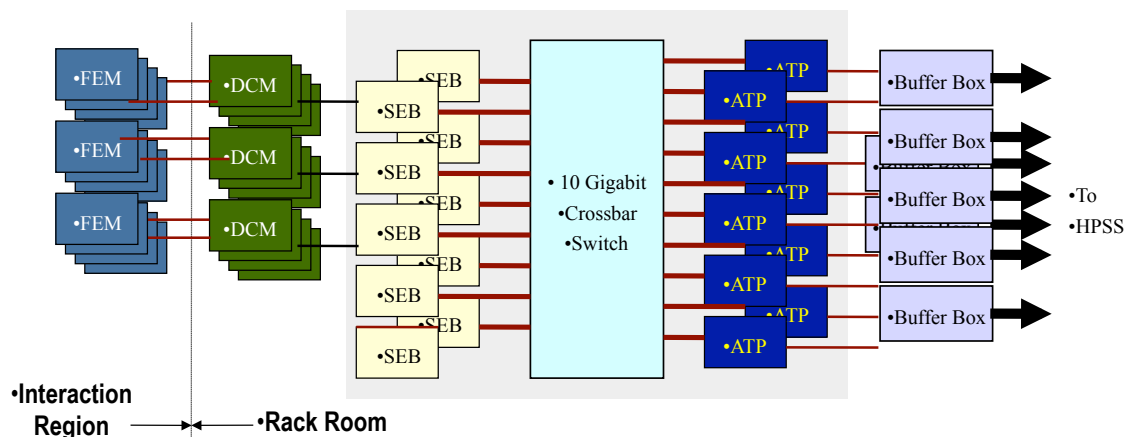


**Figure 8.2:** Overview of the event builder design. The data are digitized in the Front-End Modules and zero-suppressed and packaged in the Data Collection Modules. The data from a given collision are initially distributed over many SEBs. The data from one collision are collected in the ATP's, which sees the full complement of data of that collision for the first time. The ATP compresses the data before transmitting them to the *Buffer Boxes*, from where the data are transferred to a long-term storage system.

for the increased number of ladders to achieve full azimuthal coverage, and then by 1.1 to account for the smaller radial positions of the layers.

Fig. 8.1 gives a schematic overview of the the trigger and front-end system. The Global Level 1 system provides the trigger to the Master Timing System, which is then distributed to the Granule Timing Modules (GTM). These GTMs provide the subsystem-specific trigger signals and timing to the Front End Modules.

The Front-End Module (FEM), digitizes the data from the connected detector channels. The FEMs must be able to store up to 4 events for the multi-event buffering. The GTM's communicates with the FEMs via a data fiber (Fig. 8.1, which furnishes the trigger timing and 8 bits of additional information, referred to as "*mode bits*". The mode bits allow transmission on every crossing to the FEMs. As an example, the PHENIX experiment had a number of FEMs which needed a periodic instruction to reset an analog integration circuit; one would issue that reset instruction during an empty RHIC beam crossing.

The data selected by the trigger system flow from the FEMs to Data Collection Modules (DCM's). Only the latest generation of the data collection module, the DCM-II, will be used. The DCM-IIs, which were developed for the PHENIX silicon vertex detectors, run detector-specific FPGA code to zero-suppress and package the data. This provides the freedom to change the data format as necessary by loading a new version of the FPGA code. A DCM-II has inputs for 8 data fibers.

A group of DCM-IIs interface with the commodity computers called Sub-Event Buffers

(SEBs) via 1.6 GBit/s serial optical links through a custom PCIe interface card, the JSEB-II. Due to overhead in the data encoding, the effective bandwidth through the fiber is 1.28 GBit/s. This 4-lane PCIe card is capable of sustaining 500MB/s input into the SEB. This bandwidth is needed to achieve the envisioned event rate of about 15kHz.

The current layout for the EmCal, the largest source of data, is to read out 4 digitizers ( $4 \times 64$  channels) through one data fiber, resulting in a total number of 96 data fibers. With 8 inputs per DCM-II we need 12 DCM-IIs. These 12 DCM-IIs would connect in groups of 3 (a *DCM group*) to 4 SEBs. This is similar in scope to the PHENIX silicon detectors.

Table 8.2 breaks down the counts of the various components by subsystem.

**Table 8.2:** Counts of channels, fibers, and readout components for the subsystems from the reference design.

subsystem	channels	fibers	DCM-IIs	SEBs
EmCal	24,576	96	12	4
HCal inner	1,536	12	2	2
HCal outer	1,536	12	2	2
VTX	n/a	32	8	4
BBC	512	4	1	1

There is freedom to configure the mapping of DCM-IIs to SEBs differently, and vary the number of DCM-IIs that send their data to a given SEB. In this way, we could obtain more bandwidth by using more SEBs which connect to fewer DCM-IIs each, or save SEBs by connecting more DCM-IIs to fewer SEBs.

The zero-suppressed and packaged data are sent on to the Sub-Event Buffers. Each SEB still only holds a fragment of the data of a given collision, which now have to be combined into a full event. This is accomplished on computers called Assembly and Trigger Processors (ATP's) as shown in Figure 8.2. In addition to assembling the event fragments from a particular collision into a full event, the ATPs run a compression algorithm on the data, forming a distributed compression engine that reduces the data volume by typically 45%.

Central to the Event Builder is the network switch, which must be able to sustain the aggregated bandwidth in a non-blocking fashion. Non-blocking means that data can flow at line speeds between two arbitrary ports, while at the same time line-speed data is being transferred between any other two ports. We used a Force10 ExaScale 10Gbit/s switch, which was one of the few affordable switches in 2011. Network equipment is subject to rapid improvements and price drops. There will be a wide selection of viable network switches at commissioning time.

Data acquisition from a possible TPC would likely be quite different from the calorimeter and silicon readout, since data span many beam crossings. The PHENIX data acquisition architecture is flexible enough to adapt to such a readout, where most likely data would



be acquired and buffered continuously over many crossings and correlated with triggered calorimeter data in near time or offline.

### 8.1.1 Data Acquisition Performance

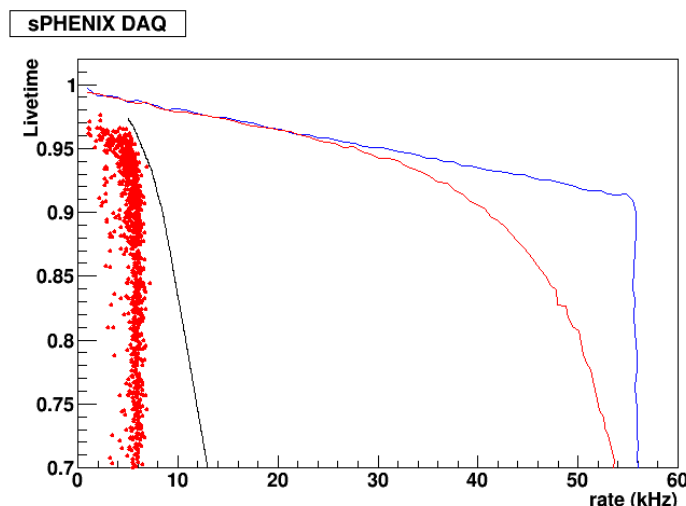


**Figure 8.3:** Livetime as a function of DAQ accepted event rate. The points are measurements from Run 14 Au+Au running in PHENIX, the black line is the measured performance from one older PHENIX system, the red line shows the simulated performance with 4 event buffering with the sPHENIX calorimeter ADC system, and the blue line shows the expected behavior with 100 events buffered in the front end.

The sPHENIX data acquisition system eliminates the slower DCM I modules, and also uses the TI TLK2501 optical links to transmit data from the front end modules to the DCM II at 1.28 Gbps. These changes, along with 4 event buffering in the front end modules, result in a predicted livetime as a function of DAQ rate following the solid red line in Figure 8.3 showing good livetime at 15 kHz.

## 8.2 Triggering

The EMCAL trigger is needed for photons and Upsilon's in  $p + p$  and  $p + A$ , and the HCAL+EMCAL trigger for jets and single hadrons. In  $Au + Au$ , only photons and the highest energy jets require a trigger beyond a minimum bias trigger. The basic strategy of triggering developed for PHENIX, using data transmitted on fiber on every crossing leading to a Level 1 accept is adaptable to sPHENIX, and as much of the trigger electronics as practical will be reused in sPHENIX.

### 8.2.1 The Minimum Bias Trigger

The basic minimum bias trigger is expected to be generated by a detector at forward rapidities that is the equivalent of the PHENIX Beam-Beam Counter (BBC) [150]. The PHENIX BB counters covered the pseudorapidity range  $3 < \eta < 3.9$ , and the negative equivalent.

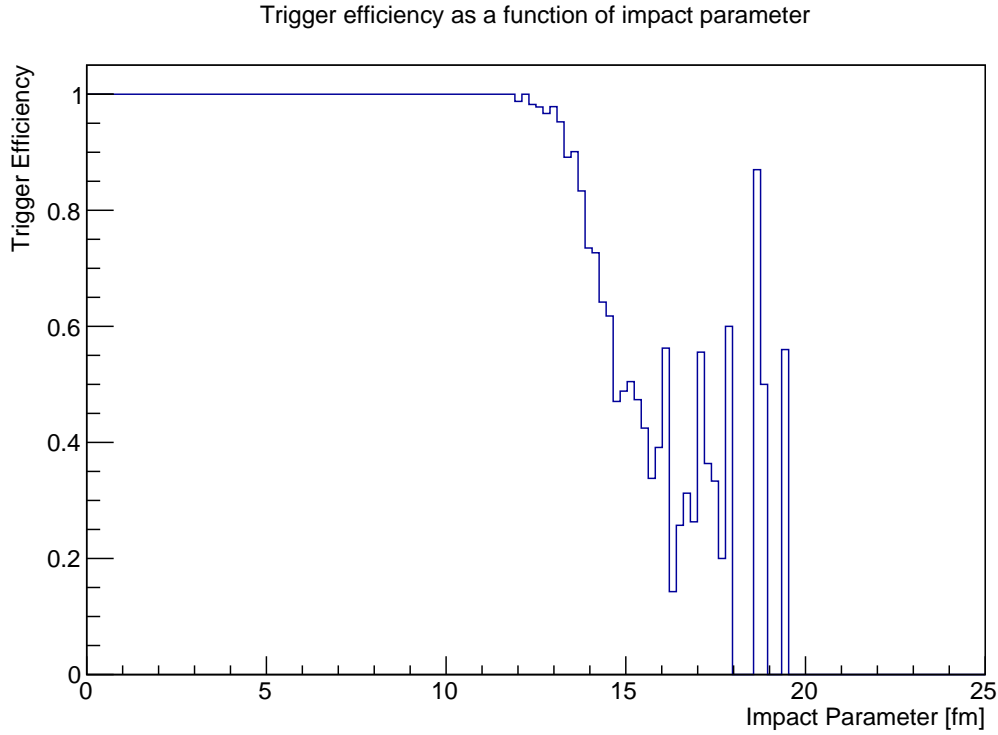


**Figure 8.4:** The trigger efficiency in Hijing events for 200 AGeV Au+Au collisions of beam-beam counters at forward pseudorapidities  $3.80 < \eta < 4.69$ , and the negative equivalent. The trigger requires at least one charged particle in the detector on each side with an energy about 200 MeV. This detector would also provide the fast timing signal to determine the collision vertex.

The sPHENIX Beam-Beam Counter will require a section that provides a timing resolution better than 100 ps for a vertex determination. One of the constraints is the magnetic field, which limits the readout choices for such a detector. With the current technology of choice in a magnetic field, Silicon Photomultipliers, the timing resolutions that can be achieved at room temperature are not better than about 200 ps for specially selected SiPMs [151], which is not good enough for the vertex measurement for the trigger. The required timing resolution can generally only be achieved with photomultipliers. This would require specially designed photomultipliers rated for applications in magnetic fields, or the detector to be located outside of the field.

One possible design is to instrument the flux return doors at  $\pm 3150$  mm with a large detector that will cover the forward region to obtain the collision topology and, offline, measure the reaction plane. It would be augmented by a small inset in the holes in those doors around the beam pipe, where the magnetic field strength is negligible. It is possible that current PHENIX Beam-Beam Counter could be re-used for this purpose, or a similar device could be built.

The fast timing signal and large dynamic range requirements will likely drive the design towards a Čerenkov detector. For reference, the PHENIX BBC consisted of two detectors forward and backward of 64 3cm quartz Čerenkov radiators each, read out with individual Hamamatsu R6178 phototubes. When moved to a  $z$  position of  $\pm 3150$  mm, the PHENIX BBC would cover the pseudorapidity range from  $3.80 < \eta < 4.69$ , and the negative equivalent.

The efficiency of this timing-providing detector is limited by the collision multiplicity, since the requirement is that at least one charged particle with an energy above 200 MeV registers on both sides. For peripheral events with an impact parameter above 13 fm, this efficiency is significantly lower than 100% (Fig. 8.4).

## 8.2.2 Jet Trigger

The calorimeters will be able to supply locally generated trigger primitives, such as energy summed up over overlapping tiles of  $2 \times 2$  calorimeter towers. This will be the basis for a jet trigger, which will be important as one requires high statistics measurements in proton-proton, proton-nucleus, light nucleus-light nucleus collisions with a wide range of luminosities. It is important to have combined EMCal and HCal information available so as to avoid a specific bias on the triggered jet sample.



# Chapter 9

## Infrastructure

The sPHENIX detector will be located in the RHIC building 1008 complex Major Facility Hall (MFH). It consists of a central hall and two expanded tunnel areas. Adjacent to the MFH is a 3700 square ft. Assembly Building, a Counting House, and Rack Room. Concrete block shielding is provided between the MFH and the assembly building. The central hall is 57 ft. long by 61 ft. wide and 47 ft. high with a 12 ton overhead crane and (2) 1-ton auxiliary cranes. A 40 ton crane is installed over the assembly area. The expanded concrete tunnel areas on either side of the Central Hall are 53 ft. long by 30 ft. wide and 21.5 ft. high with a 9 6 concrete platform to raise the floor level. The Assembly Hall is steel frame with metal siding. See figure 1.1 for a plan view of the structures.

All buildings are connected to the BNL 13.8 KV AC distribution system. The electrical substations at buildings 1008A and 1008B convert 13.8 KV to 480 volts AC for distribution into the downstream distribution network of 480 V to 208/120 volt transformers and panels.

### 9.1 Auxiliary Buildings at the Experimental Site

Auxiliary Buildings 1008B and 1008 C contain cooling water pumping stations and HVAC equipment to service the MFH, Assembly building, and Counting House.

### 9.2 Central Pedestal

The Central Pedestal will support the sPHENIX Main Magnet. Four detector systems will be constructed in the inner and outer radius of the magnet. The Beam Pipe passes axially through the magnet/detector center.

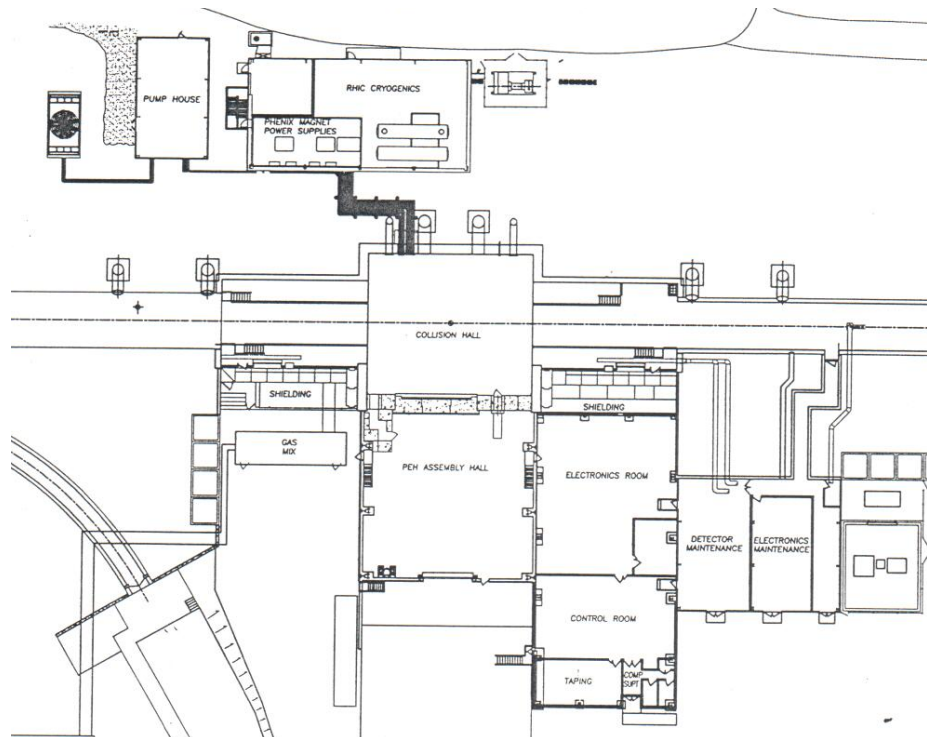


**Figure 9.1:** sPHENIX Major Facility Hall and Auxilliary Buildings

## 9.3 Electronics Racks

Electronics racks for the detectors will be mounted on the Central Pedestal and in the Counting House Rack Room. They will be fully enclosed and contain water cooled heat exchangers to remove heat. They will each contain a safety interlock system to shut their electric power & cooling water flow off during conditions such as over-temperature, smoke or water leak detected. Permanent walkways, platforms and ladders, mounted on the Central Pedestal allow for access to the racks. All will be equipped with appropriate safety railings and kick plates.

## 9.4 Beam Pipe

The sPHENIX Beam Pipe is a thin walled cylindrical tube with overall length of 101.2 inches. It is made up from a central 31.5 inch long beryllium section formed from 0.0 inch thick rolled and seam brazed sheet. The central beryllium section is then brazed to aluminum end sections which are in turn welded to explosion bonded 2.75 inch conflat flanges. The flanges are bolted to the corresponding flanges on the upstream and downstream beam tube transition sections which increase the beam pipe diameter to 5 inch OD in 2 steps. The sPHENIX tube will be supported from the flanges and also within the central pedestal by low mass supports. sPHENIX will reuse the existing central Be section and modify the transition sections as necessary to accommodate the sPHENIX detectors. In addition, gate valves and pumping ports will be added to allow removal of the central beam pipe sections.

## 9.5 Shield Walls and Openings

The sPHENIX shield wall is approximately 61 wide by 48 high by 5 6 deep, made from light concrete blocks. A large rolling shield block door measures 30 wide by 36 high. The shield blocks are 20 tons each. The wall is built on a rolling platform that rides on a number of 200 ton each rated Hillman rollers. This wall can be moved away from its opening to allow large detector pieces or other equipment into and out of the MFH. There is a rolling, motor driven personnel door and emergency egress labyrinth separate from the main rolling shield door. There are PVC pipe penetrations for utilities from the assembly hall into the MFH imbedded into a concrete sill. Two 3 tubes for cooling water services, twelve 4 tubes for electrical power cables, and eighteen tubes for signal cables are provided. No major modification to the PHENIX shielding configuration is anticipated for sPHENIX.

## 9.6 Electrical Power

Numerous distribution transformers are supplied by a 480 volt 1200 amp bus that contains eight molded case circuit breakers. This is the primary Normal Power distribution supply that powers all experimental and non-experimental loads. An emergency backup diesel generator provides 150 KW of power to critical loads in the event of on or off site power interruption. A 30 KVA Uninterruptible Power Supply (UPS) supplies battery backed-up 208/120 VAC power primarily to critical computer loads. A 3 KVA UPS supplies backup power to critical safety instruments protecting the experiment. sPHENIX will utilize the existing PHENIX power infrastructure, however, some modifications to the distribution system will be required at the 480/220 volt level.

## 9.7 Safety System and Control Room Monitoring & Alarm System

SPHENIX will have a real time, monitoring and control system that will take inputs from smoke and fire detection systems as well as crash buttons. Upon detection of an off normal situation from any input, safe shutdown of the experiment will be initiated. Existing PHENIX systems will be utilized to the maximum extent possible, although new components will be necessary to integrate new safety systems for potential new hazards, like oxygen deficiency.

## 9.8 Cooling Water

Chilled water is required at 20 degrees C for cooling the detector electronics. Pumping capacity is 300 gallons per minute (GPM). The existing cooling towers and chilled water system at the 1008 complex has the capability to meet these specifications. sPHENIX will utilize the existing PHENIX chilled water infrastructure, however, some modifications to the distribution system will be required at the rack level and to satisfy any other new water cooling needs.

## 9.9 Climate Control

Conventional heating, ventilation and air conditioning (HVAC) is required. Approximately 100 tons capacity currently is in use, 40 tons in the IR, 50 tons in the rack room and the remainder serving the rest of the complex. sPHENIX will utilize the existing HVAC system, with minor additions and upgrades as necessary.



## 9.10 Cryogenics

A cryogenics supply system is required for the sPHENIX superconducting solenoid magnet. This system is described in the Magnet section of this report.



## Chapter 10

# Installation and Integration

sPHENIX has been conceived to be straightforward to manufacture and assemble, but it still requires significant and well thought out integration and assembly schemes to achieve the specified alignment and positioning requirements of the component detectors. In addition, the design must allow for appropriate access for maintenance and servicing of the functional components of these detectors and to optimize the integration and installation concept. The goal is to balance design tradeoffs while considering the effects on performance, cost, schedule, and reliability. Figure 10.1 illustrates the overall design concept for the installed sPHENIX experiment. The following sub sections of this topic indicate how these factors will be addressed in the sPHENIX project.

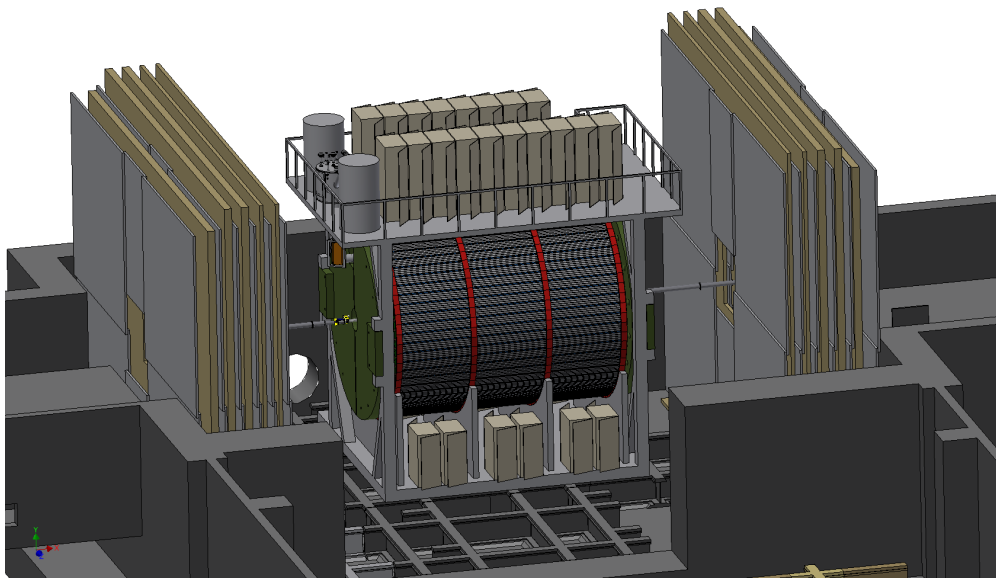


**Figure 10.1:** sPHENIX in IR

## 10.1 Specifications and Requirements

### 10.1.1 General Limits and Requirements

The following are the key general requirements that guide the integration, inter detector assembly and installation of the sPHENIX components comprising the overall sPHENIX experimental apparatus. Requirements may be superseded by individual detector subsystem requirements (see subsystem sections)

**Table 10.1:** sPHENIX General Limits and Requirements

Item	General Requirements
Location for final assembly / Installation	PHENIX Assembly Hall
Assembly Hall ("AH") Crane	rated at 40 tons
Interaction region ("IR") Crane limit	12 tons plus 2 auxiliary, 1 ton cranes
Floor Loading Limit	4000 psi max
Assembly support surface	existing PHENIX rail system
Clearance requirements	2 inches (50 mm), between subsystems
Positional precision	0.1 mm
Angular precision	10 milliradian (roll, pitch and yaw)
Positional stability	0.5 mm
Angular stability	10 milliradian (roll, pitch and yaw)
Positional repeatability	1.0 mm
Angular repeatability	10 milliradian (roll, pitch and yaw)
Positional tolerance	(see individual detector specifications)
Angular tolerance	(see individual detector specifications)
Temperature and humidity	-10 to 50 deg C and 0-100 percent R.H.
Magnetic field	0–2T inside magnet, 0–100 gauss field outside
Radiation environment	to be specified
Detector cooling requirements	(see individual detector subsystems)
Rack cooling requirements	12.0 gpm @ 50 deg F, for 2 kW per rack
Cryo requirements	(see Magnet Section)
Monitoring and safety system requirements	(see Infrastructure Section)
Overall size requirements	fit through the sPHENIX sill on existing rail system (see Figure 1

### 10.1.2 Configuration Management and Control

In order to assure that the various subsystems of the sPHENIX experiment honor the space requirements for all other components, not interfere with other subsystem and/or infrastructure features of the sPHENIX experimental location, and assure that the integration and installation concepts are achievable, envelope control drawings will be prepared for

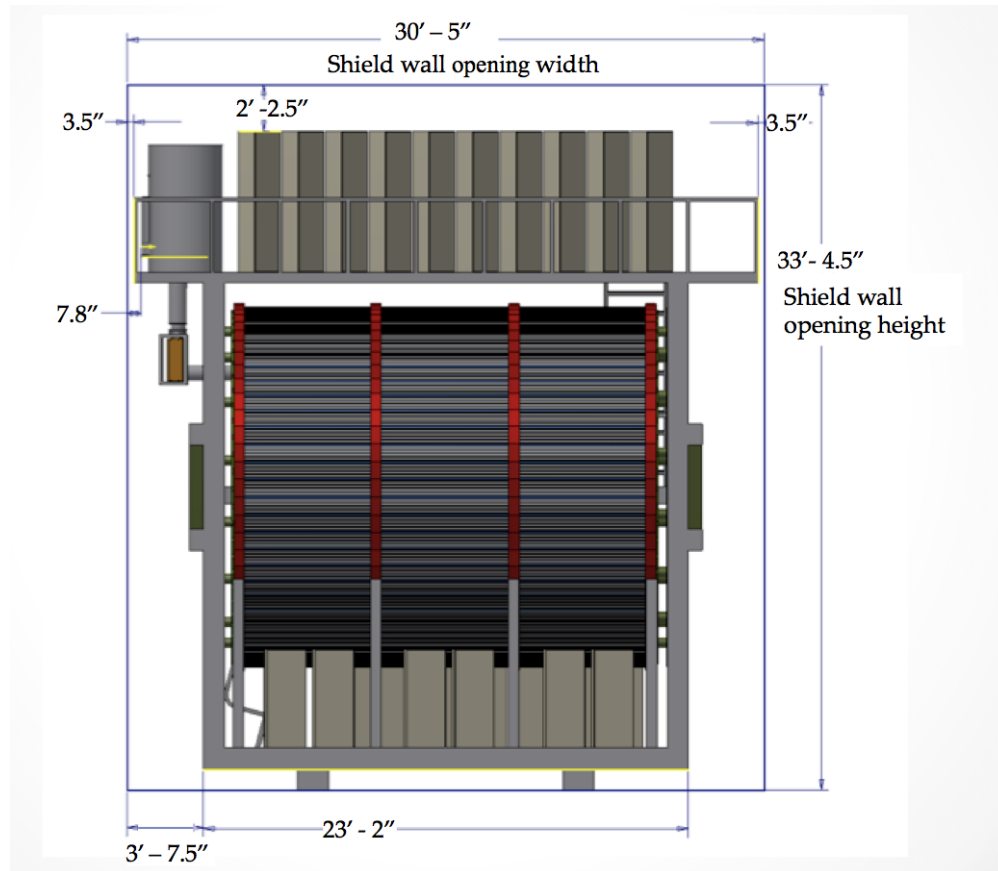


**Figure 10.2: sPHENIX Overall size**

each detector subsystem and an overall envelope control drawing will be prepared for the integrated sPHENIX experiment.

Subsystem envelope control drawings will provide the limiting envelope in to which the subsystem components must fit, key dimensions for subsystem components which interface with other subsystems and /or infrastructure, and any other information pertinent to the space to be occupied by the subsystem and its relationship to adjacent subsystems and infrastructure. Figure 10.3 is the subsystem envelope control drawing for the EMCal detector subsystem.

The overall envelope control drawing will provide the limiting space allocations for each of the detector subsystems, space allocations for structural support and integrating interfaces.

Figure 10.4 is the overall envelope control drawing for the sPHENIX experiment.

All subsystem design drawings, fabrication and assembly procedures and all other documentation which define the sPHENIX assembly, Installation and component subsystems will comply with BNL and DOE requirements that will be governed by sPHENIX controlled documents for Configuration Management and Documentation Control Systems.

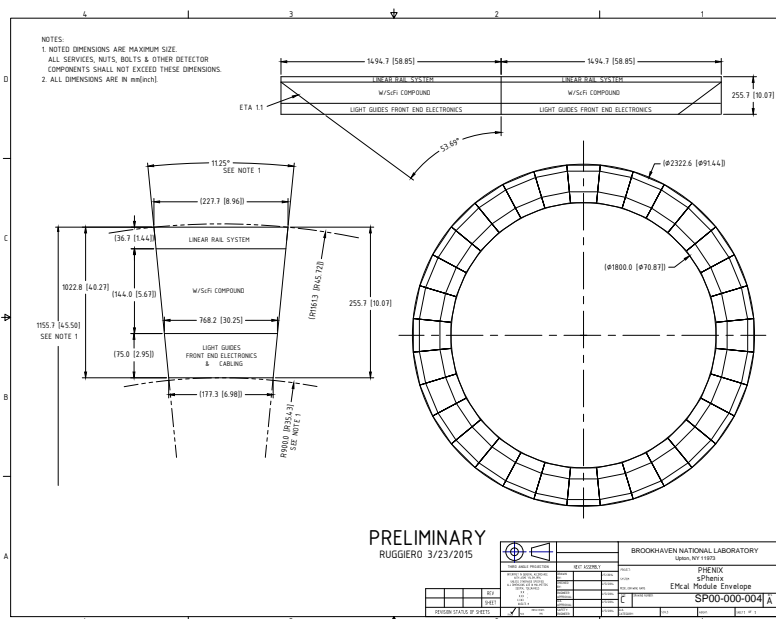


Figure 10.3: EMCal Envelope Control Drawing

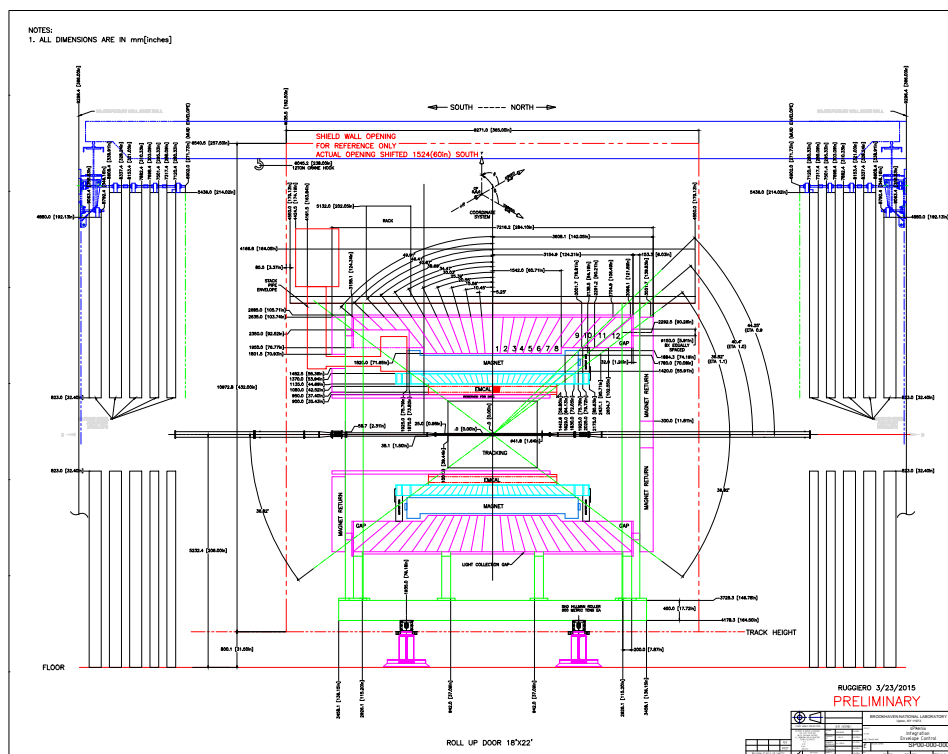


Figure 10.4: sPHENIX Envelope Control Drawing

### 10.1.3 Weight Estimates

In order to properly evaluate the design and adequacy of the integration and installation conceptual design which will proceed parallel to the detailed design of the component detector subsystems and infrastructure, it is necessary to have reasonable estimates of weights for the major components. The following table provides the estimated weights for the major subsystem components for sPHENIX.

**Table 10.2:** sPHENIX Estimated Weights of Major Components

Subsystem	Weight	Notes
Inner Hcal	64,000 lb, 32 ton	2000 lb/sector
Outer HCal	854,000 lb, 427 ton	27,000 lb/sector
EMCal (with mounting)	61,000 lb, 31 ton	900 lb/sector
Inner HCal Assy Rings	1650 lb, 1 ton	total, 2 rings
Inner to Outer load transfer rings	6400 lb, 3.5 ton	total, 2 rings
Flux return end caps	226,000 lb, 113 ton	
Magnet + stack wt	42,000 lb, 21 ton	
Total Detector load on Central Pedestal (CP)	1,255,000 lb, 628 tons	
CP weight without magnet and detectors	250,000 lb, 125 tons	

### 10.1.4 Alignment Requirements

Alignment of the detector subsystems to each other and to the RHIC nominal beam path, as reflected by the positional and angular orientations relationship of the detector subsystem components to each other and to the sPHENIX global coordinate is essential to the proposed performance of the sPHENIX experiment. Internally, each detector subsystem component is aligned to the subsystem's own coordinate system as defined by each subsystem. This alignment is then reflected to the global system by means of inspection of dimensional data with respect to reference points ("fiducials") to be established on the exterior of each component. These reference points are used in the assembly and installation process to establish position and orientation of these components and by extension the internal features of each component to the sPHENIX global coordinate system.

Each component, as it is assembled and installed into the sPHENIX support structure, is to be aligned by means of built-in adjustment to achieve specified precision with respect to the experiment support structure (i.e. the Central Pedestal) which shall have fiducial references related by survey. After the Central Pedestal is assembled with all subsystems and is moved to the Interaction Region (IR) it is to be positioned and aligned to the sPHENIX global coordinate system at the nominal Interaction Point ("IP").

The sPHENIX global coordinate system is related to the RHIC coordinate system from the Interaction Point the center of the RHIC ring and the straight line of the RHIC ring orbit through the sPHENIX IP.

Positional precision and alignment tolerances for the individual detector subsystem component internal features are established for each individual detector subsystem independently (see the appropriate subsystem for details). The subsystem components and/or the support structure will be designed with appropriate adjustment capability to achieve the specifications indicated in the previous section.

Precision is determined by combining the accuracy of the measurement method (survey) for locating the individual fiducial points for subsystem components directly with the fineness of adjustment provided in the subsystem mounting system.

Stability is the tendency for the assembly and its components to remain in the same location over a period of time, under normally varying environmental conditions for both operational and non-operational conditions.

Repeatability is the tendency of the assembly and its components to return to the same location after maintenance operations requiring disassembly and reassembly and/or temporary displacement and return of the entire assembly or any of the components (usually for maintenance purposes).

Tolerance is the amount by which a measured position or angle can vary from its nominal exact position or angle. This is the sum of measured variance plus the measurement precision, repeatability and stability. For internal components of subsystems, the tolerance with respect to global coordinates is calculated from a combination of the tolerance of the external fiducial points and the tolerance of the relative dimensional feature of internal features to the external fiducials. In some cases the tolerance calculations might require combining multiple relative tolerances.

### 10.1.5 Service Requirements

Adequate space is to be provided to route appropriate services to all of the detectors including power, signal and monitoring cables, cooling channels (air cooling) and piping (liquid cooling) for removal of heat generated by detector electronics and distribution equipment for branching and integrating electronics signals, electric power and cooling from detector service racks to module/sector front end electronic distribution panels and flow distribution manifolds to the installed detector components. Within the components these services are to be distributed to individual active components as described in the subsections describing the individual detector subsystems.

In addition, space is to be provided for cooling services, power to the subsystem racks from the cooling source(s) and line power breaker boxes. Space is to be provided as well to route signals to the rack room. Refer to the infrastructure for more detailed information



on service requirements.

During the research and development process for each of the detector subsystems, prototype mockups (dimensionally accurate, non-functional) are to be developed to assist in planning the design of adequate space for services. A mockup of an Inner HCal half-sector is shown in Figure 10.5.

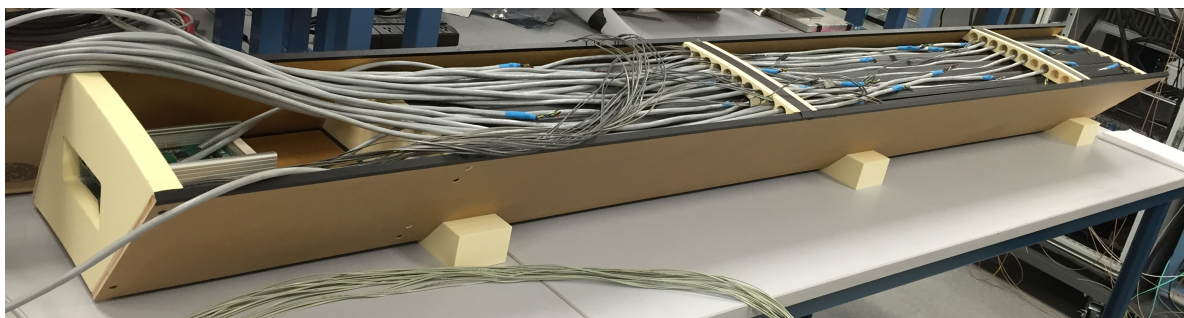


**Figure 10.5:** Inner HCal Half-sector mockup

#### 10.1.6 Accessibility

The sPHENIX detector subsystems will be designed to operate without maintenance for extended periods. Maintenance of the active detector components and the magnet is not possible during a run, except that access is provided to the subsystem rack electronics on all levels, to the magnet valve box and to power and cooling sources and primary distribution equipment. Limited access to the outer HCal detector electronics is possible, but it is not a requirement. Any individual component of any detector subsystem is to be accessible during a major shutdown of three or more months by reversing the assembly process described later in this report.

#### 10.1.7 Quality Control

sPHENIX engineering will implement the full quality assurance program described elsewhere in this document by establishing procedures to assure that the design of sPHENIX meets the requirements of BNL, DOE and industry best practices, including implementing the appropriate configuration management, documentation control, work planning, quality control testing and inspection and performance verification.

## 10.2 Component Integration

### 10.2.1 General Integration Concepts

sPHENIX is designed to be integrated into a single structural assembly wherein a central support structure, central pedestal ("CP"), provides a base on a set of roller bearings, which in turn supports a set of four structural arcs ("cradles") to support the Outer HCal detector subsystem and pillars to support an intermediate level platform, an upper platform and the north and south flux return end caps.

The superconducting solenoid magnet is support by 12 mounting feet, six each equally distributed at the north and south ends of the magnet in the annular space between the magnet outer diameter and the Outer HCal inner diameter. The Outer HCal provides two additional support rings on its interior diameter onto which the interior Inner HCal and Tracking detector subsystems are mounted. The EMCal detector subsystem is divided into 64 (32 north and 32 south) sectors which are individually mounted to adjacent Inner HCal sectors.

There will be two sets of four roller bearings under the base platform. One set will be oriented to move the entire experiment assembly north or south, while the other set of roller bearings will handle movement east or west. Relocation of the assembly in these directions is accomplished on the existing PHENIX rail system and allows for repositioning of the assembly in the IR and moving from the AH to the IR for installation, maintenance and upgrade operations. The use of two sets requires that one set be retracted when the other set is in use. Figure 10.6 shows an exploded view of the detectors which comprise sPHENIX.

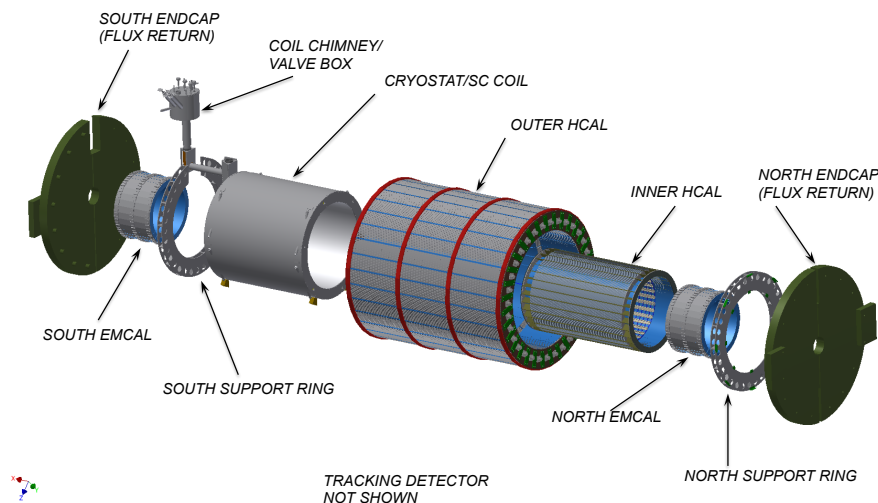


**Figure 10.6:** sPHENIX exploded view

## 10.2.2 Structural Load Support

Roller bearings for the CP are to be sized for approximately twice the estimated load of the fully assembled sPHENIX experiment. The CP base will be built of structural steel and support the four cradles and four pillars which will be welded to the base as well as provide the lower level platform for detector electronics racks. The Outer HCal will be fully supported by the cradles while the mid and upper platforms and magnet flux return end caps will be supported by the pillars.

The outer HCal is comprised of 32 sectors which are tied together at their north and south ends by splice plates. The loads of each of these sectors is transferred through the splice plates to the cradles. Interior to the Outer HCal will be the magnet mounting feet and Inner HCal support rings which will transfer the magnet and inner detector structural loads separately to the base through the Outer HCal.

The Inner HCal is comprised of 32 sectors each of which has mounting provisions on its inner diameter for two EMCal sectors. Each of the 32 Inner HCal sectors is mounted on its north and south end plate to a end rings. The north and south end rings that tie the 32 sectors together are then mounted to the north and south structural rings which transfer the load of the inner HCal sectors plus the EMCal sectors to the Outer HCal and through the Outer HCal to the cradles to the base to the roller bearings to the rails and finally to the floor.

The tracking system will also have a support structure which attaches to the north and south structural rings that will transfer its load in a similar manner. Figure 10.7 shows the load path through the support structures

## 10.2.3 Alignment

The sPHENIX overall alignment concept will be as follows:

- Internal alignment of detector subsystem components in the interior will be aligned as required by the subsystem at the subsystem subassembly level in accordance with the subsystem requirements, related to a set of external fiducials on the subassembly modules which are deliverables from the subsystem to the sPHENIX AH where final installation will take place. These fiducials will be documented to enable analytical reconstruction of the internal relevant features and to define a nominal axis and centerpoint relationship to the fiducials for each of the subassembly modules.
- The CP base and cradle assembly will be provided with adequate precision alignment features (reference fiducials and adjustment features) to define the nominal experiment axis and center point and the position of the initial Outer HCal sector to align its reference axis and center point to that of the CP Base and cradle assembly. Survey and shimming will be employed to fix the position of the initial Outer

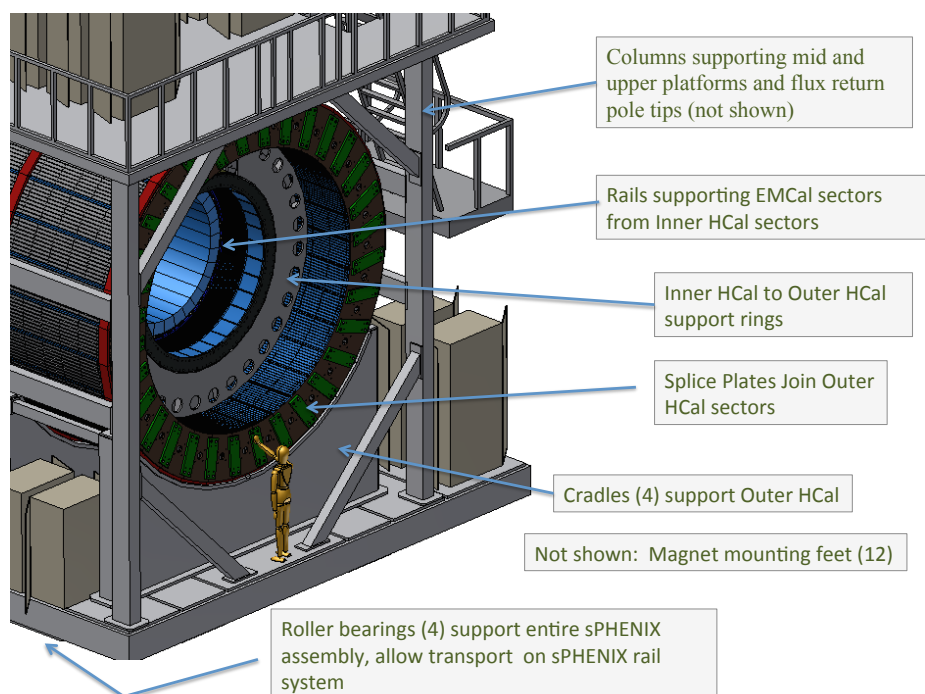


**Figure 10.7: sPHENIX Structural Support**

HCal sector within the tolerance specifications indicated in the general requirements section, above.

- As each additional Outer HCal Sector is installed it will be surveyed, adjusted and shimmed into place with respect to the required tolerances, until the lower half of the Outer HCal is completed. Figure 10.8 shows the initial Outer Hcal sector installed and aligned.
- The Superconducting solenoid magnet will have been surveyed and been sufficiently tested to establish a nominal magnetic axis and centerpoint which will have been related to external fiducial points on the magnet and those relationships recorded. The magnet will have 12 adjustable mounting supports attached to position and secure the magnet onto the inner surface of the Outer HCal.
- After the lower half of the Outer HCal installation is completed, the magnet shall be mounted surveyed, aligned and secured to the OuterHCal in accordance with requirements.
- The remaining Outer HCal Sectors are installed, surveyed, adjusted and shimmed into place with respect to the required tolerances, until the upper half of the Outer HCal is completed.

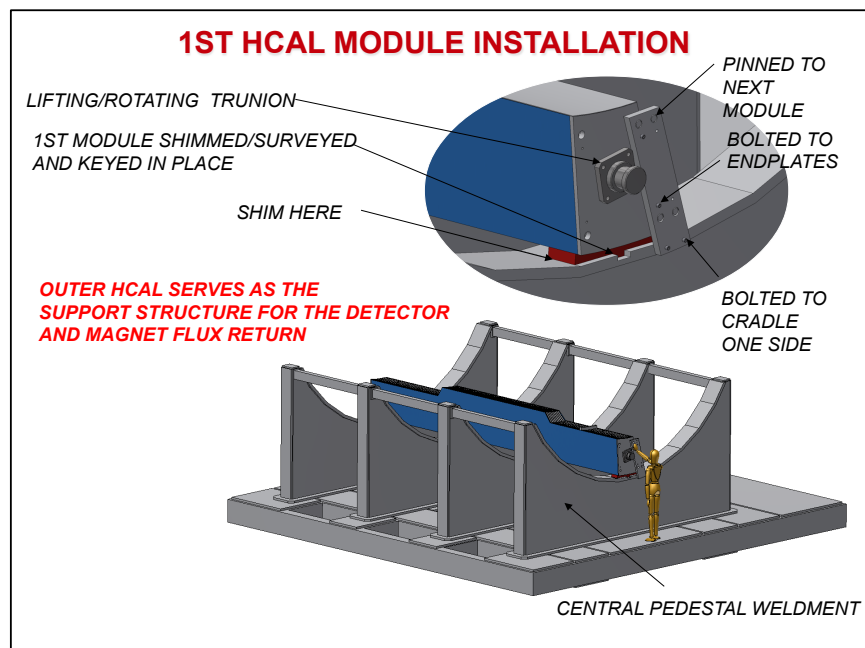


**Figure 10.8: sPHENIX Initial Alignment**

- The Inner HCal sectors are installed into a complete detector aligned using mechanical precision features, survey and shimming to achieve the desired alignment of each of the sectors to each other and external fiducial points. The entire assembly is then surveyed, aligned and secured onto the Inner HCal to Outer Hcal support rings.
- Each of the 64 EMCal sectors is then installed onto the rail systems on each of their respective Inner HCal sectors, surveyed, positioned, adjusted and secured into place in accordance with required tolerances. Figure 10.9 shows the installation of an EMCal sector.
- The detector assembly on the CP support structure is completed by installing and aligning the Tracking subsystem with the nominal axis and centerpoint.
- Finally, the entire CP is moved west on the sPHENIX rail system to the IR until its nominal axis is coaxial with the nominal RHIC beam axis then north until the CP assembly's nominal center point coincides with the sPHENIX nominal interaction point ("IP"). Survey and built in adjustments to the CP assembly are used to bring the entire assembly into tolerance as required.

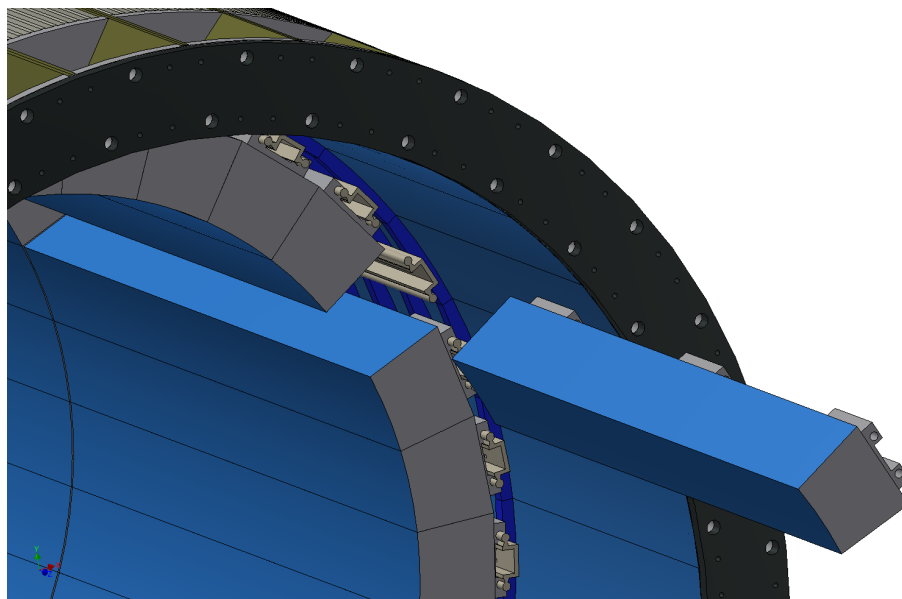


**Figure 10.9:** EMCal Sector Installation

#### 10.2.4 Routing of Services

All services to the detectors are routed from the north or south of the overall experimental assembly to service distribution points at the north and south end of each subassembly sector/module. From that point services are routed to source points (e.g. electronics racks, cooling manifolds, etc.) which will be generally segmented into quadrants at each end. The services will be layered such that the outermost detector (Outer HCal) has the inner most services routes, with the Inner HCal on top of those, then the EMCal services and finally the Tracking services.

### 10.3 Installation

Installation is defined as the final assembly of detector support structure and detector components that will take place at the sPHENIX Assembly Hall, QA testing of components at predetermined points during assembly, the relocation of the final assembly to the sPHENIX IR to its Operational location at the sPHENIX IP, installing and integrating infrastructure services, ready for final commissioning and operation.

#### 10.3.1 Installation Concept

The Installation Concept for sPHENIX is as follows:

- Internal alignment of detector subsystem components in the interior will be completed as described in the previous section and the individual sectors or modules of the detector subsystems will be operationally tested and ready for installation when shipped to the sPHENIX AH for installation, as described in the relevant subsystem section of this report.
- The subsystem sectors/modules will be provided with handling fixtures as indicated in the tooling and support equipment section below.
- As each additional Outer HCal Sector is installed it will be surveyed, adjusted and shimmed into place with respect to the required tolerances, until the lower half of the Outer HCal is completed.
- The Superconducting solenoid magnet will have been surveyed and been sufficiently tested to establish a nominal magnetic axis and centerpoint which will have been related to external fiducial points on the magnet and those relationships recorded. The magnet will have 12 adjustable mounting supports attached to position and secure the magnet onto the inner surface of the Outer HCal. Figure 10.10 shows the Outer HCal with 32 sectors installed ready for the superconducting magnet to be mounted.

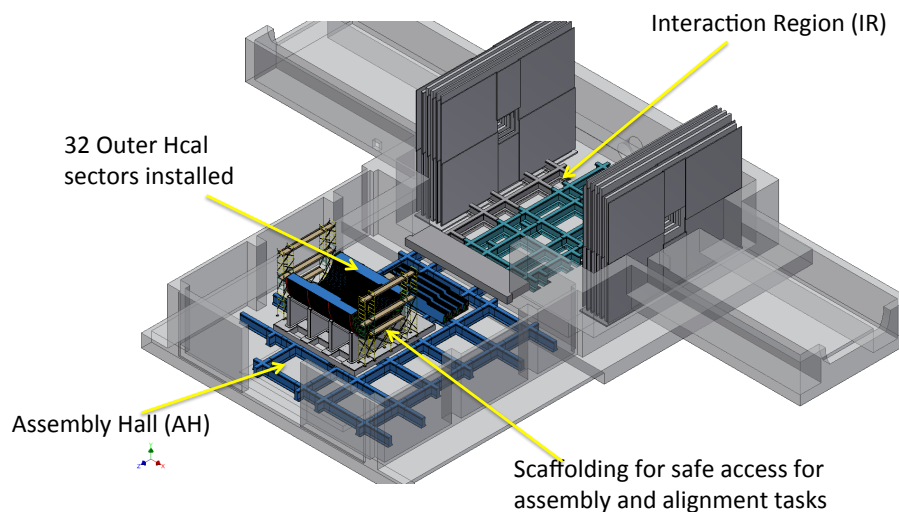


**Figure 10.10:** Outer HCal Installation, lower half

- After the lower half of the Outer HCal is completed, the magnet shall be mounted surveyed, aligned and secured to the OuterHCal in accordance with requirements.
- The remaining Outer HCal Sectors are installed, surveyed, adjusted and shimmed into place with respect to the required tolerances, until the upper half of the Outer HCal is completed.



- The pillars for supporting the upper platform and flux return end caps and are then installed followed by the installation of the upper platform and end caps themselves.
- The Magnet valve box with extension is installed and the entire assembly is moved on the sPHENIX rail system to the IR for magnet mapping. Magnet mapping is discussed in the Magnet chapter of this report. Figure 10.11 shows the Outer HCal fully installed with the magnet and magnet pole tip flux returns mounted and the upper platform in place, ready for magnet mapping and magnet tests.

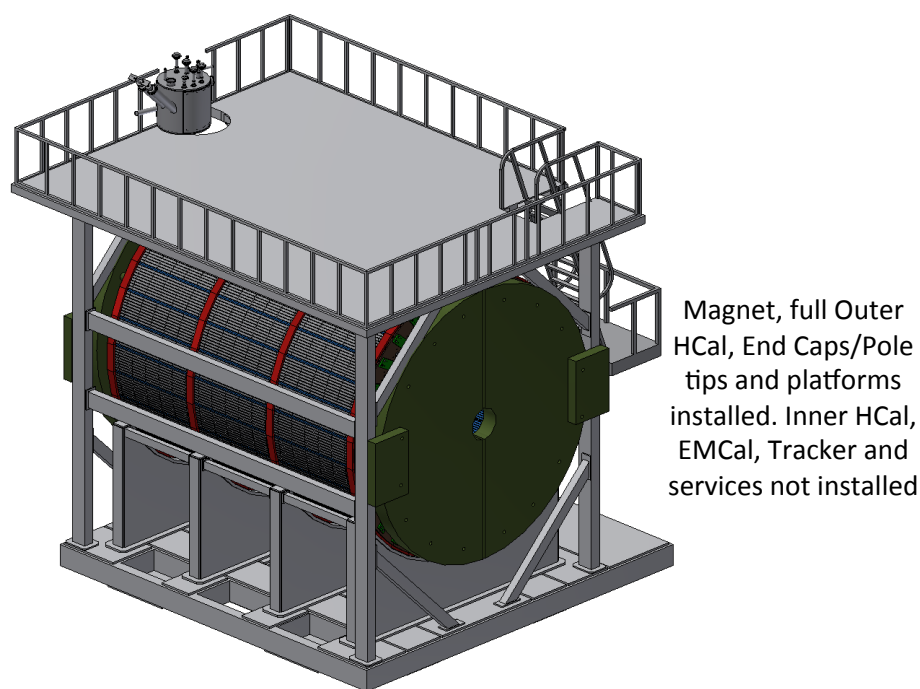


**Figure 10.11:** Ready for Magnet mapping

- After magnet mapping, the assembly is moved back to the AH to complete the assembly and installation of the remaining detectors.
- The Inner HCal sectors are to be assembled into a complete detector, aligned using mechanical precision features, survey and shimming to achieve the desired alignment of each of the sectors to each other and to external fiducial points. The entire assembly is then surveyed, aligned and secured to the Inner HCal-to-Outer Hcal support rings. Figure 10.12 shows the Inner HCal nearing assembly completion and mounted on the installation fixture
- Each of the 64 EMCal sectors is then installed onto the rail systems on each of their respective Inner HCal sectors, surveyed positioned, adjusted and secured into place in accordance with required tolerances.



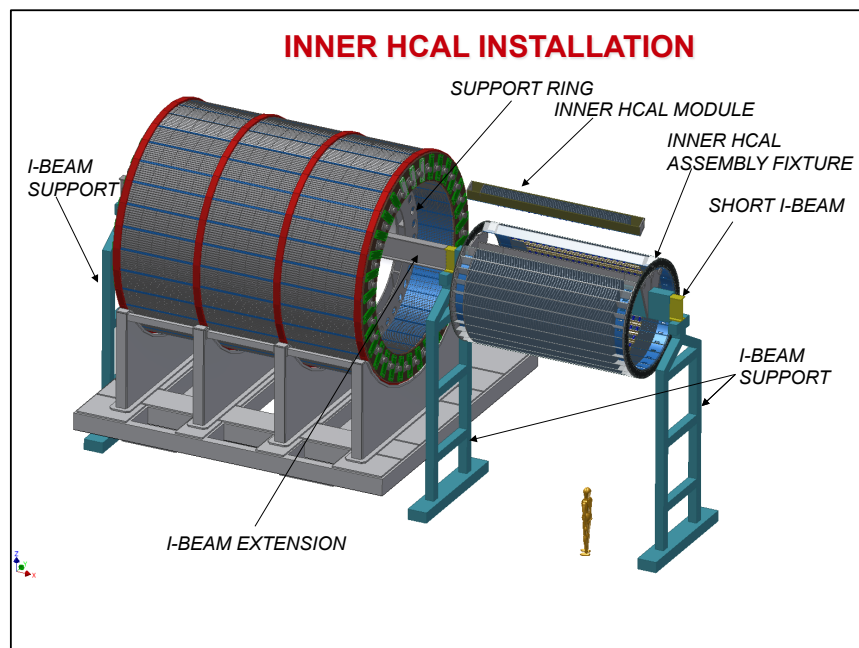


**Figure 10.12:** Inner HCal Installation

- The detector assembly on the CP support structure is completed by installing and aligning the Tracking subsystem with the nominal axis and centerpoint.
- Finally, the entire CP is moved west on the sPHENIX rail system to the IR until its nominal axis is coaxial with the nominal RHIC beam axis then north until the CP assembly's nominal center point coincides with the sPHENIX nominal interaction point ("IP"). Survey and built in adjustments to the CP assembly are used to bring the entire assembly into tolerance as required.

### 10.3.2 Tooling and Support Equipment Requirements

The following are the most significant tooling and support equipment needs for integration and installation:

- Central Pedestal (CP): standard lifting tools for CP base and rollers, cradle, support posts, bridge platform, access stairs), alignment tools for rollers and cradle.
- Outer HCal: module holding fixtures (4), indexed lifting/installation fixture, alignment tools, temporary inner and outer assembly support fixtures

- Inner HCal: module holding fixtures (4), module lifting fixture, assembly indexed/rotating fixture and insertion beam and insertion beam lifting fixture, alignment tools
- EMCal: module handling fixtures (8), rail alignment tool, indexed lifting/installation fixture
- Tracking: Handling fixture (2), alignment tool, installation tool
- SC Magnet: Lifting fixture (spreader bar), alignment tool, stack handling/lifting tool
- Infrastructure: beampipe alignment tools/fixtures, bakeout tools/fixtures

Note: some of the tools/fixtures described above will be used in subsystem sector/module assembly operations as described in their respective sections of this report prior to being used for final installation

## 10.4 Testing and Commissioning

### 10.4.1 Magnet

The superconducting solenoid magnet will be QA tested for integrity and function as described in the Magnet section of this report. After transport to the AH for assembly and again after installation into the CP, the magnet will be QA tested to assure that no damage has been done in transportation and installation. After the magnet is fully installed and instrumented, the CP, with the magnet installed, will be moved to the IR for final performance testing and magnetic field mapping. The details of these tests are found in the magnet section of this report.

### 10.4.2 Detector Subsystem Commissioning

All detector subsystem sectors/modules are QA tested at their point of assembly, as described in the relevant subsystem sections of this report, prior to transporting the sectors/modules to the AH for installation. After transport to the AH for assembly and again after installation into the CP, the sectors/modules will be QA tested to assure that no damage has been done in transportation and installation.

The detector subsystems as entireties will be run through a series of tests, as described in their respective sections of this report, to demonstrate their operational readiness, to calibrate the detector components as necessary and to verify the chains of signals from the detector elements through to the data acquisition system. In addition, all services will be tested to demonstrate performance in accordance with requirements.

## 10.5 Alternative Integration/Installation Concepts Considered

The evolution of the integration and installation concept is largely driven by the design evolution of the component detector subsystems. Several alternative integration and Installation concepts, however, have been considered during this process independent of the detector subsystems. Some of the more interesting considerations are described below, with comments as to why they are not included in the current concept.

Multiple carriages instead of one unified Central Pedestal. This option was considered early on, but it was rejected as unnecessarily expensive and it increases alignment difficulty.

Separate carriages for the flux return end caps. The current concept has hinged flux return caps to minimize cost, and simplify assembly.

Sliding door flux return end caps (both vertical and horizontal sliding), instead of hinged end caps. This concept was rejected because it increases space requirements for maintenance, increases cost and (in the case of the vertical sliding end caps) handling safety considerations.

Installing the EMCal as a complete detector instead of 64 separately supported sectors. This would require an assembly structure and complicated installation tooling fixtures, adding to cost. It also decreases the accessibility for maintenance.

Completing the assembly of the Inner HCal remotely and transporting the completed assembly to the AH for installation. This would require a complicated transport fixture added risk for damage during transportation and additional logistical considerations (additional assembly space). There are some merits to this alternative procedure and it may be revisited, if appropriate, after subsystem designs are finalized.

Using rail mounted gantry cranes to install the Inner HCal instead of a monrail system. Increased complexity and cost. There are some merits to this alternative procedure and it may be revisited, if appropriate, after subsystem designs are finalized.

Using separate pillars and rails to support the Inner HCal, instead of the load transfer rings. This is a more complicated design, which would increase cost and complexity of installation.

Having separate supports for the magnet instead of supporting the magnet with the Outer HCal. This was rejected due to increased complexity and cost.



# Chapter 11

## Project Management

### 11.1 Project Organization

The organization of the sPHENIX Project can be seen in Figure 11.1. The sPHENIX Project is managed inside the Nuclear and Particle Physics Directorate at Brookhaven National Laboratory. The management structure is organized consistent with DOE order 413.3B. The sPHENIX effort divides into nine items shown in figure 11.1. Level-2 managers, or Control Account Managers, are each responsible for one of the nine items. They report directly to the sPHENIX Project Management team. The Project Management team reports directly to the BNL office of the Associate Lab Director who in turn report to the sPHENIX Program Manager. The responsibilities of the members of the sPHENIX Project Management team are as follows:

#### 11.1.1 Project Coordinator

Edward O'Brien, Brookhaven National Laboratory

- Responsible and accountable for the successful execution of sPHENIX project scope.
- Implements a performance measurement system
- Delivers Project deliverables as defined in the Project Execution Document
- Responsible for sPHENIX functional requirements
- Allocates the contingency funds according to the procedure defined in the Baseline Change Controls Procedure.
- Approves major subcontracts

- Ensures that the work is performed and in compliance with the BNL Environmental, Safety and Health requirements.

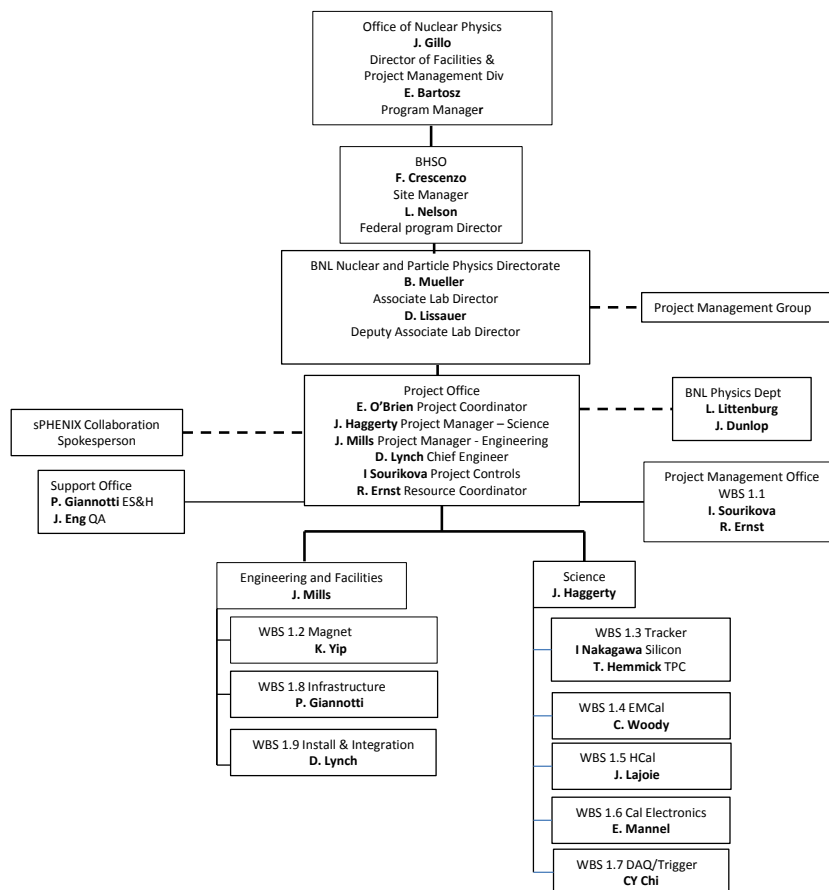


Figure 11.1: The Project Organization chart

### 11.1.2 Project Manager - Science

John Haggerty, Brookhaven National Laboratory

- Under the direction of and by delegation from the Project Coordinator, the Project Manager-Science executes project scope and supplies the deliverables of the WBS items directly related to the sPHENIX science measurements and performance: Tracker, EMCal, HCal, Calorimeter Electronics, DAQ/Trigger on time and within budget.
- Collaborates with the Project Coordinator to assemble the staff and resources necessary to complete the sPHENIX project.

- Collaborates with the Project Coordinator in the technical direction of the sPHENIX project.
- Communicates the functional requirements to the subsystem managers

### 11.1.3 Project Manager - Engineering

James Mills, Brookhaven National Laboratory

- Under the direction of and by delegation from the Project Coordinator, the Project Manager-Engineering executes project scope and supplies the deliverables of the WBS items that provide technical support functions to the sPHENIX experiment: SC-Magnet, Infrastructure, Installation/Integration on time and within budget.
- Collaborates with the Project Coordinator to assemble the staff and resources necessary to complete the sPHENIX project.
- Supervises the Project Controls Office
- Collaborates with the Project Coordinator in the technical direction of the sPHENIX project.
- Communicates the functional requirements to the subsystem managers

### 11.1.4 Chief Engineer

Don Lynch, Brookhaven National Laboratory

- Under the direction of and by delegation from the Project Coordinator, the Chief Engineer oversees the engineering content of all tasks within the project scope.
- Collaborates with the Project Coordinator to assemble the staff and resources necessary to complete the sPHENIX project.
- Collaborates with the Project Coordinator in the technical direction of the sPHENIX project.
- Communicates the engineering requirements to the subsystem managers

### 11.1.5 Project Controls Manager

Irina Sourakova - Brookhaven National Laboratory

- The Project Controls Manager advises the Project coordinator in all matters of project controls including Cost, Schedule, Earned Value, and Contingency tracking and management
- Provides Project Controls data and participates in monthly and quarterly reporting, and the annual DOE review

### 11.1.6 Resource Manager

Robert Ernst - Brookhaven National Laboratory

- The Resource Manager advises the Project Coordinator on all matters relating to project resources including budgets, workforce, space and facilities.
- Under the direction of the Project Coordinator oversees contract administration and procurement for the sPHENIX project
- Provides budget and labor data to the Project Coordinator and assists in budget and labor reporting to BNL and DOE.

### 11.1.7 Project Controls Office

The Project Controls office is overseen by the Project Manager-Engineering. The office includes the Project Controls Manager, the Environment Safety and Health manager, and the Quality Assurance manager. In addition to Project Controls, ES& H and QA, the office is responsible for all project documentation administration, DOE Project report preparation.

## 11.2 Work Breakdown Structure

The sPHENIX project has been organized into a Work Breakdown Structure(WBS) for the purposes of planning, managing and reporting project activities. Work elements are defined to be consistent with discrete elements of project work. The sPHENIX Project has nine WBS Level-2 elements of project work: Project Management, SC-Magnet, Tracker, EM-Cal, HCal, Calorimeter Electronics, DAQ/Trigger, Infrastructure, Integration/Installation. The WBS structure through Level-2 is shown in Table 11.1. The WBS for the sPHENIX



Project captures all effort that will eventually be assigned to the Total Project Cost. In addition there is a WBS structure defined for the preparation for sPHENIX. This sPHENIX-preparation WBS contains activities such as Decommissioning and removal of the PHENIX detector, generic R&D and preconceptual design for sPHENIX subsystems. The sPHENIX-preparation effort is planned, managed and tracked along with the sPHENIX project tasks because there are a number of key labor and space resource resources shared between the two activities. For instance sPHENIX infrastructure preparation can not begin until the existing PHENIX detector is completely removed from the 1008 hall.

<b>WBS</b>	<b>Project Elements</b>
<b>1.1</b>	Project Management
<b>1.2</b>	SC-Magnet
<b>1.3</b>	Tracker
<b>1.4</b>	EMCal
<b>1.5</b>	HCal
<b>1.6</b>	Calorimeter Electronics
<b>1.7</b>	DAQ-Trigger
<b>1.8</b>	Infrastructure
<b>1.9</b>	Installation-Integration

**Table 11.1:** sPHENIX WBS Structure

### 11.3 Cost Range and Basis of Estimate

The Total Project Cost of sPHENIX has been estimated to be in the range of \$55M to \$75M after applying the standard BNL capital project overhead and contingency of 30% on materials and 20% on labor. The cost has been divided between material costs that cover outside purchases and contracts, and labor costs. Justification for the material costs can be found in the sPHENIX Basis of Estimate document. The budget profile for purchases is seen in Figure 11.2 is a technically-driven profile based on required budget authority, rather than expenditure. The budget profile presumes the FY16 BNL overhead rate for capital projects, university and collaborator support for all students and certain scientists, and BNL labor rates for all other labor not covered by collaborating institutions. The estimated material broken down by WBS category can be seen in table 11.2 The on-project labor costs that are to be counted toward the Total Project Cost (TPC) have been estimated and used as a basis for the project cost range. An example budget profile for sPHENIX, fully burdened with contingency and escalation is seen in Figure 11.3.

## sPHENIX Material Costs by FY -Direct

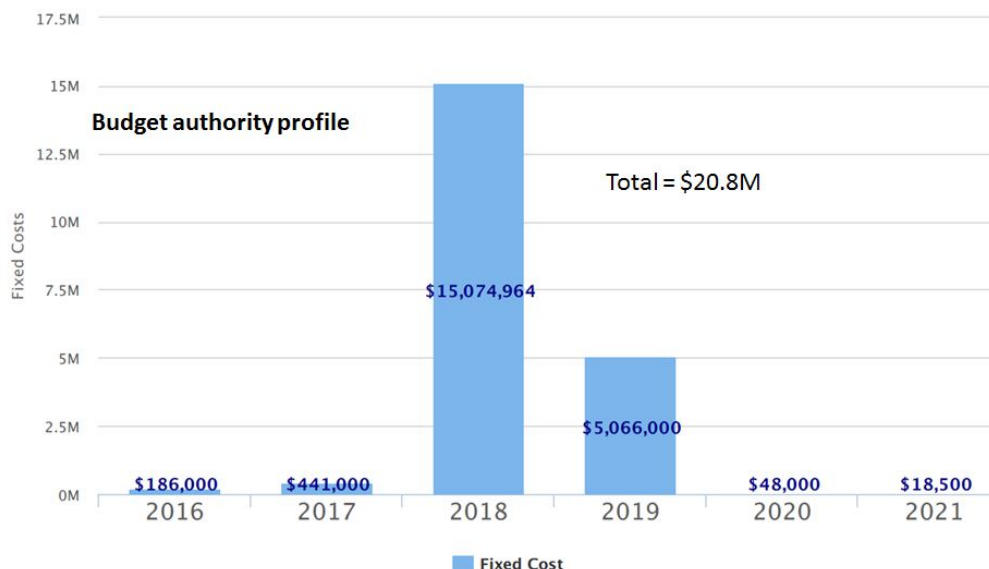


**Figure 11.2:** The estimated direct cost of all materials and purchases in the sPHENIX reference design not including the Tracker which is expected to be funded from other sources

WBS	Project Elements	FY16(\$k)	FY17	FY18	FY19	FY20	FY21	Total(\$k)
1.1	Project Man	10	20	20	20	20	5	95
1.2	SC-Magnet			1,878	28			1,906
1.4	EMCal	35	263	565	3,700			4,563
1.5	HCal			5,999	160			6,159
1.6	Cal Elec	105	107	4,162	30			4,404
1.7	DAQTrig	16	71	1,116	525			1,728
1.8	Infrastructure			1,075	593			1,668
1.9	Installation			263	8	29	12	312
<b>Total(\$k)</b>		166	461	15,078	5,064	49	17	20,834

**Table 11.2:** sPHENIX Direct Material Costs by WBS

### 11.4 Schedule and Labor

A condensed Gantt chart containing the complete project can be seen in Figure 11.4. The critical path for the project runs through the Tracker but is within three weeks of HCal production.

The schedule is fully resource-loaded and is integrated to include scope from both DOE

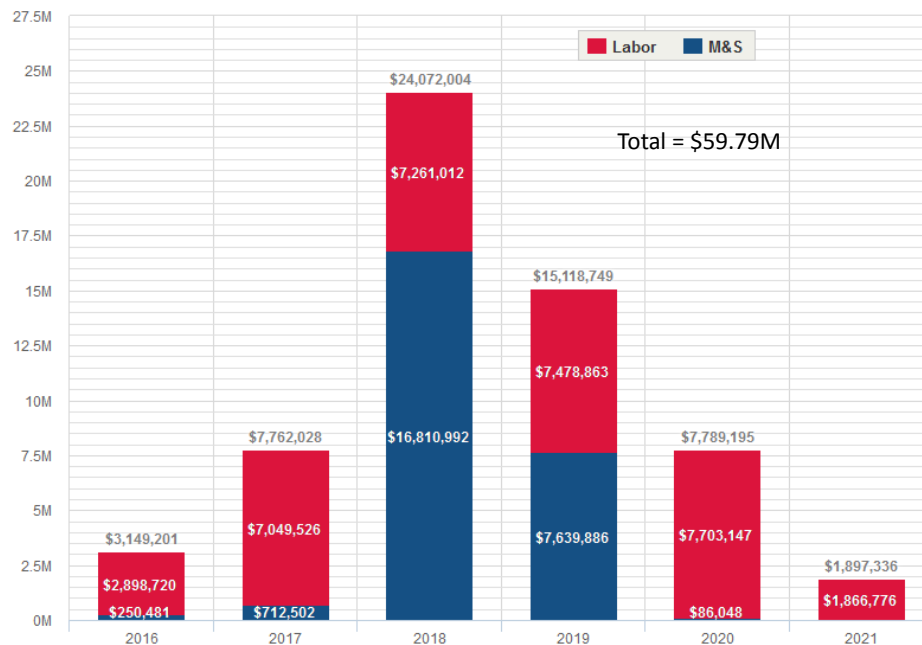


**Figure 11.3:** An example budget profile covering the Total Project Cost of sPHENIX. The labor and material are burdened with the current BNL capital project rate, escalation has been applied and contingency added in an amount 30% on materials and 20% on labor.

and non-DOE sources. The high-level project schedule can be seen in Figure 11.5. The schedule presumes that the project will receive CD-0 authorization at the end of Q2 FY16. CD-1 is planned to be authorized in Q1FY18 with CD2/3 authorization being received in at the beginning of Q4FY18. CD-4 would be received in 2QFY22 which is approximately 1 year after the final sPHENIX component is installed in the 1008 Hall. The sPHENIX resource-loaded schedule show the labor distribution by fiscal year in Figure 11.6. The figure shows the labor needs identified by category: scientist, engineer(professional), designer, technician, craft or student.

## 11.5 Risk

The cost control strategy for sPHENIX will utilize both a top-down formal risk management in addition to a bottoms-up risk-based contingency reserve. sPHENIX risk management plan (RMP) will be designed to be integral part of the Project Execution Plan in order to achieve project goals on-time and on-budget. The sPHENIX RMP provides a structured and integrated approach for identifying, evaluating, mitigating, and tracking project risks.

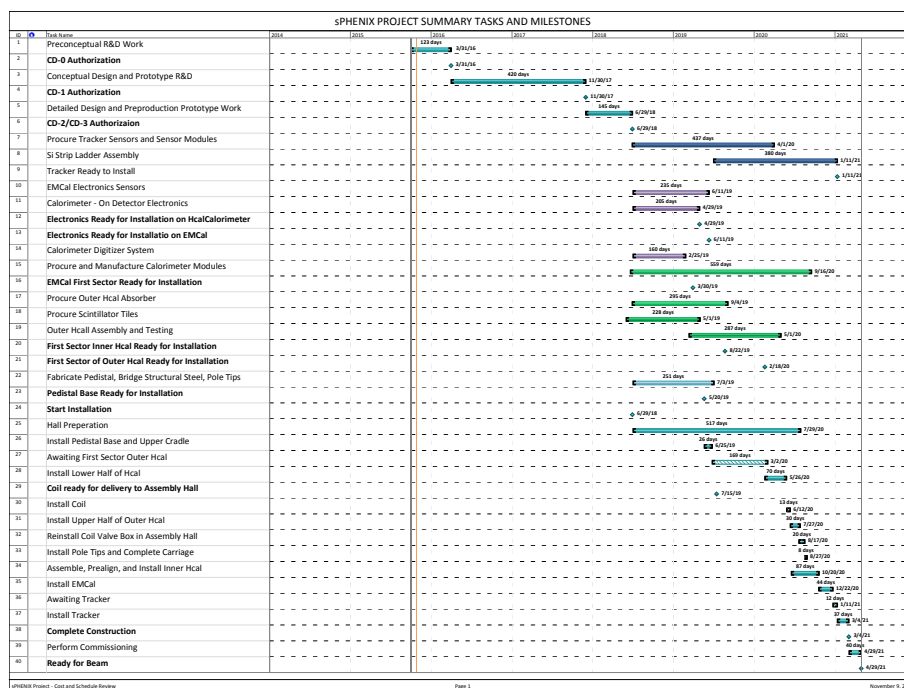


**Figure 11.4:** The Project schedule showing CD approvals, milestones and major activities.

Anticipated risks will be managed at every stage of the project life cycle in order to minimize chances of risks becoming real problems. Abatement strategies, iteratively developed and refined during regular sPHENIX meetings, will be based upon risk category as well as lessons learned from projects of similar scope and complexity. Risk registry will serve as a project-wide risk monitoring tool, while accountability will be achieved by assigning risk ownership based on the identified risk level.

Key elements of sPHENIX RMP are the following:

- Two-level approach to risk evaluation
- Mitigation plans based on three risk categories:
  - Technical
  - Cost
  - Schedule
- Clear risk ownership
- Risk registry as a logging and monitoring tool

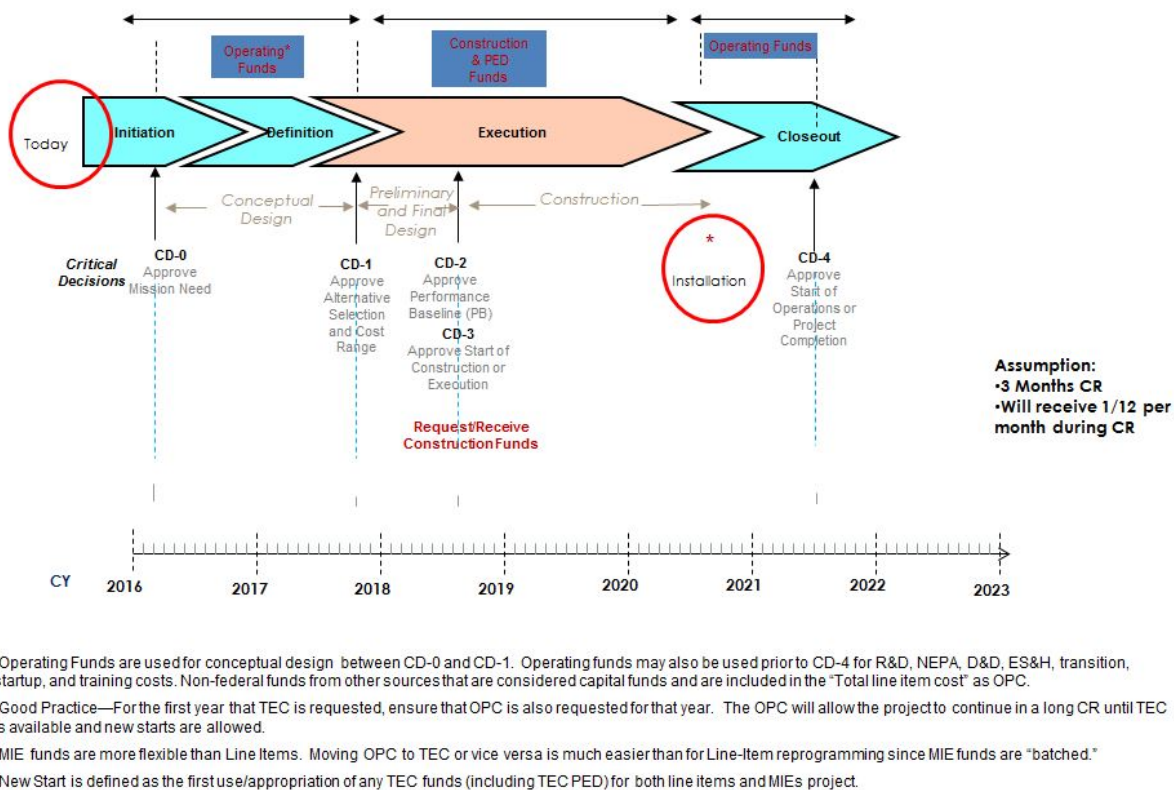


**Figure 11.5:** The high-level sPHENIX project schedule including CD milestones.

Project risks will be evaluated at two levels: risks at the WBS level which will be owned by Level 2 managers, and risks of global nature, over and above those identified and called out by the Level 2 managers, which will be held by the Project Management. The assessment matrix for the higher level risks is shown in Table RMP1 (Fig. 11.7). The final risk classification, which folds in the probability, is determined for the higher level risks using Table RMP2 (Fig. 11.8). The status of all Moderate and High risk items will be maintained in sPHENIX Risk Registry and updated as appropriate. sPHENIX RMP details the development of risk abatement strategies and outlines proven strategies for each risk category. Risk monitoring tools (database with a web interface) have been developed to support effective implementation of sPHENIX RMP.

sPHENIX RMP spans all project stages from developing preliminary cost estimates and contingency calculations, to prototyping and QA, to monitoring medium and high risk activities.

The design and construction of sPHENIX project are well within the expertise and experience of the collaborations scientific, engineering and technical staff and sPHENIX RMP will help to insure that the project objectives are reached in the most cost-effective way possible.

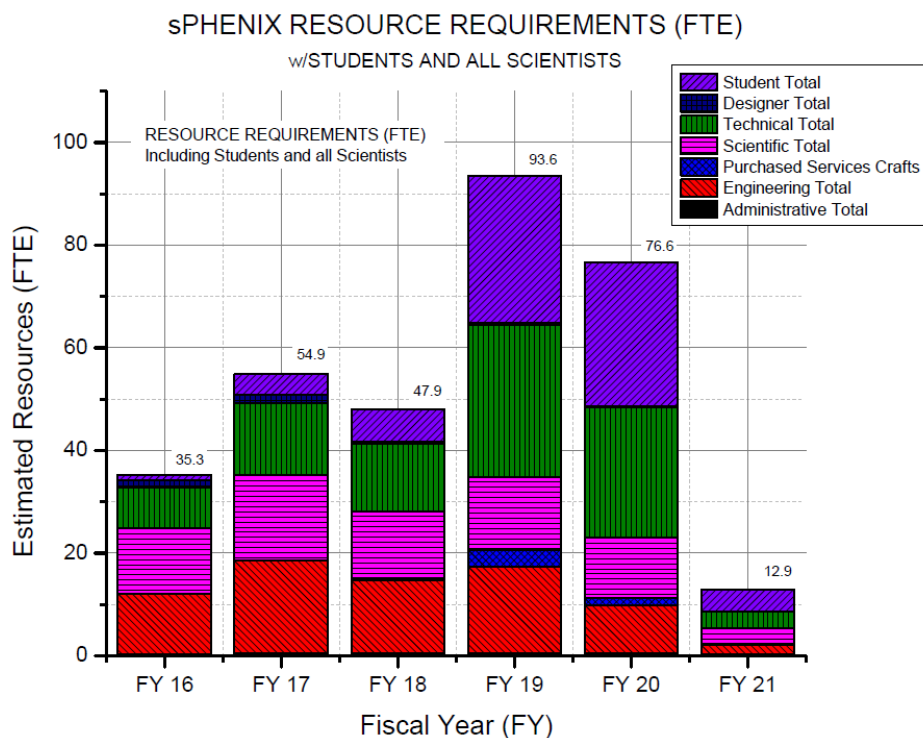


**Figure 11.6:** The sPHENIX labor distribution from all sources including BNL, universities and other institutions both US and international.

## 11.6 Quality Assurance

The sPHENIX Project will be conducted in accordance with the BNL Quality Assurance (QA) Program that applies to all work conducted at BNL. The program conforms to the requirements of DOE Order 414.1D, Quality Assurance. These requirements include:

- Program
- Personnel training and qualification
- Quality improvement
- Documents and records
- Work processes
- Design
- Procurement
- Inspection and acceptance testing

Impact Risk Area	Low	Moderate	High
Cost:	≤ \$250K	≤ \$500K	> \$500K
Schedule:	Delays Level 2 milestone or Project critical path by ≤ 3 month	Delays Level 2 milestone or Project critical path by ≤ 6 months	Delays Level 2 milestone or Project critical path by > 6 months
Scope/Technical:	Negligible, if any, degradation.	Significant technical/scope degradation.	Baseline scope or performance requirements will not be achieved.

Figure 11.7: The risk assessment matrix table RMP 1

Probability	Impact		
	Low	Moderate	High
High (probability > 75%)	Moderate	High	High
Moderate (25% < probability < 75%)	Low	Moderate	High
Low (probability < 25%)	Low	Low	Moderate

Figure 11.8: The final risk classification table RMP2

- Management assessment
- Independent assessment

A QA Plan has been developed to integrate the program requirements that apply to all sPHENIX work. The primary objective of this plan is to implement quality assurance criteria in a way that achieves the projects performance goals, taking into account the work to be performed and the associated environmental, safety and health hazards. Effective implementation of the QA Plan will enable the project to:

- Design in quality and reliability.
- Promote early detection of problems to minimize failure costs and impact on schedule.
- Develop appropriate documentation to support upgrade and operational requirements.
- Define the general requirements for design and readiness reviews for all aspects of the project.
- Assure that personnel are trained before performing critical activities, especially those that have environmental, safety, health and quality consequences.

The sPHENIX Project Coordinator is responsible for achieving performance goals. The sPHENIX L2 Managers are responsible for implementing the QA Plan within their subsystem. The sPHENIX QA Coordinator is responsible for ensuring that a quality system is established, implemented, and maintained in accordance with requirements, and for providing oversight and support to the project participants to ensure a consistent quality program.

## 11.7 Environment, Safety and Health

### 11.7.1 Institutional Requirements

The Environmental, Safety and Health (ES&H) requirements for the proposed sPHENIX Experiment begin with BNL's Institutional Assessment Process as related to Accelerator Safety. These requirements are delineated by DOE Order 420.2C Safety of Accelerator Facilities. Oversight of the above is conducted by the DOE Area Offices Radiological Control Management System. This is not limited to just ionizing radiation hazards from beams or sources. It is for analysis of the other two non-standard industrial safety hazards, namely, large volumes of flammable gas and the potential for oxygen deficiency from helium, nitrogen, or other inert gasses.

### 11.7.2 Organizational Requirements

The BNL organizational requirements for compliance with ES&H are implemented by the Collider Accelerator Department (C-AD) Occupational Safety and Health (OSH) and Environmental (E) programs. They are employed at the job level and are described in detail on the C-AD ESH Web and are compared to the Integrated Safety Management System (ISM) for DOE. Additionally, guidance is also provided by the BNL Standards Based Management System (SBMS) in the Accelerator Safety subject area.



The DOE O 420.2c Accelerator Safety Program must include a Safety Assessment Document (SAD), Accelerator Safety Envelope (ASE) and Unreviewed Safety Issue (USI) process. The sPHENIX Experiment is planned to be constructed in the existing RHIC 1008 Facility following PHENIX dismantling and decommissioning. The conceptual designs, thus far, reveal that sPHENIX will be a similar experiment to PHENIX, from an ES&H perspective, of lesser scope with the added feature of a superconducting main magnet. Therefore, the hazards and controls for sPHENIX are expected to be similar to those previously included in the C-AD 2011 SAD (up for 2016 revision). Nevertheless, mainly due to the addition of helium cooling, sPHENIX shall undergo a USI screening, evaluation and disposition work flow. By definition a USI is a significant increase in the probability of, or consequences from: 1) A planned modification that creates a previously unanalyzed postulated accident or condition that could result in a significant adverse impact; or 2) A previously analyzed postulated accident or condition. The USI process starts by using a C-AD USI Checklist that asks a set of questions. Once answered, the checklist returns an evaluation with either a positive or negative result. A negative result requires no further action in regards to the SAD or ASE. If positive, a Preliminary Hazard Analysis Report (PHAR) is then sent to the Accelerator Safety Committee, the Experimental Safety Committee, and eventually DOE for approval. Any resulting affects to the SAD and ASE are first added as appendices to the SAD prior to its 5 year revision cycle.

Beyond the SAD, A National Environmental Policy Act (NEPA) report (required by DOE Order 451.1B) must also be completed and approved.



# List of Tables

3.1	Magnetic forces and torques . . . . .	56
4.1	Summary of geometries for an inner MAPS tracker with 3 layers. . . . .	75
4.2	Summary of geometries for the silicon strip tracker and the inner tracker made of reused pixels from PHENIX. . . . .	78
4.3	Number of channel summary for the silicon strip tracker. . . . .	79
4.4	Hybrid Silicon/TPC tracker parameters . . . . .	96
4.5	Extended Glückstern parameters for each tracking option. . . . .	96
5.1	Key parameters of the EMCal . . . . .	134
5.2	EMCal module component materials . . . . .	138
6.1	Properties of HCAL scintillating tiles. . . . .	161
6.2	Properties of Kuraray Y-11 (200) wavelength shifting fibers. . . . .	161
6.3	Design parameters for the Inner Hadronic Calorimeter. . . . .	163
6.4	Design parameters for the Outer Hadronic Calorimeter. . . . .	166
7.1	Technical Specifications for the Calorimeter Electronics. . . . .	194
7.2	Electronics Component Count. . . . .	195
7.3	SiPM properties . . . . .	196
7.4	Properties of Hamamatsu S12572-015P MPPC. . . . .	198
8.1	Channel count, occupancy and data volume . . . . .	216
8.2	Channel, fiber and readout component counts . . . . .	218

## LIST OF TABLES

## LIST OF TABLES

10.1 sPHENIX General Limits and Requirements . . . . .	230
10.2 sPHENIX Estimated Weights of Major Components . . . . .	233
11.1 sPHENIX WBS Structure . . . . .	251
11.2 sPHENIX Direct Material Costs by WBS . . . . .	252

# List of Figures

1.1	Virtuality evolution as a function of temperature as represented (left) by the resolution of jet probes at the LHC (blue curves) and at RHIC (red curves). The potential range of influence of the QGP that is being investigated is represented by the bolder curves for each case. The magnified views are meant to represent pQCD scattering from bare quarks and gluons in the medium (green), scattering from thermal gluons (yellow), and a final state integration over all possible objects probed in the medium (orange). (right) Graphical depiction of the objects being probed at the various resolutions on the left. . . . .	2
1.2	Interaction scale for the interaction of partons with the QGP and possibilities for the recoil objects. (left) Diagram of the net interaction of a parton with the medium and the range of possibilities for the recoil objects as a function of $Q^2$ . (right) Diagram for a quark exchanging a virtual gluon with an unknown object in the QGP. This highlights the uncertainty for what sets the scale of the interaction and what objects or quasiparticles are recoiling. .	5
1.3	$T\hat{e}/\hat{q}$ as a function of the mass of the effective scattering centers in the medium	6
1.4	$\eta/s$ vs $T/T_c$ for water, nitrogen, and helium . . . . .	7
1.5	Calculations of $\hat{q}/T^3$ vs temperature, constrained by RHIC and LHC $R_{AA}$ data — including near $T_c$ enhancement scenarios of $\hat{q}/T^3$ . (left) Calculations from four jet quenching frameworks constrained by RHIC and LHC $R_{AA}$ data with results for $\hat{q}/T^3$ as a function of temperature. Details of the calculation are given in Ref. [27]. (right) Results from calculations within CUJET 3.0 with magnetic monopole excitations that result in enhanced coupling near $T_c$ . Plotted are the constraints on $\hat{q}/T^3$ as a function of temperature as shown in Ref. [28] . . . . .	8
1.6	The nuclear modification factor $R_{AA}$ vs transverse momentum at the SPS, RHIC, and LHC, compared to various jet quenching calculations . . . . .	11
1.7	Dijet $A_J$ in VNI parton cascade compared to the CMS data and calculation for RHIC energies of $A_J$ for different values of $\alpha_s$ . . . . .	14

1.8	$A_J$ distributions in MARTINI+MUSIC and in the model of Qin et al. at LHC and RHIC energies . . . . .	15
1.9	Calculations by Vitev et al. for the inclusive jet $R_{AA}$ vs jet energy and radius	16
1.10	Calculations by Vitev et al. of the vacuum and medium-modified $z_{J\gamma}$ distributions for direct photon-triggered reconstructed jet events at LHC (left) and RHIC (right) energies [85]. . . . .	17
1.11	Schematic of different potential path lengths through the QGP (left) and projected sPHENIX uncertainties in the photon-jet channel for these different length scales traversed in the QGP. . . . .	17
1.12	Comparison of the fraction of quark and gluon jets from leading order pQCD calculations as a function of transverse momentum for RHIC (left) and LHC (right) energies. . . . .	18
1.13	FONLL calculations of heavy flavor jets, fragmentation hadrons, and decay electrons vs $p_T$ . . . . .	19
1.14	CUJET calculations of $R_{AA}$ in central Au+Au collisions at RHIC and in Pb+Pb collisions at the LHC, with light, charm and beauty hadrons and electrons shown as separate curves. . . . .	20
1.15	CMS results on the $R_{AA}$ for beauty tagged jets in Pb+Pb collisions at the LHC.	21
1.16	Hydrodynamic simulations by Habich et al. of temperature vs time in Au+Au and Al+Al collisions at 200 GeV and Pb+Pb collisions at 2.76 TeV .	23
1.17	Calculations for Upsilon state suppression at RHIC and LHC energies vs collision centrality . . . . .	24
1.18	Estimate of the statistical precision of a measurement of the Y states in Au+Au collisions using sPHENIX, assuming that the measured $R_{AA}$ is equal to the results of a recent theory calculation by Strickland & Barzow referenced in the legend. The yields assume 100 billion recorded Au+Au events. . . . .	25
1.19	Jet, photon and $\pi^0$ rates for $ \eta  < 1.0$ from NLO pQCD calculations scaled to Au+Au central collisions for $\sqrt{s_{NN}} = 200$ GeV . . . . .	27
1.20	Statistical reach of azimuthally-sensitive hard probes in sPHENIX . . . . .	28
1.21	NLO pQCD calculations of direct photons and $\pi^0$ for RHIC and LHC, compared to PHENIX measurements of direct $\gamma$ to $\pi^0$ ratio in $p+p$ (Au+Au or Pb+Pb) collisions . . . . .	29

1.22	Statistical projections of $R_{AA}$ for hard probes in central Au+Au events with the sPHENIX detector after two years of data-taking, and kinematic reach of various jet quenching observables from previous and future RHIC and LHC data-taking . . . . .	30
1.23	Anticipated range in $p_T$ of various hard probe measurements using sPHENIX at RHIC (red) and measurements made at the LHC (blue). The color strip across the top corresponds to the regions presented initially in Figure 1.1 (left) for scattering in the medium from bare quarks and gluons (green), from thermal gluons (yellow), and integration over all possible objects that are probed (orange). . . . .	31
2.1	View of the sPHENIX detector with its component subdetectors . . . . .	34
2.2	Pseudorapidity distribution of PYTHIA jets reconstructed with the FASTJET anti- $k_T$ and the fraction of events in which the leading and subleading jet are in the specified acceptance . . . . .	37
3.1	Internal splices (extracted from the original Ansaldo drawing): 1500 mm weld of aluminum edges + 200 mm gap + 300 mm solder of aluminum faces on both sides of the weld. The welding was done with the TIG (Tungsten Inert Gas) technique. . . . .	42
3.2	Original Ansaldo drawing of the Solenoid Support Cylinder . . . . .	43
3.3	Original Ansaldo drawing: Axial Tie Rod Assembly . . . . .	44
3.4	Original Ansaldo drawing: Cryostat Assembly . . . . .	45
3.5	(Left) Exiting leads — aluminum removed and niobium titanium soldered to heavy copper stabilizer leads (overlapping aluminum; (Right) Outer heat shield. . . . .	46
3.6	Original Ansaldo drawing of the valve box. . . . .	47
3.7	The cryostat, the extension and the valve box. . . . .	48
3.8	Top: from the junction box (at the cryostat) to the valve box; Middle: coil helium supply line and heat shield; Bottom: extension lead assembly with flexible (laminated copper) connections to accommodate thermal contraction on the left and coil return helium to cool exiting leads on the right. . . .	59
3.9	sPHENIX Magnet Cryogenic Control System . . . . .	60
3.10	sPHENIX Magnet powering system . . . . .	61
3.11	sPHENIX Magnet voltage taps . . . . .	62
3.12	2D OPERA simulations of the sPHENIX setup . . . . .	63

3.13	3D OPERA Model . . . . .	63
3.14	Calculated magnetic field along the longitudinal axis (beam direction) for the symmetric return yoke model . . . . .	64
3.15	3D OPERA model detail of the field in the HCal plates . . . . .	64
3.16	Yoke and end-cap cuts from the OPERA Model, as viewed from the "south" or the "lead" end. . . . .	65
3.17	The CERN field mapper installed in the ATLAS solenoid . . . . .	65
3.18	Detail of the CERN field mapper, the red tabs are the 3D Hall sensors . . . .	66
4.1	The BaBar magnet field superimposed with the dimensions of the tracker volume. This calculation includes the effect of the field return as envisioned for future upgrades (forward arm spectrometer). The dashed line indicates the inner radius of the TPC tracking volume. . . . .	69
4.2	This figure demonstrates the contribution of position resolution to momentum resolution. . . . .	70
4.3	This figure demonstrates the contribution of multiple Coulomb scattering to momentum resolution. . . . .	70
4.4	This figure indicates how Bremsstrahlung is calculated via single photon emission as a contributor to momentum resolution. . . . .	71
4.5	The DCA resolution of the silicon tracker in three track momentum ranges, from tracks reconstructed in central HIJING events. . . . .	73
4.6	The DCA resolution of the silicon tracker in three track momentum ranges, when the inner tracker is composed of three layers of a MAPS based detector with $30\text{ }\mu\text{m}\times 30\text{ }\mu\text{m}$ pixel size. These are from all tracks reconstructed in 2000 central HIJING events. . . . .	76
4.7	CAD drawing of the silicon strip tracker. . . . .	77
4.8	(From left to right) The 3D CAD drawings for S0, S1 and S2 barrels. . . . .	78
4.9	Schematic layout strip and readout lines of the sensor. . . . .	80
4.10	Left: The fraction of all truth tracks in a central AuAu HIJING event that are reconstructed with a momentum within $3\sigma$ of the truth momentum. Right: The fraction of all reconstructed tracks in a central AuAu HIJING event that have momentum within $3\sigma$ of the truth momentum. . . . .	81
4.11	Momentum resolution of the silicon tracker for single pions. . . . .	82



4.12	Mass spectrum of the three Upsilon states, with Crystal Ball fits. The yields correspond to 10 weeks of $pp$ running. Left: The mass spectrum with the reused PHENIX pixels as the inner tracker (the configuration in Table 4.2). Right: The mass spectrum with the three layer MAPS based inner tracker option as the inner tracker. . . . .	83
4.13	The mass spectrum expected in the 0-10% centrality bin from 1 year of AuAu running. The background is estimated using a fast simulation based on measured pion and electron yields from PHENIX. . . . .	84
4.14	CAD drawing of the silicon strip tracker S1 layer. In order to minimize the dead area, every other sensor modules are staggered. . . . .	84
4.15	Illustration of S2, S1, and S0 silicon strip sensors. The active areas are segmented into $12 \times 10$ , $6 \times 10$ , $2 \times 10$ cells, respectively. . . . .	85
4.16	The mechanical drawing of the S1 sensor designed by HPK. . . . .	86
4.17	The 8 layers structure of the HDI for S1 layer. . . . .	87
4.18	The circuit drawing of HDI for S1 layer drawn by Inoue Meterial Co. . . . .	87
4.19	The CAD drawing of the Silicon module for S0 layer. . . . .	88
4.20	The CAD drawing of the carbon fiber cooling pipe for S0 layer. The dimension is given in mm. . . . .	89
4.21	The CAD drawing of the ladder for S0 layer. The dimension is given in mm. . . . .	90
4.22	The prototype silicon sensors for the S2 layer. . . . .	91
4.23	Layout for the silicon sensor for the S1 detector. . . . .	92
4.24	Layout for the silicon sensor module for the S1 detector. . . . .	93
4.25	Layout for the silicon sensor ladder for the S1 detector. . . . .	94
4.26	Schematic layout of TPC main elements. . . . .	94
4.27	Transverse momentum resolution of the silicon tracking detector design with the reused pixels. Black dots are from a full GEANT4 simulation. The dashed blue line is a free fit to the Glückstern formula, whereas the solid blue line is a first-principles prediction using the material list. The light blue line shows the contribution from position resolution alone, demonstrating that the baseline design is entirely multiple-scattering limited. . . . .	97
4.28	Momentum resolution of the baseline sPHENIX tracker and the hybrid TPC option. Solid lines in the left panel are for $\eta=0$ ( $p_T = p$ ), dashed lines are averaged over the entire aperture. . . . .	98

4.29	Simulated Mass Resolution for the Upsilon states. Black dots are the results from GEANT simulations. The black histogram is the result of the semi-analytic calculation. Blue curves are free fits to the $Y(1s)$ . . . . .	98
4.30	Statistics loss of Upsilon's due to Bremsstrahlung. . . . .	99
4.31	schematic illustration of electrons drifting to the pad plane in the TPC simulation (pad size not drawn to scale) . . . . .	100
4.32	comparison of the momentum resolution of the simulated TPC with an analytic calculation in one unit of pseudorapidity . . . . .	101
4.33	Upsilon 1S, 2S, and 3S resolution for the simulated TPC along with an analytic calculation . . . . .	102
4.34	Schematic layout of the TPC pad rows and chevron pads. . . . .	103
4.35	Schematic view not to scale of the readout element built with four layers of GEMs. Yellow lines show electron paths, brown lines show the ion paths for one single hole (simulation). . . . .	104
4.36	Ion Back Flow in ALICE. . . . .	105
4.37	Scale drawing of the outer field cage and gas enclosure for the STAR TPC. .	106
4.38	Dielectric strengths of various common circuit card materials, reproduced from figures by Sierra Proto Express, a Palo Alto-based circuitry company specializing in high voltage circuit card for both terrestrial and satellite applications. . . . .	106
4.39	Comparison of the electron transport properties of T2K gas ( $Ar:CF_4:iC_4H_{10}$ 95:3:2) and ALICE gas ( $Ar:CO_2$ 90:10). . . . .	108
4.40	Alternative gas choices that may be better compromises for sPHENIX. . . .	109
4.41	Inverse ion mobility as a function of gas fraction demonstrating Blanc's Law.	110
4.42	Block diagram of signal processing for ALICE TPC upgrade . . . . .	112
4.43	Block diagram of ALICE SAMPA chip . . . . .	112
4.44	Conceptual Board Schematics of ALICE TPC FEC . . . . .	113
4.45	Installation image of ALICE TPC FEC to TPC . . . . .	113
4.46	Diagram of power supply for ALICE TPC FEC . . . . .	114
4.47	Power Supply module, Wiener PL 500 F21, employed for ALICE TPC electronics. . . . .	114
4.48	Diagram of the cooling plant in use the the ALICE TPC. The cooling plant is an under pressure system so that any leak results in gas bubbling into the coolant rather than coolant dripping into the detector. . . . .	115

4.49	Photograph of the central membrane of the STAR TPC. The pattern of Aluminum strips is used to release electrons via laser flash as a calibration signal. . . . .	116
4.50	Calculated drift characteristics of $Ne - CO_2$ gas (same as used by ALICE). .	119
4.51	Apparatus used to measure electron drift velocities and electron attachment.	121
4.52	Results for drift velocity and electron attachment in a variety of gasses. . . .	121
4.53	Photograph of the TPC/HBD prototype along with a measurement of the $^{55}Fe$ energy deposit spectrum. . . . .	122
4.54	Measurements of the differential non-linearity of chevron pad response and demonstration of the resolution achieved after correction. . . . .	123
4.55	Ion back flow measurements for the ALICE upgrade were made by the Yale group (collaborators through EIC R&D) not only for the quad-GEM solution, but also for other alternative readout schemes. This figure shows their apparatus as setup for measurements of a hybrid gain stage utilizing two GEMs followed by a microMEGA. . . . .	124
4.56	Resolution of the hybrid gain vs ion back flow percentage. . . . .	125
4.57	Ion clearing times in the stacked grid scheme. . . . .	125
4.58	The RD6 GEM detector shown here is among the largest GEM chambers yet built. It was tested at Fermilab test beam and yielded a position resolution of better than $80 \mu m$ . . . . .	126
5.1	Visible energy density in the sPHENIX calorimeter systems in central Au+Au collisions. The electromagnetic calorimeter at radius of $\sim 100$ cm observes a high amount of background energy density, which is quantified in Figure 5.25 in a later section. Each block of the EMCal consists of two towers in the z-direction. . . . .	131
5.2	Prototype W/SciFi calorimeters tested at Fermilab in 2014. The detector on the left consists of semi-projective modules and the one on the right consists of non-projective modules . . . . .	132
5.3	Test beam results for the semi-projective prototype calorimeter. Left: Energy resolution for three different effective rapidities ( $\eta = 0.0, 0.3$ and $0.9$ ). Right: Calorimeter response as a function of electron beam energy. . . . .	133
5.4	Left: EMCal sector showing installation on the Inner HCal. Right: Mechanical detail of an EMCal sector . . . . .	135
5.5	Cross sectional drawing of an EMCal sector. . . . .	136
5.6	Technical drawing of the SPACAL block 2 tower, 1D projective block . . . .	137

5.7	Magnified photo of Technon 100 mesh powder (left), etched brass fiber positioning mesh (center), and fiber/mesh assembly in open mold (right).	137
5.8	1D projective blocks produced by THP.	139
5.9	Measured light output from first THP produced blocks. Read out directly coupled to a 2" PMT, cosmic ray trigger. Converted to photons using pmt QE = 0.20.	140
5.10	Measured light output from a THP produced block, read out through light guide with 4 SiPMs, cosmic ray trigger. The four summed sipms have a total of $4 \times 40,000 = 160,000$ micropixels, which establishes the upper end of the dynamic range.	141
5.11	Drawing of overlaid screens (left), and photo of fibers threaded through spaced screens for 2D tapered module production (right).	142
5.12	Wireframe and fiber assembly in open mold (left), "bowtie" arrangement for 2 block production (right).	142
5.13	2D tapered block production at BNL: 3D printed mold (left), filled mold, connected and ready to infuse epoxy (center), 2D tapered modules produced at BNL (right).	143
5.14	The diamond cut end of a tungsten powder/fiber/epoxy block, cut with the UIUC-developed technique.	143
5.15	Preliminary design for EMCal light guides.	144
5.16	Four-SiPM pcb and SPACAL acrylic lightguide (left), lightguides on SPACAL block (right). In the current design, the sipms will be mounted on a larger pcb with preamps and electronics. The sipms will be positioned to accomodate the mounting hole in the light guide.	144
5.17	Event display of a 10 GeV positron shower in a single SPACAL tower. Scintillation fibers as embedded in the module are also shown, while the absorber material is not displayed.	145
5.18	Simulation display of a half cut view of the 2D projective EMCal. The SPACAL modules (2x8 towers each) are display in gray; the stainless steel enclosure box is displayed in green.	145
5.19	Comparison of the eRD1 beam test data and sPHENIX GEANT4 simulation for three choices of beam energies: 4.12 GeV (top), 8.0 GeV (middle) and 12.0 GeV (bottom). The left column data (black points) are with an electron requirement based on a beam Cherenkov detector, and the right column with a non-electron requirement. Curves represent simulated electrons (green), pions (red), kaons (blue) and muons (black).	152

- 5.20 The sampling fraction of the 1D and 2D projective SPACAL as a function of pseudorapidity. Two energy ranges were chosen: the circles represent electron showers at 4 GeV, which is a typical energy for  $\Upsilon$  measurements; the squares represent photon showers at 24 GeV, which is a typical energy for  $\gamma$ -Jet measurements. . . . . 153
- 5.21 The lateral expansion of 4 GeV electron showers in the EMCal (left column), which is compared with 4 GeV negatively charged pion showers in the EMCal (middle column) and in the inner HCal (right column). The center,  $(X, Y) = (0, 0)$  cm, denotes the projection of the electron track. Then the energy deposition of all scintillator hits in GEANT4 is histogrammed versus the lateral distance from the track projection. The top row shows the energy deposition density in the 2-D lateral dimension, and the bottom row shows the energy density (black) and the shower leakage ratio (blue) vs. lateral radial distance. . . . . 153
- 5.22 For very forward pseudorapidity, the lateral distribution of 8 GeV electron showers as observed in the 2-D projective (left) and 1-D projective (right) SPACAL towers. The polar (X-axis) and azimuthal (Y-axis) distances are defined as the distance between the tower and the electron track projection, in the unit of tower width. . . . . 154
- 5.23 Left: the energy resolution for single photon clusters as reconstructed with the fully simulated sPHENIX detector, right: the energy resolution for single electron clusters as reconstructed with the sPHENIX calorimeters only (no silicon detector before EMCal). Two formulas were used to fit the resolution points: a quadratic sum of linear and statistical terms (solid line) and a linear sum of the two (dash line). Both 1D (blue curves and open points) and 2D (red curves and closed points) SPACAL options are presented. . . . 154
- 5.24 Linearity for single photon clusters as reconstructed with the full sPHENIX detector simulation and analysis chain. The linearity is calibrated for each pseudorapidity region to 1 at the low energy end, while the non-linearity towards the high energy end is quantified via a quadratic fit. . . . . 155
- 5.25 a) Energy per tower ( $\sim 1R_M^2$ ) for central Au+Au HIJING events, b) Mean energy for a  $3 \times 3$  EMCal tower-cluster. The 2-D projective SPACAL configuration is shown here. . . . . 155
- 5.26 Pion rejection vs. electron identification efficiency for a single particle simulation for the 2-D projective SPACAL, which represents the performance for  $p+p$  and EIC collisions. . . . . 156
- 5.27 The pion rejection vs electron identification efficiency for the 2-D projective (left) and 1D-projective (right) SPACAL in central Au+Au collisions (0-10% central). . . . . 156

5.28	Number of photoelectrons per tower for 50 GeV photons as the maximum energy shower targeted by this calorimeter system. To encode the maximum photoelectron count down to the pedestal noise level, a 12-bit ADC is required.	157
5.29	Rejection factor and efficiency for an Y-electron trigger, which requires some minimum amount of energy in a 4x4-tower of the 2D projective SPACAL ( $\Sigma_{4 \times 4}[E_{\text{Tower}}]$ ). Results are shown for a full PYTHIA and GEANT4 simulation of the detector response. The rejection factor for minimum bias $p+p$ events (black lines) and the efficiency for Y (red lines) are plotted as a function of the required energy $\Sigma_{4 \times 4}[E_{\text{Tower}}]$ . For the dashed lines, full bit-width ADC values were used in the trigger sum, while the solid line shows trigger performance when only the top 8-bit ADC information is used. . . . .	157
6.1	Y-11 (200) WLS fiber emission spectrum (left) and transmission loss (right).	162
6.2	Transverse cut of an Inner HCAL module, showing the tilted tapered absorber plates. Light collection and cabling is on the outer radius at the top of the drawing. . . . .	164
6.3	Assembly of inner HCAL modules. . . . .	165
6.4	The current design for electronics and cable routing from inner HCAL sector. The SiPM holders are mounted directly on the end of the tile with a single preamplifier/shaper/driver board mounted nearby. An Interface Board at the end of the sector, provides power and bias voltage distribution and local monitoring. . . . .	165
6.5	Transverse cut of an Outer HCAL module, showing the tilted tapered absorber plates. Light collection and cabling is on the outer radius at the top of the drawing. . . . .	167
6.6	Design of the small plastic fixture coupling the fiber to an SiPM. . . . .	168
6.7	Design of the LED calibration system. . . . .	169
6.8	Inner and Outer HCAL with support structure. . . . .	170
6.9	Results of finite element analysis of Outer HCAL after final assembly, showing the maximum deformation of the structure. . . . .	171
6.10	GEANT4 event display of a 10GeV $\pi$ shower in the sPHENIX calorimeter system. . . . .	172
6.11	GEANT4 visualizations of the inner (top row) and outer (bottom row) HCAL geometry for different crossing values. A crossing value of four is the reference configuration, corresponding to tilt angles of 36 and 12 degrees, respectively, in the inner and outer HCAL engineering drawings. . . . .	173

6.12	GEANT4 calorimetry material scan in nuclear interaction lengths vs. pseudorapidity for a variety of crossing angle configurations. . . . .	174
6.13	Scintillator tiles in a layer of the Outer HCAL. . . . .	175
6.14	Combined calorimeter energy resolution from GEANT4 simulations of the EMCal and inner and outer HCAL for negative pions. The dashed line is a fit to the $\eta = 0$ data points above 16 GeV corresponding to $\frac{\sigma}{E} = \frac{46\%}{\sqrt{E}} \oplus 7.4\%$ . . . . .	176
6.15	Linearity of the sPHENIX calorimetry system response for negative pions as a function of pion momentum and different $\eta$ selections. The line is a linear fit to the $\eta=0$ data points. . . . .	177
6.16	Behavior of non-Gaussian tails in the energy resolution function from GEANT4 simulations of the EMCal and inner and outer HCAL for negative pions. The dashed line at 2.5% would characterize a purely Gaussian response. . . . .	178
6.17	Variation of the EMCal and inner and outer HCAL sampling fractions as a function of number of crossings in the inner and outer HCAL. . . . .	179
6.18	Gaussian energy resolution as a function of crossing angle for 24 GeV pions. . . . .	180
6.19	Non-Gaussian tails to the energy response as a function of crossing angle for 2 GeV pions. . . . .	181
6.20	Non-Gaussian tails to the energy response as a function of crossing angle for 50 GeV pions. . . . .	182
6.21	TOP ROW: Sampling fraction in the inner (left) and outer (right) HCAL from GEANT4 simulations as a function of depth along the scintillating tiles, showing the decrease in the sampling fraction as a function of depth in each HCAL compartment. BOTTOM ROW: Sampling fractions in the inner and outer HCAL after the light yield correction has been applied, resulting in a uniform sampling fraction as a function of depth along the tile. . . . .	183
6.22	Point-by-point comparison of the energy resolution of the baseline sPHENIX calorimetry design with the inclusion of a light yield correction to even out the sampling fraction in the inner and outer HCAL. The baseline energy resolution is shown in Figure 6.14. A positive value indicates improvement in the resolution with the light yield correction. . . . .	184
6.23	Point-by-point comparison of the non-Gaussian tails in the baseline sPHENIX calorimetry design with the inclusion of a light yield correction to even out the sampling fraction in the inner and outer HCAL. The baseline non-Gaussian tails are shown in Figure 6.16. A positive value indicates improvement in the non-Gaussian tails with the light yield correction. . . . .	185

6.24	Calculated energy deposited in scintillator tiles in HCAL towers from 50 GeV protons in towers at two pseudorapidities. . . . .	186
6.25	Scintillating tiles with embedded wavelength shifting fibers (left panel) and the HCAL prototype colorimeter (right panel). . . . .	186
6.26	Side view of the layout of the HCAL prototype detector at the FNAL test beam facility. The beam enters from the right as indicated by the red arrow. . . . .	187
6.27	sPHENIX HCAL prototype energy resolution for pions and electrons obtained from the FNAL test beam data. . . . .	188
6.28	sPHENIX HCAL prototype energy linearity for pions and electrons obtained from the FNAL test beam data. . . . .	189
6.29	$e/\pi$ ratio of the HCal prototype. . . . .	190
6.30	Comparison of the energy resolution for pions (left panel) and electrons (right panel) between test beam data and the GEANT4 simulation. . . . .	191
6.31	Comparison of the $e/\pi$ ratios evaluated from test beam data and the GEANT4 simulation. . . . .	191
7.1	Block diagram of a ADC system . . . . .	193
7.2	Optical saturation in Hamamatsu S12572 MPPCs. $10\mu\text{m}$ , $25\mu\text{m}$ , and $50\mu\text{m}$ micropixels . . . . .	196
7.3	Hamamatsu S12572 MPPC (SiPM). The device is $3 \times 3 \text{ mm}^2$ with 40,000 pixels $15\mu\text{m}^2$ . . . . .	197
7.4	Hamamatsu S12572 MPPC surface mount package dimensions. . . . .	197
7.5	Percent change in LED signal amplitude vs temperature for Various SiPMs. (top) and Dependence of leakage current on Temperature in Hamamatsu S12572 MPPCs with $10\mu\text{m}$ , $15\mu\text{m}$ , and $25\mu\text{m}$ micropixels (bottom). . . . .	199
7.6	Performance as a function of temperature - Hamamatsu S12572-015P MPPCs with an sPHENIX preamp. Dark current as a function of temperature (top), signal (LED pulse) amplitude vs temperature (center), and for the LED signal, stddev/mean vs temperature (bottom) . . . . .	200
7.7	Sipms in the PHENIX IR during Run 15 p-p running. The devices – Hamamatsu S12572-025P, -015P, and -010P all showed a steady increase in leakage current with cumulative neutron fluence during Run 15. . . . .	201
7.8	Various sipms studied at BNL SSGRIF facility. Increasing leakage current vs time during neutron exposure. . . . .	202
7.9	Neutron damage in Hamamatsu MPPCs exposed at Indiana Univ LENS facility . . . . .	203



7.10	Neutron damage in Hamamatsu MPPCs exposed at Los Alamos LANSCE facility . . . . .	204
7.11	Radiation damage in Hamamatsu MPPCs exposed at BNL in the STAR FPS during Run 15. MIP peak measured at different times over the course of the run. Despite the significant increase in leakage current, only a small change is seen in the MIP peak amplitude. Vbias across the sipms was kept constant. . . . .	205
7.12	A block diagram showing the overall design of the HCal electronics for one half sector of the HCal. There are a total of 128 half sectors for the inner and outer HCal combined. Not shown are the connections for the LED monitoring system. . . . .	206
7.13	A block diagram showing the overall design for the EMCal electronics for one half sectors for the EMCal. There are a total of 384 towers per half sector and 32 half sectors for the EMCal. . . . .	206
7.14	The response of the common-base transistor amplifier as a function of the injected charge as measured in the lab. The measured RMS noise is $\sim 43$ fC which matches the charge injected by a single microcell of the SiPM firing. . . . .	207
7.15	Block diagram of a temperature compensating circuit for SiPMs . . . . .	208
7.16	Block diagram of the slow controls for the calorimeter front end electronics. The inset picture shows a prototype module of the HCal Interface board that will be used on the HCal Beam Test prototype. . . . .	209
7.17	Block diagram of the Digitizer Module electronics. . . . .	210
7.18	Preliminary grounding plan for calorimeter electronics which is based on a star grounding configuration. Not shown is the grounding of the mechanical parts of the calorimeters. . . . .	212
8.1	Schematic view of the trigger and front-end system. The Global Level 1 provides the trigger to the Master Timing System, which is then distributed to the granule timing modules, which provide the subsystem-specific trigger signals and timing to the Front-End Modules. . . . .	216
8.2	Overview of the event builder design. The data are digitized in the Front-End Modules and zero-suppressed and packaged in the Data Collection Modules. The data from a given collision are initially distributed over many SEBs. The data from one collision are collected in the ATP's, which sees the full complement of data of that collision for the first time. The ATP compresses the data before transmitting them to the <i>Buffer Boxes</i> , from where the data are transferred to a long-term storage system. . . . .	217

8.3	Livetime as a function of DAQ accepted event rate. The points are measurements from Run 14 Au+Au running in PHENIX, the black line is the measured performance from one older PHENIX system, the red line shows the simulated performance with 4 event buffering with the sPHENIX calorimeter ADC system, and the blue line shows the expected behavior with 100 events buffered in the front end. . . . .	219
8.4	The trigger efficiency in Hijing events for 200 AGeV Au+Au collisions of beam-beam counters at forward pseudorapidities $3.80 < \eta < 4.69$ , and the negative equivalent. The trigger requires at least one charged particle in the detector on each side with an energy about 200 MeV. This detector would also provide the fast timing signal to determine the collision vertex. . . . .	220
9.1	sPHENIX Major Facility Hall and Auxilliary Buildings . . . . .	224
10.1	sPHENIX in IR . . . . .	229
10.2	sPHENIX Overall size . . . . .	231
10.3	EMCal Envelope Control Drawing . . . . .	232
10.4	sPHENIX Envelope Control Drawing . . . . .	232
10.5	Inner HCal Half-sector mockup . . . . .	235
10.6	sPHENIX exploded view . . . . .	236
10.7	sPHENIX Structural Support . . . . .	238
10.8	sPHENIX Initial Alignment . . . . .	239
10.9	EMCal Sector Installation . . . . .	240
10.10	Outer HCal Installation, lower half . . . . .	241
10.11	Ready for Magnet mapping . . . . .	242
10.12	Inner HCal Installation . . . . .	243
11.1	The Project Organization chart . . . . .	248
11.2	The estimated direct cost of all materials and purchases in the sPHENIX reference design not including the Tracker which is expected to be funded from other sources . . . . .	252
11.3	An example budget profile covering the Total Project Cost of sPHENIX. The labor and material are burdened with the current BNL capital project rate, escalation has been applied and contingency added in an amount 30% on materials and 20% on labor. . . . .	253

11.4	The Project schedule showing CD approvals, milestones and major activities.	254
11.5	The high-level sPHENIX project schedule including CD milestones. . . . .	255
11.6	The sPHENIX labor distribution from all sources including BNL, universities and other institutions both US and international. . . . .	256
11.7	The risk assessment matrix table RMP 1 . . . . .	257
11.8	The final risk classification table RMP2 . . . . .	257



# Bibliography

- [1] A. Adare et al. An Upgrade Proposal from the PHENIX Collaboration. 2014. arXiv:1501.06197. (document), 1, 1.8, 2.3, 8.1
- [2] A. Adare et al. Enhanced production of direct photons in Au+Au collisions at  $\sqrt{s_{NN}} = 200$  GeV and implications for the initial temperature. *Phys. Rev. Lett.*, 104:132301, 2010. arXiv:0804.4168, doi:10.1103/PhysRevLett.104.132301. 1
- [3] M. Luzum and P. Romatschke. Viscous hydrodynamic predictions for nuclear collisions at the LHC. *Phys. Rev. Lett.*, 103:262302, 2009. arXiv:0901.4588, doi:10.1103/PhysRevLett.103.262302. 1
- [4] K. Adcox et al. Formation of dense partonic matter in relativistic nucleus-nucleus collisions at RHIC: Experimental evaluation by the PHENIX collaboration. *Nucl. Phys.*, A757:184–283, 2005. arXiv:nucl-ex/0410003, doi:10.1016/j.nuclphysa.2005.03.086. 1.1
- [5] Matthew Luzum and Paul Romatschke. Conformal Relativistic Viscous Hydrodynamics: Applications to RHIC results at  $s(NN)^{1/2} = 200$ -GeV. *Phys. Rev.*, C78:034915, 2008. [Erratum: *Phys. Rev.* C79,039903(2009)]. arXiv:0804.4015, doi:10.1103/PhysRevC.78.034915, 10.1103/PhysRevC.79.039903. 1.1
- [6] P. Danielewicz and M. Gyulassy. Dissipative phenomena in quark gluon plasmas. *Phys. Rev.*, D31:53–62, 1985. doi:10.1103/PhysRevD.31.53. 1.1
- [7] P. Kovtun, Dan T. Son, and Andrei O. Starinets. Viscosity in strongly interacting quantum field theories from black hole physics. *Phys. Rev. Lett.*, 94:111601, 2005. arXiv:hep-th/0405231, doi:10.1103/PhysRevLett.94.111601. 1.1, 1.3.1
- [8] H. Song and U. W. Heinz. Causal viscous hydrodynamics in 2+1 dimensions for relativistic heavy-ion collisions. *Phys. Rev.*, C77:064901, 2008. arXiv:0712.3715, doi:10.1103/PhysRevC.77.064901. 1.1
- [9] B. Alver, C. Gombeaud, M. Luzum, and J.-Y. Ollitrault. Triangular flow in hydrodynamics and transport theory. *Phys. Rev.*, C82:034913, 2010. arXiv:1007.5469, doi:10.1103/PhysRevC.82.034913. 1.1

- [10] D. A. Teaney. Viscous Hydrodynamics and the Quark Gluon Plasma. 2009. arXiv:0905.2433. 1.1
- [11] B. Schenke, S. Jeon, and C. Gale. Elliptic and triangular flows in 3 + 1D viscous hydrodynamics with fluctuating initial conditions. *J. Phys. G*, G38:124169, 2011. 1.1
- [12] A. Adare et al. Measurements of Higher-Order Flow Harmonics in Au+Au Collisions at  $\sqrt{s_{NN}} = 200$  GeV. *Phys. Rev. Lett.*, 107:252301, 2011. arXiv:1105.3928, doi:10.1103/PhysRevLett.107.252301. 1.1
- [13] A. Adare et al. Energy Loss and Flow of Heavy Quarks in Au+Au Collisions at  $s(NN)^{(1/2)} = 200$ -GeV. *Phys. Rev. Lett.*, 98:172301, 2007. arXiv:nuc1-ex/0611018, doi:10.1103/PhysRevLett.98.172301. 1.1
- [14] G. Aad et al. Measurement of the Azimuthal Angle Dependence of Inclusive Jet Yields in Pb+Pb Collisions at  $\sqrt{s_{NN}} = 2.76$  TeV with the ATLAS detector. 2013. arXiv:1306.6469. 1.1
- [15] G. Aad et al. Measurement of the jet radius and transverse momentum dependence of inclusive jet suppression in lead-lead collisions at  $\sqrt{s_{NN}} = 2.76$  TeV with the ATLAS detector. *Phys. Lett.*, B719:220–241, 2013. arXiv:1208.1967, doi:10.1016/j.physletb.2013.01.024. 1.1
- [16] K. Rajagopal. International Quark Matter presentation (2011). URL: <http://qm2011.in2p3.fr/node/12>. 1.2
- [17] J. Liao and E. Shuryak. Angular Dependence of Jet Quenching Indicates Its Strong Enhancement Near the QCD Phase Transition. *Phys. Rev. Lett.*, 102:202302, 2009. arXiv:0810.4116, doi:10.1103/PhysRevLett.102.202302. 1.2, 1.3.2
- [18] C. E. Coleman-Smith, G.-Y. Qin, S. A. Bass, and B. Muller. Jet modification in a brick of QGP matter. 2011. arXiv:1108.5662. 1.2, 1.6.1, 1.7
- [19] C. E. Coleman-Smith, S. A. Bass, and D. K. Srivastava. Implementing the LPM effect in a parton cascade model. *Nucl. Phys.*, A862-863:275–278, 2011. arXiv:1101.4895, doi:10.1016/j.nuclphysa.2011.05.071. 1.2, 1.6, 1.6.1
- [20] Laszlo P. Csernai, Joseph.I. Kapusta, and Larry D. McLerran. On the Strongly-Interacting Low-Viscosity Matter Created in Relativistic Nuclear Collisions. *Phys. Rev. Lett.*, 97:152303, 2006. arXiv:nuc1-th/0604032, doi:10.1103/PhysRevLett.97.152303. 1.3.1
- [21] P. B. Arnold, G. D. Moore, and L. G. Yaffe. Transport coefficients in high temperature gauge theories. 2. Beyond leading log. *JHEP*, 0305:051, 2003. arXiv:hep-ph/0302165. 1.3.1

- [22] Charles Gale, Sangyong Jeon, Bjorn Schenke, Prithwish Tribedy, and Raju Venugopalan. Event-by-event anisotropic flow in heavy-ion collisions from combined Yang-Mills and viscous fluid dynamics. *Phys. Rev. Lett.*, 110:012302, 2013. arXiv:1209.6330, doi:10.1103/PhysRevLett.110.012302. 1.3.1
- [23] H. Song, S. A. Bass, and U. Heinz. Elliptic flow in 200 A GeV Au+Au collisions and 2.76 A TeV Pb+Pb collisions: insights from viscous hydrodynamics + hadron cascade hybrid model. *Phys. Rev.*, C83:054912, 2011. arXiv:1103.2380, doi:10.1103/PhysRevC.83.054912. 1.3.1
- [24] J. L. Nagle, I. G. Bearden, and W. A. Zajc. Quark-gluon plasma at RHIC and the LHC: perfect fluid too perfect? *New J. Phys.*, 13:075004, 2011. arXiv:1102.0680, doi:10.1088/1367-2630/13/7/075004. 1.3.1
- [25] H. Niemi, G. S. Denicol, P. Huovinen, E. Molnar, and D. H. Rischke. Influence of the shear viscosity of the quark-gluon plasma on elliptic flow in ultrarelativistic heavy-ion collisions. *Phys. Rev. Lett.*, 106:212302, 2011. arXiv:1101.2442, doi:10.1103/PhysRevLett.106.212302. 1.3.1
- [26] S. Chatrchyan et al. Study of high-pT charged particle suppression in PbPb compared to pp collisions at  $\sqrt{s_{NN}} = 2.76$  TeV. *Eur. Phys. J.*, C72:1945, 2012. arXiv:1202.2554, doi:10.1140/epjc/s10052-012-1945-x. 1.3.2, 1.6
- [27] C. N. Bo et al. Extracting jet transport coefficients from jet quenching at RHIC and the LHC. 2013. URL: <https://sites.google.com/a/lbl.gov/jetwiki/documents-1/report-on-status-of-qhat>. 1.3.2, 1.5, 11.7.2
- [28] Jiechen Xu, Jinfeng Liao, and Miklos Gyulassy. Anisotropic Jet Quenching in semi-Quark-Gluon Plasmas with Magnetic Monopoles in Ultrarelativistic Heavy Ion Collisions. 2014. arXiv:1411.3673. 1.5, 1.3.2, 11.7.2
- [29] Thorsten Renk. On the sensitivity of jet quenching to near  $T_C$  enhancement of the medium opacity. *Phys. Rev.*, C89:067901, 2014. arXiv:1402.5798, doi:10.1103/PhysRevC.89.067901. 1.3.2
- [30] W. A. Horowitz and M. Gyulassy. The Surprising Transparency of the sQGP at LHC. *Nucl. Phys.*, A872:265–285, 2011. arXiv:1104.4958. 1.3.2
- [31] K. Aamodt and C. A. Loizides. Suppression of charged particle production at large transverse momentum in central Pb–Pb collisions at  $\sqrt{s_{NN}} = 2.76$  TeV. *Phys. Lett.*, B696:30–39, 2011. arXiv:1012.1004. 1.3.2
- [32] X.-F. Chen, T. Hirano, E. Wang, X.-N. Wang, and H. Zhang. Suppression of high  $p_T$  hadrons in Pb + Pb Collisions at LHC. *Phys. Rev.*, C84:034902, 2011. arXiv:1102.5614, doi:10.1103/PhysRevC.84.034902. 1.3.2

- [33] B. G. Zakharov. Variation of jet quenching from RHIC to LHC and thermal suppression of QCD coupling constant. *JETP Lett.*, 93:683–687, 2011. arXiv:1105.2028, doi:10.1134/S0021364011120162. 1.3.2
- [34] A. Buzzatti and M. Gyulassy. Jet Flavor Tomography of Quark Gluon Plasmas at RHIC and LHC. *Phys. Rev. Lett.*, 108:022301, 2012. 4 pages, 3 eps figures. arXiv:1106.3061, doi:10.1103/PhysRevLett.108.022301. 1.3.2
- [35] A. Buzzatti and M. Gyulassy. A running coupling explanation of the surprising transparency of the QGP at LHC. *Nucl. Phys.A904-905*, 2013:779c–782c, 2013. arXiv:1210.6417, doi:10.1016/j.nuclphysa.2013.02.133. 1.3.2
- [36] A. Adare et al. Evolution of  $\pi^0$  suppression in Au+Au collisions from  $\sqrt{s_{NN}} = 39$  to 200 GeV. *Phys. Rev. Lett.*, 109:152301, 2012. arXiv:1204.1526, doi:10.1103/PhysRevLett.109.152301. 1.3.2
- [37] Alexander Schmah. The beam energy scan at RHIC: Recent results from STAR. *J. Phys. Conf. Ser.*, 426:012007, 2013. doi:10.1088/1742-6596/426/1/012007. 1.3.2
- [38] B. Muller. Parton energy loss in strongly coupled AdS/CFT. *Nucl. Phys.*, A855:74–82, 2011. arXiv:1010.4258, doi:10.1016/j.nuclphysa.2011.02.022. 1.4
- [39] Thorsten Renk. Physics probed by the  $P_T$  dependence of the nuclear suppression factor. *Phys. Rev.*, C88(1):014905, 2013. arXiv:1302.3710, doi:10.1103/PhysRevC.88.014905. 1.4
- [40] A. Majumder and C. Shen. Suppression of the High  $p_T$  Charged Hadron  $R_{AA}$  at the LHC. *Phys. Rev. Lett.*, 109:202301, 2012OA. arXiv:1103.0809, doi:10.1103/PhysRevLett.109.202301. 1.4
- [41] A. Majumder and J. Putschke. Mass depletion: a new parameter for quantitative jet modification. 2014. arXiv:1408.3403. 1.4
- [42] Korinna C. Zapp. JEWEL 2.0.0: directions for use. *Eur. Phys. J.*, C74:2762, 2014. arXiv:1311.0048, doi:10.1140/epjc/s10052-014-2762-1. 1.4
- [43] A. Adare et al. Quantitative Constraints on the Opacity of Hot Partonic Matter from Semi-Inclusive Single High Transverse Momentum Pion Suppression in Au+Au collisions at  $s(NN)^{(1/2)} = 200$ -GeV. *Phys. Rev.*, C77:064907, 2008. arXiv:0801.1665, doi:10.1103/PhysRevC.77.064907. 1.4
- [44] Steffen A. Bass, Charles Gale, Abhijit Majumder, Chiho Nonaka, Guang-You Qin, Thorsten Renk, and Jorg Ruppert. Systematic Comparison of Jet Energy-Loss Schemes in a realistic hydrodynamic medium. *Phys. Rev.*, C79:024901, 2009. arXiv:0808.0908, doi:10.1103/PhysRevC.79.024901. 1.4



- [45] K. Adcox et al. Suppression of hadrons with large transverse momentum in central Au+Au collisions at  $\sqrt{s_{NN}} = 130$ -GeV. *Phys. Rev. Lett.*, 88:022301, 2002. arXiv:nucl-ex/0109003, doi:10.1103/PhysRevLett.88.022301. 1.5
- [46] C. Adler et al. Centrality dependence of high  $p_T$  hadron suppression in Au+Au collisions at  $\sqrt{s_{NN}} = 130$  GeV. *Phys. Rev. Lett.*, 89:202301, 2002. arXiv:nucl-ex/0206011. 1.5
- [47] A. Adare et al. Trends in Yield and Azimuthal Shape Modification in Dihadron Correlations in Relativistic Heavy Ion Collisions. *Phys. Rev. Lett.*, 104:252301, 2010. arXiv:1002.1077, doi:10.1103/PhysRevLett.104.252301. 1.5
- [48] A. Adare et al. Suppression of away-side jet fragments with respect to the reaction plane in Au+Au collisions at  $\sqrt{s_{NN}} = 200$  GeV. *Phys. Rev.*, C84:024904, 2011. arXiv:1010.1521, doi:10.1103/PhysRevC.84.024904. 1.5
- [49] J. Adams et al. Distributions of charged hadrons associated with high transverse momentum particles in  $p+p$  and Au+Au collisions at  $\sqrt{s_{NN}} = 200$  GeV. *Phys. Rev. Lett.*, 95:152301, 2005. arXiv:nucl-ex/0501016. 1.5
- [50] J. L. Nagle. Ridge, bulk, and medium response: how to kill models and learn something in the process. *Nucl. Phys.*, A830:147C–154C, 2009. arXiv:0907.2707. 1.5
- [51] G. Aad et al. Observation of a centrality-dependent dijet asymmetry in lead-lead collisions at  $\sqrt{s_{NN}} = 2.76$  TeV with the ATLAS detector at the LHC. *Phys. Rev. Lett.*, 105:252303, 2010. Accepted for publication at Physical Review Letters. arXiv:1011.6182, doi:10.1103/PhysRevLett.105.252303. 1.5.1
- [52] S. Chatrchyan et al. Observation and studies of jet quenching in PbPb collisions at nucleon-nucleon center-of-mass energy = 2.76 TeV. *Phys. Rev.*, C84:024906, 2011. arXiv:1102.1957, doi:10.1103/PhysRevC.84.024906. 1.5.1, 1.6.1
- [53] X.-N. Wang, Z. Huang, and I. Sarcevic. Jet quenching in the opposite direction of a tagged photon in high-energy heavy ion collisions. *Phys. Rev. Lett.*, 77:231–234, 1996. arXiv:hep-ph/9605213, doi:10.1103/PhysRevLett.77.231. 1.5.1, 1.7.1
- [54] S. Chatrchyan et al. Studies of jet quenching using isolated-photon+jet correlations in PbPb and pp collisions at  $\sqrt{s_{NN}} = 2.76$  TeV. 2012. Submitted to Physics Letters B. arXiv:1205.0206. 1.5.1
- [55] S. Chatrchyan et al. Jet momentum dependence of jet quenching in PbPb collisions at  $\sqrt{s_{NN}} = 2.76$  TeV. 2012. arXiv:1202.5022. 1.5.1
- [56] P. Steinberg. Recent Heavy Ion Results with the ATLAS Detector at the LHC. 2011. arXiv:1110.3352. 1.5.1
- [57] H. Caines. Jets and jet-like Correlations at RHIC. 2011. arXiv:1110.1878. 1.5.2

- [58] J. Putschke. STAR: Jet reconstruction, direct gamma and multi-hadron correlations: Hard probes of the initial and final state. *Nucl. Phys.*, A855:83–91, 2011. 1.5.2
- [59] J. Putschke. First fragmentation function measurements from full jet reconstruction in heavy-ion collisions at  $\sqrt{s_{NN}} = 200$  GeV by STAR. *Eur. Phys. J.*, C61:629–635, 2009. arXiv:0809.1419. 1.5.2
- [60] P. M. Jacobs. Background fluctuations in heavy ion jet reconstruction. 2010. arXiv:1012.2406. 1.5.2
- [61] Y.-S. Lai. Direct jet reconstruction in  $p+p$  and Cu+Cu collisions at PHENIX. *Nucl. Phys.*, A855:295–298, 2011. 1.5.2
- [62] Y.-S. Lai. Probing medium-induced energy loss with direct jet reconstruction in  $p+p$  and Cu+Cu collisions at PHENIX. *Nucl. Phys.*, A830:251C–254C, 2009. arXiv:0907.4725. 1.5.2
- [63] JET Topical Collaboration. URL: <http://jet.lbl.gov>. 1.6
- [64] K. C. Zapp, J. Stachel, and U. Wiedemann. LPM-effect in Monte Carlo models of radiative energy loss. *Nucl. Phys.*, A830:171C–174C, 2009. arXiv:0907.4304. 1.6
- [65] T. Renk. YaJEM: a Monte Carlo code for in-medium shower evolution. *Int. J. Mod. Phys.*, E20:1594–1599, 2011. arXiv:1009.3740, doi:10.1142/S0218301311019933. 1.6
- [66] C. Young, S. Jeon, C. Gale, and B. Schenke. Monte-Carlo simulation of jets in heavy-ion collisions. 2011. arXiv:1109.5992. 1.6, 1.6.1
- [67] I. P. Lokhtin, A. V. Belyaev, and A. M. Snigirev. Jet quenching pattern at LHC in PYQUEN model. *Eur. Phys. J.*, C71:1650, 2011. arXiv:1103.1853, doi:10.1140/epjc/s10052-011-1650-1. 1.6
- [68] N. Armesto, L. Cunqueiro, and C. A. Salgado. Monte Carlo for jet showers in the medium. *Nucl. Phys.*, A830:271C–274C, 2009. arXiv:0907.4706. 1.6
- [69] J. Casalderrey-Solana, J. G. Milhano, and U. Wiedemann. Jet quenching via jet collimation. *J. Phys. G*, G38:124086, 2011. arXiv:1107.1964. 1.6
- [70] T. Renk. Energy dependence of the dijet imbalance in Pb-Pb collisions at 2.76 ATeV. 2012. arXiv:1204.5572. 1.6
- [71] T. Renk. Jets in medium: What RHIC and LHC measurements of  $R_{AA}$  and  $I_{AA}$  can teach about the parton-medium interaction. 2011. arXiv:1111.0769. 1.6
- [72] T. Renk. Biased Showers — a common conceptual framework for the interpretation of High  $p_T$  observables in heavy-ion collisions. 2012. arXiv:1212.0646. 1.6

- [73] K. Geiger and B. Muller. Dynamics of parton cascades in highly relativistic nuclear collisions. *Nucl. Phys.*, B369:600–654, 1992. doi:10.1016/0550-3213(92)90280-0. 1.6.1
- [74] C. Wesp, A. El, F. Reining, Z. Xu, I. Bouras, et al. Calculation of shear viscosity using Green-Kubo relations within a parton cascade. *Phys. Rev.*, C84:054911, 2011. arXiv:1106.4306, doi:10.1103/PhysRevC.84.054911. 1.6.1
- [75] C. E Coleman-Smith and B. Muller. What can we learn from Dijet suppression at RHIC? 2012. arXiv:1205.6781. 1.7
- [76] G.-Y. Qin and B. Muller. Explanation of Di-jet asymmetry in Pb+Pb collisions at the Large Hadron Collider. *Phys. Rev. Lett.*, 106:162302, 2011. 4 pages, 3 figures, made corrections for numerical inaccuracies, qualitative conclusions unaffected. arXiv:1012.5280, doi:10.1103/PhysRevLett.106.162302. 1.6.1
- [77] G.-Y. Qin and B. Muller. private communication. 1.6.1, 1.8
- [78] B. Schenke, C. Gale, and S. Jeon. MARTINI: Monte Carlo simulation of jet evolution. *Acta Phys. Polon. Supp.*, 3:765–770, 2010. arXiv:0911.4470. 1.6.1
- [79] B. Schenke, S. Jeon, and C. Gale. (3+1)D hydrodynamic simulation of relativistic heavy-ion collisions. *Phys. Rev.*, C82:014903, 2010. arXiv:1004.1408, doi:10.1103/PhysRevC.82.014903. 1.6.1
- [80] C. Young, B. Schenke, S. Jeon, and C. Gale. Dijet asymmetry at the energies available at the CERN Large Hadron Collider. *Phys. Rev.*, C84:024907, 2011. arXiv:1103.5769, doi:10.1103/PhysRevC.84.024907. 1.6.1
- [81] C. Young and B. Schenke. private communication. 1.8
- [82] Y. He, I. Vitev, and B.-W. Zhang. Next-to-leading order analysis of inclusive jet and di-jet production in heavy ion reactions at the Large Hadron Collider. 2011. arXiv:1105.2566. 1.6.2
- [83] R. B. Neufeld and I. Vitev. Parton showers as sources of energy-momentum deposition in the QGP and their implication for shockwave formation at RHIC and at the LHC. 2011. 8 pages, 4 figures. arXiv:1105.2067. 1.6.2
- [84] I. Vitev and B.-W. Zhang. Jet tomography of high-energy nucleus-nucleus collisions at next-to-leading order. *Phys. Rev. Lett.*, 104:132001, 2010. arXiv:0910.1090, doi:10.1103/PhysRevLett.104.132001. 1.6.2
- [85] Wei Dai, Ivan Vitev, and Ben-Wei Zhang. Momentum imbalance of isolated photon-tagged jet production at RHIC and LHC. *Phys. Rev. Lett.*, 110:142001, 2013. arXiv:1207.5177, doi:10.1103/PhysRevLett.110.142001. 1.7.1, 1.10, 11.7.2

- [86] L. Adamczyk et al. Jet-Hadron Correlations in  $\sqrt{s_{NN}} = 200$  GeV  $p + p$  and Central  $Au + Au$  Collisions. *Phys. Rev. Lett.*, 112(12):122301, 2014. arXiv:1302.6184, doi:10.1103/PhysRevLett.112.122301. 1.7.2
- [87] W. Horowitz and M. Gyulassy. Heavy quark jet tomography of Pb+Pb at LHC: AdS/CFT drag or pQCD energy loss? *Phys. Lett.*, B666:320–323, 2008. arXiv:0706.2336, doi:10.1016/j.physletb.2008.04.065. 1.8
- [88] Y. Dokshitzer and D. Kharzeev. Heavy quark colorimetry of QCD matter. *Phys. Lett.*, B519:199–206, 2001. arXiv:hep-ph/0106202, doi:10.1016/S0370-2693(01)01130-3. 1.8
- [89] M. Cacciari. private communication. 1.8, 1.13
- [90] Jiechen Xu, Alessandro Buzzatti, and Miklos Gyulassy. Azimuthal jet flavor tomography with CUJET2.0 of nuclear collisions at RHIC and LHC. *JHEP*, 1408:063, 2014. arXiv:1402.2956, doi:10.1007/JHEP08(2014)063. 1.8, 1.14
- [91] V. Abazov et al. The upgraded D0 detector. *Nucl. Instrum. Meth.*, A565:463–537, 2006. arXiv:physics/0507191, doi:10.1016/j.nima.2006.05.248. 1.8
- [92] V. Abazov et al. b-Jet Identification in the D0 Experiment. *Nucl. Instrum. Meth.*, A620:490, 2010. arXiv:1002.4224, doi:doi:10.1016/j.nima.2010.03.118. 1.8
- [93] Jinrui Huang, Zhong-Bo Kang, and Ivan Vitev. Inclusive b-jet production in heavy ion collisions at the LHC. *Phys. Lett.*, B726:251–256, 2013. arXiv:1306.0909, doi:10.1016/j.physletb.2013.08.009. 1.8
- [94] X. Zhao and R. Rapp. Medium Modifications and Production of Charmonia at LHC. *Nucl. Phys.*, A859:114–125, 2011. 7 pages, 9 eps figures. arXiv:1102.2194, doi:10.1016/j.nuclphysa.2011.05.001. 1.9
- [95] Roberta Arnaldi. J/psi production in p-A and A-A collisions at fixed target experiments. *Nucl. Phys.*, A830:345C–352C, 2009. arXiv:0907.5004, doi:10.1016/j.nuclphysa.2009.10.030. 1.9
- [96] N. Brambilla, S. Eidelman, B. K. Heltsley, R. Vogt, G. T. Bodwin, et al. Heavy quarkonium: progress, puzzles, and opportunities. 2010. arXiv:arXiv:1010.5827. 1.9, 1.9.1, 1.9.2
- [97] B. Abelev et al.  $J/\psi$  production at low transverse momentum in Pb-Pb collisions at  $\sqrt{s_{NN}} = 2.76$  TeV. 2012. arXiv:1202.1383. 1.9
- [98] Serguei Chatrchyan et al. Observation of sequential Upsilon suppression in PbPb collisions. *Phys. Rev. Lett.*, 109:222301, 2012. arXiv:1208.2826, doi:10.1103/PhysRevLett.109.222301. 1.9.1

- [99] Betty Bezverkhny Abelev et al. Suppression of  $\Upsilon(1S)$  at forward rapidity in Pb-Pb collisions at  $\sqrt{s_{NN}} = 2.76$  TeV. 2014. arXiv:1405.4493. 1.9.1
- [100] Betty Bezverkhny Abelev et al. Production of inclusive  $\Upsilon(1S)$  and  $\Upsilon(2S)$  in p-Pb collisions at  $\sqrt{s_{NN}} = 5.02$  TeV. 2014. arXiv:1410.2234. 1.9.1
- [101] A. Adare et al. Measurement of  $\Upsilon(1S+2S+3S)$  production in  $p+p$  and Au+Au collisions at  $\sqrt{s_{NN}} = 200$  GeV. 2014. arXiv:1404.2246. 1.9.1
- [102] L. Adamczyk et al. Suppression of Upsilon Production in d+Au and Au+Au Collisions at  $\sqrt{s_{NN}} = 200$  GeV. *Phys. Lett.*, B735:127, 2014. arXiv:1312.3675, doi:10.1016/j.physletb.2014.06.028. 1.9.1
- [103] B. Muller, J. Schukraft, and B. Wyslouch. First results from Pb+Pb collisions at the LHC. 2012. arXiv:1202.3233. 1.9.1
- [104] M. Habich, J.L. Nagle, and P. Romatschke. Particle spectra and HBT radii for simulated central nuclear collisions of C+C, Al+Al, Cu+Cu, Au+Au, and Pb+Pb from  $\sqrt{s}=62.4-2760$  GeV. 2014. arXiv:1409.0040. 1.9.1, 1.16
- [105] A. Emerick, X. Zhao, and R. Rapp. Bottomonia in the quark-gluon plasma and their production at RHIC and LHC. 2011. arXiv:1111.6537. 1.9.1
- [106] L. Ruan, G. Lin, Z. Xu, K. Asselta, H. F. Chen, et al. Perspectives of a midrapidity dimuon program at RHIC: a novel and compact muon telescope detector. *J. Phys. G*, G36:095001, 2009. arXiv:0904.3774, doi:10.1088/0954-3899/36/9/095001. 1.9.1
- [107] K. Eskola, H. Paukkunen, and C. Salgado. EPS09: a new generation of NLO and LO nuclear parton distribution functions. *JHEP*, 04:065, 2009. arXiv:0902.4154, doi:10.1088/1126-6708/2009/04/065. 1.9.2
- [108] F. Arleo, P.B. Gossiaux, T. Gousset, and J. Aichelin. Charmonium suppression in p-A collisions. *Phys. Rev.*, C61:054906, 2000. 1.9.2
- [109] D.C. McGlinchey, A.D. Frawley, and R. Vogt. Impact parameter dependence of the nuclear modification of  $J/\psi$  production in d+Au collisions at  $\sqrt{s_{NN}} = 200$  GeV. *Phys. Rev.*, C87(5):054910, 2013. 1.9.2
- [110] F. Arleo and S. Peigne. Heavy-quarkonium suppression in p-A collisions from parton energy loss in cold QCD matter. *JHEP*, 03:122, 2013. 1.9.2
- [111] Betty Abelev et al. Long-range angular correlations on the near and away side in p-Pb collisions at  $\sqrt{s_{NN}} = 5.02$  TeV. *Phys. Lett.*, B719:29–41, 2013. 1.9.2
- [112] Georges Aad et al. Measurement with the ATLAS detector of multi-particle azimuthal correlations in p+Pb collisions at  $\sqrt{s_{NN}}=5.02$  TeV. *Phys. Lett.*, B725:60–78, 2013. 1.9.2

- [113] Serguei Chatrchyan et al. Multiplicity and transverse momentum dependence of two- and four-particle correlations in pPb and PbPb collisions. *Phys. Lett.*, B724:213–240, 2013. 1.9.2
- [114] A. Adare et al. Quadrupole Anisotropy in Dihadron Azimuthal Correlations in Central  $d+Au$  Collisions at  $\sqrt{s_{NN}}=200$  GeV. *Phys. Rev. Lett.*, 111:212301, 2013. 1.9.2
- [115] W. Fischer. RHIC Luminosity Upgrade Program. *Conf. Proc.*, C100523:TUXMH01, 2010. 1
- [116] RHIC Beam Projections [online]. URL: <http://www.rhichome.bnl.gov/RHIC/Runs/RhicProjections.pdf>. 1, 8.1
- [117] W. Vogelsang. private communication. 1.10.1, 1.19
- [118] C. Marquet and T. Renk. Jet quenching in the strongly-interacting quark-gluon plasma. *Phys. Lett.*, B685:270–276, 2010. arXiv:0908.0880, doi:10.1016/j.physletb.2010.01.076. 1.10.2
- [119] A. Adare et al. Azimuthal anisotropy of neutral pion production in Au+Au collisions at  $\sqrt{s_{NN}} = 200$  GeV: Path-length dependence of jet quenching and the role of initial geometry. *Phys. Rev. Lett.*, 105:142301, 2010. arXiv:1006.3740, doi:10.1103/PhysRevLett.105.142301. 1.10.2
- [120] J. Casalderrey-Solana, Doga Can Gulhan, Jose Guilherme Milhano, Daniel Pablos, and Krishna Rajagopal. Jet quenching within a hybrid strong/weak coupling approach. *Nucl. Phys., A*, 2014. arXiv:1408.5616. 1.10.2
- [121] Jorge Casalderrey-Solana, Doga Can Gulhan, Guilherme, Daniel Pablos, and Krishna Rajagopal. A Hybrid Strong/Weak Coupling Approach to Jet Quenching. *JHEP*, 1410:19, 2014. arXiv:1405.3864, doi:10.1007/JHEP10(2014)019. 1.10.2
- [122] S. Afanasiev et al. Measurement of Direct Photons in Au+Au Collisions at  $\sqrt{s_{NN}} = 200$  GeV. 2012. arXiv:1205.5759. 1.21
- [123] A. Adare et al. Direct-Photon Production in  $p + p$  Collisions at  $\sqrt{s} = 200$  GeV at Midrapidity. 2012. arXiv:1205.5533. 1.21
- [124] F. Bergsma et al. The STAR detector magnet subsystem. *Nucl. Instrum. Meth.*, A499:633–639, 2003. doi:10.1016/S0168-9002(02)01961-7. 3.3.6
- [125] V. I. Klyukhin et al. The CMS Magnetic Field Map Performance. *IEEE Trans. Appl. Supercond.*, 20:152–155, 2010. arXiv:1110.0607, doi:10.1109/TASC.2010.2041200. 3.3.6
- [126] M. Aleksa et al. Measurement of the ATLAS solenoid magnetic field. *JINST*, 3:P04003, 2008. doi:10.1088/1748-0221/3/04/P04003. 3.3.6

- [127] R.L. Glückstern. Uncertainties in track momentum and direction, due to multiple scattering and measurement errors. *Nucl. Instr. and Meth.*, 24:381, 1963. 4.2.2
- [128] B. D. Leverington et al. Performance of the prototype module of the GlueX electromagnetic barrel calorimeter. *Nucl. Instrum. Meth.*, A596:327–337, 2008. doi:10.1016/j.nima.2008.08.137. 5.2.1
- [129] S. A. Sedykh et al. Electromagnetic calorimeters for the BNL muon (g-2) experiment. *Nucl. Instrum. Meth.*, A455:346–360, 2000. doi:10.1016/S0168-9002(00)00576-3. 5.2.1
- [130] T. Armstrong et al. The E864 lead-scintillating fiber hadronic calorimeter. *Nucl. Instrum. Meth.*, A406:227–258, 1998. doi:10.1016/S0168-9002(98)91984-2. 5.2.1
- [131] R. D. Appuhn et al. The H1 lead / scintillating fiber calorimeter. *Nucl. Instrum. Meth.*, A386:397–408, 1997. doi:10.1016/S0168-9002(96)01171-0. 5.2.1
- [132] D. W. Hertzog, P. T. Debevec, R. A. Eisenstein, M. A. Graham, S. A. Hughes, P. E. Reimer, and R. L. Tayloe. A HIGH RESOLUTION LEAD SCINTILLATING FIBER ELECTROMAGNETIC CALORIMETER. *Nucl. Instrum. Meth.*, A294:446–458, 1990. doi:10.1016/0168-9002(90)90285-E. 5.2.1
- [133] O. D. Tsai et al. Development of a forward calorimeter system for the STAR experiment. *J. Phys. Conf. Ser.*, 587(1):012053, 2015. doi:10.1088/1742-6596/587/1/012053. 5.2.1, 5.3.1, 5.3.2, 5.4
- [134] O.D. Tsai, L.E. Dunkelberger, C.A. Gagliardi, S. Heppelmann, H.Z. Huang, et al. Results of & on a new construction technique for W/ScFi Calorimeters. *J. Phys. Conf. Ser.*, 404:012023, 2012. doi:10.1088/1742-6596/404/1/012023. 5.2.1, 5.4
- [135] Tungsten Heavy Powder. URL: <http://www.tungstenheavypowder.com>. 5.2.3
- [136] R. McNabb, J. Blackburn, J. D. Crnkovic, D. W. Hertzog, B. Kiburg, et al. A Tungsten / Scintillating Fiber Electromagnetic Calorimeter Prototype for a High-Rate Muon g-2 Experiment. *Nucl. Instrum. Meth.*, A602:396–402, 2009. arXiv:0910.0818, doi:10.1016/j.nima.2009.01.007. 5.2.3
- [137] S. Agostinelli et al. GEANT4: A Simulation toolkit. *Nucl. Instrum. Meth.*, A506:250–303, 2003. doi:10.1016/S0168-9002(03)01368-8. 5.3.1, 5.3.7, 6.3.1
- [138] M. Hirschberg, R. Beckmann, U. Brandenburg, H. Brueckmann, and K. Wick. Precise measurement of Birks kB parameter in plastic scintillators. *IEEE Trans. Nucl. Sci.*, 39:511–514, 1992. doi:10.1109/23.159657. 5.3.1
- [139] Klaus Alexander Tadday. *Scintillation Light Detection and Application of Silicon Photomultipliers in Imaging Calorimetry and Positron Emission Tomography*. PhD thesis, Heidelberg U., 2011. URL: <http://www.ub.uni-heidelberg.de/archiv/12959>. 5.3.2

- [140] A. Izmaylov, S. Aoki, J. Blocki, J. Brinson, A. Dabrowska, et al. Scintillator counters with WLS fiber/MPPC readout for the side muon range detector (SMRD) of the T2K experiment. *Nucl. Instrum. Meth.*, A623:382–384, 2010. arXiv:0904.4545, doi: 10.1016/j.nima.2010.03.009. 6.2.1
- [141] Inc. Saint-Gobain Ceramics & Plastics. Scintillating optical fibers. 6.2.1
- [142] Kuraray Co. Ltd. Scintillation materials catalogue. 6.2.1
- [143] T. Matsumura et al. Effects of radiation damage caused by proton irradiation on Multi-Pixel Photon Counters (MPPCs). *Nucl. Instrum. Meth.*, pages 301–308, 2009. doi:10.1016/j.nima.2009.02.022. 7.1.2
- [144] Y. Qiang et al. Radiation Hardness Test of SiPMs for the JLab Hall D Barrel Calorimeter. *Nucl. Instrum. Meth.*, pages 301–308, 2009. doi:10.1016/j.nima.2012.10.015. 7.1.2
- [145] Y. Musienko. Radiation Damage Studies of Silicon Photomultipliers for the CMS HCAL Phase 1 Upgrade. *New Developments in Photodetection Conference Presentation*, 2014. 7.1.2
- [146] Y. Fisyak et al. Thermal neutron flux measurements in the STAR experimental hall. *Nucl. Instrum. Meth.*, pages 68–72, 2014. doi:10.1016/j.nima.2014.04.035. 7.1.2
- [147] W. Anderson et al. Design, Construction, Operation and Performance of a Hadron Blind Detector for the PHENIX Experiment. *Nucl. Instrum. Meth.*, A646:35, 2011. arXiv:1103.4277, doi:10.1016/j.nima.2011.04.015. 7.2.4
- [148] M. Garcia-Valderas et al. The Effects of Proton Irradiation in CoolRunner-II<sup>TM</sup> CPLD Technology. *Radiation and Its Effects on Components and Systems (RADECS), 2008 European Conference on*, pages 131–135, 2008. doi:10.1109/RADECS.2008.5944064. 7.4
- [149] Stephen Scott Adler et al. PHENIX on-line systems. *Nucl. Instrum. Meth.*, A499:560–592, 2003. doi:10.1016/S0168-9002(02)01957-5. 8.1
- [150] M. Allen et al. PHENIX inner detectors. *Nucl. Instrum. Meth.*, A499:549–559, 2003. doi:10.1016/S0168-9002(02)01956-3. 8.2.1
- [151] S. Gundacker, E. Auffray, N. Di Vara, B. Frisch, H. Hillemanns, P. Jarron, B. Lang, T. Meyer, S. Mosquera-Vazquez, E. Vauthey, and P. Lecoq. Sipm time resolution: From single photon to saturation. *Nuclear Instruments and Methods in Physics Research Section A: Accelerators, Spectrometers, Detectors and Associated Equipment*, 718:569 – 572, 2013. Proceedings of the 12th Pisa Meeting on Advanced Detectors La Biodola, Isola d'Elba, Italy, May 20 – 26, 2012. URL: <http://www.sciencedirect.com/science/article/pii/S0168900213001393>, doi:<http://dx.doi.org/10.1016/j.nima.2013.01.047>. 8.2.1